DISSERTATION

Design and Characterization of Functional Self-assembled Monolayers in Context of Organic and Molecular Electronics

Yangbiao Liu
2024

INAUGURAL-DISSERTATION

zur

Erlangung der Doktorwürde

der

Gesamtfakultät für Mathematik, Ingenieur- und Naturwissenschaften

der

Ruprecht-Karls-Universität Heidelberg

Vorgelegt von

M.Sc. Yangbiao Liu
aus Hunan, P.R.China

Tag der mündlichen Prüfung: 06.02.2024

Dissertation

submitted to the

Combined Faculty of Mathematics, Engineering and
Natural Sciences of
Ruprecht-Karls-University of Heidelberg, Germany

for the degree of

Doctor of Natural Sciences

Presented by

M. Sc. Yangbiao Liu
born in: Hunan, P.R.China

Oral examination: 06. 02. 2024

Design and characterization of functional self-assembled monolayers in context of organic and molecular electronics

Referees:

Prof. (apl.) Dr. Michael Zharnikov

Prof. Dr. Petra Tegeder

To my parents, brother, and friends.

Abstract

This thesis deals with the design and characterization of self-assembled monolayers (SAMs) in the context of organic and molecular electronics.

Within the first subproject, I studied the effect of tail group substitution on the charge transport properties of oligophenylenethiolate SAMs on Au(111). Such a substitution is frequently used for electrostatic interface engineering in organic electronics. Specifically, thiolate SAMs with phenyl, biphenyl, and terphenyl backbone and –H, $-CH_3$, –F, and $-CF_3$ substitutions on Au(111) were studied. These SAMs were found to exhibit dense molecular packing and upright orientation. The introduction of –F and especially $-CF_3$ groups significantly elevates the work function (WF) of the system. For the SAMs with the same molecular backbone length, the current density (*J*) demonstrates pronounced dependence on the identity of the tail group (R), with the highest *J* for R= $-CH_3$, followed by R= –H, $-CF_3$, and –F, in decreasing order. No correlation of this behavior with the WF was found; it was tentatively attributed to the difference in the projected density-of-states (PDOS) in the region of the terminal tail groups, the difference in effective electrical contact area at the SAM//Ga_2O_3 interface, and the appearance of an internal electrostatic field (built-in field) within the SAMs, emerging at their contact to the top Ga_2O_3/EGaIn electrode.

Within the quest for an especially high WF for electrostatic interface engineering, thiolate SAMs with phenyl, biphenyl, and terphenyl backbone and $-SF_5$ substitution were studied. These SAMs feature dense molecular packing, upright orientation, and chemically uniform SAM-ambient interface, exclusively composed of the $-SF_5$ moieties. Most importantly, these SAMs exhibit exceptional wetting and electrostatic properties, characterized by an advancing water contact angle (WCA) of 103° and a WF reaching 5.96 eV, which probably is the highest value reported for any aromatic monolayer on gold. They also possess a relatively low tunneling decay coefficient (β) value of 0.38 ± 0.07 $Å^{-1}$, which is typical of oligophenylene backbones and is obviously unaffected by the $-SF_5$ groups. Notably, this group exerts minimal influence on *J* under specific bias compared to analogous SAMs with other electronegative tail groups.

Then, turning to molecular electronics, a further interesting system useful to couple molecular films to carbon nanotubes and graphene is pyrene-substituted SAMs. To this end, I studied two such monolayers with an alkyl (Pyr-C12) and thioether alkyl (Pyr-C4S2) backbones. These SAMs are characterized by homogeneous anchoring to the substrate, dense molecular packing, and exceptional orientational order, as evidenced by the very small inclination of the terminal pyrenyl groups. The specific character of these groups manifests in the WF and WCA of the SAMs. Analysis of charge transport data suggests that pyrene groups exhibit higher conductance compared to alkyl chains of the same length, while the S heteroatoms negatively impact the conductance of the alkyl linker.

Besides, I studied ferrocene-substituted thiofluorene (Fc-FluT) SAMs exhibiting two distinctly different conductivity states (CS) and exceptional rectification in two-terminal junctions. I confirmed the occurrence of these states and rectification with a remarkably high rectification ratio (RR) of ~2100 at 0.1 V bias at the asymmetric bias sweeping (at either positive or negative bias). In addition, I showed that these CSs can also be achieved at the symmetric bias sweeping (between positive and negative bias), with the decisive effect of the polarity of the first sweep. The above special behavior was attributed to the (quasi) non-reversible oxidation of the ferrocenes tail groups in combination with structural and conformational changes in the monolayer geometry. To explore the universality of this peculiar behavior, SAMs of Fc-substituted, triptycene-based tripodes (Fc-Trip) were investigated. These SAMs were found to exhibit similar behavior as the Fc-FluT monolayers, but with a lower RR of 400-600 (at 0.1-0.2 V) correlating well with the density of the Fc groups.

Finally, I studied another intriguing system, namely custom-designed phosphonate SAMs with potential memristor properties. My part in this project was the profound characterization of these SAMs, serving as an indispensible prerequisite for the reliable electrical measurements on these systems, performed by our partners. It was assumed that the newly designed SAMs should have largely improved performance as compared to the previously reported systems. The improvement was based on replacing Al/AlO_x with TiN as a new electrode material and employing phosphonate molecules with a rigid aromatic linker as the key design motif for the molecular backbone. This design restricted the possible molecular conformations to only two major states of opposite polarity. The above measures resulted in an increase of the current density by 5 orders of magnitude as well as in an ON/OFF conductance ratio which was more than 10 times higher than the individual scattering ranges of the high and low resistance states.

Zusammenfassung

Die vorliegende Arbeit befasst sich mit dem Design und der Charakterisierung selbstorganisierter Monoschichten (engl. *self-assembled monolayers*, SAMs) im Bereich der organischen und molekularen Elektronik.

Im ersten Teilprojekt habe ich die Auswirkung der Schwanzgruppensubstitution auf die Ladungstransporteigenschaften von Oligophenylenthiolat-SAMs auf Au(111) untersucht. Eine solche Substitution wird häufig für die elektrostatische Grenzflächentechnik in der organischen Elektronik verwendet. Insbesondere wurden Thiolat-SAMs mit Phenyl-, Biphenyl- und Terphenyl-Rückgrat und –H, $-CH_3$, –F-und $-CF_3$-Substitution an Au(111) untersucht. Es konnte festgestellt werden, dass diese SAMs eine dichte Molekülpackung und eine aufrechte Ausrichtung aufweisen. Die Einführung von –F und insbesondere $-CF_3$-Gruppen erhöhte die Austrittsarbeit (engl. *work function*, WF) des Systems erheblich. Für die SAMs mit der gleichen Molekülrückgratlänge zeigte die Stromdichte (J) eine ausgeprägte Abhängigkeit von der Identität der Schwanzgruppe (R), mit dem höchsten J für R= $-CH_3$, gefolgt von R= –H, $-CF_3$, und –F, in absteigender Reihenfolge. Es wurde keine Korrelation dieses Verhaltens mit der WF gefunden. Zurückgeführt wurde dies vorläufig auf die Unterschiede in der projizierten Zustandsdichte (engl. *projected density-of-states*, PDOS) im Bereich der terminalen Schwanzgruppen, der effektiven elektrischen Kontaktfläche an der SAM//Ga_2O_3-Grenzfläche und auf das Auftreten eines internen elektrostatischen Feldes (eingebautes Feld) innerhalb der SAMs, welches an deren Kontakt zur oberen Ga_2O_3/EGaIn-Elektrode entsteht. Bei der Suche nach einer besonders hohen WF für die elektrostatische Grenzflächentechnik wurden Thiolat-SAMs mit Phenyl-, Biphenyl- und Terphenyl-Rückgrat und $-SF_5$-Substitution untersucht. Diese SAMs zeichnen sich durch eine dichte Molekülpackung, eine aufrechte Ausrichtung und eine chemisch einheitliche SAM-Umgebungsschnittstelle aus, die ausschließlich aus den $-SF_5$-Einheiten besteht. Am wichtigsten ist, dass diese SAMs außergewöhnliche Benetzungs- und elektrostatische Eigenschaften aufweisen, die durch einen fortschreitenden Wasserkontaktwinkel (engl. *water contact angle*, WCA) von 103° und einer WF von 5.96 eV gekennzeichnet sind, was wahrscheinlich der höchste Wert ist, der für eine aromatische Monoschicht auf Gold berichtet wurde. Sie besitzen außerdem einen relativ niedrigen Wert des Tunnelzerfallskoeffizienten (β) von 0.38 ± 0.07 $Å^{-1}$, der typisch für Oligophenylen-Rückgrate ist und offensichtlich von den $-SF_5$-Gruppen nicht beeinflusst wird. Bemerkenswerterweise übt diese Gruppe im Vergleich zu analogen SAMs mit anderen elektronegativen Schwanzgruppen unter spezifischer Vorspannung nur einen minimalen Einfluss auf J aus.

Wenn wir uns der molekularen Elektronik zuwenden, stellen Pyren-substituierte SAMs ein weiteres interessantes System dar, welches sich zur Kopplung molekularer Filme an Kohlenstoffnanoröhren und Graphen eignet. Zu diesem Zweck habe ich zwei solcher

Monoschichten mit einem Alkyl- (Pyr-C12) und einem Thioether-Alkyl-Rückgrat (Pyr-C4S2) untersucht. Diese SAMs zeichnen sich durch eine homogene Verankerung am Substrat, eine dichte Molekülpackung und eine außergewöhnliche Orientierungsordnung aus, was durch die sehr geringe Neigung der terminalen Pyrenylgruppen belegt wird. Der spezifische Charakter dieser Gruppen manifestiert sich in der WF und dem WCA der SAMs. Die Analyse der Ladungstransportdaten legt nahe, dass Pyrengruppen im Vergleich zu Alkylketten gleicher Länge eine höhere Leitfähigkeit aufweisen, während die S-Heteroatome die Leitfähigkeit des Alkyllinkers negativ beeinflussen.

Außerdem habe ich Ferrocen-substituierte Thiofluoren-SAMs (Fc-FluT) untersucht, die zwei deutlich unterschiedliche Leitfähigkeitszustände (engl. *conductivity states*, CS) und eine außergewöhnliche Gleichrichtung in zweiterminalen Verbindungen aufweisen. Ich habe das Auftreten dieser Zustände und die Gleichrichtung mit einem bemerkenswert hohen Gleichrichtungsverhältnis (engl. *rectification ratio*, RR) von ~2100, bei 0.1 V Vorspannung, beim asymmetrischen Vorspannungsdurchlauf (entweder bei positiver oder negativer Vorspannung) bestätigt. Darüber hinaus habe ich gezeigt, dass diese CSs auch beim symmetrischen Bias-Sweep (zwischen positivem und negativem Bias) erreicht werden können, wobei die Polarität des ersten Sweeps den entscheidenden Einfluss hat. Das obige besondere Verhalten wurde auf die (quasi) irreversible Oxidation der Ferrocen-Schwanzgruppen in Kombination mit Struktur- und Konformationsänderungen in der Monoschichtgeometrie zurückgeführt. Um die Universalität dieses besonderen Verhaltens zu untersuchen, wurden SAMs von Fc-substituierten Triptycen-basierten Tripoden (Fc-Trip) untersucht. Es wurde festgestellt, dass diese SAMs ein ähnliches Verhalten wie die Fc-FluT-Monoschichten zeigen, jedoch mit einem niedrigerem RR von 400–600 (bei 0.1–0.2 V), was gut mit der Dichte der Fc-Gruppen korreliert.

Schließlich habe ich ein weiteres faszinierendes System untersucht, nämlich maßgeschneiderte Phosphonat-SAMs mit potenziellen Memristoreigenschaften. Mein Anteil an diesem Projekt war die tiefgreifende Charakterisierung dieser SAMs, die eine unverzichtbare Voraussetzung für die zuverlässigen elektrischen Messungen an diesen Systemen darstellt, die von unseren Partnern durchgeführt werden. Es wurde davon ausgegangen, dass die neu entwickelten SAMs im Vergleich zu den zuvor gemeldeten Systemen eine deutlich verbesserte Leistung aufweisen sollten. Die Verbesserung basierte auf dem Ersatz von Al/AlO_x durch TiN als neues Elektrodenmaterial und der Verwendung von Phosphonatmolekülen mit einem starren aromatischen Linker als Schlüsseldesignmotiv für das molekulare Rückgrat. Dieses Design beschränkte die möglichen Molekülkonformationen auf nur zwei Hauptzustände entgegengesetzter Polarität. Die oben genannten Maßnahmen führten zu einer Erhöhung der Stromdichte um fünf Größenordnungen sowie zu einem EIN/AUS-Leitfähigkeitsverhältnis, das mehr als zehnmal höher war als die einzelnen Streubereiche der Zustände hohen und niedrigen Widerstands.

Table of Contents

1. Introduction

Self-assembled monolayers (SAMs) have since long become an important part of mordern nanotechnology.[1,2] They display superior adaptability and versatility that place them at the forefront of diverse scientific disciplines. These systems have attracted a lot of attention in recent years because of their potential applications in various fields, such as surface and interface engineering, biosensors, organic and molecular electronics, and corrosion protection.[3,4] SAMs are two-dimensional molecular films formed by predominantly rod-like molecules on different substrates.[1,2,5] They are usually comprised of three essential building blocks, viz., an anchoring group, mediating the binding to a specific substrate, a functional tail group, constituting the SAM-ambient interface, and a rod-like molecular backbone, driving the self-assembly and mediating orientational order and dense molecular packing in the SAMs.[5]

The organized architecture of SAMs, rooted in the interplay of the relevant structure-building interactions, reveals a diversity of configurations and properties. At a proper choice of SAM-forming molecules, they cover a particular surface completely, with the anchoring groups bound to the substrate and the tail groups exposed to ambient. Because of this specific organization and dense molecular packing, the chemical and physical character of a particular surface can then be completely redefined, which is of primary importance in the context of applications.

Among other fields, SAMs emerge as important components in the landscape of organic and molecular electronics, offering a gateway to electronic device fabrication. They serve as an important component or even basis for building complex electronic devices, offering good precision and adaptability. This thesis delves into the design and characterization of functional SAMs within this context, emphasizing their role in advancing electronic functionalities, notably exploring charge transport and electrostatic engineering.

In the domain of organic electronics, the focus of this thesis is on the electrostatic engineering of substrates and interfaces, important for the energy level alignment at the interfaces, and on electric transport properties of the respective SAMs, important for the efficiency of charge transport across these interfaces. Since all organic electronic and organic photovoltaic devices are multilayer systems, the respective control of the interfaces is an important aspect of optimizing their efficiency and functionality.[6]

Particularly interesting systems in this context are halogen-decorated SAMs, in which the terminal hydrogen atom is substituted by a halogen atom or a halogen-containing group, possessing intrinsic electronegativity and polarizability, and introducing thus a dipole moment directed to the substrate. It was shown recently that such a substitution influences significantly the tunnelling current across the molecular junction for both aliphatic and aromatic SAMs.[7,8,9] Interestingly, not only the

absolute current value but also the tunnelling attenuation coefficient β defining the dependence of current on the molecular length, is affected by the substitution.[10,11] The latter was demonstrated for aliphatic SAMs only, with the tunnelling attenuation coefficient β decreasing noticeably when the terminal H is replaced by halogen atom (e.g. from 0.75 $Å^{-1}$ to 0.25 $Å^{-1}$ for I).[12,13] This behavior was related to such parameters as tunnelling barrier height and shape, the width of the HOMO-LUMO gap, contact resistance, and dielectric constant, but it was impossible to determine which parameter is mainly responsible.[14] In view of the above ambiguity and the different behavior of the aliphatic and aromatic SAMs at the halogen substitution of the terminal hydrogen atom/atoms,[3,4,15] we considered it reasonable to look at the effect of such a substitution on the current values and tunnelling decay coefficient in the aromatic monolayers in more detail.[16] Consequently, the first research subproject within the present thesis was focused on a series of non-substituted (−H) and −F, $-CH_3$, and $-CF_3$-substituted oligophenylthiolate SAMs on Au (111) (Fig. 1.1a), with the emphasis on their electrostatic and charge transport properties. The respective results are presented and discussed in Chapter 4.1. The length of the molecular backbone was varied by going from the single benzene ring to the biphenyl and terphenyl backbone. Apart from the electrostatic and charge transport properties, a combination of several complementary spectroscopic techniques was applied to verify the quality of the SAMs and to obtain the major parameters characterizing the molecular organization in these films.

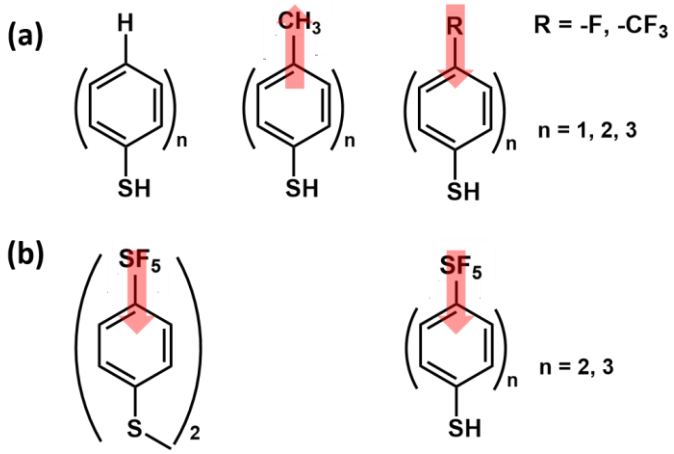

Figure 1.1 SAM-forming molecules and dipole moments of their tail groups (marked by the red arrows): (a) oligophenylthiols with different substituents (–H, $-CH_3$, –F, $-CF_3$) and (b) $-SF_5$-substituted oligophenylenethiols and disulfides.

Among the tail groups studied, the $-CF_3$ group provided the major effect in terms of an increase in the work function of the surface and hydrophobicity, which can be favorable for wetting properties

and tuning the growth morphology for deposited overlayers.[17] We speculated that these properties can be further enhanced if more than three fluorine atoms are used. This was, however, hardly possible for the tetravalent carbon atom but well accessible for sulfur, building up to six bonds to other atoms. Consequently, we targeted the $-SF_5$ substitution, relying on our experience with fluorinated SAMs and very limited literature data for the monolayers of SF_5-substituted oligophenylenethiols and disulfides.[18,19] Note that the electrostatic properties of the latter films were not monitored and the wetting properties were found to depend strongly on the length and character (perfuoroalkyl vs. alkyl) of the molecular chain. In this context, we decided to revisit this issue, designing and synthesizing (contribution by our partners) a series of SF_5-substituted oligophenylenethiols and disulfides (Fig. 1.1b) and preparing and characterizing in very detail the respective SAMs on polycrystalline Au (111) substrates. The respective results are presented and discussed in chapter 4.2. The emphasis was put on the molecular organization of these SAMs and their electrostatic properties, important in the context of applications. Note that the selection of the oligophenylene backbone, in contrast to the alkyl and perfuoroalkyl backbones used before, was intentional, in view of the better charge transport properties, important for applications as well.[20,21]

The further subprojects within the present thesis were related to molecular electronics. The basic idea of molecular electronics is design, synthesis, and assembly of molecules that can perform the same functions as individual building blocks of semiconductor electronic circuits. To this end, a variety of prototype molecular devices, such as switches, memory units, rectifiers, memristors, and even transistors were reported, performing their specific functions either as single molecules or as molecular assembles, arranged, e.g., on a solid substrate as SAMs.[22] I used the respective knowledge and published data as the basis for my research.

The first subproject in this context was related to pyrene-decorated SAMs. Pyrene, as one of the interesting and application-relevant tail groups, is a polycyclic aromatic hydrocarbon with a unique structure that contains four fused and strongly conjugated phenyl rings in a specific configuration. It has the possibility of functionalization,[23,24] which, in particular, makes it possible to tune its HOMO− LUMO gap and fluorescence behavior.[25,26] Based on the above aspects and some other favorable properties,[27,28] pyrene plays a certain role as the functional tail group of SAMs. For such SAMs, viz. those of pyrene-substituted undecanethiol (Pyr-C11), distinct rectification properties were reported.[27,28,29] However, whereas the charge transport data for these SAMs look reliable, the related spectroscopic data,[28] appear questionable in our opinion and cast therefore some doubt regarding the quality of these monolayers and, consequently, the respective charge transport data as well. To this end, we decided to revisit this system, taking a SAM of pyrene-substituted dodecanethiol (Pyr-C12; see Fig. 1.2a) on Au(111) as a representative test monolayer. Pyr-C12 has

been used in context of device fabrication before,[30] but the respective SAM has not been characterized. In addition, we also studied the SAM of 2-{[2-(Pyren-1-ylthio)ethyl]thio}ethane-1-thiol (Pyr-C4S2; see Fig. 1.2b) on Au(111), which features heteroatom (sulfur) substitution in the alkyl linker. Such a substitution is considered as a promising approach in the context of molecular electronics. Both monolayers were characterized by several complementary techniques, the focus was put on high quality spectroscopic data (in contrast to refs[31,32,33]) and on charge transport properties. The respective results are presented and discussed in Chapter 4.3.

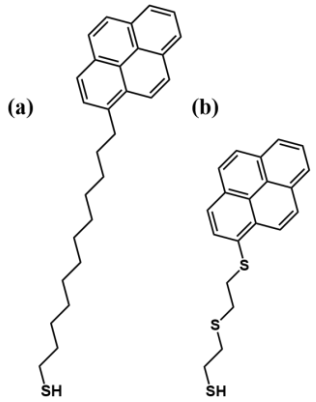

Figure 1.2 SAM-forming molecules with pyrene tail group: (a) Pyr-C12, (b) Pyr-C4S2.

A further important building block of molecular electronics is ferrocene, well known for its redox properties. A combination of ferrocenyl (Fc) and its derivatives attached to aliphatic backbones and anchored to a substrate by thiolate docking groups resulted in a family of highly efficient molecular rectifiers.[34,35] In particular, it has been reported that the rectification ratio (RR) of SAMs featuring terminal Fc units or Fc−C≡C−Fc groups are 90-180 and 10^5, respectively.[34,36] These RR values were however recorded at a bias of 1-3 V. In contrast, as shown by the previous studies in our group,[37] an efficient RR exceeding 10^3 can be achieved at the much lower bias of 0.1 V as far as SAMs of fully conjugated Fc- and ruthenocenyl (Rc)-substituted biphenyl/fluorene thiols (Fc/Rc-BPT/FluT) are used and asymmetric bias sweeping mode is applied. These SAMs exhibit two distinctly different conductivity states which can be accessed by successive sweeping at either a negative bias (high conductance state, HCS) or a positive bias (low conductance state, LCS) bias.[37] We wanted to study further the respective behavior focussing on the Fc-FluT (Fig. 1.3a) and extending the range of the bias sweeping mode to symmetric and pulsed sweeping. The respective results are presented and discussed in Chapter 4.4.

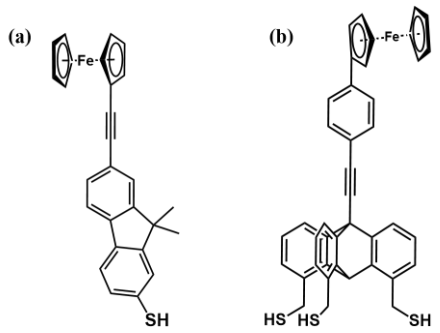

Figure 1.3 Structure of the SAMs-forming molecules with Fc redox-active tail group: (a) ferrocenyl substituted fluorene thiols (Fc-FluT) and (b) Fc-substituted, triptycene-based tripodes (Fc-Trip).

Dealing further with the Fc building block, we addressed the question of whether the observed, special rectification behavior is exclusively characteristic of the fully conjugated, rod-shaped systems, such as Fc-FluT, or it is a more general phenomenon. To address this question, investigations on a different system were conducted within my PhD project. Specifically, charge transport properties of Fc-substituted, triptycene-based tripodes (Fc-Trip; Fig. 1.2b), arranged as SAM on Au (111), were studied. This molecule, built around the versatile triptycene ´core´, is not entirely conjugated since it contains aliphatic bridges, connecting the individual phenyl blades, and methylene linker at the anchoring group, promoting tripodal self-assembly. The electrochemical properties of individual Fc-Trip molecules, embedded into a suitable matrix, were studied recently by electrochemical scanning tunneling microscopy (STM),[38] with the oxidation-state dependent changes in electron transfer being recorded. In contrast, within my PhD project, a monomolecular ensemble of these molecules was studied. A typical two-terminal junction setup, mimicking a practical device, was used. The respective results are presented and discussed in Chapter 4.5.

Finally, a novel system of electrically switchable SAMs was studied. In this context, the group of our partner, Prof. P. Kirsch (TU Darmstadt), previously reported the feasibility of memristive switching with liquid crystal-inspired SAMs embedded as tunnel junctions between solid-state contacts.[39] They covalently anchored the component molecule 1 (shown in Fig. 1.4) to the Al substrate by a phosphonic acid group and studied the $Al/Al_2O_3/1/Pb/Ag$ devices. Their dipole moments couple to an external electrical field, and changes in tunnel current are induced by a conformational reorganization and concomitant change of dipole orientation in the monolayer. Although the ON/OFF ratio of the SAM 1 was quite large, the I-V curves showed large scattering, which significantly reduced the reliably addressable states.[40] To solve this and some other problems,[14,41] it was decided to improve the device architecture by designing different switchable molecules and using different contact materials. Accordingly, aluminum oxide was replaced by

titanium nitride as the bottom electrode and lead was replaced by titanium as the top electrode. In addition, as the most important modification, molecule 2 instead of 1 (see Fig. 1.4) was designed. This molecule features better-defined conformational states, providing stability of the tunneling currents, and a large HOMO-LUMO gap due to replacing the flexible aliphatic part in molecule 1 with a rigid aromatic linker. My part in the project was the characterization of the relevant molecular films and related reference systems (molecule 15, 16, and 3 in Fig. 1.4) by spectroscopic techniques, which was an indispensible prerequisite for the reliable electrical measurements on these systems, performed by our other partner within this subproject, the group of Prof. M. Tornow (TU Munich). The respective results are presented and discussed in Chapter 4.6.

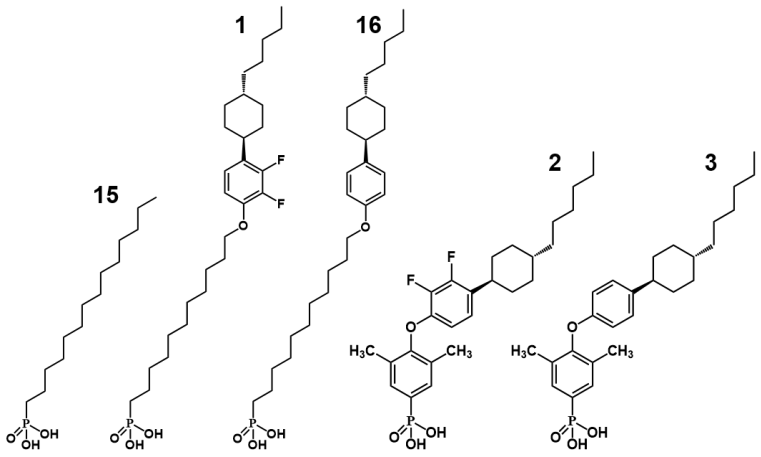

Figure 1.4 Molecular structure of the SAMs-forming molecules studied in the context of electrically switchable monolayers. Molecule 1 has high configuration flexibility and has been previously reported by Prof. P. Kirsch's group.[39] Molecule 2 represents a new design of electrically switchable molecule; in which the flexible aliphatic part in molecule 1 is replaced with a rigid aromatic linker. All other molecules represent reference systems.

Most of the results presented in this thesis have already been published or submitted to peer-reviewed journals. In each section, the respective publications will be cited. In addition, all publications that served as the basis for this thesis are listed in the Appendix. The publications have been prepared in cooperation with our partners and their contributions to the particular subprojects are specifically described as those in the text and in the captions of the corresponding figures, as far as these data are necessary for the general understanding of the issues discussed in the context of a particular project.

2. Basics and Background

2.1 Self-assembled Monolayers

Self-assembled monolayers, commonly referred to SAMs, are usually formed by the spontaneous assembly of organic molecules or nanoparticles at a solid surface, resulting in a well-defined and ordered monolayer. SAMs have been formed on various substrates according to some reports, such as Au, Ag, Pt, and Cu, etc.[42,45,46] But Au substrate is quite widely used in the laboratory, due to some advantages, such as excellent stability and chemical inertness, strong binding affinity, well-defined surface chemistry, and so on.[41,43,44]

In general, the SAMs typically consist of three parts: the anchoring group, the backbone, and the tail group, shown in the Fig. 2.1. Firstly, the anchoring group is responsible for attaching the SAMs to the substrate surface. It forms a strong and stable bond with the substrate, ensuring the monolayer's adhesion and stability. Common anchoring groups include thiol (−SH) for Au surfaces, silane ($-SiX_3$, X = alkyl or aryl group) for Si surfaces, and phosphonic acid ($-PO_3H_2$) for metal oxides.[31,39,47] We choose thiol as the anchoring group usually depending on the substrate and the corresponding chemical ambient, here it's contributed to the Au−S bond formed on Au substrate. Next, the backbone serves as a linker or spacer between the anchoring group and the tail group. It provides the necessary flexibility or rigidity to control the packing density, orientation, and ordering of the SAMs. The backbone can be composed of various chemical moieties, such as aromatic moieties and aliphatic moieties. The selection of the backbone depends on factors such as desired surface coverage, intermolecular interactions, and the overall geometry of the SAMs.[32,48] Thus the aromatic moieties were chosen here. Finally, as for the tail group, it's responsible for providing the desired surface functionality or properties to the SAMs. It determines the SAM's interaction with the surrounding environment, including its wettability, chemical reactivity, or specific molecular recognition. Their chemical composition, size, and shape can be tailored to achieve the desired surface functionality, molecular recognition, and so on.

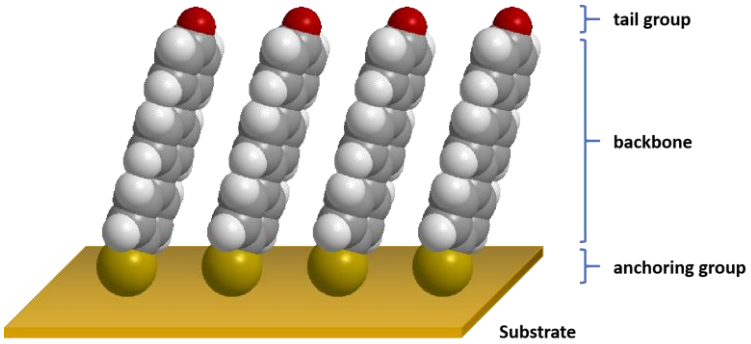

Figure 2.1 Illustration of SAMs with ideally ordered assembled (the explanation of the building blocks of SAM-forming molecules is on the right side).

Besides, the formation of SAMs is also an interesting process, which usually involves multiple self-assembly methods, such as solution-based self-assembly, vapor phase deposition, and Langmuir-Blodgett (LB) technique.[33,49] Compared with others, the solution-based self-assembly has superior versatility and accessibility, which allows for the formation of SAMs on a wide range of substrates, and can be implemented easily due to not requiring specialized equipment or complex procedures. And it can also introduce different functional groups or molecules to form SAMs with specific functionalities or hybrid structures at a low cost. In this process, SAMs are formed by immersing the Au substrate into a solution containing the precursor molecules. The self-assembling molecules in the solution adsorb onto the substrate surface, driven by various intermolecular forces and interactions. Notably, the formation of the SAMs occurs through the replacement of solvent molecules at the substrate surface with the self-assembling molecules, which typically involves several steps such as cleaning and functionalization of the substrate surface, immersion in the self-assembling molecule solution, and rinsing to remove any unbound molecules, shown in Fig. 2.2. The formation process can be assisted by factors such as temperature, time, and solution concentration.

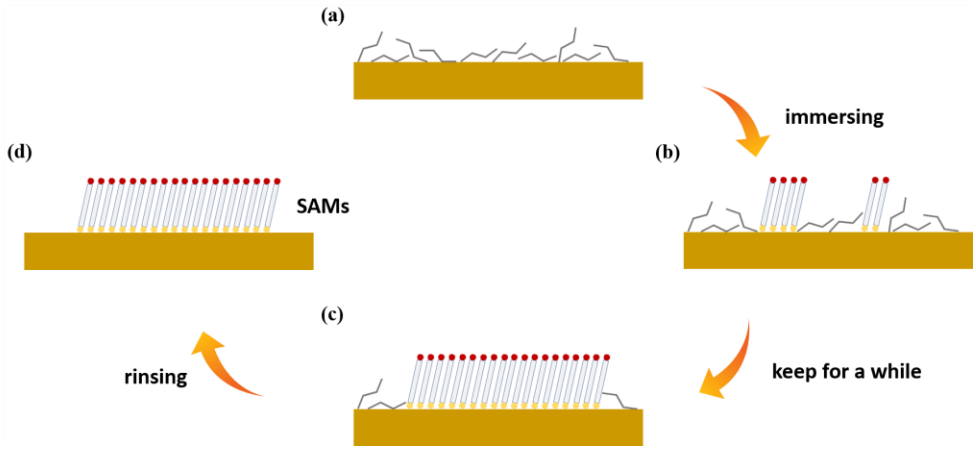

Figure 2.2 Schematic picture of the molecules' self-assembling process: (a) cleaning and functionalizing the substrate surface; (b) immersing the substrate into the solution; (c) keeping the solution with the substrate in a specific condition for a while; (d) obtaining the SAMs after rinsing.

2.2 X-ray Photoelectron Spectroscopy

X-ray photoelectron spectroscopy (XPS) has emerged as a powerful technique for the surface analysis and characterization of various materials across numerous scientific disciplines, and it has played a role as a versatile and widely used analytical technique for probing the surface composition, electronic structure, and chemical state of materials. XPS relies on the photoelectric effect, in which X-ray photons are used to eject core-level electrons from the surface of a material,[50] and the corresponding principles are illustrated in Fig. 2.3. Simply put, the electrons in sample inner shell will be ejected from the atoms after the sample absorbs X-ray photons when they are irradiated with monoenergetic soft X-rays (energies lower than ~6 KeV), which will cause the surface of the sample to emit photoelectrons. Notably, the emitted photoelectrons are the result of the complete transfer of the X-ray energy to core-level electrons,[51] and the corresponding formula are as following:

$$h\nu = BE + KE + \Phi_{spectrometer} \qquad (2-1)$$

where hν is the energy of X-ray photons being used, BE is the binding energy of the electron, KE is kinetic energy of the electron that is emitted, and $\Phi_{spectrometer}$ is the spectrometer work function. The binding energies of the photoelectrons are characteristic of the elements and their chemical environments, enabling the identification and quantification of surface species. By measuring the kinetic energies and intensities of the emitted photoelectrons, valuable information about the elemental composition chemical bonding, and oxidation states of the surface species can be obtained.

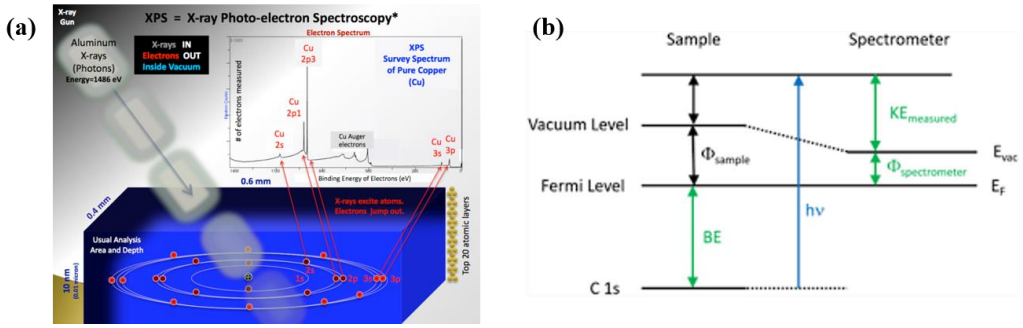

Figure 2.3 (a) Basic conditions and processes for experimental X-ray photoelectron spectroscopy.[51] (b) Energy level diagram illustrates schematically the basic XPS equation, including the x-ray source energy (hυ), the binding energy of the electron (BE), the measured kinetic energy of the electron ($KE_{measured}$), and the work function of the spectrometer ($\Phi_{spectrometer}$).[52]

Based on the above theory, P.D. Innes et al.[53] recorded the first XPS spectrum, and the XPS technology have been further developed in the following decades to become a very mature surface-sensitive quantitative spectroscopic technique at present. It typically involves three main components: an X-ray source, an energy analyzer, and an energy detector, as shown in Fig. 2.4. First, photoelectrons are excited by X-rays at a certain energy. The most commonly used source is a monochromatic X-ray source, such as MgKα X-rays source (1253.6 eV) and AlKα X-rays source (1486.6 eV).[54,55] Secondly, the energy analyzer is responsible for separating the emitted electrons based on their kinetic energy. It consists of various components, such as an electron lens system, a monochromator, and an electron energy analyzer. Its main function is to measure the kinetic energy of the emitted electrons and to filter out unwanted energy ranges or background signals. The process allows for the determination of the binding energies of the electrons, which is crucial for identifying the elements and chemical states present in the sample. Finally, the energy detector captures and measures the kinetic energy of the electrons that pass thorough the energy analyzer. It can be based on various technologies, such as a hemispherical analyzer or a cylindrical mirror analyzer. Its primary function is to convert the kinetic energy of the electrons into an electrical signal that can be analyzed and processed. By measuring the kinetic energy, the detector enables the determination of the binding energy spectra of the emitted electrons, which provides valuable information about the electronic structure and chemical composition of the sample. In summary, the X-ray source provides the necessary energy to excite the electrons, the energy analyzer separates the emitted electrons based on their kinetic energy, and the energy detector measures and converts the kinetic energy of the electrons into an electrical signal for analysis. By the way, it must be operated in ultrahigh vacuum system (< 10^{-7} Pa) in order to detect the electrons and avoid surface

reactions/contaminations. Together, these components enable the acquisition of XPS spectra, for example, shown in Fig. 2.3a.

Additionally, chemical shifts could happen when using XPS. This is caused by the fact that binding energy doesn't only depend on the shell of the electron, but also depends on the environment, that is, the bonds that the atom in question partake in.[56]

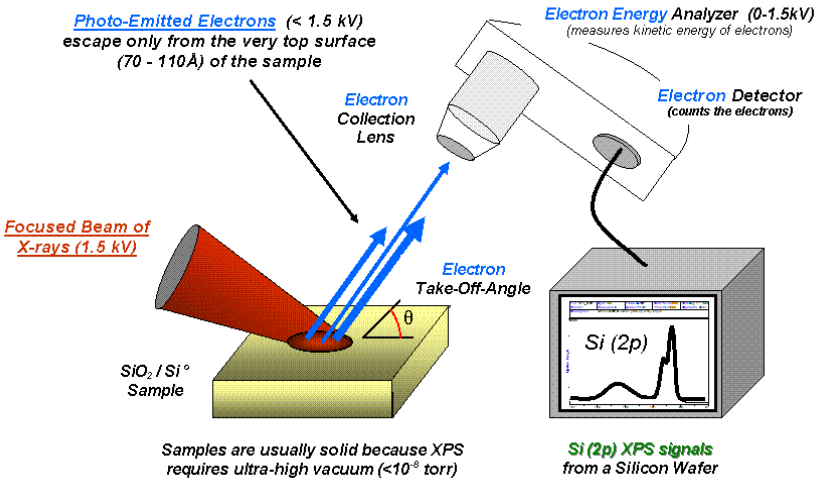

Figure 2.4 Schematic of XPS spectrometer setup.[51]

Besides, except the elemental identification and chemical state characterization, more quantitative information can be obtained from the XPS spectra. Firstly, the resonance intensity of each peak needs to be fitted, so the fitting background type needs to be selected in advance during this process. For example, the "Shirley" type is usually chosen as the background for the Au 4f element, and the "Linear" type is usually chosen for the other elements. Then we use "Lorentzian-Gaussian" function to recreate the peaks of each orbital after subtracting the background and obtain their peak area. As we know, the corresponding thickness (d) of the monolayer is usually determined by measuring the intensity of C 1s ($I_{C\ 1s}$) and Au 4f ($I_{Au\ 4f}$) signals,[57] and their calculation formulas are generally as follows:

$$\frac{I_{C\ 1s}}{I_{Au\ 4f}} = K\frac{1-\exp(-\frac{d-z}{\lambda_{C\ 1s}})}{\exp(-\frac{d}{\lambda_{Au\ 4f}})} \qquad (2\text{-}2)$$

where λ_i is the attenuation length for C 1s/Au 4f signal, z is the distance from the gold surface to the first carbon atom and K is a constant depending on the equipment specification. The K constant was determined to be 0.0613 using the Hexadecanethiol on the gold surface as a reference. The attenuation length λ_i was calculated using standard formula:

$$\lambda_i = 0.3E_k^{0.64} \qquad (2\text{-}3)$$

where the E_k is the kinetic energy of electrons. Notably, the constant K could be different as it strongly depends on the system used. When calculating the attenuation length for different substrates (such as Ag, Au, and C), we just put a proper kinetic energy of electrons from that elements to the above queation.[58]

2.3 Synchrotron-based Techniques

As mentioned above in XPS, Mg Kα and Al Kα X-rays source are the most commonly used in photoelectron spectroscopy characterization. In fact, there is a more fascinating source that can be used in testing and characterization in many fields such as physics and chemistry, that is, synchrotron radiation. Synchrotron radiation is a type of electromagnetic radiation emitted by charged particles, typically electrons or positions, as they are accelerated and forced to move along curved paths in the presence of strong magnetic fields,[59] as shown in the Fig. 2.5. Relatively speaking, it has some advantages. Firstly, synchrotron radiation is extremely intense, producing much brighter and more powerful beams of light than conventional sources, such as X-ray tubes, so samples can be studied in greater detail. In addition, it is highly collimated, meaning that the emitted light is focused into a tight, well-defined beam, which facilitates precise measurement and imaging techniques. Therefore, we performed some experiment involving synchrotron radiation using the Electron Storage Ring BESSY II in Berlin, and the details are as follows.

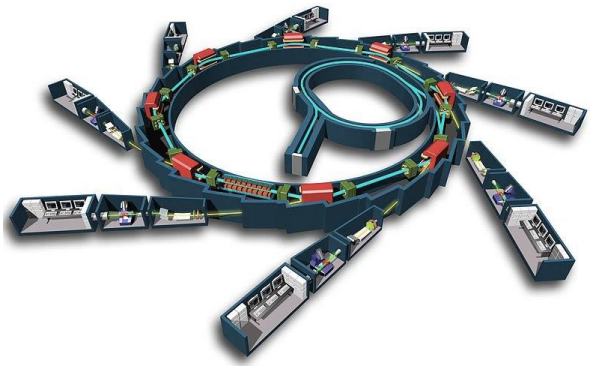

Figure 2.5 Schematic of a synchrotron radiation facility.[60]

2.3.1 High-Resolution X-ray Photoelectron Spectroscopy

In general, the overall testing mechanism of high-resolution X-ray photoelectron spectroscopy (HRXPS) is similar to that of XPS. But there are still some differences, which are mainly caused

by using synchrotron radiation as the sour ce. To illustrate these distinctions in further detail, I will use an example to explain, as shown in Fig. 2.6. Notably, both S 2p peaks were normalized and comparable. First of all, the profile of the S 2p peak obtained under synchrotron radiation source is clearer than that obtained under the laboratory, where we can clearly observe the S 2p doublet at a PE of 350 eV compared with that at 1254 eV. In addition, after fitting by the "XPS peak" software, almost all the measurement data coincide with the fitting curve at a PE of 350 eV, while they are evenly dispersed near the fitting curve at a PE of 1254 eV. And it can be found that the fitting peak area of S 2p at 350 eV is about 945, which is much larger than that of 26 at 1254 eV, which shows that the S 2p peak measured under the synchrotron radiation exhibited a greater intensity. The reason may be two aspects. On the one hand, the X-rays generated by the synchrotron radiation have higher photon energy and flux compared to the lab source (such as Mg Kα), so they can penetrate deeper into the SAMs, resulting in increased photoemission of electrons.[61,62] On the other hand, it's determined by the cross-section of the photoemission. Because the adsorption cross-section depends strongly on the X-ray photon energy, and synchrotron radiation typically operates at much higher energies compared to the Mg Kα source.[63] HRXPS measurement can help us obtain clearer and more detailed spectral data.

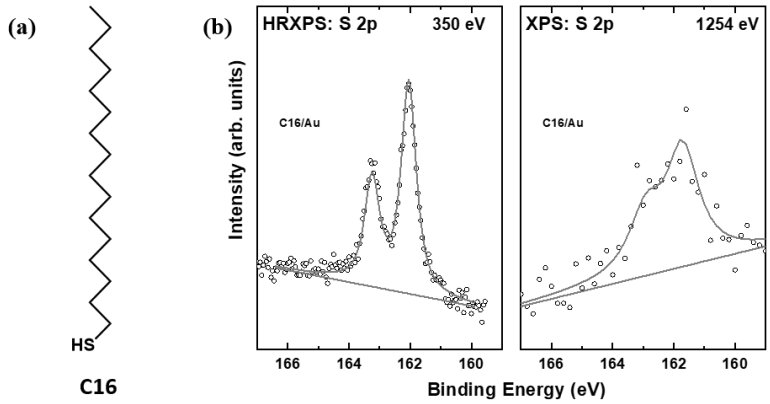

Figure 2.6 (a) Chemical structure of Hexadecanethiol (C16), (b) The S 2p XPS spectra of C16 SAMs on Au measured in the lab with Mg Kα at PE of 1254 eV and at BESSY II with synchrotron radiation source at PE of 350eV.

2.3.2 Near Edge X-ray Absorption Fine Structure Spectroscopy

Similarly, in addition to HRXPS characterization, synchrotron radiation sources can also be used for NEXAFS technology. NEXAFS is an adsorption spectrum whose core is the phenomenon of X-ray absorption.[63] The basic process behind NEXAFS spectroscopy is illustrated in Fig. 2.7. Core level electrons, such as C 1 s, N 1 s, O 1 s, etc. for organic molecules building SAMs, are excited

into unoccupied molecular orbitals with the respective increase of the absorption intensity at the corresponding excitation energy. Varying the photon energy over the specific absorption edge, the entire, system-specific pattern of unoccupied molecular orbitals can thus be sampled. A spectrum represents a superposition of slightly asymmetric absorption resonances and an absorption edge (or edges), corresponding to the excitation into continuum states above the vacuum level. The width of the resonances increases progressively with increasing photon energy, following the decrease in the lifetime of the respective excited states.[64]

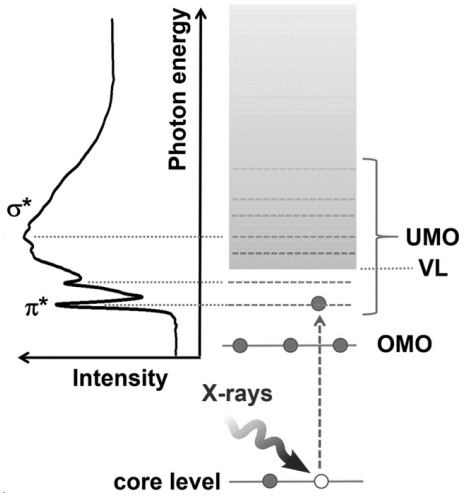

Figure 2.7 Schematic illustration of the basic process behind the NEXAFS spectroscopy.[65] Core-level electrons are excited into unoccupied molecular orbitals (UMOs) with the respective increase of the absorption intensity. Varying the photon energy over the specific absorption edge, the entire, system-specific pattern of UMOs, both below and above the vacuum level (VL), can be sampled. Occupied molecular orbitals (OMOs) can be, if necessary, complementary accessed by ultraviolet photoemission spectroscopy.

The primary excitation can be performed at different absorption edges, addressing a particular part or a building block of the SAM-forming molecules. In most cases, the pattern of the absorption resonances is more characteristic of a specific chemical moiety than the corresponding XP spectrum, allowing in particular to distinguish easily between C–C, C=C, and C≡C species.[64]

In the case of SAMs, the monitoring of the absorption intensity occurs mostly by measuring electron yield, relying on the Auger electron decay of the respective excited states. Depending on so-called threshold voltage on the detector, limiting the kinetic energy range of the collected electrons, three different acquisition modes are generally used, viz. total electron yield (TEY), partial electron yield (PEY), and Auger electron yield (AEY). Whereas AEY includes the Auger electrons only, PEY and TEY includes secondary electrons as well, either above a preset kinetic

energy (PEY) or the entire emission signal (TEY). AEY has the highest surface sensitivity and lowest background signal but the lowest total intensity. In contrast, TEY has the highest intensity but the lowest surface sensitivity and the highest background signal. PEY is somewhere between these two extremes, representing frequently a good compromise for the spectra acquisition and, consequently, the mode of choice for the data presented in this review. In addition, the surface sensitivity of PEY can be flexibly tuned by variation of the threshold voltage,[66] which is a useful option for specific experiments.

Usually, as-measured NEXAFS spectra of a particular SAM are normalized to the transmission of the beamline, measured at the best for the same substrate as for the SAM studied, and reduced to the standard form, with the pre-edge and post-edge intensities set to zero and one, respectively. In some, cases the spectra are decomposed into individual contributions and represented by a combination of absorption resources and relevant absorption edges. This procedure is in particular necessary to derive the intensities of specific absorption resonances, but it can be generally avoided for pre-edge resonances, which are well separated from other spectral features.

Along with the electronic structure of a SAM studied, NEXAFS spectroscopy provides information about the molecular orientation. Generally, X-ray absorption cross-section, defining the absorption signal, I, is proportional to the transition matrix element.

$$I \propto | < f|\boldsymbol{E} \cdot \boldsymbol{p}|i > |^2 \qquad (2\text{-}4)$$

where $\boldsymbol{E}$ is the electric field vector of the synchrotron light, $\boldsymbol{p}$ is the momentum operator, |i > is the 1 s initial state, characteristic of the relevant light elements (C, N, O, F), and |f > is the molecular orbital final state of the transition.[64] Since the initial state has the spherical symmetry, the relevant transition dipole moment (TDM), |< f |p| i >|, mimics the symmetry of the final state, which is either vector or plane orbital, characterized by a specific direction (as, e.g, π* orbitals of an aromatic ring) or spanning a plane (as, e.g, σ* orbital of an aromatic ring), respectively.[64] Consequently, the intensity is highest if $\boldsymbol{E}$ is oriented along the orbital or within its plane, respectively, and zero if it is perpendicular to them. The standard approach is to vary the incidence angle of the primary X-ray light by sample rotation, changing the angle between the surface normal and E which is perpendicular to the direction of the X-ray beam (Fig. 2.8), lying at the same time in the plane of the storage ring for bending magnets and for most linear undulators. For the threefold or higher system symmetry which is relevant for most of the SAM systems, the intensity of a particular absorption resonance is described by equations.

$$I(\alpha, \theta) = A\{P \cdot 1/3[1 - 1/2(3cos^2\theta - 1)(3cos^2\alpha - 1)\,] + (1 - P)1/2sin^2\alpha\} \quad (2 - 5)$$

for the vector orbital case and

$$I(\gamma,\theta) = B\{P \cdot 2/3[1 - 1/4(3cos^2\theta - 1)(3cos^2\gamma - 1)\,] + (1 - P)1/2[1 + cos^2\gamma]\} \quad (2-6)$$

for the plane orbital case, where A and B are constants, P is polarization factor of the primary X-rays, θ is angle between $\boldsymbol{E}$ and surface normal, α is the average tilt angle of the vector orbital with respect to the surface normal, and γ is the average angle between the normal of the plane orbital and surface normal.[64] The introduction of the polarization factor is related to the fact that the primary light is never 100% linearly polarized but contains a major component in the plane of the storage ring, $\boldsymbol{E}_{\parallel}$, and a minor component, $\boldsymbol{E}_{\perp}$, perpendicular to this plane (see Fig. 2.8), with the polarization factor defined as

$$P = |\boldsymbol{E}_{||}|^2/(|\boldsymbol{E}_{||}|^2 + |\boldsymbol{E}_{\perp}|^2) \qquad (2-7)$$

The angle θ is then related to $\boldsymbol{E}_{\parallel}$ but $\boldsymbol{E}_{\perp}$ should be considered as well, which results in the appearance of the second terms in the curly brackets in Eqs. (2-5) and (2-6). It should also be noted that for an X-ray incidence angle of ~54.7° the first term in the curly brackets in Eqs. (2-5) and (2-6) becomes equal to zero and, in view of a usually small (1–P) term, the measured intensity becomes nearly independent of the molecular orientation. This angle is named the magic angle and the respective geometry is frequently used to monitor exclusively the electronic structure of a system studied, without an admixture of molecular orientation effects.

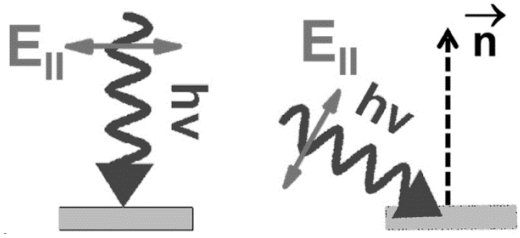

Figure 2.8 Schematic illustration of experimental geometry for the incidence plane,[65] which varies between the normal (sketch on the left) and grazing (sketch on the right) incidence, resulting in a variation of the angle between $\boldsymbol{E}_{\parallel}$ and the surface normal, **n**. $\boldsymbol{E}_{\perp}$ is perpendicular to the incidence plane. The angle between $\boldsymbol{E}_{\parallel}$ and the surface normal corresponds to the angle between the primary X-rays and the surface (so-called X-ray incidence angle, θ), which is most frequently used for the description of the incidence geometry. It is 90 ° for the normal incidence and 5 – 20° for the grazing incidence.

Alternatively, to the absolute intensities of the absorption resonances, the intensity difference corresponding to X-ray incidence angles θ and θ_r (reference angle) can be considered according to equations

$$I(\theta) - I(\theta_r) = C(1 - 3/2 sin^2\alpha)(cos^2\theta - cos^2\theta_r) \qquad (2-8)$$

for a vector orbital and

$$I(\theta) - I(\theta_r) = D(1 - 3cos^2\gamma)(cos^2\theta - cos^2\theta_r) \qquad (2-9)$$

for a plane orbital, where C and D are constants defined by the TDMs of the respective orbitals.[64] Consequently, the orientations of the orbitals with the same TDM for different systems can be directly compared or the orientation of an orbital for an unknown system can be derived using the data for a suitable reference system featuring the same orbital with a known orientation. The major advantage of this approach is that it does not require a spectra decomposition, which is in most cases quite an elaborate procedure; one has just to calculate the difference spectra directly from the experimental data and measure the amplitudes of the difference signals at the position of the given absorption resonance.[67,68] The major disadvantage of the difference approach is the necessity of a suitable reference sample, which is not always available.

Note that the derived tilt angle values represent the averages over a macroscopic area of X-ray spot and hardly allow to distinguish between a system with a homogeneous molecular orientation and a system with a superposition of several molecular orientations or even their distribution. The accuracy of these values depends on the quality of the experimental data and the system studied but is generally considered to be within ± 3 – 5°.

2.3.3 Ultraviolet Photoelectron Spectroscopy

Ultraviolet Photoelectron Spectroscopy (UPS), as an analytical technique of the electronic structure of conductive surfaces, is usually related to XPS. The HOMO energy level information will be given when the binding energy is lower than 30 eV in XP spectrum. But it's difficult to observe through XPS because of the relatively poorer photoelectric cross-section at these levels compared to core orbitals.[207,208] UPS is often used since it adopts a low-energy excitation radiation source, thus allowing to observing the valence shell photoelectron. In this thesis, synchrotron irradiation is used as the source due to its good stability and tunability, which allows the photon energy to vary in the range of approximately 10 – 100 eV depending on the beamline setup. Also, UPS is very sensitive to the characterization of 2 – 3 nm of thickness on the samples surface and doesn't provide information about the bulk.

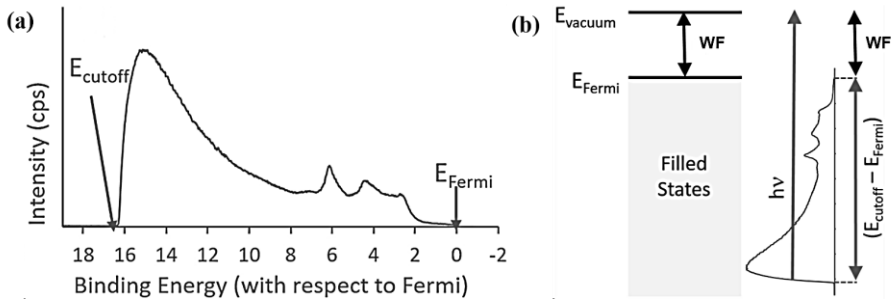

Figure 2.9 (a) UP spectrum of gold surface, and (b) shows how the UPS spectrum is a density of states diagram and explains the WF calculation.[208]

The work function (WF) of the metal surface can be determined by UPS. Fig. 2.9 gives an example of a pure gold UP spectrum. The UPS intensity in Fig. 2.9a decreases significantly in the approximately 16 eV regime, which is called the secondary electron cutoff (E_{cutoff}). The photoelectrons here have low kinetic energy and are difficult to capture by the analyzer. So, samples are normally put under bias in UPS experiment. As shown in Fig. 2.9b, the relation between Fermi level (E_{Fermi}), E_{cutoff}, and ultraviolet source excitation energy ($h\nu$) can be used to calculate samples' WF according to the equation:[208]

$$WF = h\nu - \left(E_{cutoff} - E_{Fermi}\right) \qquad (2-10)$$

2.4 Kelvin Probe

Kelvin probe measurement, also known as Kelvin probe force microscopy (KPFM), is a powerful non-destructive technique for studying the surface potential and work function of nanoscale materials.[69] Here, the work function refers to energy needed to move an electron from the Fermi energy level into vacuum.[70] The method relies on the contact potential difference and the principles of electrostatic force microscopy to precisely measure the energy required to move electrons from the materials surface to the reference electrode.[71] All measurements are performed in a high-vacuum environment to ensure accurate and repeatable results.

The basic test device is shown in Fig. 2.10,[72,73] and the corresponding measurement mechanism is shown in Fig. 2.11.[74] The probe and sample are parallel to each other in the KP test and kept electrically connected to form a parallel plate capacitor. Each component initially has a different Fermi level since the materials of probes and the chosen samples are different, shown in Fig. 2.11a. When an electrical connection is established between the probe and the sample, electron flow can occur between the probe and the sample along the direction from the high Fermi level (weak electron binding, Φ_2 in Fig. 2.11b) to the low Fermi level (Φ_1), and this flow will cause a Fermi level equilibrium between the probe and the sample. In addition, a contact potential difference

(CPD) will be caused by the redistribution of electron charges occurred at the interface due to the difference in electron affinity between different materials.[75] The electric field present in the capacitor due to these charges can then be detected, and an external potential V_c can be applied to cancel this field. So, if the field is zero when it's at equilibrium, the externally applied potential is equal to the contact potential difference, which corresponds to the difference between the two work functions (Fig.2.10c). The work function of the studied material can be given by the formula if the work function of materials 2 is known:

$$\Phi_1 = \Phi_2 - qV_c \qquad (2\text{-}11)$$

Where q is the elementary charge. In order to measure CPD accurately, a reference electrode is required, which typically has a number of well-known and stable work functions. In this work, C16 SAMs on Au are used as the reference electrode, and its work function is 4.32 eV.[76] It's also worth noting that the sample and reference sample should be placed in the same position for each measurement.

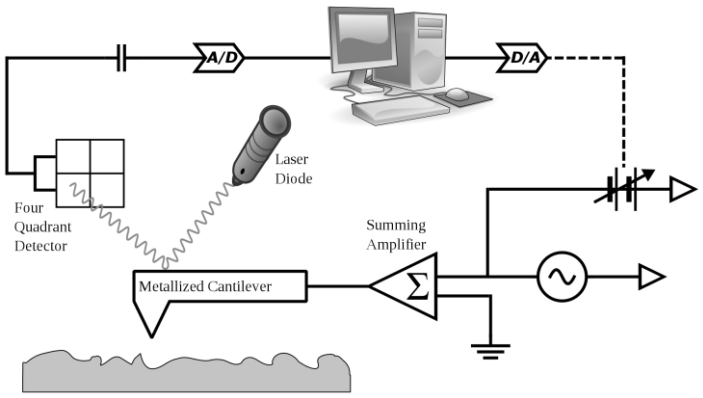

Figure 2.10 Schematic diagram of Kelvin Probe microscope measurement, where the conductive cantilever scans the sample's surface at a constant height.[73]

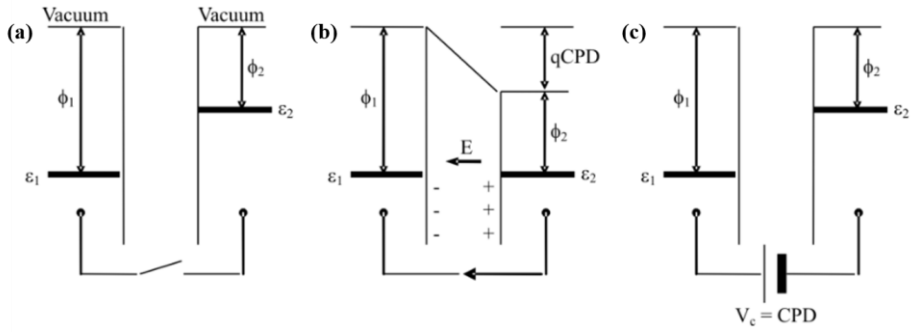

Figure 2.11 Physical schematic of the Kelvin Probe. (a) the two materials 1 and 2 have different work functions ϕ_1 and ϕ_2, corresponding to the energy difference between the Fermi level ε and the vacuum level. (b) The contact potential V_b is created when the electrons flow from 2 to 1 until the Fermi levels align due to

the electrical contact between the two materials. The electric charges present in the two materials generate an electric field E. (c) The electric field is eliminated by applying an external potential V_c equal to the contact potential.[74]

2.5 Infrared Reflection-Absorption Spectroscopy

Infrared reflection absorption spectroscopy (IRRAS) is a particularly useful spectroscopic technique to study ultrathin organic films at the surface of reflective materials. It provides information not only about the molecular groups of the film but also about their orientation relative to the metal surface.[276] It is particularly suitable for the analysis of SAMs chemisorbed on noble metals such as gold. Generally speaking, most of the light is reflected, that is external reflection, when infrared light irradiates the Au substrate with SAMs. Then the signal of the SAMs on the substrate surface can be obtained by collecting the reflected light signal and subtracting the absorption of the Au substrate itself from it. If the incident angle of the light is between 70 ~ 88°,[277] the enhanced spectral signal can be measured, which is infrared reflection absorption spectroscopy. This polarized light is directed to the detector, producing corresponding bands in the spectrum.

The absorptions are around 5×10^{-3} AU (absorbance units) since the monolayers are very thin. In this thesis, a sensitive semiconductor detector (usually so-called MCT detectors, that is mercury cadmium telluride) with liquid nitrogen cooling liquid must be used for measurements in the mid-infrared range (MIR, 400- 4000 cm^{-1}).[278] In addition, the spectrometer must be a device with a Fourier transform infrared spectrometer (FTIR spectrometer) since it can perform a large number of measurements in a short time and reduce the signal-to-noise ratio. The absolute value of the absorption wave number can be determined very precisely due to the design (laser measurement of the position of the Michelson interferometer).[279] As shown in Fig. 2.12a, IRRAS uses p-polarized infrared light, where the electric field vector E_P is parallel to the reflection plane. When the angle of incidence (α) with respect to n is less than 90°, E_p is divided into two components E_z and E_x (Fig. 2.12b). E_x lies parallel to the gold surface and is extinguished by shift polarization of the metal electrons. E_z is perpendicular to the gold surface and is reinforced accordingly. Since only light is transmitted in the E_z direction, maximum interaction of the incident light occurs preferably with functional groups whose transition dipole moment has a component in the z direction, i.e. perpendicular to the metal surface.

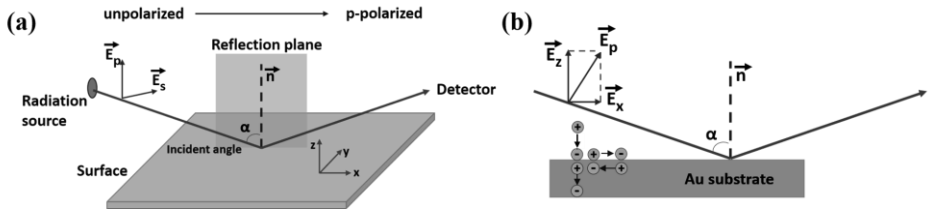

Figure 2.12 (a) Unpolarized light reflects from a surface to produce p-polarized light. Direction refers to the reflection plane. (b) Reflection of p-polarized light from gold surfaces. Light polarized parallel to the metal surface (E_x) is extinguished by the polarizing charge, while light polarized perpendicularly (E_z) is amplified.

2.6 Measurement of Charge Transport through SAMs

The study of charge transport via SAMs has become a fascinating frontier in nanoscience and molecular electronics. Understanding charge transport in SAMs not only reveals the complex interplay between molecular structure and electrical properties, but also paves the way for novel applications in fields ranging from molecular electronics to sensor technology. At the heart of the exploration is the necessity to understand how charge carriers such as electrons or holes fundamentally behave in these SAMs, which can be reflected by indicators such as current density, transition voltage, rectification ratio, and so on.

2.6.1 Current Density Measurement

As we know, the current density of SAMs represents the amount of current flowing through a unit area perpendicular to the current direction, which is closely related to the charge transport properties of SAMs.[77] The corresponding I-V curve is typically obtained through a conductive circuit, where a soft top electrode is connected to the surface of the SAMs, and the substrate forming the SAMs serves as the bottom electrode (Fig. 2.13).[78] Notably, even though there are several options for the top electrode, such as Au, Pt, Ag, Cu, and Hg,[79] EGaIn (Eutectic Gallium-Indium alloy) is the most commonly selected material for the top electrode. Because EGaIn has a low melting point, which makes it easy to manipulate and reshape, thus facilitating the establishment of precise conformal contact with SAMs, and also has a good conductivity.[80,81] Besides, it can form a thin self-passivating oxide layer (Ga_2O_3) on the surface to prevent further oxidation of the metal.[82] By studying current density, insights into the behavior of charge carriers in these nanoscale molecular structures can be gained.

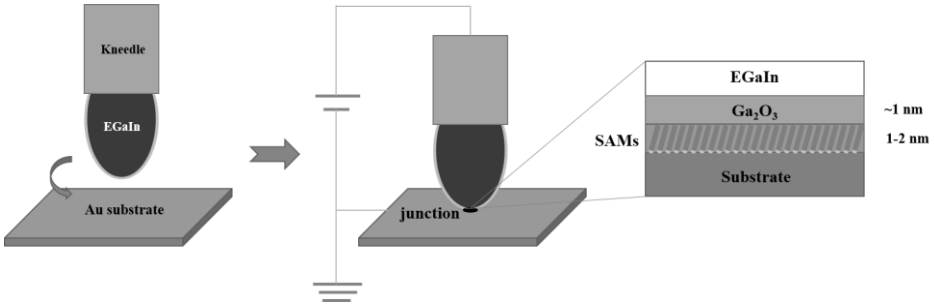

Figure 2.13 Schematic of substrate/SAMs//Ga_2O_3/EGaIn junction.

Generally, there are several conduction mechanisms for charge transport in SAMs, the most common of which is non-resonant tunneling.[82] Non-resonant tunneling occurs when electrons pass through a barrier without the need for their energy levels to align precisely with energy states within the barrier. In other words, non-resonant tunneling doesn't depend on the direct alignment of energy levels as resonant tunneling does.[83] The tunneling probability in non-resonant tunneling depends on the width, shape and energy distribution of the electrodes in the tunneling barrier. In particular, the tunneling rate will decrease exponentially with increasing molecular length, the dependence of which is given by the following formula (Simmons model):[84]

$$J = J_0 \cdot \exp(-\beta d) \qquad (2\text{-}12)$$

where J is the measured current density, d is the molecular length (either in Å or a number of carbon atoms), J_0 is a (bias-dependent) pre-exponential factor that accounts for the interfaces between the SAMs and the electrodes, and β is the tunneling decay constant. Since the Simmons model is only a predictive model rather than a statistical model, in order to better analyze the experimental data, a statistical model was developed according to the above formula. By assuming that β and J_0 are constants, the normal distribution of d will be converted into the lognormal distribution of J, that is, the informative measure of Log J predicted by the model is normally distributed. Usually, the obtained results will consist of two parts, a normally distributed component that is informative and another component comprising noninformative values of log J. In Fig. 2.14a, it's evident that majority of the histograms can be fitted by a normal distribution formula, where also some slight deviations are noticed, which are considered noninformative and can be excluded from the analysis. In this thesis, the approach is referred as Gaussian method, and the corresponding Gaussian mean (μ_G) and standard deviation (σ_G) are calculated to determine the log J location and dispersion, respectively.[84] In the meantime, an alternative method is to calculate the median (m) and related absolute deviation (σ_m), which doesn't require the above formula to be valid or the current density values to be normally distributed. It's premised by assuming that the primary data are informative

and are hardly affected by outliers. The corresponding Gaussian mean and median mean obtained from Au^{Ts}/H-TPT//Ga_2O_3/EGaIn junction are shown in Fig. 2.14b. Obviously, the values between the two are very close and can be used to verify each other, albeit with slight deviations. However, compared with the standard deviation of Gaussian, the absolute deviation obtained form median is somehow larger, although both can be used to describe the degree of dispersion of Log *J*.

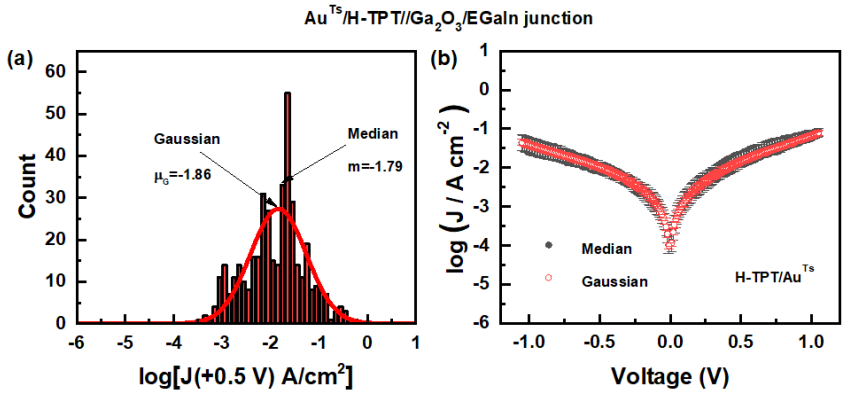

Figure 2.14 Current density of Terphenylthiol SAMs on Au^{Ts} substrate. (a) The histogram of logarithmic current density at potential = + 0.5 V, and the corresponding normal distribution fitting of the histogram is shown. (b) The median and Gaussian average log *J* as a function of voltage.

Besides, hopping is another common conduction mechanism.[85] In hopping conduction, charge carriers move through the SAMs by "hopping" between localized energy states within the molecules. This mechanism is prevalent in disordered or insulating systems and can be influenced by the degree of disorder, temperature, and molecular packing. The current density is hopping conduction usually follows a power-law dependence on voltage. Finally, there still are others conduction mechanisms, such as field-enhanced ionization (Fowler-Nordheim tunneling),[86] electron-hole recombination,[87] and thermally assisted tunneling (phonon-assisted tunneling).[88] The conduction mechanism in SAMs largely depends on the alignment of energy levels between the SAMs and the electrodes, for example, non-resonant tunneling dominates when the high difference between HOMO and LUMO reaches 8 eV in saturated alkyl SAMs.[89] Overall, analyzing the current density of SAMs can provide valuable insights into the fundamental electronic and transport properties of SAMs.

2.6.2 Transition Voltage Spectroscopy

Transition voltage spectroscopy (TVS) is a way used to study the electronic structure and charge transport properties of molecular junctions of SAMs, aiming to study the energy levels and

conduction mechanisms of nanoscale molecules.[90,91] It's derived from the idea that the position of the nearest molecular level in a two-terminal device can be determined through I-V (current-voltage) measurements, even when the bias voltage is moderate and resonance hasn't been achieved.

Here, with reference to the method of Beebe et al.,[92] an analogy is drawn between molecular charge transport and electron tunneling through a rectangular barrier, shown in Fig. 2.15.[93] The height Φ of the tunnel barrier in this framework is equal to the energy offset between Fermi level E_F and the nearest molecular orbital. In this thesis, thiol-terminated molecules are the main research objects, and their nearest energy level is usually the highest occupied molecular orbital (E_{HOMO}), so the barrier height $\Phi = E_F - E_{HOMO}$. Whereas the barrier width d is set equal to the length of the molecule. When the applied bias V is less than Φ/e (e: electron charge), shown in area II in Fig. 2.15b, the effective tunnel barrier will be reduced to Φ-eV/2. When gradually increasing to high bias, i.e., $V > \Phi/e$, the barrier shape becomes triangular and part of the barrier becomes available. The case is generally referred to as Fowler-Nordheim tunneling (FN) or field emission.[92] Region III illustrates the transition of the two different states at $V = \Phi/e$, that is, the transition voltage. Therefore, we give a FN figure using $\ln(1/V^2)$ as a function of 1/V as an example to further explain, shown in Fig. 2.15a. Notably, only the positive potential part is discussed because the mechanism is similar for positive and negative potentials. When $V > \Phi/e$, a straight line with a negative slope is generated in the FN diagram. However, the slope is completely opposite when $V << \Phi/e$. So, the minimum value between the two is the transition voltage, V_T^+ is almost 0.265 V.

TVS is a useful way for understanding the electronic properties of individual molecules and molecular junctions. It is not only helpful with energy level identification, by analyzing transition voltages to extract information about molecular energy levels and their alignment. Also, it can provide insight into the conduction mechanism of molecular junctions. Therefore, TVS is particularly useful for characterizing and optimizing molecular electronic devices and understanding the behavior of electronic systems at the nanoscale.

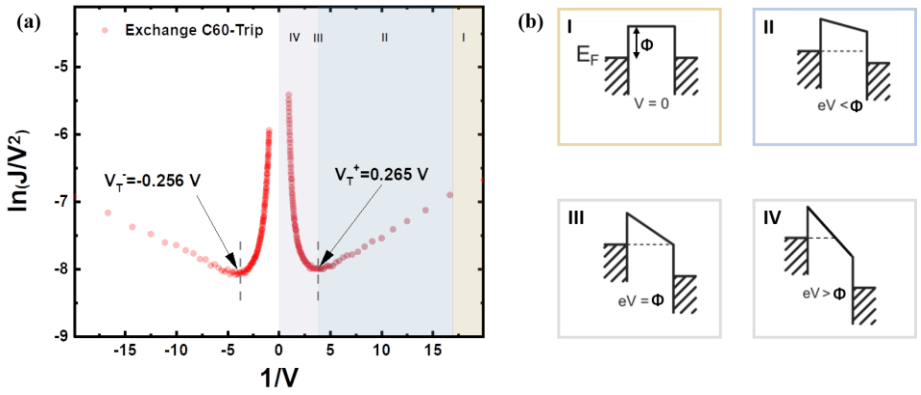

Figure 2.15 (a) Fowler-Nordheim (FN) plot of I-V traces of Au^{Ts}/exchange C60-Trip//Ga_2O_3/EGaIn junction. The dashed lines represent the required voltage to change the current dependence on applied bias. (b) Barrier height Φ is determined by the offset between molecular orbital and Fermi level EF, while the barrier width d is determined by the length of molecule in junction. Carrier transport occurs by tunneling when the rectangular barrier (area I) becomes trapezoidal (area II) at an applied bias less than the transition voltage (area III). And carrier transport is via Fowler-Nordheim (FN) tunneling when the barrier becomes triangular when the applied bias exceeds the transition voltage (area IV).[93]

2.6.3 Monitoring of Rectification

Calculating RR is a useful analytical way that plays a key role in revealing the systems of various SAMs by exploring their electrical responses.[94] RR is the ratio of the currents measured at the same value of forward and reverse bias voltages for a device with a rectifier characteristic.[95] RR is an important physical parameter for a Schottky barrier diode and p-n junctions., and the related formula is as follows:

$$RR^{+} = \left|\frac{J(+V)}{J(-V)}\right| \; or \; RR^{-} = \left|\frac{J(-V)}{J(+V)}\right| \qquad (2\text{-}13)$$

where J (+V) and J (–V) refer to the current densities of the measured SAMs in the positive and negative bias ranges, respectively. RR is always ≥ 1 in this definition. In this thesis, we obtained the RR spectra by referring the measurement of current density, shown in Fig. 2.16. For example, the Fc-Flut SAMs have two different conductance states when applied two opposite sweeping mechanism, and the corresponding RR is 2100 at V = 0.1 V. The high RR indicates a significant difference in current flow in the forward and reverse directions, which in turn provides insights into the underlying properties of the related SAMs and their charge transport mechanisms.

Firstly, RR can reflect the asymmetry of electron transport from the above analysis.[96] A higher RR typically signifies that the SAM can more effectively restrict reverse currents or allow current to flow predominantly in one direction when subjected to current passage. This aspect holds

significant importance for applications in electronic devices, sensors, or energy conversion devices, as it can influence the efficiency and performance of these devices. In addition, it can be used to judge the charge transport mechanism.[97] Finally, RR can also reveal the coupling strength between SAMs and the underlying electrode to a certain extent since the strong coupling can enhance the RR due to their efficient charge transfer.[98] In short, the advantage of studying the rectification ratio is the current measured in one direction of bias serves as a reference for the current measured at the opposite bias and, thus, eliminates many of the uncertainties related to contact areas or contact distances.[53]

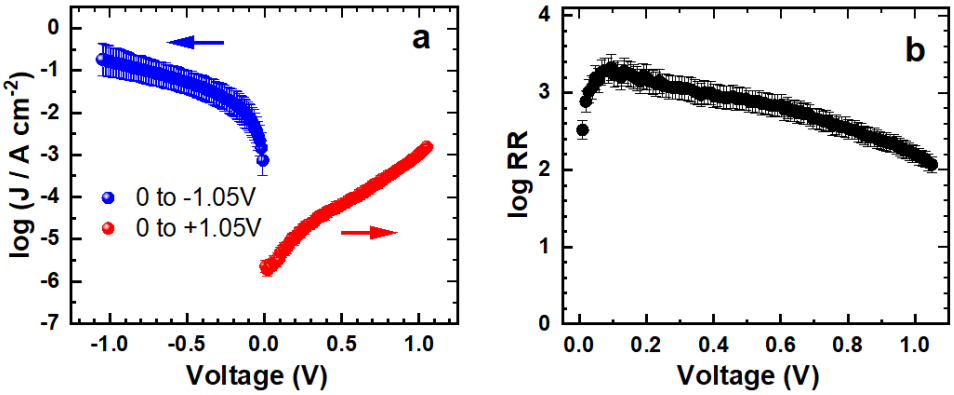

Figure 2.16 (a) Averaged semilogarithmic *J*-V plot for the Au^{Ts}/Fc-FluT//Ga_2O_3/EGaIn. (b) Effective RR for Fc-FluT SAM vs bias voltage.

2.7 Contact Angle Goniometry

Contact angle goniometry is a simple and versatile setup to precisely manipulate and measure the contact angle of the SAMs, whose core is a mechanical platform that can rotate objects along one or more axes with extreme precision, shown in Fig. 2.17. We can quickly measure the contact angles of the SAMs at different positions by simply adjusting the mechanical platform. Notably, the contact angle occurs when the droplet reaches equilibrium on the substrate with SAMs, and their shape of the droplet is shown in Fig. 2.18a. Here, its shape is defined by the specific properties of the liquid, solid, and gas phases at the interface, which usually obey Young's equation,[99] as follows:

$$\gamma_{SV} = \gamma_{SL} + \gamma_{LV} \cdot cos\theta \qquad (2\text{-}14)$$

where γ_{SV}, γ_{SL}, and γ_{LV} is the interfacial tension of solid-gas, solid-liquid, and liquid-gas respectively, θ is the contact angle. The contact angle generally reflects the wettability and hydrophobicity/hydrophilicity of SAMs.[99] The larger the contact angle, the stronger the surface

hydrophobicity; conversely, the smaller the contact angle, the stronger the surface hydrophilicity. In general, SAMs with specific functional groups can alter surface wettability and thus affect contact angle.

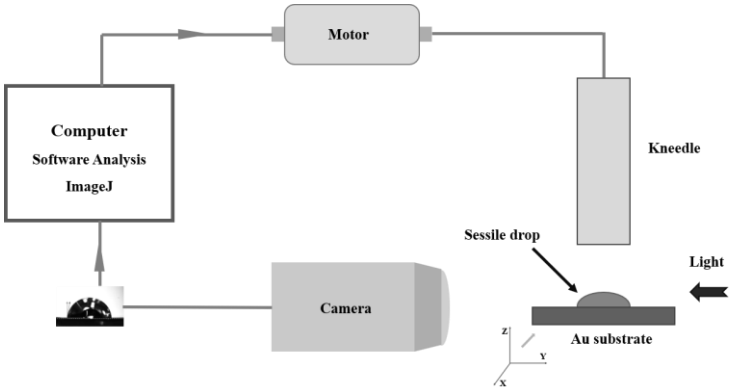

Figure 2.17 Schematic of contact angle goniometry.

Besides, the measurements of contact angle can be divided into two methods, one is directly measuring the static contact angle (shown in Fig. 2.18b),[100] and the other is to measure the advancing (θ_A) and receding (θ_R) contact angle (shown in Fig. 2.18c).[101] The static contact angle is the angle between the liquid and solid surfaces during measurement, where the contact area between them remains unchanged from an external perspective. As for θ_A and θ_R, the thesis mainly refers to the test method of Frey S. et al.[101] And a hysteresis can be observed by the difference between θ_A and θ_R. The main difference between these two different angles is that static contact angle provides information about the equilibrium wetting state of the droplet on the SAMs, whereas θ_A and θ_R characterize the behavior of a droplet as it spreads across the SAMs and as it recedes, respectively. In all, the measurement of the contact angle provides a clear guide for us to understand the wettability of the SAMs.

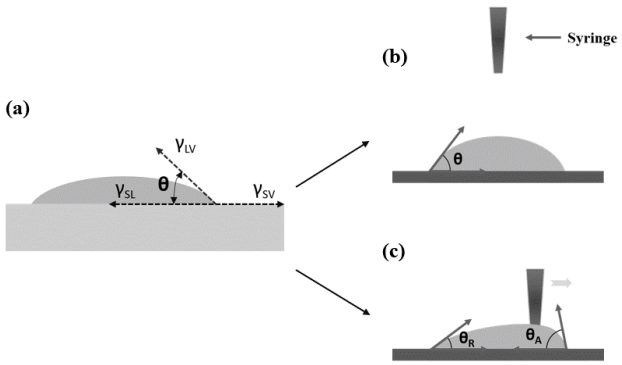

Figure 2.18 (a) Schematic diagram of a drop on the substrate. (b) and (c) are the static contact angles (θ) and corresponding advancing (θ_A) and receding (θ_R) contact angles, respectively.

3. Methods

3.1 Materials & Preparation Procedures

In this chapter, all used materials and the preparation procedures for the relevant SAMs will be presented one by one in the following experimental methods, to better help us understand and master their physical and chemical properties.

3.1.1 Substrates and Substrate Cleaning

As for the gold substrates, there are two different types used in the thesis. Both of them were purchased from Georg Albert PVD-Beschichtungen. The first one was normal Au substrate, which was prepared by thermal evaporation of 30 nm of gold (99.99% purity) onto polished single-crystal silicon (100) wafers, that had been precoated with a 9 nm Ti adhesion layer. The Au films were polycrystalline, exposing preferably (111) orientated surfaces of individual crystallites. And the RMS was estimated at ~ 0.8 nm as average over the 0.5 × 0.5 μm^2 and 5 × 5 μm^2 scans. The another one is template-stripped Au substrates (Au^{Ts}), and it has almost the same preparation process as Ag^{Ts} substrates. The RMS of Au^{Ts} substrate was estimated to be 0.06 nm for both 1 μm × 1 μm and 5 μm × 5 μm scans, and their bearing volume was estimated as 0.0184 ± 0.001 μm^3.

Besides, substrate cleaning is very important and necessary before preparing the required SAMs. As for the Au substrate, it should first be irradiated with ultraviolet light (UV treatment) for about 30 min, and then put them into glass bottles containing a certain amount of ethanol for ultrasonication for 15 min. After sonication, they are rinsed several times with an appropriate amount of ethanol, and dry by a soft nitrogen stream before being stored for use. But it's a little different for Au and Au^{Ts} substrate cleaning. Au^{Ts} substrates are usually cleaned by rinsing them with ethanol and by blowing them dry with a stream of nitrogen or argon.

3.1.2 SAMs Precursors and Preparation

The SAMs precursors were either purchased from Sigma Aldrich or custom-synthesized by our partner groups, according to the corresponding literature recipes.[102,103,104,105,106,107,108] In addition, all organic solvents used in the experiment, such as ethanol and THF, were also purchased from Sigma Aldrich. Then the corresponding precursor solution preparation process of all SAMs can be found in the following chapters. And the chemical structures of all used molecules are shown in Fig. 3.1.

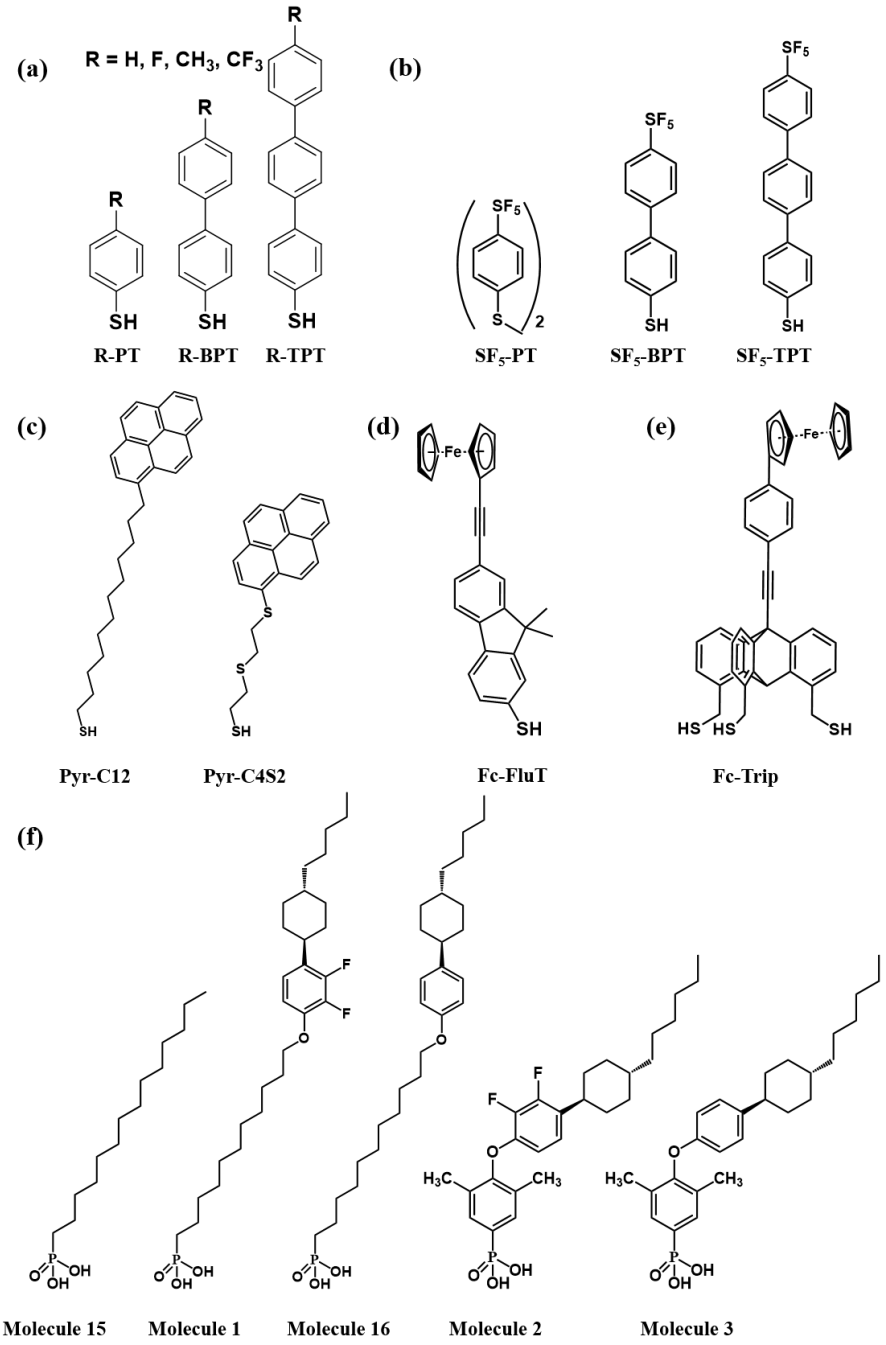

Figure 3.1 Molecular structures of the SAM precursors used in the thesis. (a) H-PT, F-PT, CH_3-PT, CF_3-PT, and H-BPT were purchased from Sigma-Aldrich; F-BPT was custom-synthesized by our partner, Prof. A. Ulman (New York University); CH_3-BPT, CF_3-BPT, H-TPT, F-TPT, CH_3-TPT, and CF_3-TPT were custom-synthesized by the group of our partner, Prof. A. Terfort (Frankfurt University); (b) SF_5-PT, SF_5-BPT, and SF_5-TPT were custom-synthesized by the group of our partner, Prof. A. Terfort (Frankfurt University); (c) Pyr-C12 and Pyr-C4S2 were custom-synthesized by the group of our partner, Prof. H. Lang (Chemnitz University). (d) Fc-FluT was custom-synthesized by the group of our partner, Prof. H. Lang (Chemnitz University); (e) Fc-Trip was custom-synthesized by the group of our partner, Prof. T. Fukushima (Tokyo

Institute of Technology); (f) Molecules 1-6 were designed and custom-synthesized by the group of our partner, Prof. P. Kirsch (Technische Universität Darmstadt). Most of the substances were in powder form.

All SAMs were obtained by immersion procedures. Generally, SAMs can be obtained after immersing for almost 24 h, but there are some differences in different molecule preparation procedures. It's necessary to sonicate again for several minutes after immersion to remove physiosorbed thiol on the substrate surface. By the way, when ethanol is used as the solvent, rinse with ethanol several times after immersion and then blow dry with a gentle nitrogen stream. However, when other organic solvents are used as the solvent, it needs to be rinsed with the corresponding organic solvent for several times after immersion, then rinsed with ethanol, and finally dried with nitrogen flow again before use.

3.2 Characterization & Analysis

In this chapter, all the experimental characterizations and setups used are introduced one by one, as well as the experimental parameters set during the measurements. Then the calculation methods used in the corresponding data processing will also be explained.

3.2.1 XPS and HRXPS

The XPS measurements were performed at two different locations, one at the Physical-Chemistry Institute, Heidelberg University, and the other at the HE-SGM beamline (bending magnet) of the synchrotron storage ring BESSY II in Berlin. The first setup located at Physical-Chemistry Institute (Heidelberg University) uses MAX200 (Leybold-Heraeus) spectrometer equipped with a non-monochromatized Mg Kα X-ray source (200 W) and a hemispherical analyzer. It uses the normal emission geometry, and the corresponding recorded spectra were normalized by spectrometer transmission. Meanwhile, the binding energy of Au $4f_{7/2}$, namely 84.0 eV, is often used as a reference to calibrate other elements.

The synchrotron-based HRXPS were usually performed in synchrotron lab in Berlin, Germany. Generally, it uses a custom-made experimental station equipped with a Scienta R3000 electron energy analyzer in normal emission geometry to acquire the spectra. And synchrotron light served as the primary X-ray source. The selection of the photon energy (PE) can also be changed according to the acquisition ranges, generally between 350 eV, 580 eV, and 750 eV, which corresponds to the corresponding energy resolution of ~0.3 eV, ~0.6 eV, and ~0.8 eV, respectively. The spectra were recorded in the specific regions, such as Au 4f, C 1s, O 1s, F 1s, S 2p, Fe 3p, and so on, depending

on the SAMs and their substrate. And the binding energy was referred to the Au $4f_{7/2}$ emission at 84.0 eV for all recorded spectra.[104]

We used the software "XPS Peak 4.1" to process the XPS data. As for Au 4f, a Shirley-type background was subtracted and the XPS spectra were fitted by symmetric Voigt functions.[109] The other elements subtracted the Linear-type background in this thesis. But there is a little difference for S 2p, it subtracts the Linear-type background and uses a pair of such peaks with the same full width at half-maximum (FWHM) values, branching ratios of 2, and spin-orbit splitting of ~1.2 eV to fit the S $2p_{3/2,1/2}$ doublets. Notably, these fits were performed self-consistently because the same fitting parameters were used for the same spectral regions.

Finally, the effective thickness (Å) and packing density (molecules/cm^2) can be calculated by using the evaluated data from XPS spectra.[104] Specifically, they can be obtained based on the C 1s / Au $4f_{7/2}$ and S $2p_{3/2,1/2}$ / Au $4f_{7/2}$ intensity ratios, respectively. The standard, exponential attenuation of the photoemission signal was assumed, and the literature values for the attenuation lengths of the photoelectrons in densely packed SAMs were used. At the same time, a hecadecanethiol (C16) SAMs was used as a reference, which was defined as a well-known thickness (18.9 Å) and packing density (4.63×10^{14} molecules/cm^2).[104]

3.2.2 NEXAFS Spectroscopy

The NEXAFS spectra were measured at the same beamline as the HRXPS ones, and they were measured at the carbon K-edges in the partial electron yield (PEY) mode with retarding voltages of -150 V (C K-edge), corresponding to the excitation of the C 1s core-level electrons into the unoccupied molecular states. The linearly polarized synchrotron light with a polarization factor of ~90% was used as the primary X-ray source. The incidence angle of the light was changed in steps between the normal and grazing geometry, setting to 90°, 55°, 30°, and 20° with respect to the SAMs surface, to monitor the linear dichroism effects associated with molecular orientation and orders. As for the C K-edge, the energy resolution was ~0.3 eV. And the PE scale was referenced to the significant π* resonance of highly oriented pyrolytic graphite at 285.38 eV. The spectra were corrected for the PE dependence of the incident photon flux.[110]

There are usually two kinds of spectra for NEXAFS, one is the spectra acquired at the so-called magic angle of X-ray incidence (55°) and the other is the difference spectra between normal (90°) and grazing (20°) X-ray incidence. The former spectra are independent of orientation effects and merely represent the electronic structure of the system. The latter spectra represent the so-called linear dichroism in X-ray absorption. Here, the inclination angle of the corresponding SAMs can be obtained by calculating the relative intensity of the π* resonance at every incidence angle

according to papers.[104] It's worth noting that whether the molecules are plane orbit or π orbit, or whether their anchoring groups are monothiol or triptycene, their calculation processes are somewhat different.

3.2.3 UPS

Some of the work function measurements were performed at the HE-SGM beamline of the synchrotron storage ring BESSY II. The work function was determined according to the secondary electron cutoff in XP spectra, with the samples biased by −29 V. The photon energy was set to 160 eV, which guaranteed a sufficiently high energy resolution, comparable with that of ultraviolet photoelectron spectroscopy. The work function values were referenced to that of a C16 SAM on Au(111), 4.32 eV,[76] measured at the same settings of all parameters.

3.2.4 KP Measurements

Other work function measurements were performed by using a UHV Kelvin Probe 2001 system (KP technology Ltd., UK). The pressure in the UHV chamber was ~10^{-8} mbar. The fresh C16 SAMs on Au was used as a reference, whose work function was ~4.32 eV.[76] The reference value is verified by comparing with the W.F. of pure Au substrate, viz. 5.2 eV.[111] And note the change in pressure in each chamber during the measurement.

3.2.5 IR Measurements

Infrared reflection−absorption spectroscopy (IRRAS) measurements were performed by using a Thermo Nicolet 6700 Fourier transform spectrometer with a narrow-band mercury cadmium telluride semiconductor detector at a resolution of 4 cm^{-1}. The optical path was purged with dried and CO_2-free air during the measurements. The spectra were recorded at an angle of 80° relative to the sample surface normal with p-polarized radiation against a reference SAM of perdeuterated dodecanethiolate on Au.

3.2.6 Electrical Conductance Measurements

The charge transport properties of the SAMs were measured by a custom-made two-terminal molecular junction setup, based on the Keithley 2635A source meter that can apply different biases to the SAMs. The setup's reliability has been proven by previous experiments. It's necessary to prepare a well-defined shaped eutectic GaIn alloy (EGaIn) tip before measuring and oxidizing it in air for 1 h to form an ultrathin oxide layer of ~0.7 nm Ga_2O_3. The Au substrate was used as the

bottom electrode and the EGaIn tip was used as the top electrode. Then, the tunneling junction was formed by gradually moving the sharp EGaIn tip close enough to touch the SAMs' surface (shown in Fig. 3.2), where the diameter of the contact area should not be too larger, otherwise it will cause leakage current.[112] In the thesis, the diameter of the junctions was generally controlled in the range of 20 μm to 60 μm. And the applied bias voltage was varied in the range of ± 1.05 V during the measurement, while the step was set as 0.01 V and dwell time was ~2 s. In order to avoid experimental errors, we generally prepared at least two or more SAMs for each molecule, and then measured at different positions of each SAMs. And every measurement controlled the cycle number to no more than 20 times at each position and then changed to a new position. Besides, a new EGaIn tip should be prepared after the EGaIn tip had been used for several hours. We had collected at least 100 *J*-V curves for each molecule, and ensured that each molecule has a high yield, that is, high reliability. Next, the obtained data were subjected to standard statistical analysis through the software "Origin 2021" after completing the measurement, relying on either Gaussian mean and standard deviation or median and absolute deviation. The results of both methods leaded to a similar value, illustrating the reliability of the statistical analysis results. And the confidence (CI) is 99%, which is used to express the dispersion of the samples. Finally, the current density curves can also be converted through a serious of mathematics, which can be used to calculate the rectification ratio and transition voltage.

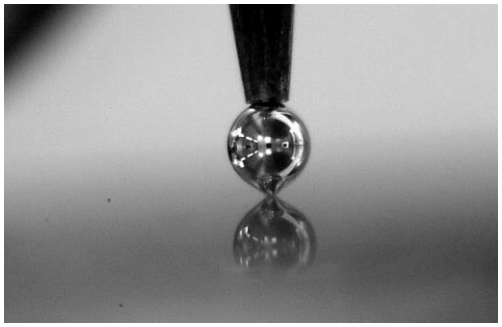

Figure 3.2 Au/SAMs//Ga_2O_3/EGaIn junction formed by moving the tip of EGaIn to contact the surface of SAMs.

3.2.7 Contact Angle Measurements

Here, three kinds of contact angles were considered, which are static contact angle (θ), advancing contact angle (θ_A), and receding contact angle (θ_R), respectively. All of them were measured on freshly prepared SAMs with millipore water with contact angle goniometry. All measurements were performed at ambient conditions. In order to ensure accuracy, generally each SAMs will be

measured at least three different positions, and then averaged the obtained angles and mark the error bars. Notably, the measurements of θ and θ_A and θ_R are slightly different. The θ can be obtained directly by allowing the droplet to fall from the kneedle at a fixed height to the SAMs' surface and the equilibrate. On the basis of the above, when the kneedle was inserted into the water drop to a certain depth, and then moves horizontally at a slow and fixed rate, the angle obtained at the moment when the two ends of the water drop is about to move is the θ_A and θ_R, respectively.

4. Results & Discussions

4.1 Effect of Substitution on the Charge Transport Properties of Oligophenylenethiolate SAMs

4.1.1 Motivation

The charge transport properties of SAMs are usually affected by different factors, among which electrostatic effects, associated with an introduction of a dipolar group into the molecular framework, have recently attracted noticeable attention.[113,114] Particularly interesting systems in this regard are halogen-decorated SAMs, in which the terminal hydrogen atom is substituted by a halogen atom possessing intrinsic electronegativity and polarizability, and introducing thus a dipole moment directed to the substrate, which will influence the tunnelling current across the molecular junction for both aliphatic and aromatic SAMs significantly,[115] showing however no unequivocal correlation with the halogen-mediated variation of the work function (WF) of the sample.

In view of the different behavior of the aliphatic and aromatic SAMs at the halogen substitution of the terminal hydrogen atom/atoms,[104,116] it would be reasonable to look at the effect of such a substitution on the tunnelling decay coefficient in the aromatic monolayers as well. In this context, we studied a series of non-substituted (–H) and –F, $–CH_3$, and $–CF_3$-substituted oligophenylthiolate SAMs on Au(111), shown in Fig. 4.1. Along with the measurements of the tunneling rate across the junctions containing these SAMs (Fig. 4.1), we also applied a combination of several complementary spectroscopic techniques to verify their quality and to obtain the major parameters characterizing the molecular organization and electrostatic effect of the monolayers. Whereas such data for the biphenylthiolate SAMs can be found in the literature,[117,118] the data for the terphenylthiolate SAMs are available to a limited extent only,[119] and the quality of the benzenethiolate monolayers depends strongly on the preparation procedure and varies noticeably in particular reports.[119,120]

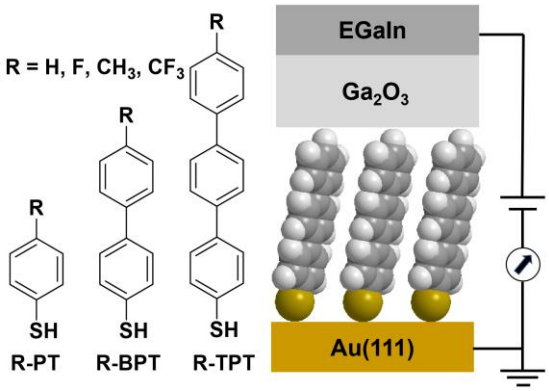

Figure 4.1 SAM-forming molecules used in this subproject along with description of their acronyms and a schematic of two-terminal Au/SAM//Ga_2O_3/EGaIn junction, with the bottom Au electrode (substrate), top EGaIn electrode, and the H-TPT SAM as example. Note that "/" indicates interfaces with strong electronic coupling - either between the SAM and substrate (covalent bonding) or between Ga_2O_3 and EGaIn, while "//" indicates the interface between the tail groups of the SAMs and Ga_2O_3, characterized by a weak electronic coupling. H-PT, F-PT, CH_3-PT, CF_3-PT, and H-BPT were purchased from Sigma-Aldrich; F-BPT was custom-synthesized by our partner, Prof. A. Ulman (New York University); CH_3-BPT, CF_3-BPT, H-TPT, F-TPT, CH_3-TPT, and CF_3-TPT were custom-synthesized by the group of our partner, Prof. A. Terfort (Frankfurt University).

4.1.2 SAM Preparation

The R-nPT SAMs were formed by immersion of the Au substrates into solutions of the SAM precursors in ethanol for 24 h / 48 h, under ambient conditions and at room temperature. The substrates were preliminary cleaned by ultraviolet light and either ultrasonicated (Au/Ti/Si) or cleaned (Au^{Ts}) in ethanol. The concentration of the precursors in the solvent was varied from 0.5 to 5 mM, depending on the compound, with the only exception of F-BPT, which was dissolved at 10 μM in accordance with the literature receipt.[118] After immersion, the samples were extensively rinsed with ethanol and finally blown dry with a stream of nitrogen or Ar.

In addition to the R-nPT monolayers, a reference C16 SAMs was prepared using the analogous immersion procedure (1 mM in ethanol; 24 h; room temperature).

4.1.3 XPS

The spectroscopic characterization was only performed for the R-PT and R-TPT SAMs. The analogous data for the R-BPT monolayers can be found in refs.[104,118] The S 2p, C 1s, and F 1s XP spectra of the R-TPT SAMs are presented in Fig. 4.2. The S 2p spectra in Fig. 4.2a exhibit a single S $2p_{3/2,1/2}$ doublet at a BE of ~162.0 eV (S $2p_{3/2}$), characteristic of the thiolate species bound to

noble metal substrates,[121] which means that all molecules in the R-TPT films are bound to gold in such a fashion, forming the monolayers. The C 1s XP spectra in Fig. 4.2b are dominated by a peak at a BE of 284.2-284.3 eV, characteristic of the TPT backbone (C–C). In accordance with the molecular composition, this peak is the only feature for the H-TPT and CH_3-TPT SAMs (apart from a low intense shoulder at the high BE side of the main peak in the latter case). In the case of the F-TPT SAM, this peak is accompanied by a distinct low intense peak at a BE of ~286.5 eV, representing the carbon atom of the terminal phenyl ring bonded to fluorine.[122] In the case of the CF_3-TPT monolayer the main peak is accompanied by a distinct low intense peak at a BE of ~2.8 eV, representing the carbon atom in the CF_3 tail group.[104] Other features are not observed suggesting a contamination-free character of the R-TPT monolayers. The F 1s spectra of the F-TPT and CF_3-TPT SAMs in Fig. 4.2c exhibit a single peak at a BE of either 686.8 eV or 687.3 eV, respectively. The upward BE shift in the latter case is related to a stronger electronegativity of the -CF_3 group compared to -F. The noticeably higher intensity of the F 1s signal for the CF_3-TPT SAM compared to that for F-TPT monolayer reflects the difference in the number of the terminal fluorine atoms.

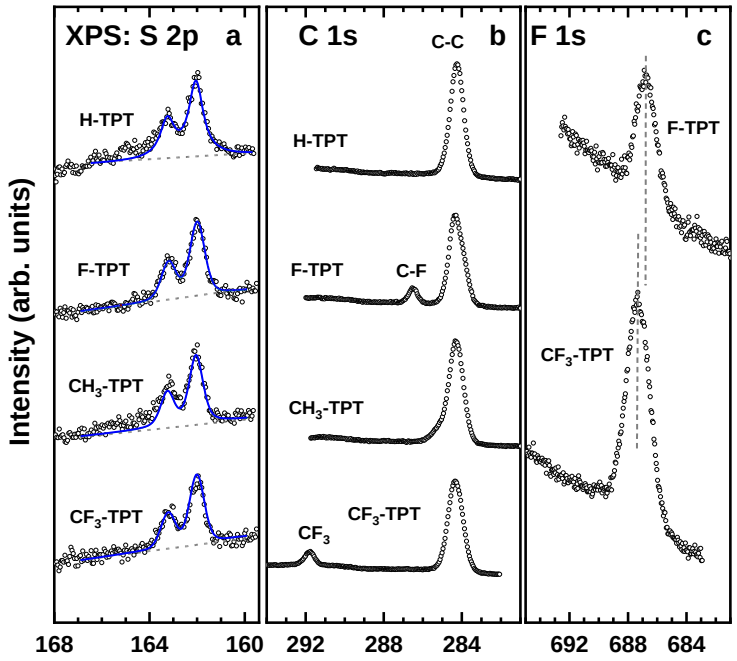

Figure 4.2 S 2p (a), C 1s (b), and F 1s (c) XP spectra of the R-TPT SAMs. The spectra were measured at PEs of 350 eV (a,b) and 750 eV (c). The S 2p spectra are fitted by a single S $2p_{3/2,1/2}$ doublet (blue solid lines) and a linear background (gray dashed lines). Individual peaks in the C 1s spectra (b) are marked (see text for details). Vertical gray dashed lines in (c) trace the BE positions of the F 1s peaks.

The S 2p, C 1s, and F 1s XP spectra of the R-PT SAMs are presented in Fig. 4.3. The spectra are quite similar to those in Fig. 4.2 but there are few differences which should be discussed. First, along with the doublet characteristic of the thiolate species bound to noble metal substrates, the S 2p spectra in Fig. 4.3a exhibit an additional feature at ~161.1 eV (S $2p_{3/2}$), which, in our opinion, represents atomically adsorbed sulfur (see refs[123,124,125] for alternative assignments). This assignment relies primarily on the literature[126] and our own[118] data for the strongly annealed alkanethiolate SAMs on Au(111), which exhibit the S 2p doublet at ~161.1 eV (S $2p_{3/2}$) at the full disappearance of the C 1s signal. The intensity of the ~161.1 eV doublet is however noticeably lower than that of the thiolate feature and the presence of the comparably small amount of S atoms at the SAM-substrate interface should not distort it noticeably.[128] Second, the C 1s spectra in Fig. 4.3b exhibit several very weak peaks, viz. at ~286.2 eV for the H-PT SAM and at ~288.6 eV for the H-PT and F-PT monolayers, stemming from minor contamination in these films (most likely, residuals of the substrate contamination which was not completely removed by self-cleaning process upon the SAM assembly). Third, the F 1s peaks in the spectra in Fig. 4.3c have a lower intensity compared to these in Fig. 4.2c, which suggests lower packing densities of the R-PT SAMs compared to the R-TPT monolayers.

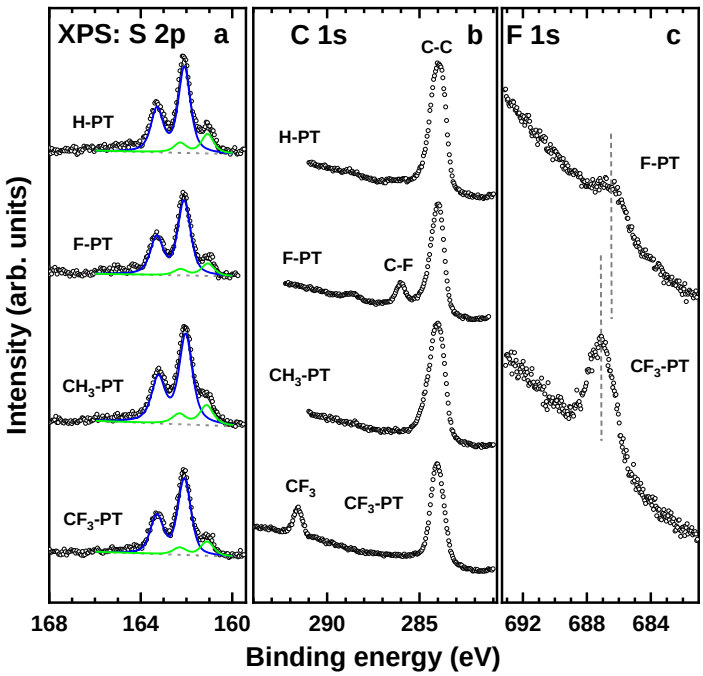

Figure 4.3 S 2p (a), C 1s (b), and F 1s (c) XP spectra of the R-PT SAMs. The spectra were measured at PEs of 350 eV (a,b) and 750 eV (c). The S 2p spectra are fitted by a combination of two S $2p_{3/2,1/2}$ doublets at BEs of ~162.0 eV (blue solid lines) and 161.1 eV (green solid lines) and a linear background (gray dashed lines).

Individual peaks in the C 1s spectra (b) are marked (see text for details). Vertical gray dashed lines in (c) trace the BE positions of the F 1s peaks.

The packing density of the n-TPT and n-PT SAMs was tentatively calculated on the basis of the S 2p (thiolate)/Au 4f intensity ratios using the standard approach,[104,118] the literature values for the attenuation lengths,[118] and the C16 monolayer with a known packing density (4.63×10^{14} molecules/cm^2)[112] as the reference. The respective values are compiled in Table 4.1 along with the analogous values for the R-BPT SAMs taken from refs.[104,118] The packing densities of the R-TPT SAMs are similar and close to that of the reference C16 monolayer, in full agreement with the recent STM data.[129] The packing densities of the R-PT SAMs are indeed somewhat lower (by 10-17%).

A further important parameter, which was evaluated on the basis of the XPS data, using the ratio of the entire specific C 1s signal and the Au 4f signal, is the effective thickness of the R-nPT SAMs (Table 4.1). Once again, we used the standard procedure,[104] the literature values for the attenuation lengths, and the C16 monolayer with a known thickness (18.9 Å)[33] as the reference. The values of the effective thickness are compiled in Table 4.1, with probably somewhat less accurate values for the R-PT SAMs because of the presence of contamination. Nevertheless, all the effective thicknesses correlate well with the molecular length of the respective SAM-forming molecules, underlining once more the SAM character of the R-nPT films.

Table 4.1. Parameters of the R-nPT SAMs derived from the XPS and NEXAFS data: effective thickness, packing density (±7.5%), average tilt angle of the π* orbitals, and average molecular tilt angle (all angles with respect to the surface normal). The values for the R-BPT SAMs are taken from refs.[104,118]

Monolayer	Effective thickness (Å)	Packing density molecules/cm^2	Tilt angle of the π* orbitals (°)	Molecular tilt angle (°)
H-PT	5.7 ± 0.5	3.8×10^{14}	51 ± 3°	48 ± 3°
F-PT	5.6 ± 0.5	3.9×10^{14}	51 ± 3°	48 ± 3°
CH_3-PT	5.9 ± 0.5	4.0×10^{14}	52 ± 3°	46.5 ± 3°
CF_3-PT	6.8 ± 0.5	4.2×10^{14}	66 ± 3°	29 ± 3°
H-BPT	11.5 ± 0.3	4.6×10^{14}	82 ± 3°	10 ± 3°

F-BPT	9.8 ± 0.3	4.1×10^{14}	68.5 ± 3°	25.5 ± 3°
CH_3-BPT	13.1 ± 0.3	4.1×10^{14}	76 ± 3°	16.5 ± 3°
CF_3-BPT	13.3 ± 0.3	4.1×10^{14}	77 ± 3°	15.5 ± 3°
H-TPT	15.0 ± 0.3	4.5×10^{14}	74 ± 3°	19 ± 3°
F-TPT	15.2 ± 0.3	4.6×10^{14}	72 ± 3°	21 ± 3°
CH_3-TPT	17.8 ± 0.3	4.6×10^{14}	73 ± 3°	20 ± 3°
CF_3-TPT	18.0 ± 0.2	4.4×10^{14}	79 ± 3°	13 ± 3°

4.1.4 NEXAFS Spectroscopy

Complementary information on these films is provided by the NEXAFS spectroscopy data, which are presented in Fig. 4.4 and 4.5 for the R-TPT and R-PT SAMs, respectively (analogous data for the R-BPT monolayers can be found in refs[104,118]). The data in these figures are organized in such a way that the left panels show the spectra acquired at the so-called magic angle of X-ray incidence (~55°), which are exclusively representative of the electronic structure of the SAMs (unoccupied molecular orbitals), and the right panels show the difference spectra, which are representative of the molecular orientation in the films.[64]

Let us first discuss the data in Fig. 4.4. The 55° spectra of all R-TPT SAMs in Fig. 4.4a exhibit the characteristic resonance pattern of phenyl,[64] observed for terphenyl-based monolayers as well.[119,130] This pattern includes the most intense π_1* resonance at a PE of ~285.0 eV (1), a R*/C–S* resonance at a PE of ~287.0 eV (2), π_2* resonance at a PE of ~288.8 eV (4), and several σ* resonances (5-7) at the higher excitation energies. The spectrum of the F-TPT SAM exhibits an additional π* resonance at a PE of ~287.2 eV (3) associated with the splitting of the π_1* resonance into two individual resonances (1 and 3) driven by the electronegative 4'-substituent.[129] The less intense resonance (3) overlaps with the R*/C–S* feature. Also, the spectrum of the CF_3-TPT SAM contains an additional resonance at a PE of ~295.0 eV (8), characteristic of the terminal $-CF_3$ group.[131]

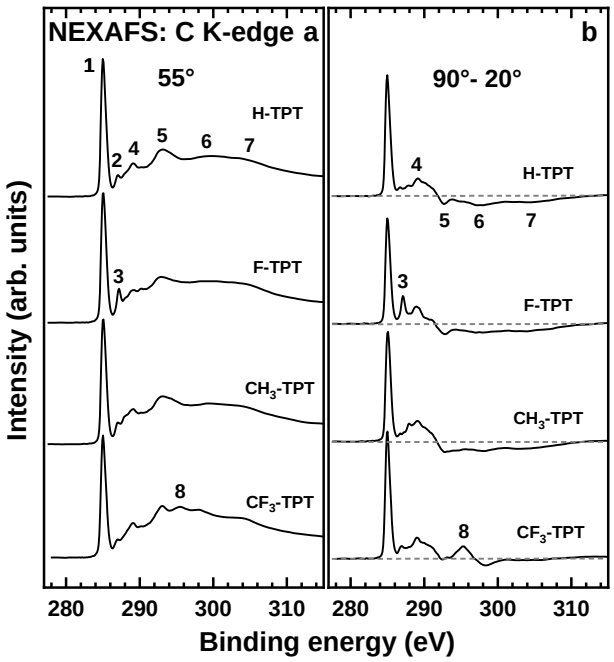

Figure 4.4 C K-edge NEXAFS spectra of the R-TPT SAMs: (a) the spectra acquired at an X-ray incidence angle of 55°; (b) the difference between the spectra collected under normal (90°) and grazing (20°) incidence geometry. Individual absorption resonances are marked by numbers (see text for details). The horizontal gray dashed lines in panel b correspond to zero.

The difference spectra in Fig. 4.4b show distinct peaks at the positions of the absorption resonances, manifesting thus an orientation order in the SAMs.[129] Significantly, these peaks are positive for the π* resonances and negative for the σ* features. Since the π* orbitals are oriented perpendicular to the phenyl rings and the σ* orbitals are spread within the ring planes, such a behavior suggests an upright molecular orientation in all R-TPT monolayers. Note that the dihedral rotation, typical of terphenyl in the molecular state,[132,133] is most likely lifted or nearly lifted in the densely packed SAMs,[134] so that the phenyl rings of the R-TPT adsorbates build the common molecular plane.

The 55° spectra of the R-PT SAMs in Fig. 4.5a are similar to those of the R-TPT monolayers but there are few differences. First, the intensity of the π_1* resonance is lower because of the stronger interaction of the respective excited state of the shorter molecules with the substrate, resulting in a partial quenching of the excitation.[119] Second, some resonances are less pronounced. Third, there are few additional resonances, such as π* resonance of COOH/C=O group[129] (a minor contamination; see above) at a PE of ~288.6 eV (9) in the spectrum of the F-PT SAM.

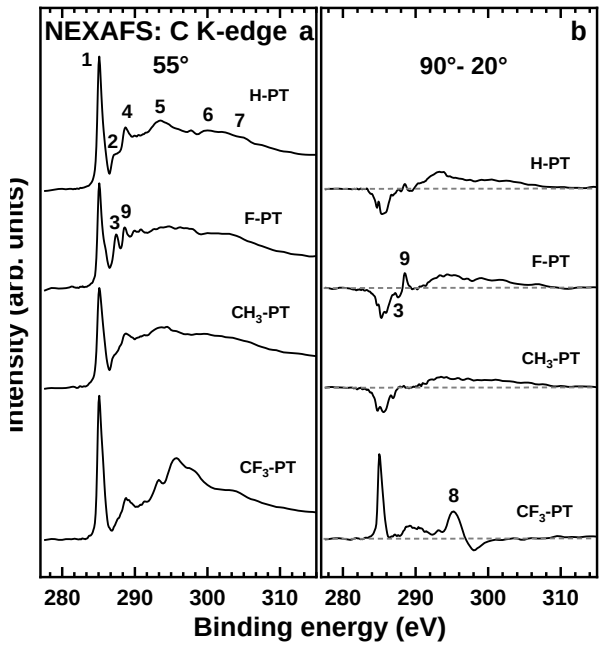

Figure 4.5 C K-edge NEXAFS spectra of the R-PT SAMs: (a) the spectra acquired at an X-ray incidence angle of 55°; (b) the difference between the spectra collected under normal (90°) and grazing (20°) incidence geometry. Individual absorption resonances are marked by numbers (see text for details). The horizontal gray dashed lines in panel b correspond to zero.

The difference spectrum of the CF_3-PT SAM in Fig. 4.5b is quite similar to that of the CF_3-TPT monolayer, whereas the spectra of the other R-PT SAMs differ noticeably from their TPT counterparts. The major difference is the reverse of the linear dichroism, with the (weak) negative peaks for the π^* resonances and positive peaks for the σ^* resonances. Such a behavior is characteristic of a larger molecular inclination compared to the R-TPT SAMs.

In addition to the above qualitative conclusions, numerical evaluation of the entire sets of the NEXAFS spectra for the R-PT and R-TPT monolayers was performed relying on the intensity of the π_1^* resonance as the most prominent and well-defined absorption feature in the spectra.

The standard theoretical framework for a vector-like orbital,[129] specifically adapted to SAMs,[119,131] was used. The derived values of the average tilt angles of the π_1^* orbitals are compiled in Table 4.1, along with the literature data for the R-BPT monolayers.[104,118] Using these values, the average molecular tilt angles can be calculated, as far as the molecular twist angle describing the rotation of the molecular plane around the main molecular axis,[135] is known. Taking the twist angle value from the bulk biphenyl crystals (32°),[136,137] which, in our opinion, is also realistic for oligophenylenethiolate SAMs on Au(111),[135] the average molecular tilt angles of the R-nPT monolayers were calculated (Table 4.1). The values for the R-TPT SAMs are expectedly

lower than those for the R-PT monolayers. The values for the R-BPT films are close to those of the R-TPT SAMs and in some cases even lower. The presence of the $-CF_3$ group seems to have a positive impact on the molecular inclination, resulting in the comparably small average tilt angle values for the CF_3-PT and CF_3-TPT SAMs. One can speculate that the presence of the bulky $-CF_3$ groups imposes certain sterical demands onto the assembling molecules, promoting upright orientation.

4.1.5 Work Function

Whereas the H-nPT molecules are non-polar, the $-CH_3$, –F, and $-CF_3$ terminated ones are polar, mediated by the dipole moment of the tail group. For the molecules anchored by the thiolate moiety, the dipole moment is directed away from the substrate for the $-CH_3$ group and to the substrate for the –F, and $-CF_3$ groups. The relative change of the molecular dipole with respect to the non-polar case can be estimated at +0.43 D, –2 D, and –4.43 D, based on the literature data for a series of substituted oligo(phenylene ethynylene)thiols.[138] The work functions of the respective SAMs on gold[138] as well as those of F-TPT, F-PT and CF_3-PT on copper[139,140] follow coarsely the above relation of the dipole moments.

The WF values determined from the SECO spectra are presented in Fig. 4.6, along with the literature data[104,118] for the R-BPT monolayers. In the R-TPT case, the behavior of the WF correlates perfectly with the dipole moments of the tail group (see above), with the slightly lower value for R = CH_3 compared to the non-polar case (R = H) and successively higher WF values for R = F and R = CF_3. Note that the lower WF value for the non-polar SAM as compared to the surface of clean gold (5.2-5.3 eV)[141] is related to the bond dipole at the SAM-substrate interface, associated with the charge rearrangement upon SAM adsorption.[142,143] Consequently, the entire electrostatic effect of a particular SAM represents a "superposition" of the bond and molecular dipoles. In addition, the length of the molecular backbone should be of importance as well, because of depolarization effect of the SAM matrix (see, e.g. ref[144] and references therein).

In Fig. 4.6, the WF behavior in the R-BPT case is similar to that of the R-TPT SAMs, albeit with a somewhat higher WF value for R = CH_3 and slightly lower values for R = F and R = CF_3. In the R-PT case, the WF values for R = H and R = CH_3 are comparably high (smaller variation compared to clean gold), which is most likely related to the lower packing density and the stronger molecular inclination in the R-PT SAMs compared to the biphenyl and terphenyl monolayers (see section 4.1.3). The WF values for R = F and R = CF_3 are similar to those of F-BPT and CF_3-BPT.

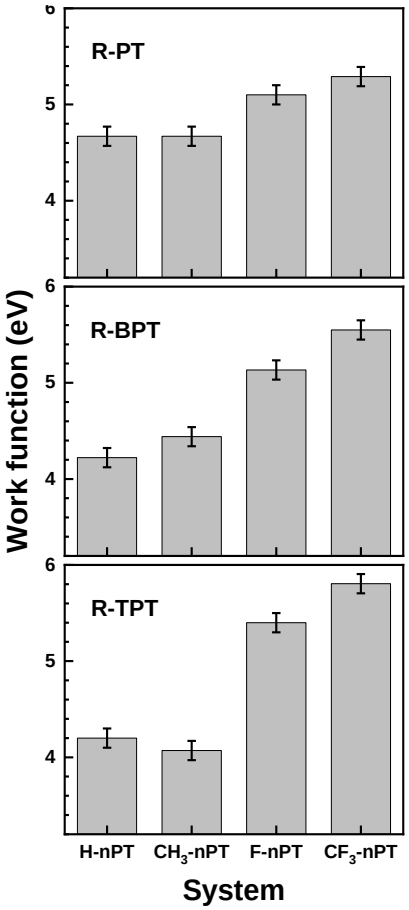

Figure 4.6 Work function values of the R-PT and R-TPT SAMs, along with the literature data[104,118] for the R-BPT monolayers. The values have been measured by UPS. The values for the R-BPT SAMs have been measured by A. Asyuda.[104,118]

4.1.6 Charge Transport Properties

Semilogarithmic current-density versus voltage (bias) plots for the Au^{Ts}/SAM//Ga_2O_3/EGaIn (SAM = R-nPT) junctions are presented in Fig. 4.7, with the data for the H-nPT, F-nPT, CH_3-nPT, and CF_3-nPT shown in Fig. 4.7a, 4.7b, 4.7c, and 4.7d, respectively. The detailed information about the number of junctions, scans, and data yield can be found in the Supporting Information (Table A.1). The heat maps for the individual curves can also be found in Fig. A.4 in the Supporting Information. As expected, for all R, the current density values decrease with the increasing length of the molecular backbone. The curves are nearly symmetric, with only a slight asymmetry for some of the SAMs and only pronounced asymmetry in the CF_3-TPT and CF_3-PT case. The respective rectification ratios, RR = J (+V)/ J (–V), at V = 1 V are ~4 and ~7, respectively (see the Fig. A.5), which are quite small values compared to the best performing molecular rectifiers (RR

= 10^3-10^5).[145,146] It is interesting, however, that the higher current density is observed at the positive bias, in contrast to the majority of molecular rectifiers, for which the opposite is the case.[145]

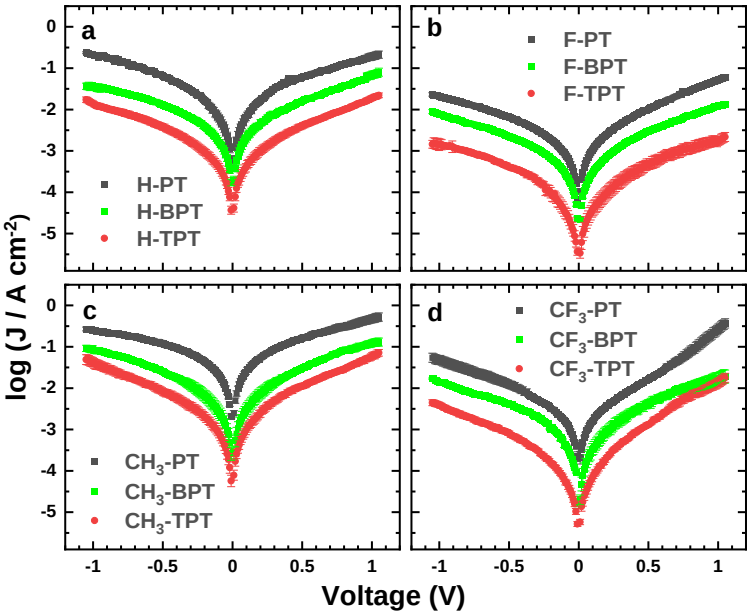

Figure 4.7 Semilogarithmic current-density versus voltage (bias) plots for the Au^{TS}/SAM//Ga_2O_3/EGaIn junctions with the H-nPT (a), F-nPT (b), CH_3-nPT (c), and CF_3-nPT (d) SAMs. The legends are given in the plots. The error bars represent the standard deviations.

The *J*-V curves for the backbones of the same lengths exhibit a strong dependence on the character of the tail group. This dependence is specifically visualized in Fig. 4.8, in which the values of $\ln|J|$ at a bias of +0.5 V (Fig. 4.8a) and −0.5 V (Fig. 4.8b) are plotted versus the molecular length (the respective $\log|J|$ histograms and heatmaps are shown in Fig. A.1-A.4 in the Supporting Information). Note that we intentionally use the molecular length in contrast to the film thickness, relying on the more realistic through-bond tunneling model.[147] For both the positive and negative bias and for all the SAMs studied, the current values show the same relation between the identity of the tail group and the current across the junction: the current decreases progressively at going from CH_3-nPT to H-nPT and further to CF_3-nPT and F-nPT. This relation is not only valid for a particular value of the molecular length selected at the x-axis but also when comparing the current values for the molecules with the same molecular backbone (PT, BPT or TPT).

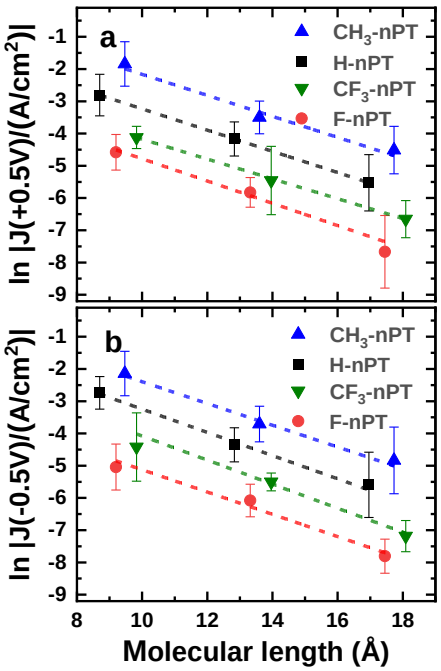

Figure 4.8 $\ln|J|$ at a bias of +0.5 V (a) and –0.5 V (b) for the Au/SAM//Ga_2O_3/EGaIn junctions containing the R-nPT monolayers. The values were derived from the *J*-V curves in Fig. 4.7. The legends are given in the plots. The error bars represent the standard deviations. The molecular lengths refer to the distances from the sulfur atoms to the terminal atom/atoms of the tail groups, including the van der Waals radii of S and H/F; note, however, that the S–Au bond length (~2.4 Å)[148,149] is somewhat larger than the van der Waals radius of S (1.8 Å). The color-coded dashed lines represent linear fits of the experimental data.

The data in Fig. 4.8 are well suited to get the values of the decay coefficient, β, for the SAMs studied. According to the equation $J = J_0 \exp(-\beta d)$, introducing this coefficient, it will be represented by the slope of the straight line fitting the experimental data in the given, semilogarithmic representation. The respective fits are explicitly shown in Fig. 4.8, representing the nearly parallel lines for all the SAMs studied. The corresponding β and J_0 values, obtained from the fits, are compiled in Table 4.2. Most important, the β values, ranging stochastically between 0.31 $Å^{-1}$ and 0.36 $Å^{-1}$ (+0.07 $Å^{-1}$ if corrected for the variation of the packing density with the chain length; see Table 4.1), do not vary noticeably over the series, showing no dependence on the identity of the tail group. These values are at the low end of the literature values for the decay coefficient of oligophenylene chain, ranging from 0.42 to 0.7 $Å^{-1}$ for the molecules which are not coupled chemically to the top electrode.[150,151,152] Note, however, that according to the literature,[151,152] the value of β depends strongly on the coupling to the top electrode and was reported to be 0.37 $Å^{-1}$ for a particular good coupling, mediated by the thiol tail group.[152] Also the charge transfer dynamics experiments, featuring an ultimate "coupling" of the resonant photon and

the excitable tail group of the SAM-building molecules, report a β value of 0.28 Å^{-1}.[153] As to the J_0 values, they are distinctly different for the different tail groups, reflecting the vertical shift of the ln J vs d curves.

Table 4.2 Decay coefficient and ln J_0 values derived from the data in Fig. 4.8a (V = +0.5 V) and Fig. 4.8b (V = –0.5 V). The accuracy of the β and J_0 values is ±5%.

Monolayer	β (V = +0.5 V) (Å^{-1})	β (V = –0.5 V) (Å^{-1})	ln J_0 (V = +0.5 V) (A/cm^2)	ln J_0 (V = –0.5 V) (A/cm^2)
CH_3-nPT	0.33	0.34	1.09	0.98
H-nPT	0.33	0.36	0.05	0.35
CF_3-nPT	0.31	0.37	-1.10	-0.35
F-nPT	0.35	0.35	-1.33	-1.67

4.1.7 Discussion

As expected, the quality of the R-nPT SAMs was found to vary over the series with the highest quality for the R-BPT case (according to the literature data)[104,118] and for the R-TPT monolayers and somewhat lower quality of the R-PT films. The latter is reflected by the comparably lower packing densities (Table 4.1), larger molecular inclination (Table 4.1), and the smaller variation of the work function with respect to clean gold upon the SAM formation (Fig. 4.6). Nevertheless, even the R-PT SAMs are characterized by a well-defined anchoring to the substrate (Fig. 4.3a), sufficiently dense molecular packing (Table 4.1), and upright molecular orientation (Table 4.1). Consequently, these films are well suited for the charge transport experiments within the entire R-nPT series.

The identity of the tail group seems to have a minor effect on the packing density but a noticeable effect on the molecular inclination. In particular, the $-CF_3$ group seems to promote the upright molecular orientation, which is especially obvious in the R-PT case but is also visible for the R-BPT and R-TPT SAMs (Table 4.1). This behavior is most likely related to the combination of sterical effects and the interaction between the $-CF_3$ groups, entering into the balance of the structure-building interactions.

The data for the work function (Fig. 4.6) show that the R-TPT SAMs most adequately mirror the molecular dipole moments of the precursors. The R-BPT monolayers do this as well for the R = F

and R = CF_3 cases but not for the R = CH_3 case. The data for the R-PT SAMs suggest that one should not entirely rely on the molecular dipole moments of the precursors in this particular case but always check the value of the work function for one's specific system. Whereas the one-ring SAMs are most favorable in context of superior charge transport properties (Fig. 4.7), their quality and consequently the value of the work function depend strongly on the parameters of the preparation procedure and can vary significantly from system to system. In some cases, it would be probably more favorable to use the R-BPT or even R-TPT SAMs for electrostatic engineering of a particular interface, as far as their somewhat higher resistivity is acceptable.

The most important results are however the charge transport data (Fig. 4.7 and 4.9). The one-, two-, and three-ring R-nPT SAMs consistently show the same effect of the tail group on the charge transport properties: the highest current density at a given bias is observed for R = CH_3 and is subsequently lower for R = H, R = CF_3, and R = F. This behavior correlates neither with the molecular lengths of the SAM precursors (see the x-axis in Fig. 4.8) nor with the work functions of the respective SAMs. Significantly, the height of the tunneling barrier, related to the R-nPT//Ga_2O_3/EGaIn interface, most likely does no change noticeably at the R variation at the given length of the molecular backbone.[117,154] It is assumed and shown by the example of the halogen-substituted BPT SAMs on Au(111) that the charge transport in these systems is predominantly mediated by the HOMO-derived state, which is delocalized over the entire molecular backbone.[117] This behavior can also be expected for the R-PT and R-TPT monolayers, even though the exact value of the HOMO offset varies with the length of the oligophenylene chain.[152] In contrast, the energy barrier at the Au/R-nPT interface should not vary much over the entire series, relying on the efficient electronic coupling provided by the thiolate-gold bond.

The difference in size between the terminal hydrocarbons and fluorocarbons can also be hardly a decisive factor for the observed differences in the current density between the R-nPT SAMs with the different R. According to estimates,[155] a rather small difference (a factor of ~1.3 for C–H versus C–F) is expected, which is much lower than the differences observed in our experiments (see Fig. 4.8).

Possible influence of water at the SAM/contact interface can also be excluded. The recorded humidity at the experiment site was ~30% and all the SAM studied are hydrophobic. Also, the respective water contact angles, decreasing in particular from 95° (R = CF_3), to 85° (R = CH_3 and F) and to 71° (R = H) for the R-BPT series,[102] show no correlation with the current density values, decreasing at going from R = CH_3 to –H to –CF_3 and to –F.

The most likely reasons for the observed effect of the tail groups on the charge transport properties of the R-nPT SAMs are (i) the difference in the projected density-of-states (PDOS) in the region

of the terminal tail groups,[156,157] (ii) the difference in effective electrical contact area at the SAM//Ga_2O_3 interface,[155] and (iii) the appearance of an internal electrostatic field (built-in field) within the SAMs, emerging at their contact to the top Ga_2O_3/EGaIn electrode.[117,158] The difference in the PDOS was in particular demonstrated by the DFT calculations for the Au/SAM//Au junctions featuring the CH_3-BPT and CF_3-BPT SAMs.[156,157]Accordingly, the PDOS in the proximity of the Fermi energy for the $-CH_3$ tail group is noticeably larger than that for the $-CF_3$ termination, resulting in a noticeably higher (by a factor of ~5) tunneling current in the former case.[156] Analogous behavior was also assumed and verified experimentally[159] for the $-CH_3$ and $-CF_3$ substituted aliphatic SAMs, suggesting a general character of the tail-group-mediated PDOS effect. The possible differences in effective contact area between the H/Ga_2O_3 and F/Ga_2O_3 interfaces were discussed in ref[155], on the basis of fundamental study presented in ref [78]. They are not related to the differences in geometrical contact area, precisely measured in the experiment, but stem from the differences in surface energy and the tail-group-mediated differences in the strength of the van der Waals interactions across the interface. The third factor, built-in field, represents a means to achieve an equilibrium in a molecular junction.[117] The exact profile of such a field depends strongly on the polarity of the tail group in the vicinity of the top electrode. The changes in this profile impose a renormalization of the relative energy level alignments for individual molecular building blocks, changing also the absolute positions of these energy levels with respect to the Fermi level of the system.[158]

The final issue, representing the major goal of the present study, is the possible effect of the tail group on the decay coefficient. According to the data in Fig. 4.8 and Table 4.2, no effect is observed, in contrast to the recent data for the halogen-substituted alkanethiolate (R-Cn; R = F, Cl, Br, and I) SAMs on Ag.[105] Note, however, that the recorded values of β for the H-nPT and CH_3-nPT SAMs (0.33-0.34 $Å^{-1}$, averaged over the values for V = $\pm$ 0.5 V) are rather low compared to the analogous values for the non-substituted alkanethiolate SAMs (ca. 0.75 $Å^{-1}$).[105,160] which makes their further decrease, triggered by the F/CF_3 substitution, quite questionable. Note also that the major effect of the halogen substitution on the decay coefficient for the R-Cn SAMs on Ag was recorded for iodine (0.25 $Å^{-1}$),[105] whereas the value for R = F was only slightly different from that for the non-substituted monolayers. Also, the halogen-substitution-induced variation of β in the R-Cn SAMs was on the one hand associated with the change of the tunneling barrier height and, on the other hand, with the change of the dielectric constant of the SAMs. However, as mentioned above, the tunneling barrier height does not vary noticeably in the R-nPT case and the dielectric constants of non-substituted and CH_3/F/CF_3-substituted R-nPT SAMs are most likely quite close, which was explicitly verified for the H-BPT and F-BPT monolayers.[117]

4.2 Effect of pentafluoro-λ⁶-sulfanyl Termination on Molecular Organization and Charge Transport of Aromatic SAMs

4.2.1 Motivation

As discussed in the previous chapter, $-CF_3$ exhibits strong particular polarity and hydrophobicity, due to the presence of highly electronegative fluorine atoms. In order to achieve a higher work function in electrostatic interface engineering, we hypothesize that employing more than three fluorine atoms could further realize this goal.

Due to the limitation of the coordination number of carbon atoms, it's possible to realize this idea by replacing C with S atoms. It has been evidenced that the dipole moment of $C_6H_5-SF_5$ is significantly higher than that of C_6H_5-CF_3 (3.44 D vs. 2.68 D, respectively[161]). Following this strategy, SF_5-terminated perfluoroalkane thiols and dialkyl disulfides were synthesized and used for SAM formation on gold substrates.[107,162] In this paper, we prepared corresponding SAMs on polycrystalline Au(111) substrate by using the molecules as shown in Fig. 4.9, and characterized them in great detail. The emphasis was put on the molecular organization of these SAMs and their electrostatic properties, important in context of applications. Note that the oligophenylene backbone was chosen as it provides a much better charge transport[160,163,164] than the alkyl and perfluoroalkyl backbones used before in combination with the $-SF_5$ tail group.[107,162] Therefore, this paper also focuses on their charge transfer characteristics.

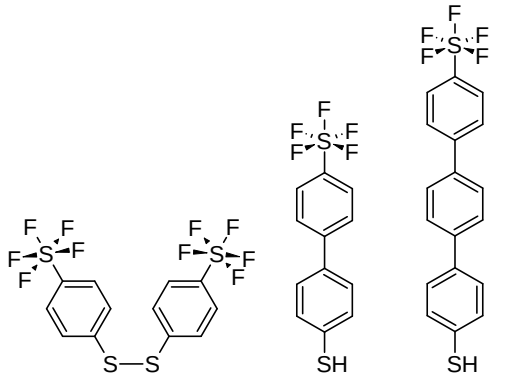

SF_5-PT **SF_5-BPT** **SF_5-TPT**

Figure 4.9 SAM-forming molecules used in this subproject along with their acronyms. Note that both thiols and disulfides are generally considered to be equivalent in their ability to form thiolate-anchored SAMs on coinage metal substrates, including Au(111) in particular.[1] The substances were custom-synthesized by the group of our partner, Prof. A. Terfort (Frankfurt University).

4.2.2 SAM Preparation

The SF_5-nPT SAMs were formed by the standard immersion procedure. Precursor solutions of SF_5-nPT were prepared by dissolving the neat substances in 10 mL of freshly degassed (3 freeze-pump-thaw cycles) p.a. grade ethanol (Fisher Scientific) and stored in an inert atmosphere. The precursor concentration in all solutions was kept around 0.1 mM for all depositions. Substrates were immersed in the precursor solutions for 20 h at room temperature. After removal from the solutions, the substrates were rinsed with p.a. grade ethanol and subsequently dried in a nitrogen stream. Additionally, a reference C16 SAMs were prepared using the analogous immersion procedure (1 mM in ethanol; 24 h; room temperature).

4.2.3 XPS

The characteristic XPS data of the SF_5-nPT SAMs are presented in Fig. 4.10. The Au $4f_{7/2}$ spectra in Fig. 4.10a show a progressive decrease in intensity at going from SF_5-PT to SF_5-TPT, correlating with the lengths of the SAM-forming molecules (Fig. 4.9). The S 2p spectra in Fig. 4.10b exhibit a S $2p_{3/2,1/2}$ doublet at a BE of ~ 162.0 eV (S $2p_{3/2}$), characteristic of the thiolate species bound to noble metal substrates,[107] and a further doublet at a BE of 171.0–171.3 eV (S $2p_{3/2}$) assigned to the $-SF_5$ tail group.[107] The presence of the former doublet and the absence of the features characteristic of the weakly bound molecules (multilayers) indicate that all molecules in the films are bound to gold in thiolate fashion, evidencing the monomolecular (SAM) character of these films. For all these monolayers, the intensity of this doublet is noticeably lower than that of the $-SF_5$ feature because of the attenuation of the signal from the thiolate species at the SAM-substrate interface.[165] The extent of attenuation increases with the SAM thickness, related to the length of the molecular backbone, and, accordingly, the intensity of the thiolate doublet decreases at going from SF_5-PT to SF_5-TPT. In contrast, the signal of the terminal group, which hardly experiences any attenuation, does not vary much over the series, suggesting a similar packing density in all three monolayers. Interestingly, the BE of the respective doublet is the lowest for SF_5-PT/Au (171.0 eV) and the highest for SF_5-TPT/Au (171.3 eV), which is also the case for the C 1s and F 1s signals discussed below. The reason for this effect is the screening of the photoemission hole by conduction electrons in the substrate, with the extent depending on the distance between the hole and the substrate. Consequently, the respective lowering of the BE is stronger for the shorter SF_5-PT and weaker for the longer SF_5-TPT, suggesting an upright molecular orientation within the SAMs.

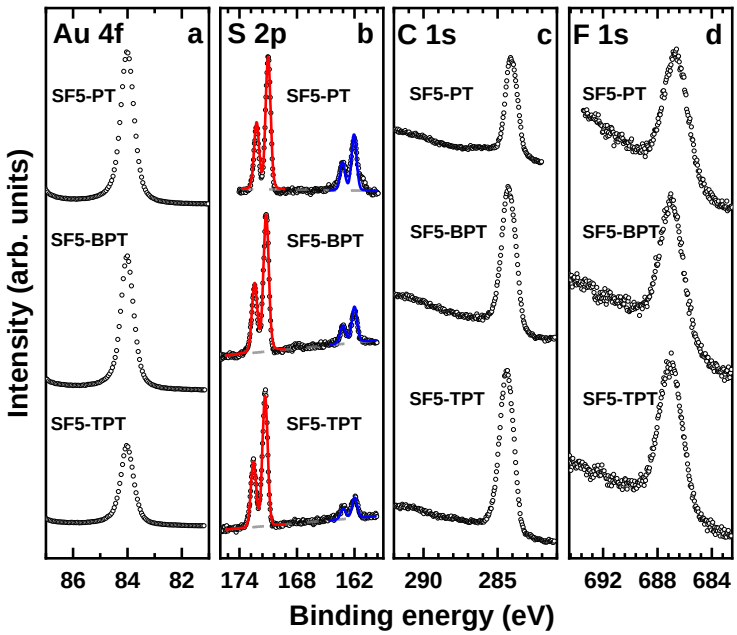

Figure 4.10 (a) Au $4f_{7/2}$, (b) S 2p, (c) C 1s, and (d) F 1s XP spectra of the SF_5-nPT SAMs. The spectra were measured at PEs of ((a)–(c)) 350 eV and (d) 750 eV. The S 2p spectra exhibit two S $2p_{3/2,1/2}$ doublets related to thiolate (blue) and $-SF_5$ (red).

The C 1s spectra in Fig. 4.10c exhibit a single peak at a BE of 284.05–284.35 eV, characteristic of the oligophenylene backbone of the SF_5-nPT molecules. In accordance with the molecular composition, this peak is the only feature in the spectra,[119,122] except for a small shoulder at a BE of 286.3 eV for the SF_5-PT SAM, stemming most likely from minor contamination at the substrate, which was not removed completely upon the SF_5-PT assembly (self-cleaning). The F 1s spectra in Fig. 4.10(d) show a single peak at a BE of 686.7–686.05 eV, associated with the fluorine atoms in the terminal SF_5 group. The intensity of this peak increases progressively at going from SF_5-PT to SF_5-TPT, suggesting that there does exist a small, but non-neglectible packing density variation between the SAMs studied.

The values of the packing density in the SF_5-nPT SAMs could be tentatively evaluated on the basis of the S 2p (thiolate)/Au 4f intensity ratios using the standard approach.[166,167,168] For the evaluation, we used the literature values for the attenuation lengths[58] and the C16 monolayer with a known packing density (4.63×10^{14} molecules/cm^2) as the reference, to determine the spectrometer-specific constants. The respective values are compiled in Table 4.3, along with a variety of other parameters, discussed below. The derived packing densities of the SF_5-nPT SAMs are lower than those of alkanethiolate SAMs (see above) and those of oligophenylene monolayers with $-CH_3$ and $-CF_3$ tail groups, viz., $(4.0 - 4.2) \times 10^{14}$ molecules/cm^2,[169] which is understandable

in view of the larger van der Waals radius of the $-SF_5$ group. A decrease in the packing density with decreasing molecular length is also understandable in view of a weaker intermolecular interaction, driving the self-assembly.

Table 4.3 Parameters of the SF_5-nPT SAMs: molecular length (including the van der Waals radii of the terminal F and S atoms), effective thickness (±8%), packing density (±8%), average tilt angle of the π* orbitals (±3°), and average molecular tilt angle (±5°), both with respect to the surface normal.

SAM	Molecule length (nm)	Effective thickness (nm)	Packing density (molecules/cm^2)	Tilt angle of the π* orbitals	Molecular tilt angle
SF_5-PT	1.056	0.98	3.0×10^{14}	67°	27.5°
SF_5-BPT	1.469	1.40	3.2×10^{14}	68°	26.5°
SF_5-TPT	1.881	1.83	3.6×10^{14}	71.5°	22°

Along with the packing densities, effective thicknesses of the SF_5-nPT SAMs were calculated, relying on the intensity of the Au 4f signal. We used the general expression for attenuation of photoelectron signal,[170] the literature value for the attenuation length,[58] and the C16 monolayer with a known thickness (1.89 nm[33]) as the reference, to determine the spectrometer-specific constants. The derived values of the effective thickness are compiled in Table 4.3. They correlate well with the molecular lengths representing the distance between the S atom and the terminal F atom of the $-SF_5$ group plus the van der Waals radii of sulfur and fluorine. Note, however, that the S–Au bond length (~ 0.24 nm[148,149]) is somewhat larger than the van der Waals radius of S (0.18 nm), so that the theoretical thicknesses of the SF_5-nPT SAMs with the strictly upright molecular orientation will be even higher (+0.06 nm). The XPS-derived effective thicknesses of all SAMs are close to these corrected values but somewhat lower, which suggests a certain degree of molecular inclination in the monolayers.

4.2.4 STM

STM images were measured by our partner group of Prof. A. Terfort (Frankfurt University). They are shown in Appendix B. As the SF_5-TPT monolayers turned out to be the densest, they were

characterized by STM. Images acquired at different magnifications are presented in Fig. B.1. The morphology of the surfaces is typical of thiolate monolayers in which the sulfur atom is bound directly to the aromatic moiety.[171] In Fig. B.1a, two islands of about 20 nm diameter and a few disordered sites in between domains can be seen. Domain sizes range from 5 to 10 nm as demonstrated in Fig. B.1b. In Fig. B.1c, a representative molecular-resolution image of an individual domain is shown. Within this domain, a (2 × 4) unit cell can be found. The lengths of the unit cell vectors are 1.20 ± 0.10 and 0.64 ± 0.05 nm. The experimentally determined distances between the molecules of 0.60 to 0.64 nm (Fig. B.1d) are in good agreement with the van der Waals dimensions of the $-SF_5$ unit (a lateral diameter of ~ 0.62 nm), indicating that the molecules form the closest packing possible. The packing density corresponding to this unit cell is 3.48×10^{14} molecules/cm^2, in excellent agreement with the XPS-derived value for the SF_5-TPT SAM (3.6×10^{14} molecules/cm^2, see Table 4.3).

4.2.5 NEXAFS Spectroscopy

The C K-edge NEXAFS spectra of the SF_5-nPT SAMs are presented in Fig. 4.11, including the spectra acquired at a "magic" angle of X-ray incidence of 55° (Fig. 4.11a) and the difference between the spectra acquired X-ray incidence angles of 90° and 20° (Fig. 4.11b). The data in Fig. 4.11a are exclusively representative of the electronic structure of the SAMs and are not affected by molecular orientation.[129] Complementarily, the data in Fig. 4.11b are representative of the molecular orientation in the SAMs.[129]

The spectra in Fig. 4.11a are dominated by the π_1* resonance of the oligophenylene backbone at a PE of ~ 285.1 eV (1),[119,129,171,172] accompanied by the weaker π* resonances at 287.15 eV (2) and 289.2 eV (3) as well as by σ* resonances at 293.05 eV (4), 296.3 eV (5), 298.8 eV (6) and 305.6 eV (7). The resonances 2 and 3 contain contributions from the R*/C–S* (~ 287.0 eV) and π_2* (~ 288.8 eV) resonances typical of non-substituted oligophenylene-based SAMs,[119] but are somewhat stronger. Their appearance can be related to the spitting of the π* orbitals of the terminal phenyl ring due to its 4'-substitution with the strongly electronegative $-SF_5$ moiety, similar as this occurs for the –F and $-CF_3$ substituted oligophenylene monolayers.[122,169] The pattern of the σ* resonances is generally similar to that of non-substituted oligophenylenes,[119,172] but has some differences, stemming once again from the presence of the $-SF_5$ moiety. The relative intensities of the individual resonances vary to some extent over the series, differing marginally for the SF_5-TPT and SF_5-BPT SAMs but noticeably for the SF_5-PT monolayer. The observed strong reduction of the resonance intensity in the latter case is typical of aromatic SAMs on metal substrates, and is

presumably related to the partial quenching of the respective excited states by the interaction with the substrate.[119] In addition, this reduction is a fingerprint of a somewhat lower quality of the SF_5-PT monolayer compared to the SF_5-BPT and SF_5-TPT SAMs.

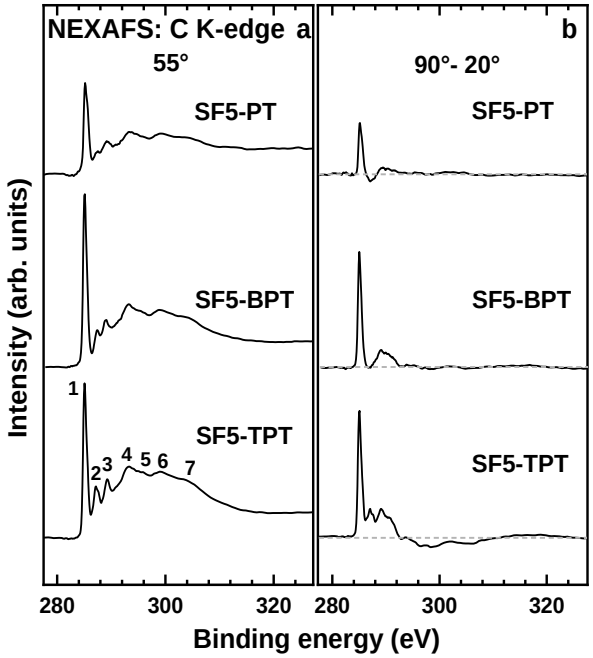

Figure 4.11 C K-edge NEXAFS spectra of the SF_5-nPT SAMs: (a) the spectra acquired at an X-ray incidence angle of 55°, and (b) the difference between the spectra collected under normal (90°) and grazing (20°) incidence geometry. Individual absorption resonances are marked by numbers (see text for details). Panels ((a) and (b)) have the same vertical scaling, so that the height of the difference peaks can be directly compared to that of the respective resonances. The horizontal gray dashed lines in panel (b) correspond to zero.

According to the data in Fig. 4.11b, the spectra of all SF_5-nPT SAMs exhibit pronounced linear dichroism, i.e., dependence of the resonance intensity on the X-ray incidence angle. Positive signs of the difference peaks for the π^* resonances in the difference spectra in Fig. 4.11b mean that the parallel orientation of the ***E***-vector of the synchrotron light with respect to the substrate (90°) gives a higher intensity than its orientation nearly perpendicular to the substrate (20°). Considering that the π^* orbitals are oriented perpendicular to the oligophenylene backbone, such a behavior suggests an upright molecular orientation in all SAMs studied. Considering the entire set of the NEXAFS data and using the standard framework describing the intensity variation of a particular resonance with X-ray incidence angle,[129] average tilt angles of the π_1^* orbitals in the SF_5-nPT SAMs, α, were calculated (Table 4.3). These angles are directly related to the tilt angle β of the molecular axis with

respect to the surface normal and to the twist angle γ of the aromatic rings with respect to the plane spanned by the surface normal and the molecular axis

$$\cos \alpha = \sin \beta \cdot \cos \gamma \qquad (4\text{–}1)$$

with γ defined as zero if the π_1* orbitals lie within this plane.[129] The twist angle cannot be directly measured by NEXAFS spectroscopy[135] but reasonably assumed on the basis of literature data for bulk oligophenylenes[136] and specifically decorated aromatic SAMs.[135] Accordingly, the twist angle was assumed to be close to 32°,[137] which resulted in the molecular tilt angles compiled in Table 4.3. In agreement with the XPS data (Section 4.2.3), the molecules are oriented upright but inclined to some extent (see Table 4.3), with the smallest inclination for the SF_5-TPT SAM and somewhat larger inclinations for the SF_5-BPT and SF_5-PT monolayers. This tendency is understandable since a longer molecular backbone promotes generally higher orientational order and smaller molecular inclination in SAMs.[119]

4.2.6 Wetting Properties

The advancing, receding, and static WCAs of the SF_5-nPT SAMs were determined as a descriptor for their hydrophobicity induced by the $-SF_5$ tail group (Table 4.4; see also Fig. A.6 and A.7). For the advancing and receding contact angles, a clear trend could be observed not only for the absolute values, but also for the margin of error: With the longer nPT backbone, the contact angles increase (advancing WCAs from 92° to 102°), while the variance decreases. This hints on a better definition of the packing with increasing length of the backbones. Significantly, these values are higher than the analogous values for the SAMs of CF_3-substituted biphenylthiolates on gold, which exhibit advancing and receding WCAs of 85° and 81°, respectively.[102] This relation underlines higher hydrophobicity of the $-SF_5$ group compared to $-CF_3$.

At the same time, the WCA values for the SF_5-nPT SAMs are lower than those for the analogous aliphatic SAMs, with the static values varying from 90° to 112°, depending on the length of the perfluoroalkane backbone.[104] In contrast, the static WCAs for the SF_5-PT, SF_5-BPT, and SF_5-TPT monolayers are determined at 84°, 86°, and 87°, respectively (Table 4.4). This relation is understandable, since the WCA values for aromatic SAMs are generally lower than those for the aliphatic monolayers with the same termination (compare, e.g., the values in refs.[102,174]), which is explained by the polarizability of the aromatic backbone, with the major effect provided by the ring adjacent to the tail group.[102] Obviously, the resulting field reaches through the topmost part of the SF_5-nPT SAMs, causing thus the observed reduction of WCA compared to the SF_5-terminated perfluoroalkanethiolate monolayers.

Table 4.4 Wetting behavior of the SF_5-nPT SAMs. Given are the advancing, receding, and static WCAs as well as the respective hysteresis

SAM	Adv. WCA	Rec. WCA	Hysteresis	Static WCA
SF_5-PT	92° ± 3°	70° ± 1°	22° ± 4°	84°
SF_5-BPT	98° ± 1°	78° ± 1°	20° ± 2°	86°
SF_5-TPT	102° ± 1°	80° ± 0.5°	24° ± 1.5°	87°

4.2.7 Work Function

Apart from the S–Au bond dipole (see below), the changes in the work function associated with the SF_5-nPT assembly, $\Delta\Phi$, can be described by the formula (see, e.g., refs[175,176])

$$\Delta\Phi = \rho_{SAM} \cdot \mu \cdot \cos\beta/(\varepsilon_{SAM}\cdot\varepsilon_0) \quad (4\text{-}2)$$

where ρ_{SAM} is the packing density of the SAMs (Table 4.3); μ the molecular dipole moment defined predominantly by the polar $-SF_5$ group; β the molecular tilt (Table 4.3); ε_{SAM} the dielectric constant of the SAM[176] and ε_0 the vacuum permittivity. Accordingly, the highest value of the work function can be expected for the SF_5-BPT and SF_5-TPT SAMs and a somewhat lower value for the SF_5-PT monolayer, in view of the lower packing density and the larger molecular inclination.

Work function of the SF_5-nPT SAMs was measured by XPS, on the basis of SECO. The derived work function values are shown in Fig. 4.12, viz., 5.62 eV, 5.95 eV, and 5.96 eV for the SF_5-PT, SF_5-BPT, and SF_5-TPT SAMs, respectively. These values are noticeably higher than those for monolayers of CF_3-substituted biphenylthiolates on gold (~ 5.5 eV[169]) and even higher than those of perfluorinated alkanethiolates monolayers on gold.[177] For the latter systems, an increase in the work function of up to 0.46 eV as compared to blank Au(111) was reported.[177] Assuming the work function of clean evaporated gold as 5.1 eV,[141] values up to 5.56 eV can be obtained—well below even the work function value for the SF_5-PT SAM. The latter value, in turn, is noticeably lower than those for the SF_5-BPT, and SF_5-TPT monolayers, which are quite similar and nearly reach 6.0 eV. This relation is most likely related to the inferior quality of the SF_5-PT SAM, formed by the rather short molecules, having generally a lower SAM-forming ability compared to molecules with a longer backbone.[119]

Note that non-substituted thiolate SAMs, both aliphatic and aromatic, generally lower the work function of gold, bringing it down to 4.3–4.4 eV,[175] mostly because of the pushback effect and

interfacial dipole at the SAM-substrate interface.[144] These can thus be considered as the reference values for the exclusive effect of the electronegative SF_5-groups, raising the work function nearly up to 6.0 eV.

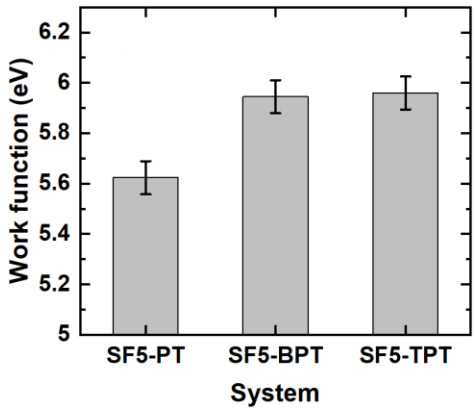

Figure 4.12 Work function values of the SF_5-nPT SAMs. The values have been measured by UPS.

4.2.8 Charge Transport Properties

A schematic of the charge transport experiments is shown in Fig. 4.13 and the respective data are presented in Fig. 4.14 (see Fig. A.8 and A.9 for more details). Semilogarithmic current-density vs. voltage (bias) plots for the Au^{TS}/SF_5-nPT//Ga_2O_3/EGaIn junctions are presented in Fig. 4.14a. The plots have a standard form, except for small deviations at bias values close to +1 V for the SF_5-BPT and SF_5-TPT SAMs. At a given absolute *V*, the current density values at positive and negative polarization are very close to each other, with a rectification ratio, RR = $|J(+V)/J(-V)|$, close to 1 for the nearly entire bias range and maximal values of 2–3 for the SF_5-BPT and SF_5-TPT SAMs at $V = \pm 1$ V. Thus, no rectification occurs.

As expected, the current density values at a given bias exhibit progressive decrease with increasing molecular length, with the highest values for the SF_5-PT SAM and the lowest values for the SF_5-TPT monolayer. Significantly, the current density values for the SF_5-BPT SAM at a given bias are not lower but even somewhat higher than those for the analogous CF_3-substituted monolayer,[169] in spite of the larger molecular length. This means that the exchange of the electronegative and strongly hydrophobic $-CF_3$ group for the even more electronegative and hydrophobic $-SF_5$ moiety does not result in a deterioration of the charge transport properties.

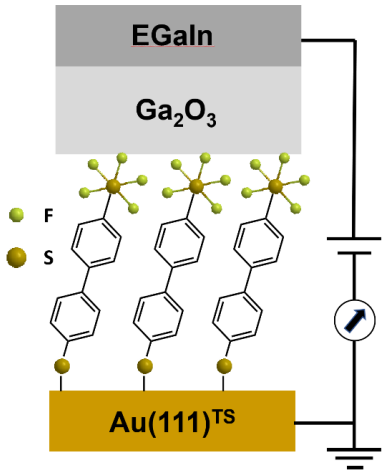

Figure 4.13 Schematic of the charge transport experiments. See Section 2 for technical details.

The values of the current density, J, across a molecular junction are generally defined by the equation

$$J = J_0 \exp(-\beta d) \quad (4\text{-}3)$$

where J_0 is a pre-exponential factor, β is the so-called tunnelling decay coefficient, and d is the molecular length.[10,160,171] Accordingly, the tunnelling decay coefficient is of primary importance. This parameter is predominantly defined by the identity of the molecular backbone, being close to ~ 0.75 $Å^{-1}$ for most of alkanethiolate SAMs[12] and ranging from 0.42 to 0.7 $Å^{-1}$ for most of oligophenylene monolayers.[150,163] At the same time, the value of β can be strongly affected by the character of the tail group, defining the coupling of molecules to the top electrode and triggering appearance of an additional (electrostatic) barrier at the SAM/top electrode interface.[153,179] For instance, according to a recent report,[164] the value of β is reduced from 0.54 to 0.37 $Å^{-1}$ if the oligophenylene thiolates are decorated with thiol tail groups, which have a strong affinity to the metal top electrode. In another, even more striking example, the substitution of alkanethiolates with just a single halogen atom (F, Cl, Br, and I) resulted in a progressive decrease of β from 0.75 to 0.25 $Å^{-1}$ (for I).[180]

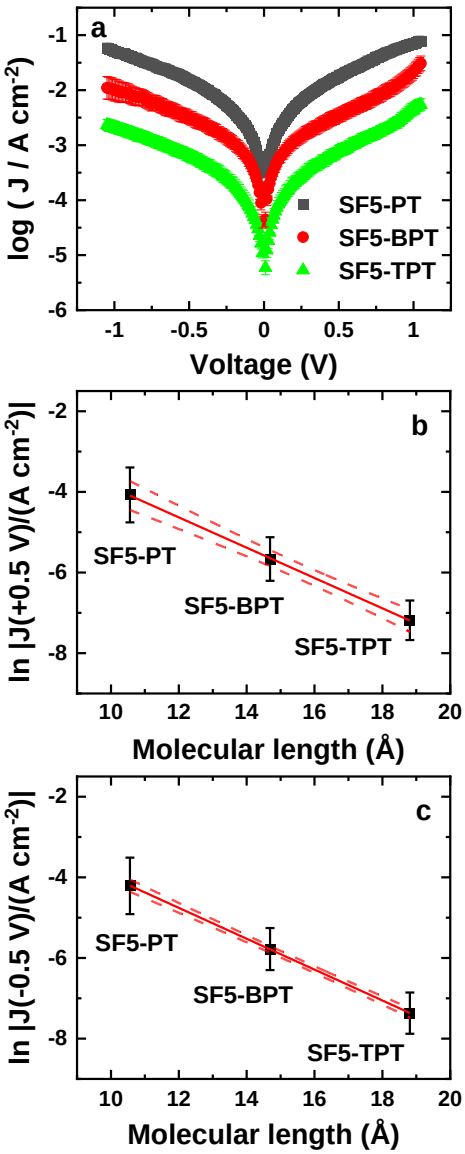

Figure 4.14 (a) Semilogarithmic current-density vs. voltage (bias) plots for the Au^{TS}/SF_5-nPT//Ga_2O_3/EGaIn junctions. The error bars represent the standard deviations. (b) The derived $\ln|J|$ at a bias of (b) +0.5 V and (c) −0.5 V as functions of the molecular length. The red solid lines represent linear fits of the experimental data. The error bars represent the standard deviations; the red dashed lines mark a CI of 95%.

In view of such a behavior, it was particular interesting to estimate the value of the tunnelling decay coefficient for the SF_5-nPT SAMs. For this purpose, I plotted $\ln|J|$ at biases of +0.5 V and −0.5 V as functions of the molecular length in Fig. 4.14b and 4.15c and performed linear fits to the experimental points. The resulting values of β are 0.38 ± 0.07 Å^{-1} for both V = +0.5 V and V = –0.5 V (J_0 = 0.88/0.85 V). They correlate closely with the lowest literature values for other oligophenylenethiolate SAMs, viz., 0.37 Å^{-1} [164] and 0.42 Å^{-1} [150]. Also, as shown by the

comparison of the SF_5-BPT and CF_3-BPT SAMs (see above), the pre-exponential factor behaves similarly. Consequently, the decoration of nPT with $-SF_5$ does not deteriorate the charge transport properties of oligophenylene backbone but probably even improves them to some extent. Note also that the value of β, the major parameter characterizing the charge transport, differs noticeably of that of aliphatic SAMs (~ 0.75 $Å^{-1}$),[12,13] undelaying the superior properties of the conjugated backbone of SF_5-nPT in this context.

4.2.9 Discussion

I have applied several complementary experimental techniques to verify the quality of the SF_5-nPT SAMs, to study molecular organization in these systems, and to monitor their most important (in context of application) characteristics, such as wetting, electrostatic, and charge transport properties.

According to the XPS, NEXAFS spectroscopy, and STM data, the SF_5-nPT films are indeed monolayers, with all the molecules bound to the substrate by the thiolate anchoring groups and the terminal $-SF_5$ groups building the SAM-ambient interface. In accordance with this organization, the molecules are oriented upright with respect to the substrate, with just a small inclination, increasing gradually at going from SF_5-TPT (22°) to SF_5-BPT (26.5°) and further to SF_5-PT (27.5°). Molecular packing in the SF_5-nPT SAMs is closest possible, defined by the dimensions of the comparably bulky $-SF_5$ group, as evidenced by the correlation of the van der Waals dimensions of this group (a lateral diameter of ~ 0.62 nm) with intermolecular spacings of 0.64 ± 0.05 and 0.60 ± 0.05 nm, derived from the STM data (Section 4.2.4).

These data suggest a (2×4) molecular structure, at least for the SF_5-TPT SAM, the only system for which STM data were obtained. The packing density corresponding to this unit cell is 3.48×10^{14} molecules/cm^2, in excellent agreement with the XPS-derived value of 3.6×10^{14} molecules/cm^2 (see Table 4.3). The packing densities of the SF_5-BPT and SF_5-PT SAMs are progressively lower, as follows directly from the values in Table 4.3 and, indirectly, from the behaviour of the F 1s XP spectra (Fig. 4.10d), showing progressively decreasing intensity at going from SF_5-TPT to SF_5-BPT and further to SF_5-PT.

The differences in the packing density, orientational order, and molecular inclination affect to some extent the wetting properties of the SF_5-nPT SAM, with only minor static WCA variation at going from SF_5-PT (84°) to SF_5-BPT (86°) and further to SF_5-TPT (87°) and somewhat larger advancing WCA variation across the series (from 92° to 102°; see Table 4.4). According to these values, the SF_5-nPT SAMs represent the most hydrophobic aromatic monolayers ever reported (to the best of

our knowledge) but are less hydrophobic than $-CF_3$ and even $-CH_3$ substituted aliphatic monolayers because of the polarizability of the oligophenylene backbone, affecting the WCA values.

In contrast, the differences in the packing density, orientational order, and molecular inclination are of importance for the electrostatic properties of the SF_5-nPT SAM, as evidenced by the noticeably lower work function value for the SF_5-PT monolayer (5.62 eV) compared to those for the SF_5-BPT (5.95 eV) to SF_5-TPT (5.96 eV) films. But even the value for the SF_5-PT monolayer (5.62 eV) is higher than those reported for any aromatic CF_3-substituted SAMs, which is the most electronegative tail group used so far (except for the single report on SF_5-terminated SAMs,[107] in which, however, work function was not mentioned). The values for the SF_5-BPT and SF_5-TPT, close to 6.0 V, are absolutely exceptional and the highest reported so far for gold substrates (to the best of our knowledge).

Significantly, the decoration of the nPT backbones with the $-SF_5$ group does not change noticeably the charge transport properties of the respective SAMs as compared to the analogous CF_3-substituted monolayers. This refers both to the absolute values of the current density at a specific bias and to the value of the tunnelling decay coefficient. The latter parameter was estimated as 0.38 $\pm$ 0.07 $Å^{-1}$, corresponding to the lowest values of β reported so far for oligophenylene SAMs and, as expected, being significantly lower than the value characteristic of the aliphatic monolayers (see above).

4.3 Pyrene-substituted alkanethiolate SAMs: Molecular Organication and Charge Transport

4.3.1 Motivation

Pyrene shows certain potential to be applied in the functional tail group of SAMs,[181] demonstrating the possibility of its functionalization,[182,183,184,185] which is based on some advantages, such as tuning the HOMO-LUMO gap and fluorescence behavior.[186] Although some studies have been performed on pyrene-substituted undecanethiol (Pyr-C11) monolayers,[187,188,189] the NEXAFS spectra are not, in our opinion, entirely convincing.[189]

To this end, I decided to revisit this system, taking a SAM of pyrene-substituted dodecanethiol (Pyr-C12; see Fig. 4.15) on Au(111) as a representative test monolayer.[189] In addition, I also studied the SAM of 2-{[2-(Pyren-1-ylthio)ethyl]thio}ethane-1-thiol (Pyr-C4S2; see Fig. 4.15) on Au(111) which features heteroatom (sulfur) substitution in the alkyl linker.[108] Both Pyr-C12 and Pyr-C4S2 SAMs were characterized by several complementary tools, including XPS, NEXAFS,

Kelvin probe technique, and contact angle goniometry. The emphasis was, however, put on the charge transport properties, which seem to be of particular interest in the context of the previous publications.[189]

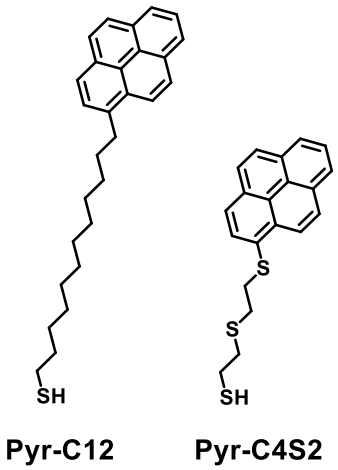

Figure 4.15 SAM-forming molecules used in this subproject along with their acronyms. The substances were custom-synthesized by the group of our partner, Prof. H. Lang (Technische Universität Chemnitz).

4.3.2 SAM Preparation

The SAMs were formed by the standard immersion procedure.[104,190] Solutions of the SAM precursors were prepared by dissolving the neat substances in 2 mL of freshly degassed (3 freeze-pump-thaw cycles) p.a. grade ethanol (Fisher Scientific) and stored in an inert atmosphere. The concentration of Pyr-C12 and Pyr-C4S2 in solutions was kept around 1 mM for all depositions. The substrates were rinsed by ethanol, dried in nitrogen stream, and immersed into the precursor solution, where they were kept at ambient temperature and in the dark for 24 h. Afterwards, the samples were extensively rinsed with ethanol, blown dry with a stream of nitrogen, and, for some experiments, stored in a plastic box filled with inert atmosphere until the measurements. As the references, C12 and C16 SAMs were prepared using the same immersion procedure (1 mM in ethanol; 24 h; room temperature; in the dark).

4.3.3 XPS

The Au $4f_{7/2}$, S 2p, and C 1s XP spectra of the Pyr-C12 and Pyr-C4S2 films are presented in Fig. 4.16. The intensity of the Au $4f_{7/2}$ peak for the former film is significantly lower than that for the latter layer (Fig. 4.16a), suggesting a higher effective thickness – in accordance with the molecular composition (Fig. 4.15). The S 2p spectrum of the Pyr-C12 film in Fig. 4.16b exhibits a single S

$2p_{3/2,1/2}$ doublet at a BE of 162.0 eV (S $2p_{3/2}$), which is characteristic of the thiolate species bound to Au substrate.[121] This means that all molecules in this film are bound to the substrate by the anchoring group and this film represents a SAM. The analogous doublet is also observed for the Pyr-C4S2 film, proving the monolayer character for this system as well. This doublet is, however, accompanied by a more intense one at 163.07 eV (S $2p_{3/2}$), assigned, in accordance with the molecular composition (Fig. 4.15) and the BE value,[121] to the two sulfur heteroatoms in the backbone of the Pyr-C4S2 molecules. The higher intensity of this doublet compared to the thiolate one is related to the two in-chain S atoms compared to one of the anchoring group and to smaller attenuation of the photoelectron intensity because of the closer proximity of the in-chain S atoms to the SAM-ambient interface. Note that physisorbed sulfur, characteristic of weakly bound molecules or multilayers, has somewhat higher BE (163.2-163.5 eV for S $2p_{3/2}$)[121] so that the presence of the respective species in the Pyr-C4S2 SAM can be excluded. Note also that small traces of atomically bound S, represented by a doublet at 161.1 eV (S $2p_{3/2}$)[121,126] cannot be completely excluded (see the spectrum for Pyr-C12), which, however, does not affect the molecular assembly.

The C 1s spectra of the Pyr-C12 and Pyr-C4S2 SAMs in Fig. 4.16c exhibit a single peak at a BE of ~284.3 eV and ~284.5 eV, respectively. These values are smaller than that for unsubstituted alkanethiolate SAMs (~284.9 eV for the C12 monolayer)[191] but similar to that for the anthracene-substituted alkanethiols (~284.3 eV)[192] underlining the effect of the pyrenyl substitution. The somewhat higher BE of the C 1s peak for the Pyr-C4S2 SAM is most likely related to the presence of the S heteroatoms. The lower intensity of this peak compared to the Pyr-C12 case agrees well with the Au $4f_{7/2}$ data (Fig. 4.16a) and the molecular composition (Fig. 4.15). A very small feature at ~286.9 eV observed in the spectrum of the Pyr-C12 SAM stems most likely from a minor contamination (COO^-).[193]

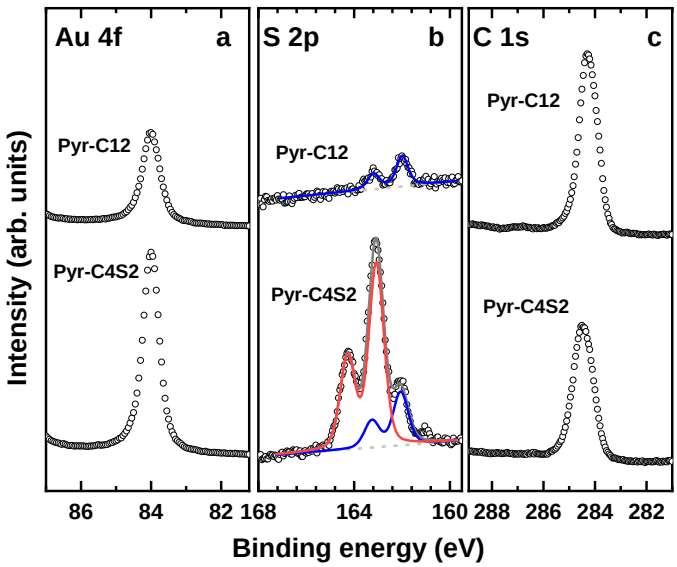

Figure 4.16 Au $4f_{7/2}$ (a), S 2p (b), and C 1s (c) XP spectra of the Pyr-C12 and Pyr-C4S2 SAMs. The spectra were measured at a PE of 350 eV. The S 2p spectra are fitted by a superposition of the S 2p doublets associated with the thiolate (blue lines) and in-chain sulfur (red solid line) and a linear background (gray dashed lines); the overall fit is drawn by gray solid line.

Apart from the above qualitative analysis of the spectra, they were evaluated quantitively. Specifically, the packing densities of the Pyr-C12 and Pyr-C4S2 SAMs were calculated on the basis of the S 2p (thiolate)/Au 4f intensity ratio using the established approach.[167,168] The standard formula for the attenuation of the photoelectron signal was applied[169] and the literature values of the attenuation lengths at the given kinetic energies of the photoelectrons were used.[58] The spectrometer-specific constants were calculated using the C16 monolayer with a known packing density (4.63×10^{14} molecules/cm^2) as the reference. The corresponding values are summarized in Table 4.5, along with a series of other parameters, discussed below. The obtained packing densities of the Pyr-C12 SAMs and Pyr-C4S2 SAMs are 3.6×10^{14} and 3.2×10^{14} molecules/cm^2, respectively. Both these values are lower than that for unsubstituted alkanethiolates, which is related to the bulky character of the pyrene tail group. The somewhat lower packing density in the Pyr-C4S2 case compared to Pyr-C12 stems most likely from the shorter linker of the former film (less efficient "drive" for the self-assembly) and a disturbing effect of the S heteroatoms. Note that the relations between the packing densities of the Pyr-C12 and Pyr-C4S2 SAMs and that of the non-substituted monolayer (0.78 and 0.69, respectively) correlate well with the analogous parameter reported recently for pyrene-substituted alkanethiols on Au (0.74),[194] even though the absolute values of the packing densities in ref[194] are somewhat too high, which can be related to either the presence of a multilayer fraction or an overestimate by the technique (microbalance

measurements).

Table 4.5 Parameters of the Pyr-C12 and Pyr-C4S2 SAMs: molecular length; effective thickness (±10%); packing density (±10%); average tilt angle of the π* orbitals (±3°); and average tilt angle of the pyrenyl groups (±3°), both angles are given with respect to the surface normal.

SAM	Molecular length/nm	Effective thickness/nm	Packing density molecules/cm^2	Tilt angle of the π* orbitals	Pyrenyl tilt angle
Pyr-C12	2.4	2.4	3.6×10^{14}	82°	9°
Pyr-C4S2	1.5	1.45	3.2×10^{14}	79°	12°

Along with the packing density, the effective thickness was also calculated. To this end, the ratio of the entire specific C 1s /Au 4f intensity ratio was used following the standard procedure.[168,195] Once again, the literature values of the attenuation lengths of the respective photoelectrons were used [58] and the C16 monolayer with a known thickness (1.89 nm)[49] served as the reference. The derived values are compiled in Table 4.5. They both are similar to the molecular lengths, which is typical of SAMs formed by upright-oriented molecules.

4.3.4 NEXAFS Spectroscopy

A more precise information about the chemical character and molecular orientation of the SAMs is provided by NEXAFS spectroscopy.[196] The C K-edge NEXAFS spectra are shown in Fig. 4.17, including the spectra acquired at a so-called "magic" angle of X-ray incidence of ~55° (Fig. 4.17a) and the difference between the spectra acquired at X-ray incidence angles of 90° and 20° (Fig. 4.17b). Whereas the "magic" angle data are exclusively representative of the electronic structure of the SAMs, without an admixture of orientation effects, the difference spectra are useful fingerprints of molecular orientation in the SAMs.[129] Note that at incidence angles of 90° and 20°, the **E** vector of the primary X-rays is oriented parallel and nearly perpendicular to the substrate, respectively. Note also that a high absorption intensity is generally observed if the orientation of this vector coincides with that of a vector orbital or coplanar with a plane orbital (linear dichroism).[129,196]

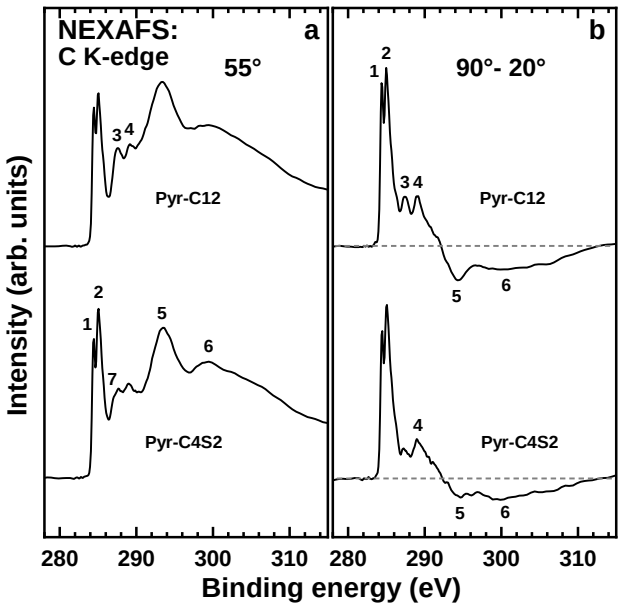

Figure 4.17 C K-edge NEXAFS spectra of the Pyr-C12 and Pyr-C4S2 SAMs: (a) the spectra acquired at an X-ray incidence angle of 55°; (b) the difference between the spectra collected under normal (90°) and grazing (20°) incidence geometry. Individual absorption resonances are marked by numbers (see text for details). Panels (a) and (b) have the same vertical scaling so that the heights of the difference peaks can be directly compared to those of the respective resonances. The horizontal gray dashed lines in panel (b) correspond to zero.

Both, the 55° and the difference spectra of the Pyr-C12 and Pyr-C4S2 SAMs are very similar, in spite of the difference in the length and character of the linker. This means that the observed features stem predominantly from the pyrenyl groups, which are common for the both monolayers. The 55° spectra of these monolayers in Fig. 4.17a are dominated by the intense double π* resonance at a PE of 284.45 eV (1) and 285.0 eV (2), which is the most characteristic feature of pyrene, ascribed to the LUMO and LUMO+1 orbitals of this moiety, respectively.[197] Note that the previously reported spectra of the pyrene-substituted monolayers did not show such a feature but a single π* resonance with a low intensity compared to the other peaks in the spectra, which casts some doubt in the identity of these monolayers.[187,189] In addition to the dominant feature, the 55° spectra of the Pyr-C12 and Pyr-C4S2 SAMs contain several other resonances at 287.5-287.7 eV (3), ~289.05 eV (4), ~294.4 eV (5), and ~299.4 eV (6). Whereas the resonances at 287.5-287.7 eV represent the so-called ´C–H´ band of the aliphatic linkers, associated both with valence C–H orbitals and Rydberg states,[198,199,200,201] that at 289.05 eV is most likely the π_2* resonance of pyrene (analogous to that in benzene),[129] while those at 294.4 eV and 299.4 eV are σ* resonances with the contributions from orbitals of both pyrene and alkyl linker. As can be expected because of the longer alkyl linker,

the resonance (3) for the Pyr-C12 SAM is more intense than that for the Pyr-C4S2 monolayer. However, in the latter case, this resonance is accompanied by an additional shoulder at 286.9 eV (7), most likely related to the C–S bonds in the alkyl linker.

The spectra of both Pyr-C12 and Pyr-C4S2 SAMs exhibit strong linear dichroism (i.e., dependence of the resonance intensity on the acquisition geometry), as emphasized by the difference spectra in Fig. 4.17b. The resonances with the π* and σ* character exhibit positive and negative peaks, respectively, in these spectra. In view of the orientation of these orbitals perpendicular (π*) and parallel (σ*) to the pyrenyl groups, this behavior suggests an upright orientation of these moieties in the SAMs. Also, the difference peak associated with the ´C–H´ band has the positive sign for both SAMs studied. Considering that the respective orbitals have the plane character and are perpendicular to the axis of the alkyl linkers,[198,200] I can conclude that these linkers are also oriented upright to the substrate.

Apart from the above qualitative considerations, quantitative evaluation of the NEXAFS data was performed in context of the orientation of the terminal pyrenyl groups. This evaluation was based on the standard theoretical framework for a vector-type orbital,[129] which, in the given case were the π* orbitals of the pyrenyl moieties. The intensities of the respective resonances (1 and 2) were plotted as a function of X-ray incidence angle, θ, and the respective data were fitted by a suitable equation, [129] with the tilt angle of the π* orbitals with respect to the surface normal, α, as parameter (see the Supporting Information for details: Fig. A.11-A.12 and Table A.3). The derived values of α are compiled in Table 4.5. These angles are directly related to the tilt angle of the pyrenyl moieties with respect to the surface normal, β, as far as the twist of these functional groups with respect to the tilt plane, described by angle γ, is considered according to the formula[135,202]

$$cos\alpha = sin\beta * cos\gamma \quad (4-4)$$

Note that γ is defined as zero when the π* orbitals lie within the tilt plane (see ref [135] for more details). Note also that the twist angle cannot be directly measured by NEXAFS spectroscopy but can be reasonably assumed to be close to 24° according to the literature data for pyrene-based compounds.[176,203] Note that this value is also very close to the analogous parameter for bulk anthracene, viz. 26°.[204] The derived values of β are compiled in Table 4.5. They are very small, suggesting a nearly upright orientation of the pyrenyl groups and a high orientational order in the respective part of the Pyr-C12 and Pyr-C4S2 SAMs. This order is presumably related to the strong interaction between the pyrenyl groups, arranged most likely in the herring-bone fashion, typical, e.g., for acene-terminated SAMs.[205,206] Note that similar to the latter systems,[192] the pyrenyl groups of Pyr-C12 and Pyr-C4S2 are attached nonsymmetrically to the adjacent alkyl linkers,

which provides additional rotational degree of freedom of these units in the SAMs. This permits the adoption of an almost upright orientation of the pyrenyl groups regardless of the length of the alkyl linker, which is of the primary importance in the context of so-called odd-even effects. The latter effects represent the dependence of the molecular orientation and packing density of substituted alkanethiolate SAMs on the number of the methylene groups (*n*) in the linker, with the parity of *n* being the decisive parameter.[192,193] I assume that these effects are strongly suppressed in the Pyr-C12 and Pyr-C4S2 SAMs because of the specific molecular architecture (see above).

4.3.5 IR Spectroscopy

Considering that the NEXAFS spectroscopy provided only limited information regarding the alkyl and alkyl-thioether linkers of the Pyr-C12 and Pyr-C4S2 SAMs, complementary IRRAS measurements were performed. The spectra for the most relevant range of C–H stretching bands of methyl and methylene units are presented in Fig. 4.18. The spectrum of the reference, unsubstituted C12 SAM exhibits the characteristic asymmetric (a) and symmetric (b) stretching bands of methyl and methylene units and a Fermi-resonance (FR) bands of methyl (all bands are marked in the figure). As expected, the spectra of the Pyr-C12 and Pyr-C4S2 SAMs show the methylene bands only, with their shift and splitting for the latter system. As known, the positions of these bands reflect the conformation of the alkyl chains, being 2918 cm^{-1} (ν_a) and 2850 cm^{-1} (ν_s) for all-trans conformation[280,281] and 2928 cm^{-1} (ν_a) and 2856 cm^{-1} (ν_s) for liquid alkane at room temperature, with ~40% of gauche defects.[280] In our case, the identical values of 2919 cm^{-1} (ν_a) and 2850 cm^{-1} (ν_s), characteristic of all-trans conformation of alkyl chains with a very low concentration of gauche defects, were measured for both C12 and Pyr-C12 SAMs. This suggests that the pyrene substitution does not disturb noticeably the conformational order of the alkyl chains and high orientational order is not only characteristic of the pyrenyl part of the SAM but of the alkyl part as well.

As to the Pyr-C4S2 SAM, the positions of the $\nu_a(CH_2)$ and $\nu_s(CH_2)$ are 2928 cm^{-1} and 2857 cm^{-1}, respectively, characteristic of significant disturbance of all-trans conformation of the alkyl linkers. It is, however, not surprising in view of the presence of two sulfur heteroatoms in these linkers.

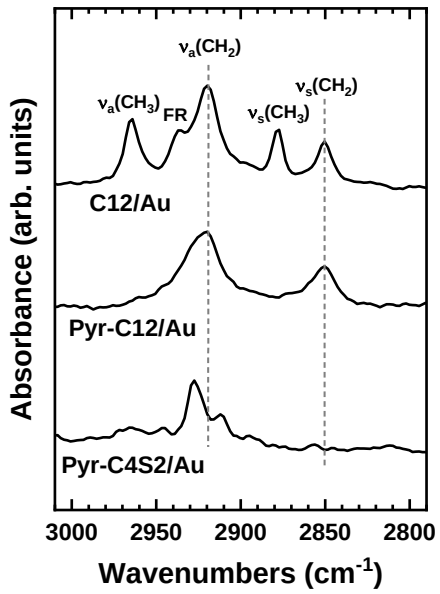

Figure 4.18 IRRAS spectra of the C12, Pyr-C12, and Pyr-C4S2 SAMs on Au in the range of C–H stretching bands of methyl and methylene unit. The characteristic absorption bands are indicated. The positions of the methylene-stemming bands for the C12 SAM are traced by the dashed lines.

4.3.6 Wetting Properties

The advancing (θ_A), receding (θ_R), and static (θ) water contact angles (WCAs) of the Pyr-C12 and Pyr-C4S2 SAMs are given in Table 4.6, along with the analogous values for the reference C12 monolayer, which agree well with the literature data[209] (see Fig. A.13 and A.14 in the Supporting Information for the raw data). The WCAs for the former SAMs are noticeably lower than those for the non-substituted reference (C12), which is predominantly related to the higher polarity of the pyrenyl groups compared to the terminal methyl groups of the reference film. A lower packing density and higher molecular disorder, which can generally diminish the WCA value, are hardly of importance here, in view of the dense molecular packing and high orientational order of the pyrenyl groups comprising the SAM-ambient interface. Note that the obtained WCA values are similar to those of the biphenylthiolate SAMs ($\theta_A \approx 73°$ and $\theta_R \approx 69°$),[210] terphenyl-substituted alkanethiolate SAMs ($\theta_A \approx 90°$ and $\theta_R \approx 79°$),[211] and those of anthracene-substituted alkanethiolate monolayers (θ = 73-83°)[192] on Au and Ag. The lower WCA values for the Pyr-C4S2 SAM compared to those for the Pyr-C12 monolayer are presumably related to the shorter linker (analogous to the series of the anthracene-substituted alkanethiolate SAMs)[192] and the somewhat larger disorder at the SAM-ambient interface, emphasized by the larger average tilt angle of the pyrenyl groups (see section 4.3.4).

Table 4.6 Wetting behavior of the C12, Pyr-C12, and Pyr-C4S2 SAMs. Given are the advancing (θ_A), receding (θ_R), and static (θ) WCAs as well as the respective hysteresis.

SAMs	θ_A	θ_R	Hysteresis	θ
C12	112.9° ± 0.8°	94.7° ± 0.4°	18.2° ± 1.2°	105°
Pyr-C12	90.0° ± 0.7°	68.9° ± 0.7°	21.1° ± 1.4°	81°
Pyr-C4S2	74.3° ± 1.2°	56.0° ± 0.7°	18.3° ± 1.9°	63°

4.3.7 Work Function

Even though pyrene is not a polar moiety, electrostatic properties of the Pyr-C12 and Pyr-C4S2 SAMs, reflected by the respective work functions, are certainly of interest, above all in context of organic electronics. The derived work function values of these SAMs and the reference C12 monolayer, measured by Kelvin Probe, are presented in Fig. 4.19. As expected, the values for the Pyr-C12 and Pyr-C4S2 SAMs do not differ much from those of the reference C12 SAM (~4.4 eV, in good agreement with the literature data[76]), being either slightly higher (~4.5 eV for the Pyr-C12 case) or slightly lower (~4.17 eV for the Pyr-C4S2) than the reference value. Whereas the former value most likely reflects the difference in the dielectric properties between the pure aliphatic matric and hybrid alkyl-pyrene framework, the latter value is presumably related to the presence of the S heteroatoms in the alkyl linker of Pyr-C4S2.

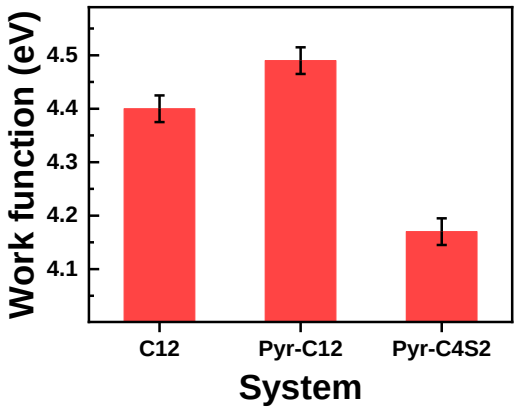

Figure 4.19 Work functions of the C12, Pyr-C12, and Pyr-C4S2 SAMs. The values have been measured by Kelvin probe.

4.3.8 Charge Transport Properties

The semilogarithmic current density versus voltage plots for the Au^{TS}/SAM//Ga_2O_3/EGaIn (SAM = Pyr-C12 or Pyr-C4S2) junctions are presented in Fig. 4.20a. I recorded statistically large numbers

of the *J(V)* curves to determine the Gaussian mean, and the details are shown in the Table A.4, Fig. A.15 and A.16 in the Supporting Information. Over the entire bias range, the Pyr-C4S2 SAM exhibits a higher current density than the Pyr-C12 monolayer, which is related to the longer aliphatic linker in the latter case. Generally, the values of the current density *J* follow t he Simmons model, according to the equation[84]

$$J = J_0 e^{-\beta d} \quad (4-5)$$

where J_0 is the current associated with the contact resistance, β is the tunneling decay parameter, and *d* is the molecular length. The value of β depends on the character of the molecular "wire" and is, in particular, much higher for the alkyl chain (0.76 $Å^{-1}$)[212,213,214] when compared to oligoacene backbones (0.2-0.5 $Å^{-1}$, depending on the coupling to the top electrode),[179] representing a strongly conjugated aromatic moiety, analogous to pyrene. In this context, the *J* values across the Pyr-C12 and Pyr-C4S2 SAMs, comprising both pyrene and alkyl parts, can be compared with those of non-substituted alkanethiolates of the same lengths (abbreviated as C_n), which is performed in Fig. 4.20b for a representative bias of +0.5 V. Note that the reference values for the Cn SAMs, shown as the dashed line in this figure, were calculated on the basis of the measured value for the C12 monolayer (see Fig. A.17 in the Supporting Information) and the attenuation factor for the given type of molecular wires (see above).

According to the data in Fig. 4.20b, the *J* value for the Pyr-C12 SAM is noticeably higher than that for the Cn monolayer with the same molecular length, which emphasizes the higher conductance of pyrene compared to alkyl chain (as expected). In contrast, the *J* value for the Pyr-C4S2 SAM is lower than that of the Cn monolayer with the same molecular length, in spite of the high conductance of pyrene. The reason for this behavior is the presence of the S heteroatoms in the alkyl linker of Pyr-C4S2. According to the literature data,[107] the introduction of these heteroatoms into an alkyl backbone does not change noticeably the attenuation parameter but results in a significant increase of the effective contact resistance, associated with a lift of degeneration and a space redistribution of the HOMO, playing the primary role in the charge transport. These changes result in a respective decrease of the J_0 value for the Pyr-C4S2 SAM, leading to the observed negative offset of the log *J* value compared to the Cn reference.

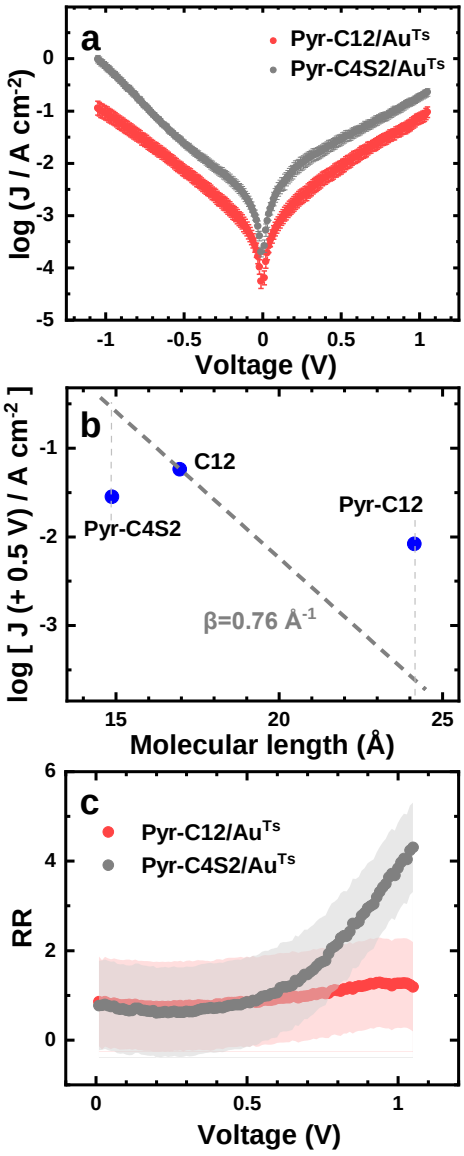

Figure 4.20 (a) Semilogarithmic J−V plots for the Au^{Ts}/SAM//Ga_2O_3/ EGaIn junctions comprising the Pyr-C12 and Pyr-C4S2 SAMs. The error bars represent the standard deviations. (b) Comparison of the log J values at a bias of +0.5 V for the junctions comprising the C12, Pyr-C12, and Pyr-C4S2 SAMs, plotted versus the respective molecular length. The gray dotted line represents the expected log J values for the C_n monolayers, simulated according to the log J value for the C12 monolayer and the attenuation constant of 0.76 $Å^{-1}$. (c) Effective RR versus bias voltage plots corresponding to the J−V curves in panel (a) (the shaded parts indicate the error bars). The legends are given in the panels.

$$RR = \left|\frac{J(-V)}{J(+V)}\right| \qquad (4-6)$$

(or other way around to be not less than 1)[215] and shown in Fig. 4.20c is close to 1 over the entire bias range. It is difficult to say what is the reason for this difference to the literature data but I can speculate that this is the specific orientation and arrangement of the pyrenyl moieties in the Pyr-C12 SAM of the present study. According to the literature data,[189] the *RR* value for Pyr-C11 films depends strongly on the molecular orientation, being particularly high for Pyr-C11/Ag (log *RR* = 2.2 ± 0.3 at V = 1 V), featuring small molecular inclination, and small for Pyr-C11/Au (log *RR* = 1.3 ± 0.6 at V = 1 V), featuring large molecular inclination. However, the C K-edge NEXAFS spectra of the respective films did not exhibit the specific signature of pyrene (see section 4.3.4) but just a single π*-like resonance at ~284.5 eV (along with few other resonances at higher excitation energies), having comparably low intensity, especially in the case of Pyr-C11/Ag. In contrast, this signature of pyrene is observed for the Pyr-C12 SAM of the present study (see Fig. 4.17), verifying the chemical identity of these monolayers.

Whereas the Pyr-C12 SAM does not exhibit a rectification behavior, it could be recorded for the Pyr-C4S2 monolayer. The respective log *J* vs *V* curve in Fig. 4.20a is slightly asymmetric, with higher values at negative biases compared to those at positive biases. The derived rectification ratio is shown in Fig. 4.20c; it starts to deviate from 1 at $V \approx 0.6$ V and increases progressively up to ~4.5 at $V = 1$ V. Such a different behavior with respect to the Pyr-C12 SAM can be related to either the presence of the S heteroatoms or the different orientation and arrangement of the terminal pyrenyl moieties. Note that according to the literature,[108] the introduction of the S heteroatoms does not result in the appearance of any asymmetry of the *I*(*V*) curves, so that this factor is presumably of no importance for the rectification and these are the pyrenyl groups which are responsible for this behavior.

The energetics in the junction can be tentatively probed by the so-called transition voltage, measured usually at both positive (V_T^+) and negative (V_T^-) bias.[83,216] This parameter corresponds to the change in the tunneling regime from Simmons tunneling (rectangular barrier) to Fowler-Nordheim (F-N) tunneling (triangular barrier).[97] Even though its precise physical meaning is still under debate,[217,218] it is generally believed that V_T represents an approximate measure of the tunneling barrier height, i.e. the difference between the energy of the accessible frontier orbital of a molecule and the Fermi level of the electrode in an assembled junction.[218,220] This parameter can be in particular determined from a F-N plot, $\ln(I/V^2)$ versus $1/V$, corresponding to the minima of such a plot.[90] The respective data are shown in Fig. 4.21, with the F-N plots depicted in Fig. 4.21a and the derived V_T values presented in Fig. 4.21b. Accordingly, the absolute values of both V_T^+ and V_T^- for the Pyr-C4S2 SAMs are somewhat lower than those for the Pyr-C12 monolayer, which means that the tunneling conditions (barrier height) are somewhat different for these two systems.

Interestingly, according to the literature,[108] the introduction of S heteroatoms into alkyl chains changes neither the V_T value nor the height of the effective tunneling barrier. Accordingly, this is most likely the difference in the orientation and arrangement of the pyrenyl moieties which is responsible for the observed V_T difference between the Pyr-C12 and Pyr-C4S2 SAMs. Whereas the orientation was directly derived from the NEXAFS data, differences in the molecular arrangements can be reasonably assumed, in view of the differences in the packing density and the orientation.

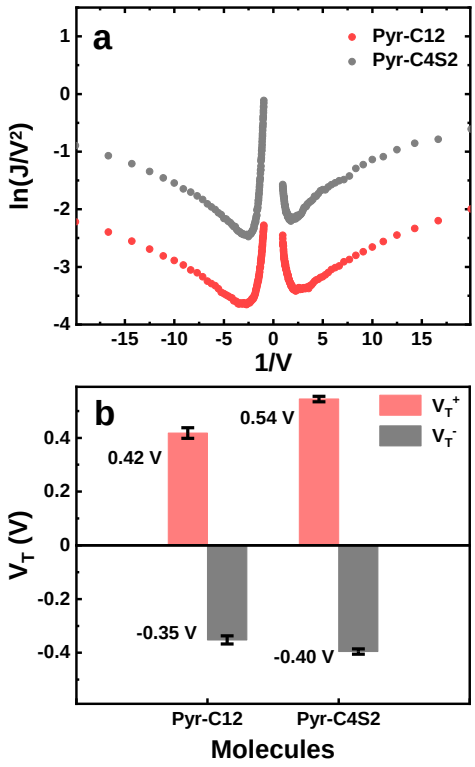

Figure 4.21 (a) Fowler-Nordheim plots for the Pyr-C12 and Pyr-C4S2 SAMs embedded into Au^{Ts}/SAM//Ga_2O_3/EGaIn junctions. (b) The derived transition voltage at the positive and negative bias, V_T^+ and V_T^-, respectively.

4.4 Sweep-Character-Dependent Switching of the Conductance State in Ferrocene-Substituted Thiofluorene SAMs

4.4.1 Motivation

Redox groups are widely used in various molecular blocks due to their different oxidation states and sensitivities to external stimuli.[221,222,223,224] Ferrocenyl (Fc), as one of the most popular redox-active moieties, is capable of attaching to aliphatic backbones and anchoring to substrates, such as

Au, Ag, and Pt, via thiolate docking groups, thus, resulted in a family of highly efficient molecular rectifiers.[35,225] In recent studies, the SAMs,[37] embedded into Fc-substituted fluorene thiols (Fc-FluT) molecular junction with a bottom Au and a top EGaIn electrode (EGaIn-eutectic GaIn alloy) showed two distinct conductance states, with the current densities differing by a factor of 10^2~10^3, depending on the bias value. However, the peculiar conductance state switching behavior in the Fc-FluT SAMs is not fully explored and understood.

In the present study, I focus on the Fc-FluT system (Fig. 4.22), as for the measurements discussed in ref[37] equivalent data for the entire Fc/Rc-BPT/FluT family have been observed. The major goal of the study is to gain a more profound insight of how changing the bias sweeping can impact the conductivity switching. In particular, I show that the pronounced effective rectification discussed above disappears, when symmetrically sweeping the junction and I discuss, how the final conductance state is impacted by the biasing history of the SAM. On more technical grounds, I analyze to what extent, the switching can be triggered also by a step-wise modulation of the applied bias. Here I show clearly that the conductance-state switching is not an instantaneous process, but requires several voltage pulses to complete. In order to clarify, whether the surface roughness of the bottom electrode (= Au substrate) might be a factor contributing to the peculiar switching behavior, I now prepared the Fc-FluT SAMs on ultraflat, template-striped Au(111) substrates (Au^{TS}) rather than on the previously used evaporated Au thin films that had been applied in ref[37].

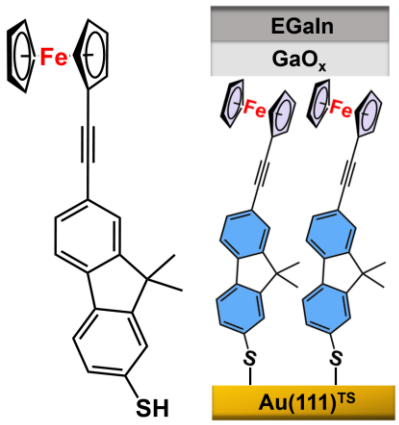

Figure 4.22 Structure of the Fc-FluT molecule and schematic picture of the Au^{TS}/Fc-FluT//GaOx/EGaIn junction. Note that "/" and "//" indicate interfaces with strong and weak electronic coupling, respectively. The substance was custom-synthesized by the group of our partner, Prof. H. Lang (Technische Universität Chemnitz).

4.4.2 SAM Preparation

Fc-FluT was synthesized according to the literature procedure.[106] The respective characterization data, including the ^{1}H NMR and ^{13}C NMR spectra, can be found in ref[106]; the purity of the compound exceeded 99%. All other chemicals, solvents, and reagents were purchased from Sigma-Aldrich and used as received. As substrates, I used Au^{TS}, representing a generally accepted standard for charge transport experiments on SAMs, to avoid any disturbing effects related to the substrate roughness.[226,227] These substrates were fabricated starting from commercial (Georg Albert PVD-Beschichtungen) gold films (99.99% purity Au; 300 nm), thermally evaporated onto polished single-crystal silicon (100) wafers (Silicon Sense). Thin glass slides were first glued to the outer surface of these films using a commercial glue and the gold/glue/glass trilayers were then peeled off the silicon support, exposing the ultraflat bottom face of the evaporated gold film. The root mean square (RMS) roughness value of the Au^{TS} substrates was estimated as 0.06 nm for both 1 μm × 1 μm and 5 μm × 5 μm scans. The bearing volume was estimated as 0.0184 ± 0.0001 μm^3. The respective atomic force microscopy (AFM) images are presented in the Supporting Information (Fig. A.18).

Right before the SAM preparation, the substrates were cleaned by rinsing them with ethanol and by blowing them dry with a stream of nitrogen or argon. The SAMs were formed by immersion of the substrates into 1 mM solutions of Fc-FluT in N,N-dimethylformamide (DMF) for 24 h, under ambient conditions and at room temperature, following an established procedure.[113] After immersion, the samples were extensively rinsed with DMF (to remove physisorbed material) and blown dry with a stream of nitrogen or Ar. In addition, SAMs of biphenylthiol (BPT; Sigma-Aldrich) on Au^{TS}, used for reference experiments, were prepared using the literature procedure.[118] Note that biphenylthiol and fluorenethiol have very similar charge transport properties.[228]

Charge transport measurements were performed with a custom-made, two-terminal molecular junction setup featuring a Keithley 2635A sourcemeter.[229] The gold substrate and a sharp EGaIn tip, covered by a naturally formed, thin (~ 0.7 nm)[230] GaO_x film, served as bottom and top electrodes, respectively (Fig. 4.22). The junctions were formed by contacting grounded Au^{TS}/SAM samples by the EGaIn tips with a contact area of 700-2000 μm^2 and applying a potential (bias) to the top electrode. The voltage was swept in several different ways, as will be specifically described below. Overall, a bias range from −1.05 V to +1.05 V was covered, the bias step was set to 0.01 V, and a typical duration of an asymmetric sweep (either from +0.01 V to +1.05 V or from –0.01 V to −1.05 V) was about 90 sec. Around 200 *J–V* curves were recorded for each sweeping type for several different samples and at various spots on each sample with maximal 20 sweeps at each spot

(to ensure the stability of the junction). The yield of reliable data varied between 62% and 89%; more details are provided in the Supplementary Information (Table A.2). Average values of the current density were calculated with either a Gaussian mean or median with a confidence interval of 99% (CI 99%) to express the precision of the statistical estimation.[231] Both procedures resulted in nearly identical values of the current density but somewhat different error bars. For the sake of clarity, I only present the data calculated with a Gaussian mean. The data are presented in different fashions including heat maps (Supporting Information), which are a useful way to capture details on junction quality irrespective of the total size of the data set or molecules used.[232]

In addition to sweeping the bias voltage, I also pulsed several measurements spots varying the bias either between +0.01 V and +1.05 V or between −0.01 V and −1.05 V. The duration of the bias pulses was about 1 sec and 50 pulses were successively applied at each spot. Again, the data were statistically processed.

Beyond the above-described experiments involving statistical averaging, I also studied the evolution of the system at the bias sweeping, analyzing individual I-V curves. The details of these measurements will be described below.

4.4.3 Sweep at Either a Positive or Negative Bias

The charge transport characteristics for the Au^{TS}/Fc-FluT//Ga_2O_3/EGaIn junction for bias sweeps either from +0.01 to +1.05 V or from –0.01 to –1.05 V are shown in Fig. 4.23; the corresponding heat maps, histograms of the $\log_{10}|J|$ values at several different biases, and characteristics with a linear current-density-axis are shown in Fig. A.19-A.21 in the Supporting Information. The semilogarithmic *J*-V curves in Fig. 4.23a represent the results of a statistical analysis over ca. two hundred sweeps (see Table A.5 in the Supporting Information), which is the standard data processing procedure for large-area molecular junctions.[231] These curves fully reproduce the results of ref [37] showing distinctly different current density values in the negative and positive bias ranges despite the use of much more flat Au^{TS} electrodes (see above). This shows that the observed effect is not related to the substrate roughness. The massive differences in the current densities are attributed to the high and low conductance states of the Fc-FluT SAM. The respective effective *RR*, calculated employing the standard definition $|J(-V)/J(+V)|$, is shown in Fig. 4.23b also on a semilogarithmic scale. The *RR* has a value of 330 at V = 0.01 V, reaches a maximum of ~2100 at V = 0.1 V, and then drops to a value of ~120 at V = 1.05 V. While *RR* values on the order of 10^3 and even higher have been reported for a variety of molecular assemblies,[146] they are usually observed at comparably high bias voltages of 1-3 V. Thus, the exceptionally high *RR* value already

at very low bias represents a promising feature of our system. In this context it should, however, be stressed that the values in Fig. 4.23b do not reflect "true" rectification, as they are observed for a specific way of sweeping the junctions (applying either only positive or only negative bias). They rather emphasize the difference between the high and low conductance states.

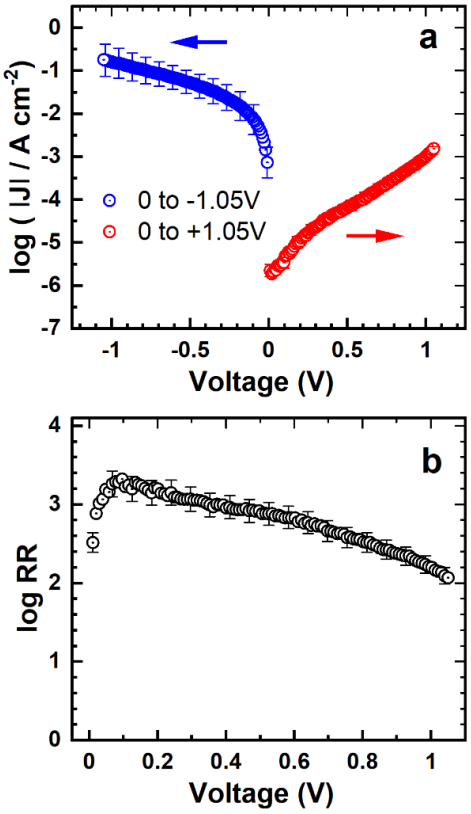

Figure 4.23 Occurrence of two different conductance states for the Au^{TS}/Fc-FluT//Ga_2O_3/EGaIn junction: Averaged semilogarithmic *J*-V plot (a) and effective *RR* versus bias voltage (b). Either positive (from +0.01 to +1.05 V) or negative (from –0.01 to –1.05 V) bias sweeps were repeatedly applied. Sweep directions are marked by arrows. The curves in (a) represent the results of a statistical analysis over a large number of sweeps (for more details see the Supporting Information).

While the curves in Fig. 4.23a represent the results of a statistical analysis over a large number of sweeps, the transfer from one conductance state to the other is expected to be a dynamical process. This is illustrated in Fig. 4.24, in which the *J*-V curves for individual, successive sweeps are shown for a representative measurement spot. Another example is provided in the Supporting Information, Fig. A.23a. For positive bias sweeps (from +0.01 to +1.05 V), the system, which was initially in the intrinsic, high conductance state, gradually switches into the low conductance state (Fig. 4.24a). The switching requires several sweeps, with the behavior being highly reproducible for different

measurement spots and different Fc-FluT samples. Even a prior sweeping at negative bias does not affect this behavior significantly, resulting in the same evolution of the *J*-V curves when sweeping at positive bias voltages (see Fig. A.24 in the Supporting Information).

Notably, the switched low conductance state is not transient but stable.[37] Still, a switching back from the low to high conductance state can be triggered by a succession of sweeps at negative bias (from –0.01 to –1.05 V), as exemplarily shown in Fig. 4.24b and Fig. A.23b in the Supporting Information. Here, the exact shape and evolution of successive *J*-V curves differ noticeably from spot to spot and sample to sample, with the high conductance state not always recovering to its full extent. This indicates that the "low-to-high" switching does not occur in an as straightforward and as reproducible way as the switching from the high to low conductance state.

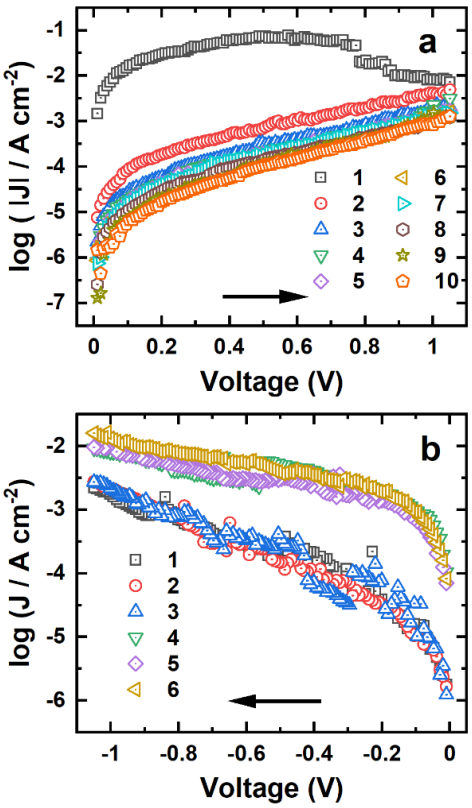

Figure 4.24 Evolution of the conductivity for the Au^{TS}/Fc-FluT//Ga_2O_3/EGaIn junction at the bias sweeping: (a) semilogarithmic *J*-V plots corresponding to ten successive scans for a particular measurements spot, with the bias scanned from +0.01 to +1.05 V (scan direction marked by the arrow); (b) semilogarithmic *J*-V plots corresponding to 6 successive scans for a particular measurements spot, with the bias scanned from –0.01 to –1.05 V; here, the sample initially was in the switched, low conductance state. In contrast to Fig. 4.23a, which contains averaged *J*-V curves, in the present plot individual scans are shown.

4.4.4 Application of Bias Pulses

As shown in previous experiments,[37] the switching from the high to low conductance state occurs only if the maximum applied voltage in the sweeps exceeds a certain threshold value. For the Fc-FluT SAM, this value lies between +0.55 V and +0.75 V. This raises the question, whether for triggering the switching process it is really necessary to sweep the voltage, or whether pulses at a sufficiently large positive bias would also induce the low conductance state. Accordingly, in the next set of experiments for several spots the bias was successively cycled between +0.01 V and +1.05 V with a bias pulse duration of about 1 sec and the current densities at +1.05 V were recorded. These are shown in Fig. 4.25a along with the current density values at the same bias in the case of sweeping. The data show that the switching into the low conductance state occurs also when pulsing the voltage, where it takes 15-20 cycles to complete the process. The results also emphasize that for both measurement sequences considered in Fig. 4.25 the switching between the two conductance states is a slow process characterized by a gradually decreasing current density. Notably, applying negative voltage pulses (i.e., switching the bias between –0.01 V and –1.05 V) does not result in a change of the conductance state (Fig. 4.25b), in analogy to the situation for negative bias sweeps.

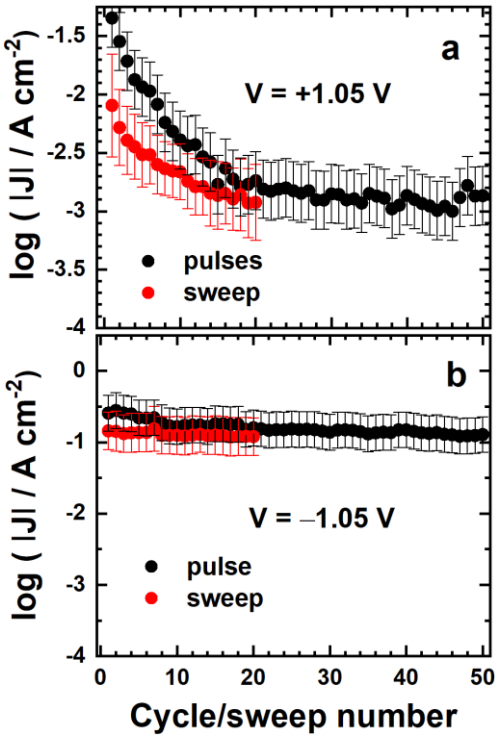

Figure 4.25 Evolution of the conductivity for the Au^{TS}/Fc-FluT//Ga_2O_3/EGaIn junction in the course of applying voltage pulses and upon bias sweeping: (a) Semilogarithmic plots of the current density at either

+1.05 V (a) or –1.05 V (b) for applying voltage pulses (cycling) and for sweeping the voltage from 0 V to +1.05 V (a) or from 0 V to –1.05 V (b). The data represent the results of a statistical analysis over several junctions (3 for the pulsed mode and 12 for the sweeping mode).

4.4.5 Sweep between Maximum Positive and Negative Bias

Significantly, the separate sweeping at either positive or negative bias discussed above (in the following denoted as + or – sweeping, respectively) does not represent the standard measurement procedure for molecular junctions. Usually junctions are continuously swept alternatingly in the negative and positive bias range or between maximum negative and positive bias values (or *vice versa*). Therefore, I adapted also our procedure and consecutively varied the bias in a voltage range between –1.05 V and +1.05 V, sweeping it from +0.01 V to +1.05 V and from –0.01 V to –1.05 V and setting the junction to 0 V between the negative and positive bias sweeps. For that, I considered two measurement sequences: one in which the first sweep was in the positive bias range (denoted as +/– sweeping) and one in which during the first sweep negative biases were applied (denoted as –/+ sweeping). The results of these measurements are presented in Fig. 4.26a (see also the respective heat maps and linear-scale *J*-V plots in the Supporting Information – Fig. A.29 and A.30). The data in Fig. 4.26a show that both +/– and –/+ sweeping results in essentially symmetric *J*-V curves, differing drastically from those in Fig. 4.23a. This means that when applying a more "conventional" mode of bias, no rectification is observed, which is in sharp contrast to the situation observed for the ferrocene-containing aliphatic and hybrid SAMs mentioned in the introduction. as can be seen in Fig. 4.26b where the respective *RR*s are shown as functions of the applied bias. This behavior is in sharp contrast to the situation depicted in Fig. 4.23b.

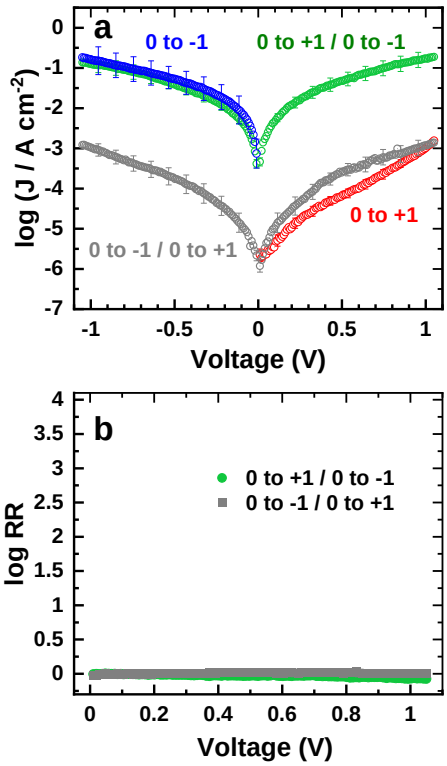

Figure 4.26 Sweep-character-dependent switching between the conductance states for the Au^{TS}/Fc-FluT//Ga_2O_3/EGaIn junction: (a) Averaged semilogarithmic *J*-V plots for the symmetric +/– and –/+ sweeps and (b) effective *RR* versus (bias) voltage plots for these sweeping modes (for comparative reasons we use the same vertical scale as in Fig. 4.23b). The plots characteristic of the non-symmetric + and – sweeps (from Fig. 4.23a) are included in panel (a) for comparison. The sweeping order for the four displayed cases is described by color-coded notes in the panels: ´to´ means a bias sweep and ´/´ means a step-like bias change to 0; finally, the bias was changed to 0 (step-like) and the sweep/sequence was started again. The curves in (a) represent the results of a statistical analysis over a large number of sweeps (for more details see the Supporting Information).

A further striking observation in Fig. 4.26a is that in all studied junctions the current density values differ by ca. two orders of magnitude depending on the direction of the first sweep. In the case of the +/– sweeps, the values characteristic of the high conductance state are observed at both positive and negative bias. The shape of the respective curves reproduces precisely the shape of the *J*-V curve at the – sweeps. In contrast, in the case of the –/+ sweeps, the values correspond to the expectations for the low conductance state but the exact shape of the respective curves differs somewhat from the shape of the *J*-V curve acquired in the + sweeping mode. Considering that the shape measured for the –/+ sweeps is more typical for molecular junctions, mimicking in particular

also that of the high conductance state, I consider it to better reflect the properties of the low conductance state than the shape originating from the + sweeps.

The evolution of the *J*-V curves at successive +/– and –/+ sweeps is shown in Fig. 4.27 for two representative measurement spots; analogous data for two additional spots for each sweeping mode (exhibiting a similar shape) are provided in Fig. A.27. For the +/– sweeps, the first + sweep shows particularly high *J* values and a deviation from the "standard" shape of the curves especially at high positive biases (Fig. 4.27a), similar to the data in Fig. 4.24a. The *J* values stabilize however at the successive – sweep and remain nearly invariable upon further sweeping. In the case of –/+ sweeps, the *J*-V curve for the first – sweep corresponds to that of the high conductance state, while the successive curve for the + sweep shows a distinct kink at high biases. Upon further sweeping, one observes a gradual evolution of the *J*-V curves towards the low conductance state.

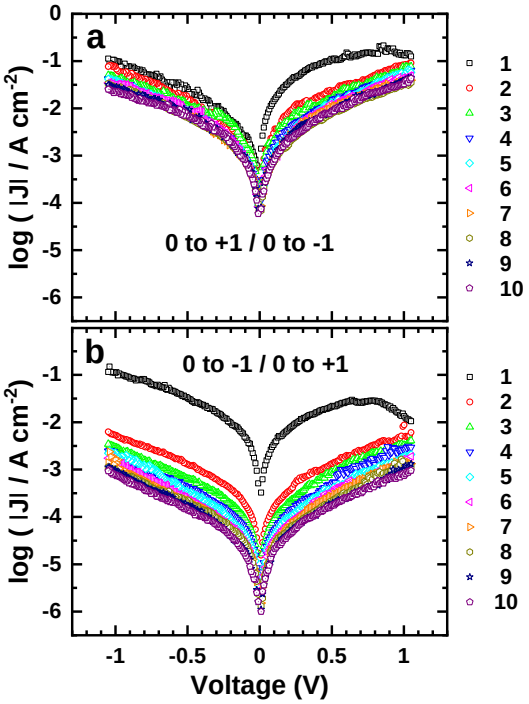

Figure 4.27 Evolution of the conductivity at the symmetric sweeping of the Au^{TS}/Fc-FluT//Ga_2O_3/EGaIn junction: Semilogarithmic *J*-V plots for the symmetric +/– (a) and –/+ (b) sweeps starting either in the positive (a) or negative (b) bias range. Ten successive sweeps for a particular measurement spot (for each sweeping mode) are shown. The sweeping order is described in the panels: ´to´ means a bias sweep and ´/´ means a step-like bias change to 0 V; finally, the bias was changed to 0 V (step-like) and the sequence was started again. In contrast to Fig. 4.26, which contains averaged *J*-V curves, in the present plot individual scans are shown.

The difference between the first sweeps for the +/– and –/+ modes as well as the evolution of the current density values at the successive sweeping is additionally illustrated in Fig. 4.28. Fig. 4.28a underlines the special character of the first + sweep for the +/– mode (exceptionally high *J* values) and an abrupt change in the slope of the *J*-V curves at the first + sweep of the –/+ mode as soon as the bias exceeds the "threshold" voltage for the transition into the low conduction state (0.55-0.75 V).[37] This change in the slope results in a noticeable decrease of the successive *J* values, so that the current density already in the second negative sweep of the –/+ mode differs strongly from that in the first sweep. This is illustrated by the first two red data points in Fig. 4.28b, which reveal a drop in current density by one and a half orders of magnitude. Besides, the evolutions of the successive *J* values at V = +1.05 V and V = –1.05 V shown in Fig. 4.28b for the +/– and –/+ sweeping modes show that it takes 7-10 sweeps to stabilize the *J* values at the +/– sweeping mode and more than 10 sweeps to achieve analogous stabilization at the –/+ mode.

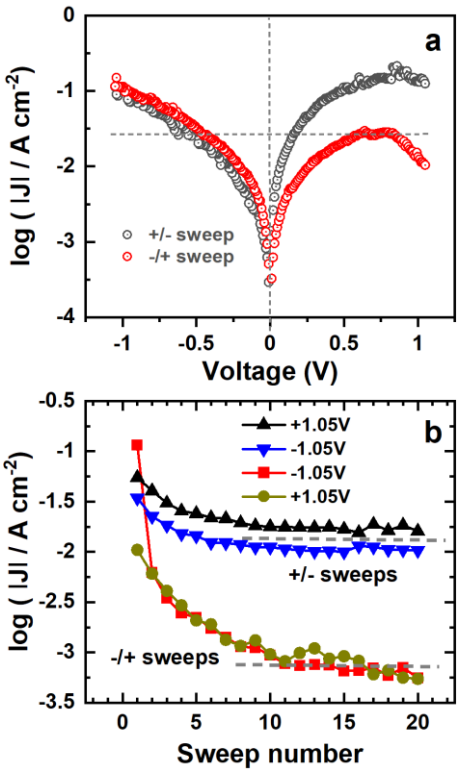

Figure 4.28 Evolution of the conductivity at the symmetric bias sweeping in the Au^{TS}/Fc-FluT//Ga_2O_3/EGaIn junction: (a) Comparison of the *J*-V curves for the first sweep for the +/– and –/+ sweeping modes (measured at two different spots). (b) log *J* values at +1.05 V and –1.05 for successive sweeps for the +/– and –/+ sweeping modes. Gray dashed lines in (a) are guides to the eye.

To verify that the difference between the *J*-V curves acquired for the Au^{TS}/Fc-FluT//Ga_2O_3/EGaIn junction at the +/– and –/+ sweeping modes is not related to any specific feature of the experimental setup, reference measurements on the non-substituted BPT SAM were performed. The respective *J*-V curves for the Au^{TS}/BPT//Ga_2O_3/EGaIn junction are presented in Fig. A.28 in the Supporting Information (see also Fig. A.29 for the heat maps). As expected, for these junctions no difference between the curves obtained for the +/– and –/+ sweeping modes is observed.

4.4.6 Discussion

In full agreement with the results of our previous study,[37] in the "steady situation" the Fc-FluT SAM embedded into the Au^{Ts}/SAM//Ga_2O_3/EGaIn junctions exhibit two distinct conductance states (Fig. 4.23a), viz. the original high conductance state and a bias-induced low conductance state, which can be reached by successive sweeping at positive bias in the +0.01/+1.05 V range (Fig. 4.24a). The respective effective *RR* reaches ~2100 at V = 0.1 V (Fig. 4.23b), which is an exceptionally high value for such a low bias. The switching to the low conductance state by sweeping at positive bias occurs in a gradual and reproducible way (Fig. 4.24a) and requires ca. 10 sweeps to be nearly completed (Fig. 4.24a and 4.27a). Such switching can also be triggered by sufficiently large positive voltage pulses (in our case at +1.05 V). Here, it takes ~20 bias pulses (each for 1 s) to fully establish the low conductance state (Fig. 4.25a). Significantly, the high conductance state can be recovered by sweeping at negative bias, in the –0.01/–1.05 V range, which, however, again, is a gradual process, occurring in somewhat different fashions for different measurement spots and not always yielding a complete recovery (Fig. 4.24b).

Notably, the rectification behavior of the Fc-FluT SAM disappears when alternatingly sweeping the junction at positive and negative biases, as the standard measurement procedure for two-terminal molecular junction. In other words, symmetric sweeping the junction results in an effective *RR* close to 1 in the entire bias range (Fig. 4.26b). This, together with the comparably slow evolution of the conductance switching mentioned in the previous paragraph implies that traditional explanations for the rectification in ferrocene junctions[233,234,235,236] cannot be applied here. One could then expect instantaneous rectification, with higher current values at the negative biases, which is definitely not the case.

Even more surprisingly, the direction of the first sweep at the symmetric sweeping turns out to be of crucial importance. One obtains a junction in the high conductance state, when the first sweep is applied at positive biases and a junction in the low conductance state, when the first sweep occurs at negative biases. This is not only a very peculiar behavior, but also shows that the both

conductance states (and intermediate states during the switching procedure, see Fig. 4.24 and 4.28) are intrinsic to the system. Note that the observed behavior for all sweeping modes is fully persistent at the variation of the sweeping rate (see Fig. A.30 in the Supporting Information), underlining the reliability of the results.

For identifying the origin of the peculiar behavior of the Fc-FluT SAM, one needs to be aware of high reliability of EGaIn-based junctions.[237] Moreover, the structural characteristics of the SAMs studied here, including a high packing density (~4.0×10^{14} molecules/cm^2)[37] and an upright molecular orientation,[106] are not out of the ordinary for thiolate-anchored monolayers. It should also be mentioned that a variety of non-substituted and –F, $-CH_3$, and $-CF_3$ substituted biphenylthiolate SAMs on Au(111) that I measured with the same molecular junction setup, both in the non-symmetric and symmetric fashion, neither display different conductance states nor any dependence of the *J*-V curves on the character of the sweeping.[37] This clearly shows that the conductance switching observed here is not related to the setup of the monolayer junction with Au^{TS} substrate and EGaIn top electrode, but that it must be a consequence of the presence SAMs consisting of ferrocenes and fully conjugated linkers. Accordingly, it is reasonable to assume that the redox properties of this moiety in combination with the conformationally rigid and fully conjugated FluT backbone are responsible for the observed behavior of the Fc-FluT-based junctions.

Bearing in mind that the switching into the low conductance state only occurs at a sufficiently high positive bias, typical of an irreversible redox process[106] and that the redox behavior of ferrocene is structure and media dependent,[238] it was proposed that the transition of the junction to the low conductance state is triggered by a (quasi) irreversible oxidation of the Fc moieties, stabilized most likely by a structural reorganization of the monolayer.[37] The oxidation of the Fc moieties causes a localization of the orbitals relevant for charge transport and, more importantly, creates a significant potential barrier within the junction, which diminishes the current.[37] Interestingly, recent experiments on molecular junctions comprising Fc-substituted alkanethiolate SAMs between bottom Au and top graphene electrodes showed distinctly different *J*-V curves for the neutral and (extrinsically) oxidized terminal Fc groups, with significantly lower *J* values in the latter case,[235] supporting our tentative explanation (see above). The respective difference amounted to up to 2.5 orders of the magnitude (depending on the bias),[235] which is comparable to the difference between the high and low conductance states in our case.

The redox-state conductance variation in ref[235] was explained by the electrostatically-driven change in the separation between the molecules and top electrode at the SAM-graphene interface. Also dynamic fluctuations of dipoles and head-group orientations have been shown to impact

current densities.[249,240] These factors can certainly play a role but, in our opinion, one must also not disregard the massive electrostatic impact of the formation of the space charge layer of oxidized Fc on the potential distribution within the junction. A further aspect is the dipole-dipole interaction between the oxidized Fc moieties, changing the balance of the structure-building interactions in the monolayer. Accordingly, changes in the junction geometry are possible which not only include the separation but also the exact geometry of the SAM-top electrode interface. This geometry depends on molecular orientation and conformation, which are presumably affected by the oxidation process and which, therefore, play a crucial role for the observed effects. In this context one has to consider that oxidation and reduction are electronic processes, occurring nearly instantaneously on the timescale of our experiments; conversely, the switching between the conductance states occurs rather slowly and gradually. This strongly suggests that the formation of the oxidized Fc moieties requires additional, comparably slow modifications of the SAM geometry, which stabilize the charged species.[241] In view of the rigid character of Fc-FluT, the most likely conformation change affecting the current across the junction,[241] is a rotation of the Fc moiety along the molecular axis. In addition, a change in the molecular tilt is possible, which, along with the rotation of the Fc moiety, would affect the coupling of the Fcs to the top electrode. Note that the presence of the ultrathin (~ 0.7 nm)[228] GaO_x layer at this electrode is, in our opinion, hardly of importance for the observed behavior, since it represents a standard part of EGaIn-based junctions also in the above-mentioned cases of SAMs not containing ferrocenes in which no switching has been observed. Moreover, in our opinion the trapping of counter charger in the oxide would be inconsistent with the symmetric *J*-V characteristics observed for symmetrically sweeping the junctions as discussed in the Supporting Information of ref.[37]. Still, it should be mentioned there exist inorganic junctions in which the oxide has been held responsible for conductance switching involving the appearance of conduction channels in the oxide, which, however, appears at variance with our observation of a reduced conductance in the switched state.[242]

In passing I note that the gradual nature of the quasi non-reversible oxidation (including geometrical changes) also has a direct impact on the shape of the *J*-V characteristics, especially in the first sweep at high positive bias voltages. There, it causes the current density to increase less steeply at high biases than one would expect in the absence of changes in the SAM. In some cases, it even results in a drop of the current density at high biases.

What remains to be discussed in more detail is the massive dependence of the observed *J*-V characteristics on the sweeping mode and how that relates to the above model. The first + sweep for both +/– and –/+ sweeping mode is apparently decisive for whether the final conductance state is either high or low.

In the first + sweep of the +/– mode, a particularly high conductance is observed below +0.55 - 0.75 V (i.e., in the voltage range in which no switching to the low-conductance state is recorded).[37] At higher bias voltage, the conductance deteriorates and the current density essentially saturates. The following negative sweep restores a situation equivalent to that observed when sweeping the junction only at negative biases (see Fig. 4.23). Successive +/– sweeps occur in a nearly symmetric fashion (Fig. 4.27a). I.e., the particularly high conductance of the first + sweep is never recovered, but possible detrimental effects of further + sweeps are (largely) recovered by – sweeps such that the system stabilizes in the high conductance state after 8-10 sweeps (Fig. 4.24b).

Conversely, the first + sweep for the –/+ sweeping mode mirrors the prior – sweep for positive biases below +0.55-0.75 V (Fig. 4.28a). I.e., like in the previously discussed +/– case, after the first – scan, the particularly high low-bias conductance situation cannot be observed. Beyond +0.55-0.75 V (the threshold value for the proposed partly irreversible oxidation) the value of J drops dramatically (Fig. 4.28a), now also starting from a much lower current density than for the +/– case. Consequently, the current density for the first + sweep is more than an order of magnitude smaller in the –/+ than in the +/– case. The successive sweeps in + and – direction are again largely symmetric, but at significantly reduced current densities. The maximum values of $|J|$ drop gradually for further sweeps (Fig. 4.27b) and the system stabilizes in the low conductance state after 10-12 sweeps (Fig. 4.28b).

These considerations imply that the main origin of the difference between the –/+ and the +/– sweeping mode can be traced back to marked differences in the first + sweep. Apparently, a prior – sweep preconditions the junction in a way that the particularly high conductance state for the first + sweep can no longer be reached. This then causes the massive changes that are irreversible for the chosen biasing conditions and that drive the junction into the low conductance state. The microscopic origin of that preconditioning must primarily lie in changes of the structure and conformation of the SAM and the SAM-electrode interface, since no oxidation processes can occur at negative biases.

I, thus, hypothesize that the entire behavior of the system originates from a fine interplay between redox processes involving the terminal Fc moieties and the structural changes involving the entire SAM and its interface with the top electrode. Overall, the system exhibits a variety of metastable conductance states, observed during the bias sweeping within the different sweeping modes, but only two of these states appear to be stable, which I attribute to specific favorable molecular structures and oxidation degrees.

4.5 Appearance of Different Conductance States in Monomolecular Films of Ferrocene-Decorated Triptycene-Based Tripods

4.5.1 Motivation

An interesting question is whether the above behavior based on Chapter 4.4 is exclusively characteristic of the specific, fully conjugated systems of the above system[37,243] or it is also typical of other ferrocene-decorated molecules. To this end, in the present work I studied the charge transport properties of Fc-substituted, triptycene based tripodes (Fc-Trip; Fig. 4.29), arranged as SAM on Au(111). This molecule, built around the versatile triptycene ´core´,[244,245,246,247] is not entirely conjugated since it contains an aliphatic bridge, connecting the individual phenyl blades, and methylene linker, promoting tripodal self-assembly.[244] The electrochemical properties of individual Fc-Trip molecules, embedded into a suitable matrix, were studied recently by electrochemical scanning tunneling microscopy (STM), with the oxidation-state dependent changes in electron transfer being recorded.[109] In contrast, here, I studied a monomolecular ensemble of these molecules, in the typical two-terminal junction setup, mimicking a practical device.

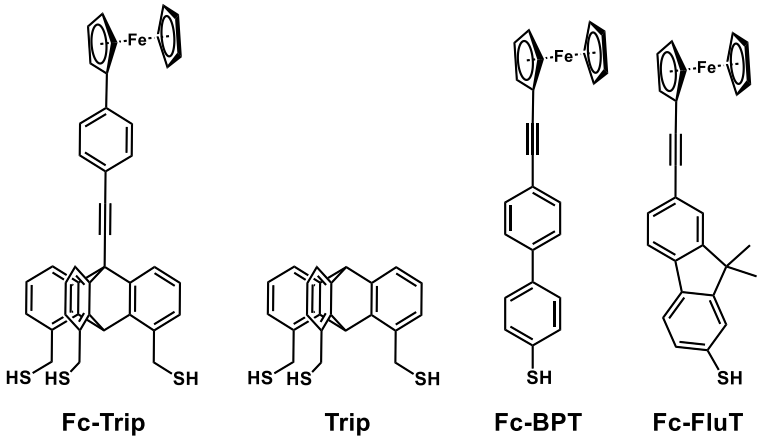

Figure 4.29 Structure of the Fc-Trip molecule and the reference Trip molecule as well as Fc-BPT and Fc-FluT molecules studied before and described in the previous chapter (Fc-FluT).[37,243] Acronyms of all molecules are given. The orientation of the Fc-Trip and Trip molecules corresponds to the ideal, tripodal adsorption geometry. The Fc-Trip and Trip substances were custom-synthesized by the group of our partner, Prof. T. Fukushima (Tokyo Institute of Technology).

4.5.2 SAM Preparation

Fc-Trip SAMs were prepared by immersion of the fresh gold substrates into 0.1 mM solution of Fc-Trip in acetone at room temperature for 12 h. After immersion, the samples were extensively rinsed with acetone and ethanol (consecutively) and finally blown dry with a stream of nitrogen. In addition to the Fc-Trip films, reference SAM of non-substituted triptycene-based tripods (1,8,13-trimercaptomethyltriptycene), abbreviated as Trip (see Fig. 4.29), was prepared on Au^{TS} substrates according to the literature recipes.[244] Further, reference C16 SAM was prepared on the Au/Ti/Si substrate using a standard immersion procedure (1 mM in ethanol; 24 h; room temperature).

4.5.3 XPS

The XPS data for the Fc-Trip SAM are presented in Fig. 4.30. The Au $4f_{7/2}$ spectrum in Fig. 4.30a exhibits a single peak, set to 84.0 eV in the course of the BE scale calibration (see previous section). The C 1s spectrum in Fig. 4.30b exhibits a single peak at ~284.5 eV, assigned to the molecular framework,[109,244] and a weak should at ~286.0 eV, stemming most likely from a minor contamination (C-O).[248] The Fe 3p spectrum in Fig. 4.30d exhibits a Fe $3p_{3/2,1/2}$ doublet at ~55.0 eV(Fe $3p_{3/2}$), assigned to the Fe atoms in the terminal Fc groups.

The S 2p spectrum in Fig. 4.30c can be decomposed into three individual doublets, at ~162.0 eV (I), ~163.5 eV (II), and ~161.1 eV (III) with the relative weights of 47%, 37%, and 16%, respectively. The first doublet is characteristic of the thiolate species bound to noble metal substrates.[121] The second doublet is characteristic of unbound or weakly bound thiol or disulfide.[121] The third doublet was alternatively assigned to atomically bound sulfur[133,175] and a differently bound thiolate.[123,124,125] I favor the first assignment but cannot completely exclude the second one, which brings a certain ambiguity in the interpretation of the data. However, in any case, the anchoring of the Fc-Trip molecules to the substrate is not entirely homogeneous, with some of the molecules anchored in monopodal and dipodal fashions and, probably, the presence of a portion of the physisorbed molecules, trapped in the chemisorbed monolayer. Note that this conclusion agrees well with results of the previous XPS measurements for the same system,[109] but the spectral weight of the thiolate doublet, characteristic of the proper anchoring to the substrate, is much higher in the present work.

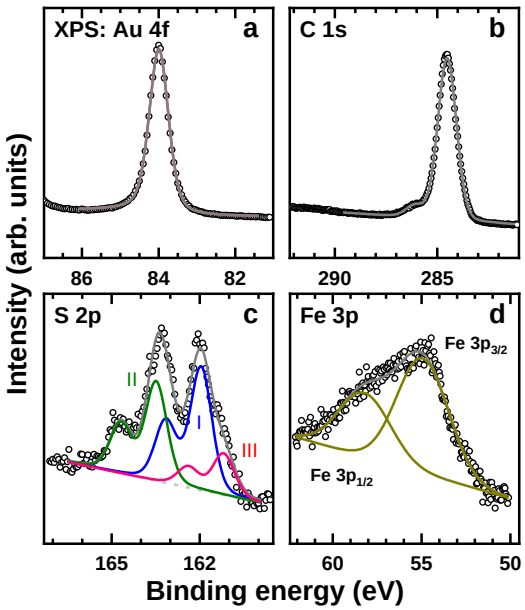

Figure 4.30 Au $4f_{7/2}$ (a), C 1s (b), S 2p (c), and Fe 3p (d) XPS spectra of the Fc-Trip SAM. The spectra were measured at a PE of 350 eV. The S 2p spectrum is fitted by a combination of three doublets (I-III; see text for details) and linear background (light gray dashed line). The Fe 3p spectrum is decomposed into Fe $3p_{3/2}$ and Fe $3p_{1/2}$ components.

Additional information was obtained by the numerical evaluation of the XPS data. Based on the S 2p/Au 4f intensity ratio and using the C16 SAM with a known packing density (4.63×10^{14} molecules/cm^2) as a reference,[244] the packing density of the thiolate groups in the Fc-Trip SAMs was estimated at ~2.7×10^{14} thiolates/cm^2. This is a reasonable number, taking into account the relative weight of the thiolate signal (~47%) and the ultimate packing density for the tripodal-anchored, triptycene-based SAM (4.6×10^{14} thiolates/cm^2).[244] The second important parameter, determined on the basis of the C 1s/Au 4f intensity ratio and, once again, the C16 SAM (1.89 nm) as a reference, is the effective thickness. This parameter was estimated at ~1.62 nm, which is quite close to the ´height´ of the properly anchored Fc-Trip molecule (1.67 nm; see Fig. 4.29). Thus, according to the XPS data, the Fc-Trip represents a SAM-like film with a certain degree of heterogeneity and a small contamination.

4.5.4 NEXAFS Spectroscopy

Further information is provided by the NEXAFS data, compiled in Fig. 4.31. The spectra of the Fc-Trip SAMs acquired at the different X-ray incidence angles, are presented in Fig. 4.31a. The spectra are dominated by the characteristic π* resonance of triptycene[244,245] at ~285.3 eV (I), which is, however, slightly asymmetric in the present case, presumably, due to the admixture of the π_1*

resonance (~285.0 eV)[129,171] from the phenyl ring in the Fc linker (see Fig. 4.29). The further prominent feature is the characteristic π*($3e_{2u}$) resonance of Fc at ~287.1 eV.[249,250,251] The second, much less intense, characteristic π*($4e_{1g}$) resonance of Fc at ~285.6 eV[250,251] is not really perceptible, merging with the strong π* resonance of triptycene. Further resonances, with predominantly σ* character, at higher photon energies, contain overlapping contributions from the different building blocks of Fc-Trip and are therefore less specific.

The spectra in Fig. 4.31a exhibit strong linear dichroism, which is a dependence of the resonance intensity on the X-ray incidence angle.[129,196] This effect is additionally emphasized by the difference spectrum in Fig. 4.31b. Accordingly, the intensities of the π* resonances are higher at the normal X-ray incidence (90°) and those of the σ* resonances are higher at the grazing incidence (20°). Considering that the **E** vector of the primary X-rays is perpendicular to the beam direction and the π* and σ* orbitals are perpendicular and parallel to individual rings in the molecular framework of Fc-Trip, predominantly upright molecular orientation, such as in Fig. 4.29, can be assumed.

Apart from this qualitative conclusion, a certain degree of heterogeneity in terms of molecular orientation can be assumed. A quantitative measure of this heterogeneity is the average tilt angle of the molecules with respect to the surface normal, β. For triptycene-based molecules this angle can be calculated by numerical evaluation of the NEXAFS data, according to the approach suggested in ref[252] on the basis of the 3-fold symmetry of the triptycene framework. According to this approach, the intensity of the π* resonance of triptycene is described by the equation

$$I = 3BP/2 \cdot (3/2 \sin^2\beta - 1) \cdot \cos^2\theta + 3B/2 \cdot (1 - 1/2 \sin^2\beta) \qquad (4\text{-}7)$$

where B is a scaling factor and P is the polarization degree of the synchrotron light and θ is the incidence angle of the synchrotron light. Based on this equation, β can be determined by plotting the relative intensity of the π* resonance versus $\cos^2\theta$ and fitting the experimental data by a straight line, as this is performed in Fig. 4.31c for the $I(\theta)/I(90°)$ ratio. The derived value of β is 30° ± 3°, which deviates noticeably from the ultimate value of 0°, corresponding to the ideally upright orientation of all Fc-Trip molecules in the SAMs. Note, however, that this ultimate value could never be achieved in the triptycene based SAMs, which even in the case of homogeneous tripodal adsorption geometry exhibit an average tilt angle of ~7.5°.[244] In any case, the value of β for the Fc-Trip SAMs suggests, as assumed, a certain degree of heterogeneity in terms of molecular orientation. This result agrees well with the XPS data which, in their turn, assume a certain heterogeneity of the bonding configurations. However, apart from the above heterogeneities, Fc-

Trip represents a well-defined SAM-like film with the molecules chemically coupled to the substrate and having upright orientation.

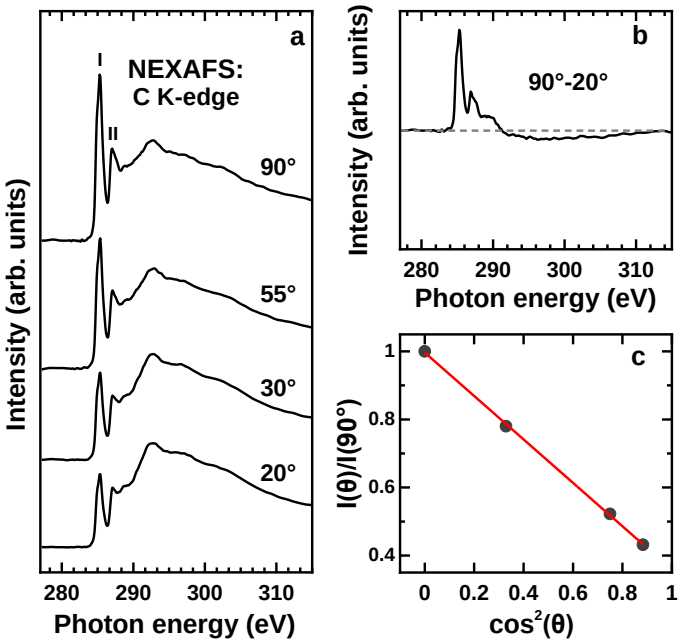

Figure 4.31 (a) C K-edge NEXAFS spectra of the Fc-Trip SAMs acquired at the different X-ray incidence angles, given at the spectra; (b) the difference between the spectra collected under normal (90°) and grazing (20°) incidence geometry; and (c) dependence of the I(θ)/I(90°) intensity ration on $\cos^2\theta$. Individual absorption resonances are marked by numbers (see text for details). The horizontal gray dashed line in panel b corresponds to zero. X-ray incidence angles are determined with respect to the surface of the substrate.

4.5.5 Charge Transport Properties

The charge transport properties of the Fc-Trip SAMs were characterized both within the asymmetric and symmetric sweeping modes. The data for the asymmetric sweeping mode are presented in Fig. 4.32; the respective statistical information, *J*-*V* heat maps, and histograms of $\log_{10}|J|$ at bias values of ±0.5 V can be found in the Supporting Information (Table A.6, Fig. A.31 and A.32). The bias was repeatedly swept either from +0.01 V to +1.05 V or from –0.01 V to –1.05 V which I term as the "+" and "**–**" sweeping modes, respectively. As seen in Fig. 4.32a, these sweeping modes result in distinctly different conductance states, with much higher *J* values at the same $|V|$ for the **–** mode (HCS) compared to the + case (LCS). The effective RR, calculated in the standard way as *J(–V)/ J(+V)*, is shown in Fig. 4.32b. It varies considerably over the bias range, with a maximum value of 400-600 at 0.1-0.2 V.

The observed behaviour is exclusively related to the presence of the Fc group. This fact was verified by the control experiments performed under the same condition on the Trip SAM, comprised of the non-substituted version of Fc-Trip. The respective *J*-*V* curves, measured individually in the the "+" and "–" sweeping modes and combined together in the joint plot, show neither distinctly different conductance states nor a significant asymmetry (see Fig. A.33a in the Supporting Information). The respective *RR* does not exceed 2 for the entire range of the bias variation (see Fig. A.33b and A.33c in the Supporting Information). Interestingly, the absolute *J* values for the Trip SAM are lower than those for the Fc-Trip film in the HCS for the entire range of the negative bias values (see Fig. A.34 in the Supporting Information). This is an interesting fact suggesting that the presence of Fc and the fully conjugated phenyl-ethynyl linker does not decrease (as expected from the increase in the molecular length) but increase the molecular conductance. This suggests a resonant tunneling across this entire unit and its good electronic coupling with the Trip framework.

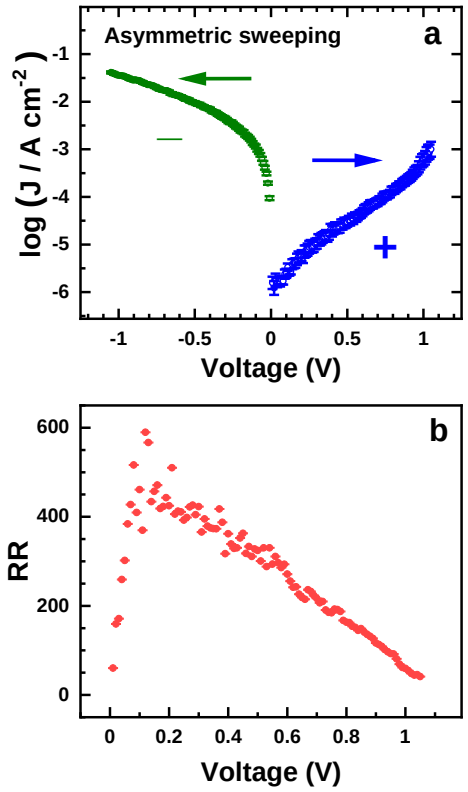

Figure 4.32 (a) Averaged semilogarithmic *J*-*V* plot and (b) effective *RR* versus bias voltage for the asymmetric sweeping mode for the Au^{TS}/Fc-Trip//Ga_2O_3/EGaIn junction; "/" and "//" indicate interfaces with strong and weak electronic coupling, respectively. Either positive ("+", from +0.01 V to +1.05 V) or negative ("–", from –0.01 V to –1.05 V) bias sweeps were repeatedly applied. Sweep directions are marked by arrows. The curves in (a) represent the results of a statistical analysis over a large number of sweeps.

A characteristic feature of the *J*-*V* curves in Fig. 4.32a is the discontinuity at $V = 0$, which, at first sight, is hardly explainable. The reason for this discontinuity is the evolution of the curves at the repeatable + sweeping. This is illustrated in Fig. 4.33a, in which the *J*-*V* curves for 20 successive + sweeps are shown. Accordingly, the first + sweep starts from the value close to that at V = –0.01 V but the successive values of *J* at higher V deviate progressively from those at the respective negative bias. Even more difference occurs at the second + sweep, which starts again from +0.01 V, showing from very beginning distinctly lower *J* values than those at the respective negative biases. The evolution of the *J*-*V* curves towards lower *J* values continues at the subsequent sweeps coming to a saturation-like behavior after the first 5-10 sweeps. The statistical averaging over the entire set of curves results than in the resulting + *J*-*V* curve, shown in Fig. 4.32a. In contrast, the *J*-*V* curves acquired in the – sweeping mode reproduce each other quite nicely, with nearly no variation in their shape and *J* values at the successive sweeping (Fig. 4.33b).

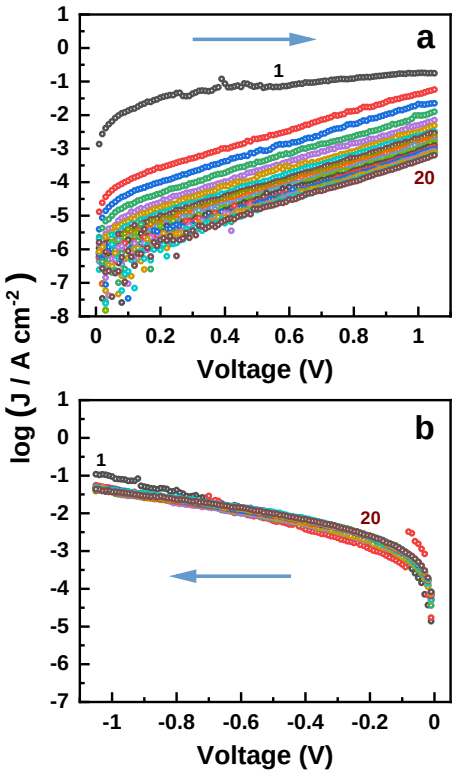

Figure 4.33 Semilogarithmic *J*-*V* plots for the Au^{TS}/Fc-Trip//Ga_2O_3/EGaIn junction. Either + (a) or – (b) sweeping modes were repeatedly applied and 20 successive individual sweeps within each of these modes are shown. Sweep directions are marked by arrows.

The HCS, characteristic of the – sweeping mode and transforming to the LCS at the successive sweeping in the positive bias range (+ sweeping mode), can be completely recovered by subsequent sweeping in the negative bias range. An example is given in Fig. 4.34. The Fc-Trip SAM was first brought into the LCS by successive sweeping from +0.01 V to +1.05 V (10 sweeps), as shown in Fig. 4.34a, and then recovered to the HCS by subsequent sweeping from −0.01 V to −1.05 V (6 sweeps), as shown in Fig. 4.34b. Note, however, that the recovery of the HCS does not always occur in the same fashion in relation to the exact shape of individual *J*-*V* curves and the number of sweeps required. However, the possibility of the recovery suggests that the changes associated with the appearance of the LCS are reversable and the system can be switched between the HCS and LCS and back to HCS even though each switching requires not one but several sweeps.

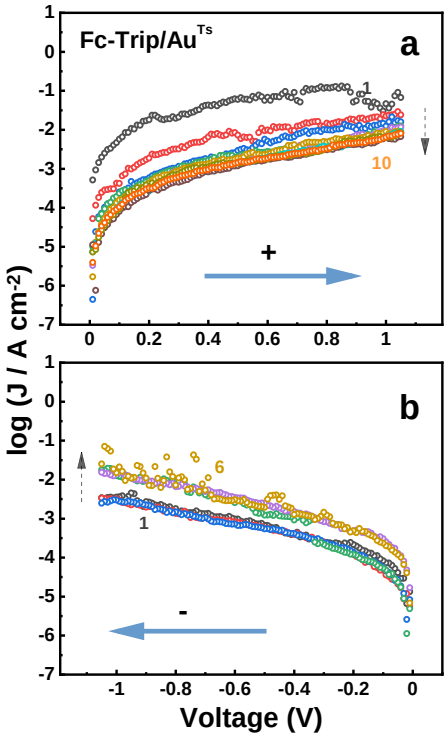

Figure 4.34 Evolution of the conductivity for the Au^{TS}/Fc-Trip//Ga_2O_3/EGaIn junction at the bias sweeping: (a) semilogarithmic *J*-*V* plots corresponding to 10 successive individual sweeps for a particular measurement spot, with the bias sweeping from +0.01 V to +1.05 V (the scan direction is marked by the horizontal arrow) and (b) semilogarithmic *J*-*V* plots corresponding to 6 successive individual sweeps for the same measurement spot, with the bias scanned from –0.01 V to –1.05 V (the scan direction is marked by the horizontal arrow). The – sweeping was performed directly after the + sweeping. The vertical dotted arrows indicate the changing trend of the *J*-*V* curves.

In addition to the asymmetric sweeping mode, the standard, symmetric sweeping mode was tried as well. In this case, the bias was swept between −1.05 and +1.05 V with the first scan either starting from +0.01 V and going to +1.05 V or starting from −0.01 and going to −1.05 V, which will be termed as +/− and −/+ sweeping modes, respectively. The resulting *J*-*V* curves for both these sweeping modes are presented in Fig. 4.35; the respective statistical information, *J*-*V* heat maps, and histograms of $\log_{10}|J|$ at bias values of ±0.5 V can be found in the Supporting Information (Table A.6, Fig. A.35 and A.36). In contrast to the data in Fig. 4.32a, these curves are nearly symmetric, with only a slight deviation from the symmetric behavior for the −/+ case. The respective *RR* values are close to 1 for the entire bias range for the +/− sweeping mode and only moderately deviate from 1 (up to 6) at low biases for the −/+ mode (see Fig. A.37a in the Supporting Information). At the same time, the curves for the +/− and −/+ sweeping modes are distinctly different, corresponding to the HCS and LCS, respectively.

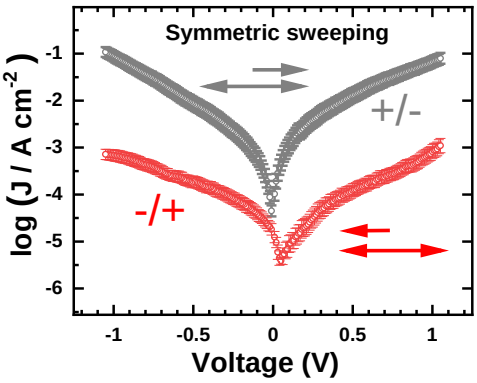

Figure 4.35 (a) Averaged semilogarithmic *J*-*V* plots for the symmetric sweeping modes for the Au^{TS}/Fc-Trip//Ga_2O_3/EGaIn junction. The voltage was swept between −1.05 and +1.05 V with the first scan either starting from +0.01 V and going to +1.05 V (+/−) or starting from −0.01 and going to −1.05 V (−/+) as also schematically shown by the arrows. The curves represent the results of a statistical analysis over a large number of sweeps.

4.5.6 Discussion

The observed behavior of the tripodal Fc-Trip films is similar to that of monopodal Fc-BPT and Fc-FluT SAMs: all these systems exhibit two distinctly different conductance states, HCS and LCS, at the asymmetric bias sweeping. Thus, the behavior of the Fc-BPT and Fc-FluT SAMs, featuring similar structures and differing only in the exact character of the fully conjugated backbone (with either biphenyl or fluorene), is not unique but characteristic of a variety of Fc-substituted monomolecular films. The role of Fc in the appearance of the HCS and LCS is deciding; the SAMs

comprised of the reference non-substituted molecules, such as Trip for Fc-Trip, do not exhibit any distinctly different conductance states at the asymmetric sweeping mode but rather nearly symmetric *J*-*V* curves.

The occurrence of the HCS and LCS for the Fc-Trip films results in the effective *RR* in the range of ~500 at such a small bias as 0.1 V. It is interesting to compare this value with the analogous parameter for the Fc-BPT and Fc-FluT SAMs, viz. ~3200 and ~3000, respectively.[37] This relation can be tentatively explained assuming that the effect is mediated by the Fc group, as follows from the reference experiments. Indeed, the density of these groups in the Fc-Trip film, featuring only one Fc group for three thiolate anchoring groups, is at least 3 times lower than that in the Fc-BPT and Fc-FluT case. In addition, the quality of the Fc-Trip film, which does not exhibit fully homogeneous tripodal assembly and features a certain degree of disorder (see section 4.5.3), is lower than that of the well-defined Fc-BPT and Fc-FluT SAMs.[251,253] Consequently, the factor of ~6 in the effective *RR* value is quite reasonable.

Significantly, the HCS and LCS are observed not only at the asymmetric but also at the standard, symmetric sweeping (Fig. 4.35). The resulting *J*-*V* curves are then symmetric but the *J* values correspond to either HCS or LCS, depending on the direction of the first sweep. The curves for the asymmetric and symmetric sweeping do not reproduce each other exactly but are very close to each other (see Fig. A.37b in the Supporting Information) assuming that these two conductance states are truly characteristic of the Fc-Trip film. The reversable character of the LCS and HCS switching (Fig. 4.34) suggests that the appearance of the LCS is not just related to a bias-induced degradation of this film.

According to the tentative model, developed in our previous publications dealing with the Fc-BPT and Fc-FluT SAMs,[37,79] the behavior of the Fc-Trip film can be explained by the bias-induced switching of the junction to a metastable state comprising oxidized Fc entities, which are characterized by less delocalized frontier orbitals and which cause the formation of a significant potential barrier within the junction. It was hypothesized that this state can be stabilized by structural changes in the monolayers, affecting also their coupling to the top electrode. In the case of the Fc-Trip film these changes are a rotation of the Fc group with respect to the phenyl-ethynyl linker or a rotation of the entire Fc-phenyl-ethynyl entity with respect to the Trip platform and the top electrode. Also, changes in the molecular inclination are possible but this factor is probably less important in the Fc-Trip case in view of a partial disorder within the respective film. Note that the involvement of the structural changes, requiring probably some time, is very likely considering the slow character of the HCS-LCS transformation in contrast to the nearly instantaneous oxidation and reduction processes.

4.6 The Electrical Switching of Phosphonate SAMs with Restricting Conformational Space

4.6.1 Motivation

As reported by Prof. P. Kirsh and coauthors,[254] the feasibility of memristive switching with liquid crystal-inspired SAMs embedded as tunnel junctions between solid-state contacts has been demonstrated. The dipole moments, based on SAM 1 (Fig. 4.36), coupled with an external electrical field and changes in tunnel current are induced by a conformational reorganization and concomitant change of dipole orientation in the monolayer.[255,256] The disadvantage that I-V curves show large scattering is presumably caused by the high conformational flexibility of the long linker connecting the dipolar portion of the molecule to the phosphonate anchoring group. Therefore, for practical applications, a limitation of conformational flexibility is needed, preferably in a system with only two major dipolar conformations.

Since both the separation of states and the retention would be controlled by the change of the activation energy barrier (EA) for the switching between the two major dipole orientations. Thus, this subproject used SAM 2 (shown in Fig. 4.36) as a representative test monolayer, characterized by the replacement of the flexible aliphatic moiety originally belonging to SAM 1 by a rigid aromatic linker. The SAM components are intentionally designed with a large HOMO-LUMO gap, which is considered a promising approach in the context of molecular electronics. The above-mentioned SAMs were characterized by a variety of complementary tools, including synchrotron-based XPS and NEXAFS spectroscopy, but the focus was on the study of the charge transport behavior, in the context of switching. Our part in the project, conducted by me, was the characterization of the above-mentioned SAMs by suitable experimental tools, including synchrotron-based XPS and NEXAFS spectroscopy.

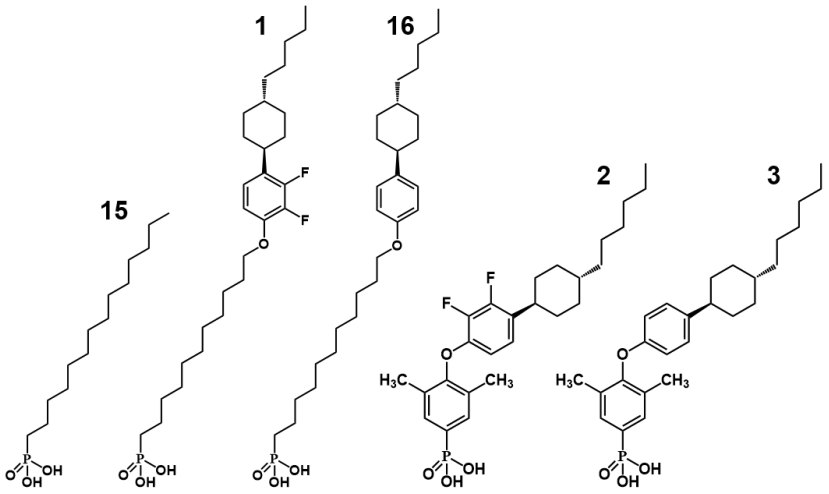

Figure 4.36 Chemical structures of the SAM-forming molecules for the SAMs studied within the given subproject. The substances were designed and custom-synthesized by the group of our partner, Prof. P. Kirsch (Technische Universität Darmstadt).

4.6.2 XPS

SAMs from all compounds under study (2, as well as 1 and 3 – the non-fluorinated and thus practically non-polar analogue of 2) were deposited on non-structured, planar TiN reference chips and investigated thoroughly with respect to their structural and surface chemical properties. In particular, XPS data clearly verified the presence of the respective SAMs.

Along with the SAM 2 and the reference SAMs 1 and 3, I have also studied two other reference systems, viz. the SAMs 15 and 16. The structure of 16 is similar to that of 1 except for the partial fluorination of the phenyl ring. Also, the parameters of the SAMs 16 and 3 can be compared to each other in the same way as the parameters of the monolayers 1 and 2, provided additional information on the molecular-structure-related changes in the molecular organization in the SAMs. As for 15, it represents a pure aliphatic SAM with the same anchoring group as that in all other SAMs, serving as a spectroscopic reference for the phosphonate anchoring groups and aliphatic chains in the multicomponent molecular backbones. Finally, the bare substrate was characterized as well, providing general reference to all the SAMs.

The Ti 2p, C 1s, P 2p, F 1s, and O 1s XP spectra of the blank TiN substrate and the phosphonate SAMs are shown in Fig. 4.37. The Ti 2p spectra in Fig. 4.37a show a single Ti $2p_{3/2,1/2}$ doublet, with the characteristic[257,258] shape and spin-orbit splitting of ~5.6 eV and the BE energy of the Ti $2p_{3/2}$ peak of 458.83 eV. This energy is distinctly different from that of TiN (455.03 eV,[259] 455.2 eV,[260] 455.8 eV)[248] and is characteristic of TiO_2 (458.7 eV,[261] 459.0 eV[260] and 459.1 eV).[258] Consequently, the topmost part of the TiN substrate is comprised of TiO_2. Considering the

attenuation length (λ) of ~0.65 nm for the Ti $2p_{3/2}$ photoelectrons at the given kinetic energy (~125 eV),[262] one can assume that the thickness of the TiO_2 layer is at least 2 nm (3λ).[58] The intensity of the Ti 2p signal in the SAM spectra is much lower than that for the bare TiN substrate, which is expectable. However, the latter substrate is not entirely clean but contaminated to some extent, as evidenced by the respective C 1s XP spectrum in Fig. 4.37b, which shows a broad peak associated with C-/C=C carbon at ~285.1 eV, a shoulder at ~286.8 eV related to C-O, and a weak peak at ~289 eV assigned to C=O/COOH carbon. The character of the C 1s spectra changes noticeably in the case of the SAMs. The spectra of the SAMs 15, 16, and 3 exhibit a strong single peak at ~285.0 eV, assigned to the molecular backbone. For the SAMs 1 and 2, this peak is accompanied by an additional shoulder at ~287.0 eV, associated with the carbon atoms in the phenyl ring bonded to fluorine.[263]

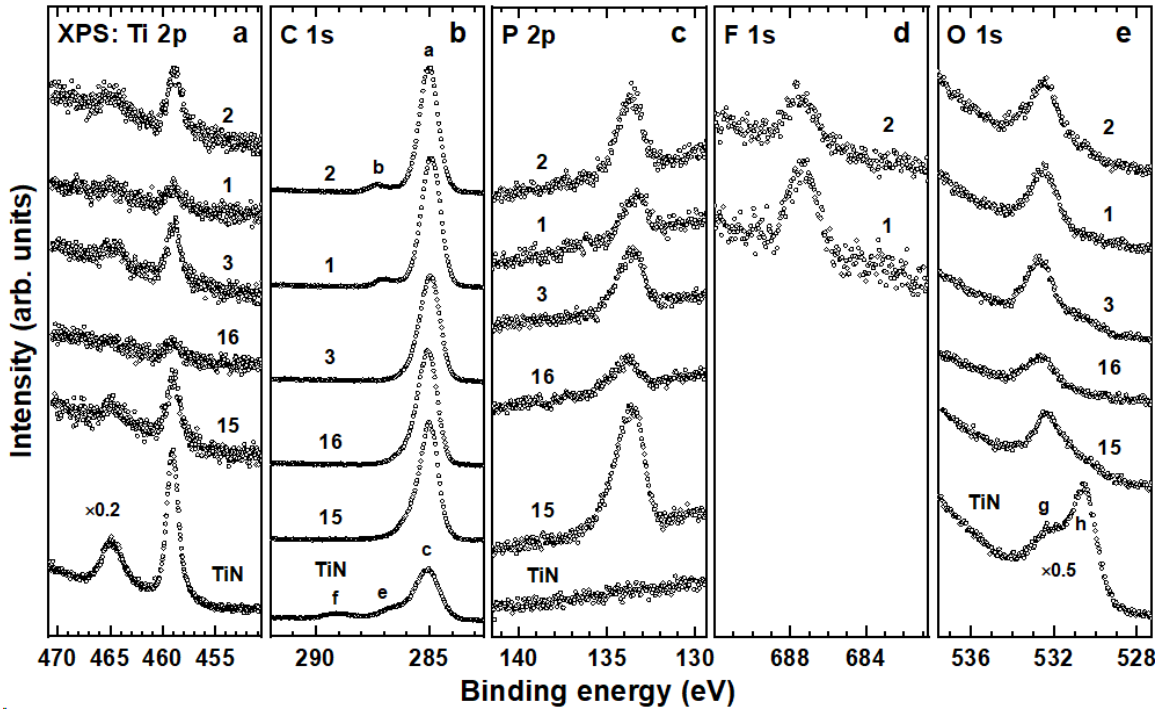

Figure 4.37 Ti 2p (a), C 1s (b), P 2p (c), F 1s (d), and O 1s XP spectra of the phosphonate SAMs and the bare TiN substrate. The Ti 2p and O 1s spectra of TiN are scaled down by the specific factors marked in the figure. Individual peaks in (b) and (e) are marked by letters (see text for details). The spectra were acquired at photon energies of 350 eV (C 1s and P 2p), 580 eV (Ti 2p and O 1s), and 750 eV (F 1s).

The intensity of the Ti 2p signal for the SAM 16 is lower than that for the SAM 3, which also is the case for the SAMs 1 and 2. Thus, as expected, the effective thickness of the SAM 16 is larger than that for the SAM 3 and the same relation takes also place for the monolayers 1 and 2. Note,

however, that these thickness relations are not fully reflected by the C 1s XP spectra which rather show similar intensities for all SAMs studied. The reason for this behavior is self-saturation of the C 1s signal at the given kinetic energy of the photoelectrons (~60 eV).[58]

The P 2p spectra of all the SAMs in Fig. 4.37c exhibit a single P $2p_{3/2,1/2}$ doublet at ~133.5 eV assigned to the phosphonic acid anchoring groups bonded covalently to the substrate. The absence of other doublets and the similarity of the BE positions and the entire doublet shapes for all the SAMs suggest a similar bonding configuration for all SAM-forming molecules.[264,265,266,267] The intensity of the P 2p signal for the SAM 16 is lower than that for the SAM 3, which also is the case for the SAMs 1 and 2, reflecting, similar to the Ti 2p signal, the differences in the effective thicknesses of these SAMs. Finally, as expected, the P 2p spectrum of the blank TiN substrate does not exhibit any P 2p signal, which confirms that this signal in the case of the SAMs does not stem from any contamination but is indeed related to the phosphonic acid anchoring groups.

The F 1s spectra of the SAMs 1 and 2 in Fig. 4.37d exhibit a single peak at a BE of ~687.2 eV, representative of the fluorine substitution of the phenyl ring in the molecular backbone. The intensity of this peak is higher in the case of 1, corresponding to the higher effective thickness, associated most likely with a higher packing density.

The O 1s spectrum of the bare TiN substrate in Fig. 4.37e exhibits a superposition of two peaks, at ~530.5 eV (h) and 532.4 eV (g). The latter peak, disappearing or nearly disappearing in the spectra of the SAMs, is most likely related to contamination, wiped away upon the SAM formation. The former peak, observed also in the spectra of the SAMs, stems completely (TiN) or predominantly (SAMs) from the oxygen atoms in the TiO_2 overlayer. For the SAMs, it also contains contributions from the phosphonate anchoring groups but they can be hardly distinguished.

Apart from the above qualitative consideration, numerical evaluation of the effective thickness of the SAMs was performed. For this purpose, I used the intensity of the Ti 2p signal assuming the exponential attenuation of the respective signal by the SAMs[58] with the kinetic-energy-specific attenuation length measured for alkanethiolate (AT) SAMs on Au[263] and the signal of the bare TiN substrate taken as the reference. This signal is of course underestimated to some extent as compared to the really blank substrate because of the presence of contamination but can still be used for a coarse evaluation. The resulting values of the effective SAM thicknesses are 1.5, 2.4, 1.6, 2.35, and 1.6 nm (±0.15 nm) for the SAMs 15, 16, 3, 1, and 2, respectively, corresponding indeed to the values expected for monolayers. Also, these values reflect the expected differences in the SAM thicknesses between the SAMs 16 and 3 and between the SAMs 1 and 2. Interestingly, the thicknesses of the SAMs 2 and 3 are close to that of 15 but the P 2p signal of the latter film is noticeably higher (Fig. 4.37c). Consequently, the packing density of the SAMs 2 and 3 is noticeably

lower than that of 15, which is reasonable in view of the structure of the SAM-forming molecules. Note that, generally, an XPS-derived effective SAM thickness represents a "coalescence" of the real thickness and the packing density. This is also a reason for an additional underestimation of the effective thickness values for all the SAMs of the present study (but, especially, for the monolayers 1, 16, 2, and 3 featuring complex backbones), since their packing density is certainly lower than that of the reference AT SAMs on Au and, consequently, the respective attenuation length is slightly higher. Considering both this aspect and the underestimation of the signal of the bare substrate (see above), I can reasonably assume that the real thicknesses of the SAMs studied are by 0.3-0.5 higher than the calculated values, in good agreement with the STEM-derived thickness of 2 (see Fig. B.2).

4.6.3 NEXAFS Spectroscopy

The C K-edge NEXAFS spectra of the phosphonate SAMs and the bare TiN substrate are presented in Fig. 4.38. In Fig. 4.38a, the spectra acquired at the so-called magic X-ray incidence angle (~55°) are shown, which are exclusively characteristic of the electronic structure of the systems studied and are not affected by molecular orientation effects.[129] Complementary, in Fig. 4.38b, the difference between the spectra collected under normal (90°) and grazing (20°) incidence are shown, which represents a fingerprint of orientational order and molecular orientation in the systems studied, relying on the linear dichroism effects in X-ray absorption.[129]

The 55° spectrum of the blank TiN substrate exhibits a typical signature of contamination, with a weak π* resonance of C=C/phenyl moieties at ~285.0 eV (e),[129] characteristic π* resonance of COOH at 288.4 eV (f),[193] and a variety of further, non-specific resonances at higher excitation energies. The 55° spectrum of the reference SAM 15 exhibits the characteristic resonances of alkyl chains,[201,268,269] viz. a most prominent feature at ~287.7 eV (a), representing the so-called 'C–H' band[268,269] and comprised of several mixed σ* C–H/Rydberg resonances, and two broader resonances at ~293.4 eV (b) and ~301.6 eV (c) related to valence, antibonding C–C σ* and C–C' σ* orbitals, respectively. These resonances exhibit pronounced linear dichroism, i.e., intensity dependence on X-ray incidence angle, as evidenced by the appearance of the intense peaks at the positions of these resonances in the difference spectra in Fig. 4.38b. This suggests a high orientational order in the SAM 15. Considering that the TDM of the 'C–H' band and σ* C–C resonances are oriented perpendicular and along the alkyl backbones[201,268,269] the positive and negative signs of the respective difference peaks suggest an upright orientation of the molecular chains in the SAM 15 (as expected). A tentative evaluation of the 'C–H' band intensity as a function

of X-ray incidence angle, performed within the standard formalism for a plane-like orbital,[129,270] gave the average molecular tilt angle with respect to the surface normal of 30 ± 5°.

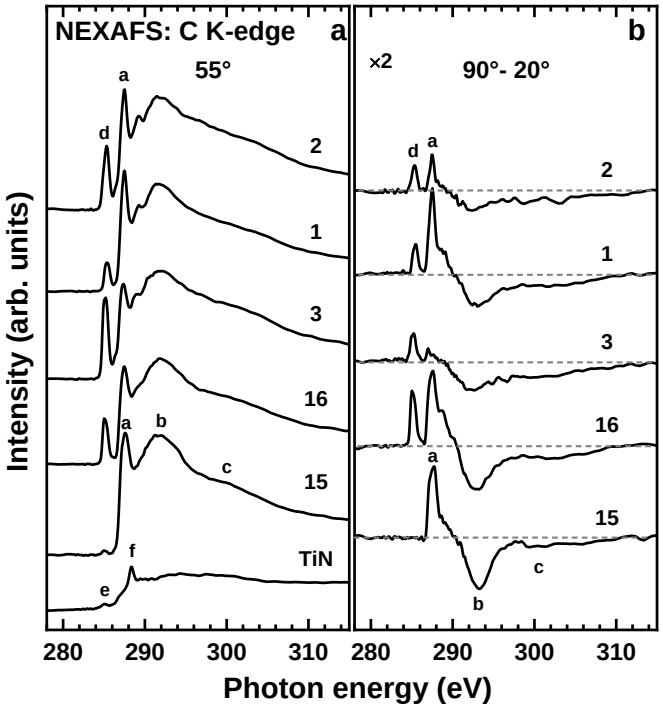

Figure 4.38 C K-edge NEXAFS spectra of the phosphonate SAMs and the bare TiN substrate: (a) the spectra acquired at an X-ray incidence angle of 55°; (b) the difference between the spectra measured under normal (90°) and grazing (20°) incidence. Most prominent absorption resonances are marked by letters (see text for details). The horizontal gray dashed lines in panel b correspond to zero. The vertical scale in (b) is scaled up by a factor of 2 compared to (a) to make the linear dichroism effects better visible.

The 55° spectra of the other SAMs (16, 3, 1, and 2) also exhibit the characteristic absorption resonances of the alkyl chain, which is expectable since the respective moieties build a part of the molecular backbones. The spectral weights of the respective resonances, which are larger for the SAMs 16 and 1 compared to the SAMs 3 and 2, correlate with the lengths of the alkyl moieties in the backbones. In addition to the above resonances, the characteristic[129,193] π_1* resonance of the aromatic rings in the backbones at either 285.05 eV (16 and 3) or 285.3 eV (1 and 2) is also observed in the spectra (d). The spectral weight of this resonance correlates well with the presence of either one (16 and 1) or two (3 and 2) phenyl rings in the molecular backbones. The upward shift of the π_1* resonance energy for the SAMs 1 and 2 compared to the monolayers 16 and 3 is related to the fluorine substitution.[271] The contributions of the cyclohexane ring are comparably non-intense and less specific,[272] and cannot therefore be unequivocally distinguished in the spectra.

Similar to the ref[257], the spectra of the other SAMs (16, 3, 1, and 2) exhibit pronounced linear dichroism, as manifested by the peaks at the positions of the characteristic absorption resonances in the difference spectra (Fig. 4.38b). In all the spectra, the difference peaks associated with the π* resonance of the phenyl rings and the 'C–H' band of the alkyl chains are positive and those related to the C–C σ* and C–C' σ* orbitals of the molecular backbone are negative. In view of the TDM orientation for the alkyl chain (see above) and the fact that the TDM of the π_1* resonance of the aromatic rings is directed perpendicular to the ring plane,[129,193] the data in Fig. 4.38b suggest an upright orientation of the entire molecular backbones in all the SAMs (16, 3, 1, and 2).

The relative height of the difference peaks with respect to the corresponding resonances in the 55° spectra represents a fingerprint of the extent of the orientational order and the average molecular inclination. Considering the data in Fig. 4.38b in this context, one can conclude that the SAMs 16 and 1 have much higher orientational order and smaller molecular inclination compared to the monolayers 3 and 2. This behavior correlates well with the structure of the SAM-forming molecules and agrees perfectly with the XPS data, suggesting a higher effective packing density for the SAMs 16 and 1. Nevertheless, both the reference SAM 3 and the electric-field-switchable monolayer 2 exhibit a certain degree of the orientational order with an upright orientation of the SAM-forming molecules.

4.6.4 Charge Transport Properties

The charge transport data were measured by our partner group of Prof. M. Tornow (Technical University of Munich), and the related figures are shown in Appendix B. Comparison of the *J*-V characteristics of 1 and 2 (Fig. B.3a) indicates an extremely low cycle-to-cycle and device-to-device variability of 2 - as intended by the molecular design. The *J*-V trace of its non-fluorinated, non-polar analogue 3 (Fig. B.3b), which was prepared as a reference, shows only a small hysteresis occurring in a different voltage range.

Further, the current density for 2 is at least 3 orders of magnitude higher than the one for 1 (at ±1 V). As a higher current density for 2 in comparison to 1 was one of our initial molecular design targets, it should be mentioned again that also for compound 1 the current density of the TiN/1/Ti/Au device is at least 2 orders of magnitude higher at these read-out voltages than for the Al/Al_2O_3/1/Pb/Ag device described in our previous communication,[39] cf. Fig. B.3c. Presumably, this is mainly due to the absence of the insulating Al_2O_3 anchoring layer. This renders the current density of the optimized TiN/2/Ti/Au device altogether at the minimum 5 orders of magnitude higher than for the first, proof-of-concept device (Al/Al_2O_3/1/Pb/Ag).

This effect can be immediately discerned with the help of Fig. 4.39, which directly compares the HRS (high resistive state) and LRS (low resistive state) current densities as a function of sweep number, of one first-generation device ($Al/Al_2O_3/1/Pb/Ag$) with those of one new TiN/2/Ti/Au device. Having both major improvements (molecular design and electrode material) implemented, the resulting strong increase in current density as well as the already observed, greatly enhanced state stability are evident. In fact, at the voltage with the highest average ON/OFF conductance ratio (ratio between conductance in LRS and HRS), system 1 shows large scattering of the LRS with successive sweeps. In contrast, the novel TiN/2/Ti/Au device exhibits an excellent repeatability of its HRS and LRS with an ON/OFF ratio J_{LRS}/J_{HRS} >10 for all measured 20 switching cycles – not only on average. Importantly, this ratio is also more than ten times higher than the individual scattering ranges (max/min conductance ratio) of HRS and LRS, in contrast to the first-generation device data (see, the numerical range limits included in Fig. 4.39). As the average ON/OFF ratios for 1 and 2 are still quite comparable for the same contact materials (Fig. B3c), we conclude that the dominating current switching mechanism is mainly related to the dipole orientation of the polar 2,3-difluorophenylene unit in both cases.

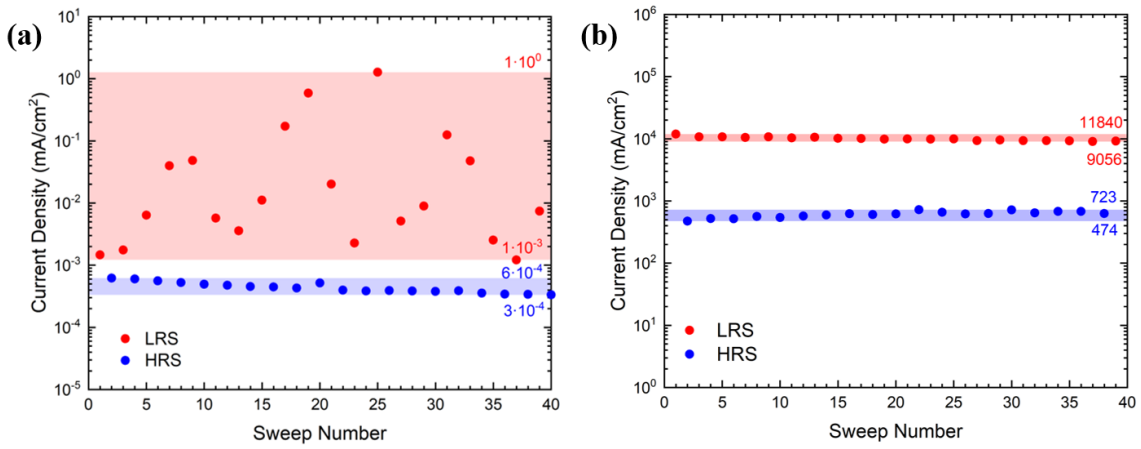

Figure 4.39 Current density in the HRS and LRS states, as function of sweep number (here, two sweeps make up one cycle). (a): measured at –1.0 V for compound 1 in the first-generation $Al/Al_2O_3/1/Pb/Ag$ device stack.[39] (b): at –0.45 V for compound 2 in the TiN/2/Ti/Au device stack. Our previously reported system, $Al/Al_2O_3/1/Pb/Ag$ (25 x 25 μm^2), shows large scattering of the LRS as well as a slight downward drift of the current density with successive sweeps. In contrast, the TiN/2/Ti/Au device (5 x 5 μm^2) has a stable ON/OFF ratio of about one order of magnitude, with low scattering of LRS and HRS. The presented data were measured by the partner group (Prof. M. Tornow, Technical University Munich).

5. Conclusions & Outlook

5.1 Conclusions

Within my PhD project, I studied a variety of functional molecular films in the context of organic and molecular electronics, with the emphasis on electrostatic engineering of interfaces, charge transport properties, and specific functional behaviors.

Within the first subproject, charge transport properties of the R-nPT SAMs (n = 1-3; R = H, F, CH_3 and CF_3) on Au(111) were investigated by assembling two-terminal Au^{Ts}/SAM//Ga_2O_3/EGaIn junctions and measuring their *J*-V characteristics. The quality of the SAMs was verified and their basic parameters were determined by a combination of XPS and NEXAFS spectroscopy. The work functions of the SAMs, manifesting the effect of the polar tail groups, showed the expected correlation with the molecular dipole moments.

Independent of the length of the oligophenylene chain, the current density at a given n varied significantly (more than by the order of magnitude) at the R variation, being the highest for R = CH_3, and then successively lower for R = H, R = CF_3, and R = F. This behavior correlated with neither the size of the tail group nor the evolution of the work function and, consequently, was exclusively attributed to the identity of the tail group.

In contrast to the halogen-substituted aliphatic SAMs, the decoration of the aromatic SAMs with fluorine or trifluoromethyl tail group did not result in a noticeable change of the decay coefficient (0.33 - 0.34 $Å^{-1}$ for all monolayers). The most likely reasons behind this behavior are a comparably small effect expected for fluorine, the intrinsically low values of decay coefficient for H-nPT SAMs, and only a minor variation of the tunneling barrier height at the SAM/top electrode interface and dielectric constant of the SAMs at the given n.

Within the next subproject, I dealt with the SF_5-nPT SAMs on Au(111). The SF_5-nPT molecules combine the exceptionally hydrophobic and electronegative $-SF_5$ tail group and the conjugated oligophenylene backbone, uniting thus the favorable properties of both these building blocks. The quality of the SF_5-nPT SAMs was verified by several complementary experimental techniques, which also delivered information about the molecular organization in the monolayers and provided a variety of important parameters in this context. Accordingly, the monolayers feature dense molecular packing, defined by the lateral dimensions of the $-SF_5$ group, constituting the SAM-ambient interface.

Such a molecular organization results in superior wetting and electrostatic properties of the SF_5-nPT SAMs compared to the analogous $-CF_3$ terminated monolayers (reference), with $-CF_3$ being the most hydrophobic and electronegative tail group used so far. Especially the work function

values for SF_5-BPT and SF_5-TPT SAMs, close to 6.0 eV, are truly exceptional and, to the best of our knowledge, the highest ones reported for SAM-engineered gold substrates so far.

The exceptional work function values make SF_5-nPT SAMs attractive for applications in organic electronics and photovoltaics, extending the possibility of energy level alignment at specific interfaces in the devices. In view of the favorable charge transport properties of the nPT backbone, electrostatic engineering of the respective interfaces by the SF_5-nPT SAMs should not involve an increase of charge transport resistance across the interface, which would be advantageous for the performance of the devices.

Within a further subproject, I have fabricated and characterized in detail two different pyrenyl-substituted alkanethiolate SAMs on Au(111). The respective Pyr-C12 and Pyr-C4S2 monolayers featured either an unmodified or heteroatom-substituted alkyl linker of different lengths. In the latter case, two methylene groups in the linker were substituted by two S heteroatoms.

The identity of the fabricated SAMs and the anchoring of all SAM-constituents to the substrate by the thiolate groups were verified by XPS and NEXAFS spectroscopy, which also allowed to determine the effective thickness, packing density, and orientation of the terminal pyrenyl groups. The effective thickness correlated well with the lengths of the SAM-forming molecules, as expected for monolayers. The packing density of the Pyr-C12 and Pyr-C4S2 SAMs correspond to the tight molecular packing, determined by the bulky pyrenyl groups. The average tilt angle of the pyrenyl moieties in these SAMs was estimated as $9 \pm 3°$ and $12 \pm 3°$, respectively, suggesting an exceptionally high orientational order. The work functions of the SAMs agree well with the nonpolar character of the molecular backbone, while the WCAs of the SAMs correspond well to the identity of the SAM-ambient interface.

The electrical conductance of the pyrenyl moiety was found to be superior to the alkyl chain of the same length, while the introduction of the S heteroatoms in the alkyl linker resulted in significant worsening its conductive properties, in good agreement with the literature data.[108] At the same time, in contrast to the previous reports,[187,188,189] no rectification behavior was found for the Pyr-C12 SAM and only a weak rectification with an RR of 4.5 at a bias of 1 V was recorded for the Pyr-C4S2 case. The different behavior of both SAMs is presumably related to the different orientations and arrangements of the terminal pyrenyl moieties in these monolayers, reflected also by the somewhat different values of the transition voltage. The former parameters seem to be of primary importance for the charge transport properties of the pyrenyl-containing SAMs, which probably explains the difference between the results of the present study and those of the previous reports in context of the rectification, apart from the issue of the chemical identity of the films reported before.

Further, charge transport properties of the Fc-FluT SAM embedded into the Au^{TS}/SAM//Ga_2O_3/EGaIn junctions were studied. Several different sweeping modes were applied, including asymmetric sweeping the bias at only positive or negative polarity as well as its symmetric variation between both bias polarities. Depending on the sweeping character, the SAM exhibits two different conductance states, high (HCS) and low (LCS), and also a distinctly different rectification behavior. While the original HCS is preserved at the successive sweeping at negative bias, it can be gradually transformed into the LCS by sweeping at positive bias. A combination of both partial *J*-V curves for the two bias polarities results in a distinct effective rectification behavior, with an effective RR of ~2100 at V = 0.1 V, which is an exceptionally high value for such a low bias. In contrast, symmetric sweeping (as a more common experimental approach that has traditionally been applied to other ferrocene-containing junctions), results in the lack of the rectification behavior, with RR values close to 1 over the entire bias range. The observed current densities for these symmetric curves, however, depend strongly on the direction of the first scan: the junction is in the HCS when starting with a positive bias sweep and in the LCS in the case of a negative bias sweep. Consequently, depending on the direction of the first sweep, the steady state currents reproducibly differ by 2-3 orders of magnitude, which is quite an exceptional behavior. Also, the occurrence of the both conduction states not only at the asymmetric but also symmetric sweeping shows that these states are truly intrinsic for the system studied.

As an extension of the above subproject, to prove the generality of the observed behavior, molecular organization and charge transport properties of the Fc-Trip films were studied using a combination of several complementary spectroscopic techniques and two-terminal junctions with the top EGaIn electrode. Fc-Trip films represent a model tripodal system, in contrast to the most frequently used, in the context of self-assembly, monopodal molecules. The spectroscopic data suggest that the Fc-Trip films have a SAM-like character with the molecules chemically coupled to the substrate and featuring upright orientation, even though with a certain heterogeneity of the bonding configurations and a certain degree of orientational disorder. The two-terminal junctions containing the Fc-Trip films also exhibit, similar to the Fc-FluT case, two distinctly different conductance states, HCS and LCS. The junction remains in the HCS at the successive sweeping at the negative bias but dynamically transforms into the LCS at the successive sweeping at the positive bias. Comparison of the *J* values for the both bias polarities results in a high effective RR of ~500 at such a low bias as 0.1 V. The difference in RR with respect to Fc-FluT (~2100) correlates well with the density of the Fc groups, emphasizing their primary role in the rectification behavior.

Also similar to Fc-FluT, the HCS/LCS asymmetry is not observed at the standard symmetric sweeping mode which results in nearly symmetric *J*-V curves and the lack of the rectification

behavior. However, the *J* values of these curves correspond to either the HCS or LCS values, depending on the direction of the first sweep, suggesting a certain metastability of these conductance states. The fact that these states can be achieved not only at the asymmetric but also symmetric sweeping modes suggests that they are truly intrinsic for the system studied.

The observed behavior is rationalized on the basis of the tentative literature model linking the appearance of the LCS with the partial non-reversible oxidation of the Fc groups, triggered by the positive bias.[37] Most likely, this oxidation is stabilized by conformational changes in the film, which, in the case of Fc-Trip, are only rotations of the Fc-linker units along the symmetry axis.

As mentioned above, the occurrence of the two distinctly different conductance states and the strong influence of the sweeping mode on the observed charge transport properties for the Fc-Trip film are very close to the behavior of Fc-FluT and several other analogous molecules.[37,244] This suggests that these phenomena are probably not unique for the above systems but can also be observed in other molecular assemblies featuring redox groups, including metallocenes in particular.

Finally, in collaboration with our partners from the TU Darmstadt and TU Munich we studied a series of custom-designed phosphonate SAMs, serving as prototypes of molecular memristor systems. The switching was assumed to be driven by the electric field, relying on the changes in molecular conformation. As compared to the previously reported systems,[254] better conductive electrode materials and conformationally rigid (limited number of states) molecular backbone were introduced. My part in this subproject was profound characterization of these monolayers by spectroscopic techniques, serving as the basis for reliable charge transport measurements performed by our partners. The identity of the SAMs was verified and their key parameters, such as the effective thickness, packing density, and molecular tilt angle, were determined. On this basis, specific conclusions regarding the molecular organization in all the SAMs studied were derived. The optimal monolayer exhibited extremely reproducible switching behavior, showing stable and no-drift operation (switching) in molecular junction for the entire number of cycles applied in the test experiments.

5.2 Outlook

The results presented in my thesis can serve as basis for further research. First, it would be interesting to perform the charge-transport experiments with iodine-substituted aromatic SAMs, since such a substitution resulted in the strongest variation of the tunneling decay coefficient in the case of aliphatic monolayers (from 0.75 to 0.25 $Å^{-1}$).[180] This, however, will require specific synthetic work, which, according to the statements of our partners, is not an easy task. Another

option is to analyze the charge transport data in the framework of the theoretical approach suggested in ref.[273], which can provide specific information on the energy level alignment and molecule-electrode coupling in the junctions. Examples of such analysis can be found in ref.[164,274]. Note, however, that so far this analysis has been exclusively applied to the atomic force microscopy data, with a comparably small contact area and the distinctly different top electrode,[164,275] and it is unclear whether it will work for the EGaIn-based junctions as well. Our first attempts in this regard were not successful.

Second, the SF_5-substitution system shows an unexpectedly large frequency shift of the ν SF vibration of the apical fluorine atom (experiments by our partners, Frankfurt University), which could not be explained. This effect should be clarified in the future, which, however, will require some dedicated experiments beyond the main scope of my thesis.

Third, a practical application of the rectification behavior of the Fc-FluT and Fc-Trip SAM is, regretfully, not entirely straightforward, because of the slow and gradual character of the switching between the conductance states triggered either by sweeping or by pulsing the applied bias. Still, these SAMs represent interesting test systems for molecular electronics, revealing a variety of fascinating effects like bias-triggered conductance switching that depends on the biasing history of the junction. Thus, it will certainly open additional options for future research, bearing in mind that on a microscopic level the relevant processes occurring in these SAMs are not fully understood and further efforts by theory are highly desirable. Our data show that applying only one specific biasing routine and analyzing only sweep-averaged data might very well miss significant parts of the effects actually occurring in molecular junctions. This is apparently particularly true for junctions comprising redox-active molecules and molecular ensembles, where the obtained results and the observed effects might very well depend on the applied measurement procedure.

Finally, future work should be directed towards developing SAM-based tunneling junctions for practical applications, such as synapses in neuromorphic circuitry. For the molecules studied by us, this should include an extended study and optimization of device retention, switching dynamics (time dependence) and spike-time dependent state potentiation and depression (under pulsed operation).

List of Publications included into this thesis

[1] Liu, Y.; Katzbach, S.; Asyuda, A.; Das, S.; Terfort, A.; Zharnikov, M. Effect of substitution on the charge transport properties of oligophenylenethiolate self-assembled monolayers. Phys. Chem. Chem. Phys. 2022, 24, 27693-27704.

[2] Liu, Y.; Zeplichal, M.; Katzbach, S.; Wiesner, A.; Das, S.; Terfort, A.; Zharnikov, M. Aromatic self-assembled monolayers with pentafluoro-λ^6-sulfanyl ($-SF_5$) termination: Molecular organization and charge transport properties. Nano Res. 2023, 16, 7991-8002.

[3] Liu, Y.; Notz, S.; Lang, H.; Zharnikov, M. Pyrene-Terminated Self-Assembled Monolayers on Au Substrate: Molecular Organization and Charge Transport Properties. J. Phys. Chem. C 2023, 127, 19290-19300.

[4] Liu, Y.; Zojer, E.; Zharnikov, M. Sweep-Character-Dependent Switching of the Conductance State in Ferrocene-Substituted Thiofluorene Self-Assembled Monolayers. ACS Appl. Mater. Interfaces 2022, 14, 52499–52507.

[5] Liu, Y.; Fukushima, T.; Zharnikov, M. Appearance of Different Conductance States in Monomolecular Films of Ferrocene-Decorated Triptycene-Based Tripods. J. Phys. Chem. C, DOI: 10.1021/acs.jpcc.3c06634.

[6] Kirsch, P.; Dlugosch, J. M.; Kamiyama, T.; Seim, H.; Resch, S.; Voges, F.; Lieberman, I.; Liu, Y.; Zharnikov, M.; Essen, C.; Tornow, M. Restricting Conformational Space: A New Blueprint for Electrically Switchable Self-Assembled Monolayers. Small, submitted.

Other Publications

[1] Fischer, C.; Das, S.; Zhang, Q.Z.; Liu, Y.; Weinhardt, L.; O'Hagan, D.; Zharnikov, M.; Terfort, A. Lateral dipole moments induced by all-cis-pentafluorocyclohexyl groups cause unanticipated effects in self-assembled monolayers. Nano Res. 2023, 16, 11030-11041.

Appendix A. Supplementary Data

Table A.1 Overview of the charge transport measurements for the Au^{Ts}/R-nPT//Ga_2O_3/EGaIn junctions. (R = -H, -F, -CH_3, and -CF_3; n = 1 (PT), 2 (BPT), and 3 (TPT))

SAMs	Samples	Junctions	Scans	Processed	Yield
H-PT	5	29	381	233	61.2%
H-BPT	4	25	283	199	70.3%
H-TPT	3	23	317	241	76.0%
F-PT	4	25	430	291	67.7%
F-BPT	3	24	232	157	67.7%
F-TPT	4	17	243	153	63.0%
CH_3-PT	3	30	254	160	63.0%
CH_3-BPT	2	16	241	146	60.6%
CH_3-TPT	3	17	292	184	63.0%
CF_3-PT	3	18	244	179	73.4%
CF_3-BPT	2	21	232	161	69.4%
CF_3-TPT	3	30	272	181	66.5%

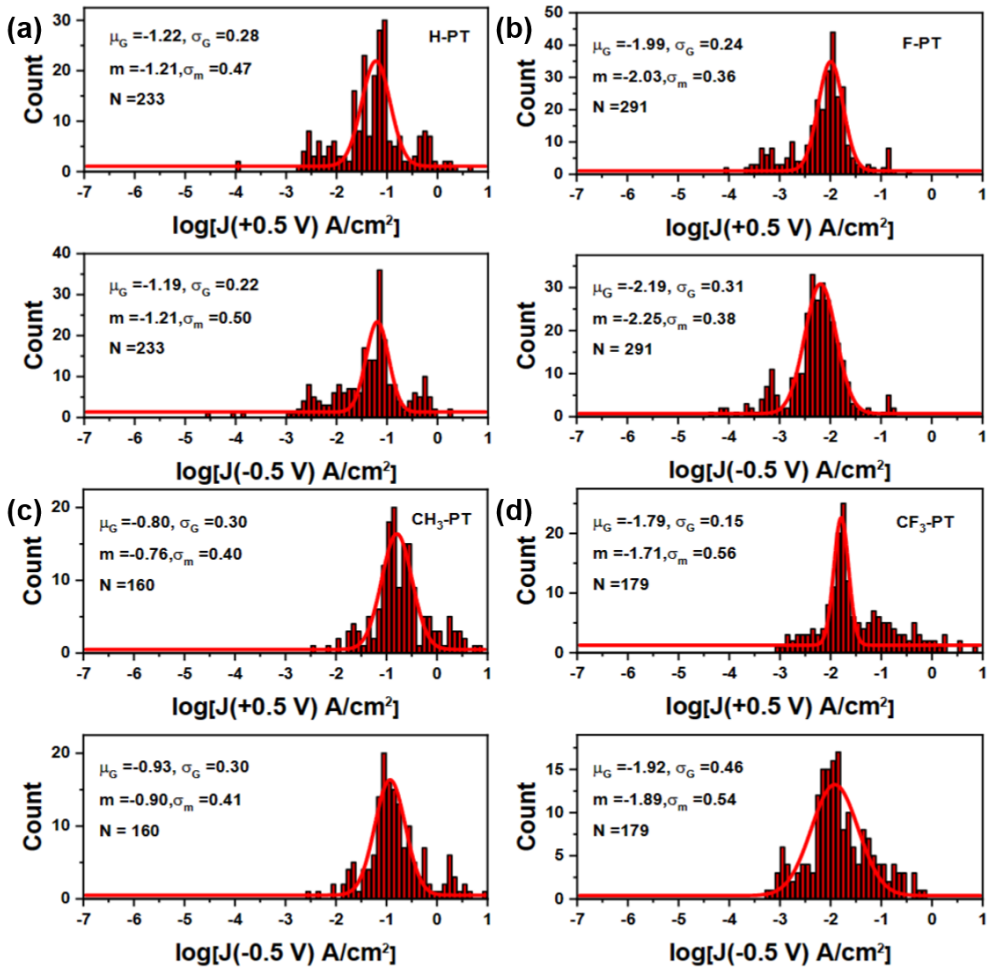

Figure A.1 Electrical characteristics of the Au/R-PT//Ga_2O_3/EGaIn junction: Histograms of the $\log_{10}|J\ (V)|$ at V = +0.5 V (top panel) and V = -0.5 V (bottom panel). The characteristic parameters are given: μ_G – Gaussian average; σ_G – Gaussian standard deviation; m – median average; σ_m - adjusted median absolute deviation; and N – number of scans. (R = -H (a), -F (b), -CH_3 (c), and -CF_3 (d)).

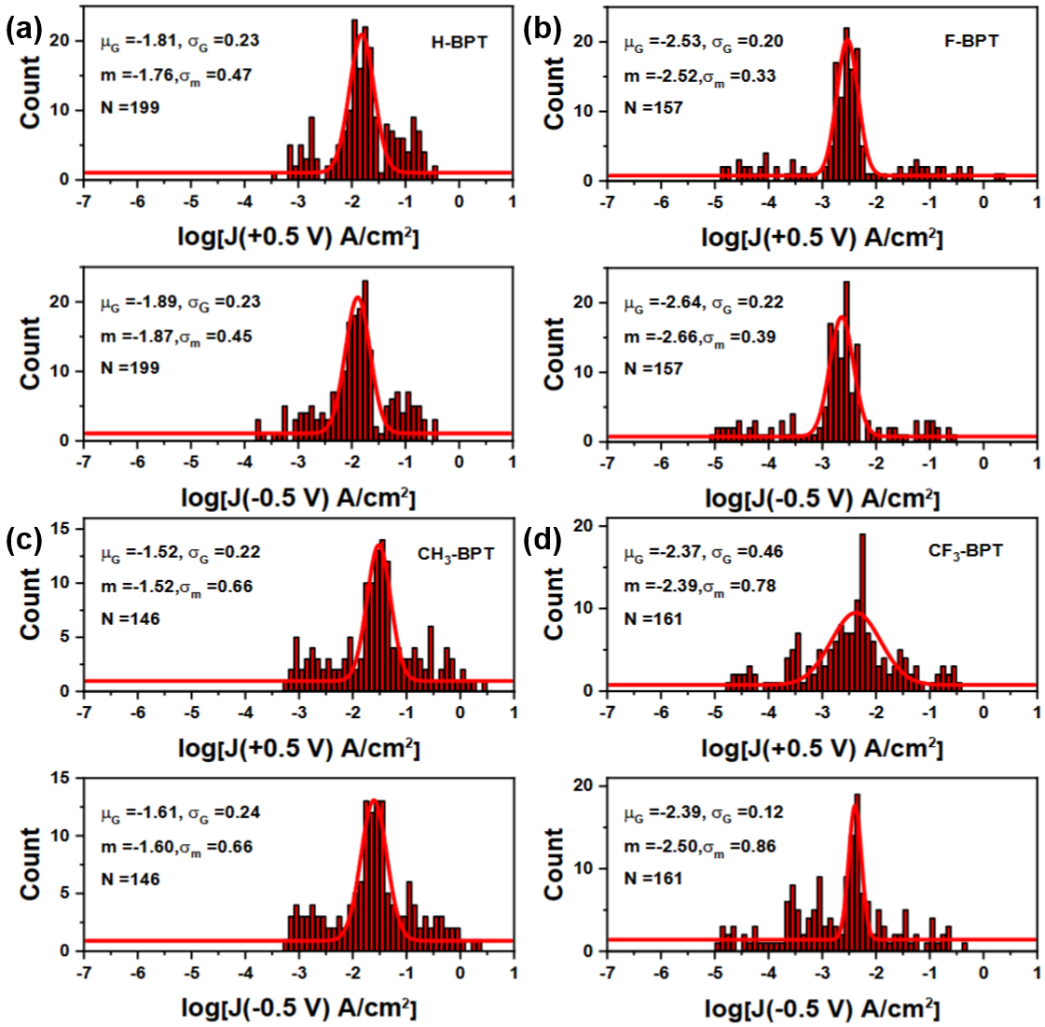

Figure A.2 Electrical characteristics of the Au/R-BPT//Ga_2O_3/EGaIn junction: Histograms of the $\log_{10}|J\ (V)|$ at V = +0.5 V (top panel) and V = -0.5 V (bottom panel). The characteristic parameters are given: μ_G – Gaussian average; σ_G – Gaussian standard deviation; m – median average; σ_m - adjusted median absolute deviation; and N – number of scans. (R = -H (a), -F (b), -CH_3 (c), and -CF_3 (d)).

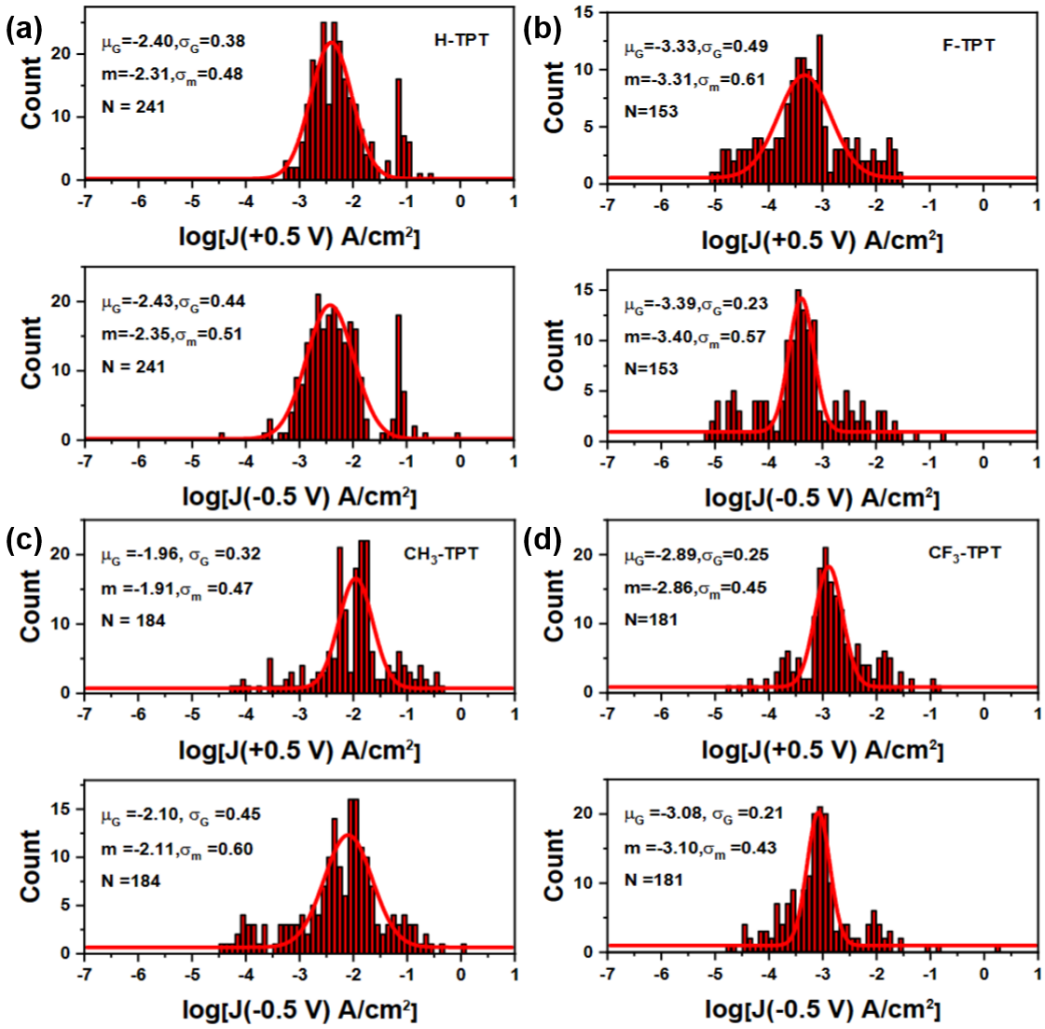

Figure A.3 Electrical characteristics of the Au/R-TPT//Ga_2O_3/EGaIn junction: Histograms of the $\log_{10}|J\ (V)|$ at V = +0.5 V (top panel) and V = -0.5 V (bottom panel). The characteristic parameters are given: μ_G – Gaussian average; σ_G – Gaussian standard deviation; m – median average; σ_m - adjusted median absolute deviation; and N – number of scans. (R = -H (a), -F (b), -CH_3 (c), and -CF_3 (d)).

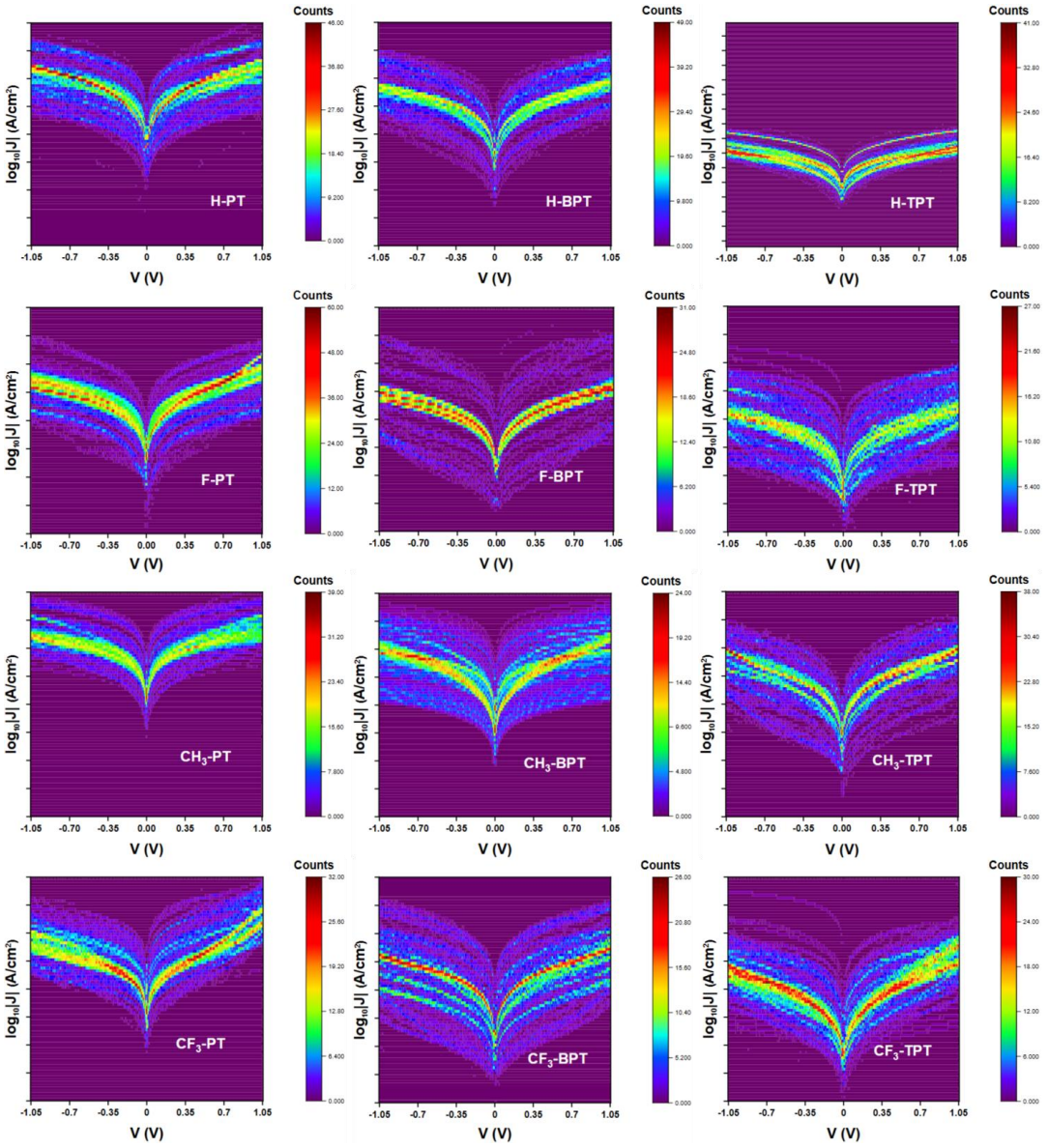

Figure A.4 Electrical characteristics of the Au/R-nPT//Ga_2O_3/EGaIn junction: Heat map of the semi-$\log_{10}$ |J(V)| curves. (R = -H, -F, -CH_3, and -CF_3; n = 1 (PT), 2 (BPT), and 3 (TPT)).

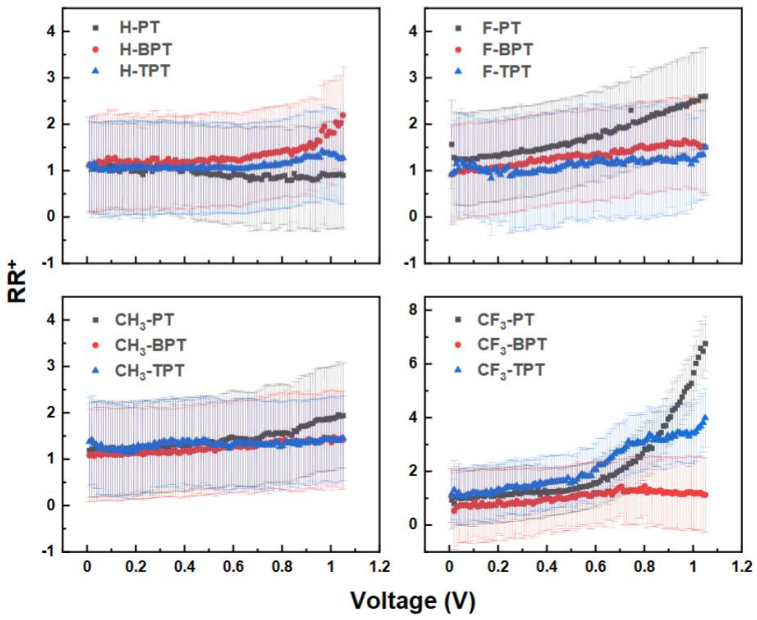

Figure A.5 Rectification ratio of the R-nPT SAMs measured in the Au/SAM//Ga_2O_3/EgaIn junctions. The higher current density was observed at the positive bias voltages.

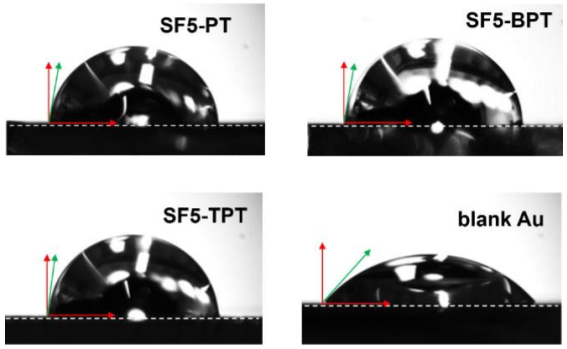

Figure A.6 Water drops on the surface of the SF_5-nPT/Au and blank Au (reference). Surface normal and direction along the surface are marked by red arrows; static water contact angles are marked by green arrows.

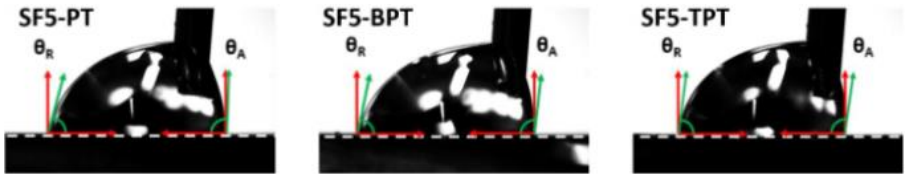

Figure A.7 Water drops on the surface of the SF_5-nPT/Au. Surface normal and direction along the surface are marked by red arrows; the advancing and receding water contact angles are marked as θ_A and θ_R with green arrows, respectively.

Table A.2 Overview of the charge transport measurements for the Au^{Ts}/SF_5-nPT//Ga_2O_3/EGaIn junctions.

SAMs	Samples	Junctions	Scans	Processed	Yield
SF_5-PT	2	21	397	296	74.6%
SF_5-BPT	2	11	154	124	80.5%
SF_5-TPT	1	12	189	143	75.7%

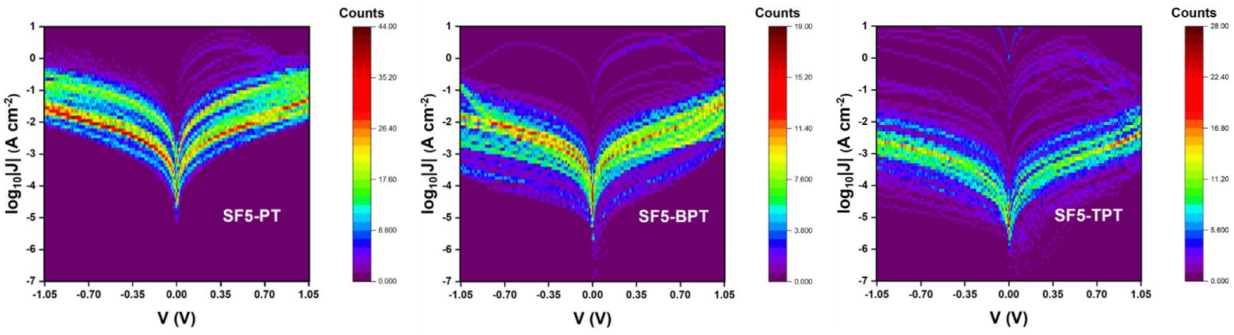

Figure A.8 Electrical characteristics of the Au^{TS}/SF_5-nPT//Ga_2O_3/EGaIn junction (n = 1, 2, and 3): Heat map of the semi-$\log_{10}|J\ (V)|$ curves.

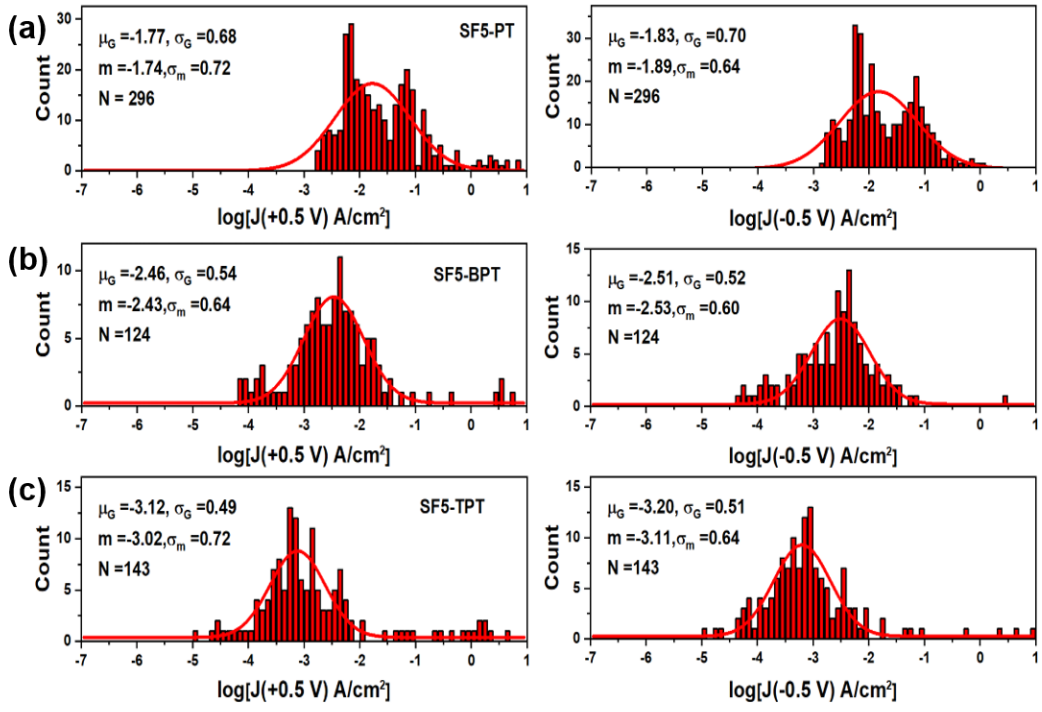

Figure A.9 Electrical characteristics of the Au^{TS}/SF_5-nPT//Ga_2O_3/EGaIn junction (n = 1 (a), 2 (b), and 3 (c)): Histograms of the $\log_{10}|J\ (V)|$ at V = +0.5 V (top panel) and V = -0.5 V (bottom panel). The characteristic

parameters are given: μ_G – Gaussian average; σ_G – Gaussian standard deviation; m – median average; σ_m - adjusted median absolute deviation; and N – number of scans.

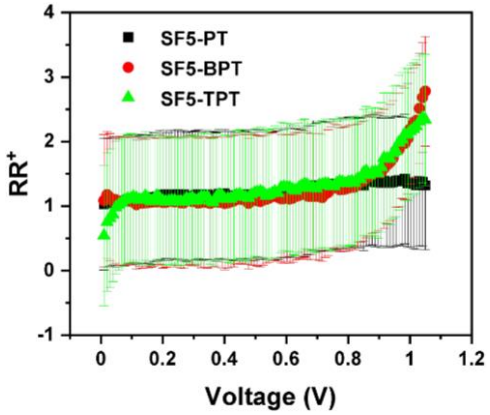

Figure A.10 Rectification ratio of the SF_5-nPT SAMs measured in the Au^{TS}/SAM//Ga_2O_3/EGaIn junctions. The higher current density was observed at the positive bias voltages.

Table A.3 Overview of the charge transport measurements for the Au^{Ts}/SAMs//Ga_2O_3/EGaIn junctions (SAM = Pyr-C12 and Pyr-C4S2). The number of successive sweeps for each measurement spot (junction) varied to some extent but never exceeded 20.

SAM	Samples	Junctions	Scans	Processed	Yield
Pyr-C12	2	13	245	245	100%
Pyr-C4S2	2	15	300	290	96.7%

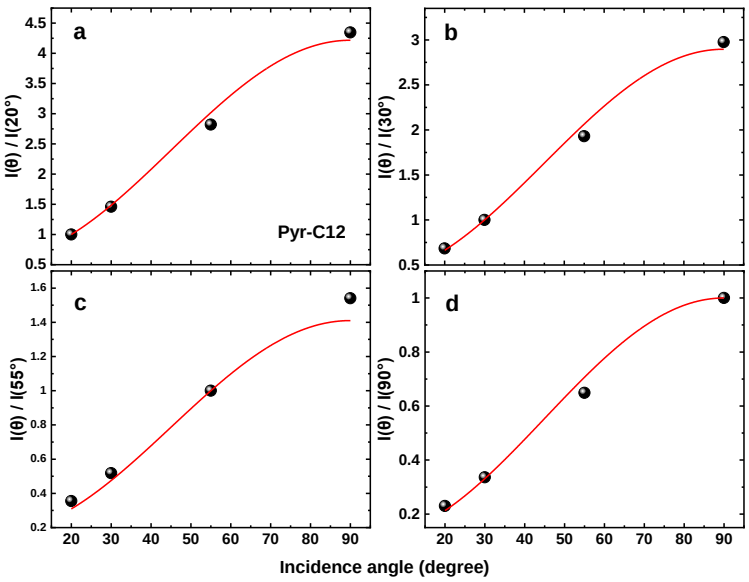

Figure A.11 $I(\theta)/I(\theta_{ref})$ ratios versus θ for the most prominent π* resonances (1 and 2) of the pyrenyl moieties in the Pyr-C12 SAM, with θ_{ref} = 20° (a), 30° (b), 55° (c), and 90° (d). The experimental data are shown by black circles; the fitting curves – by the red solid lines.

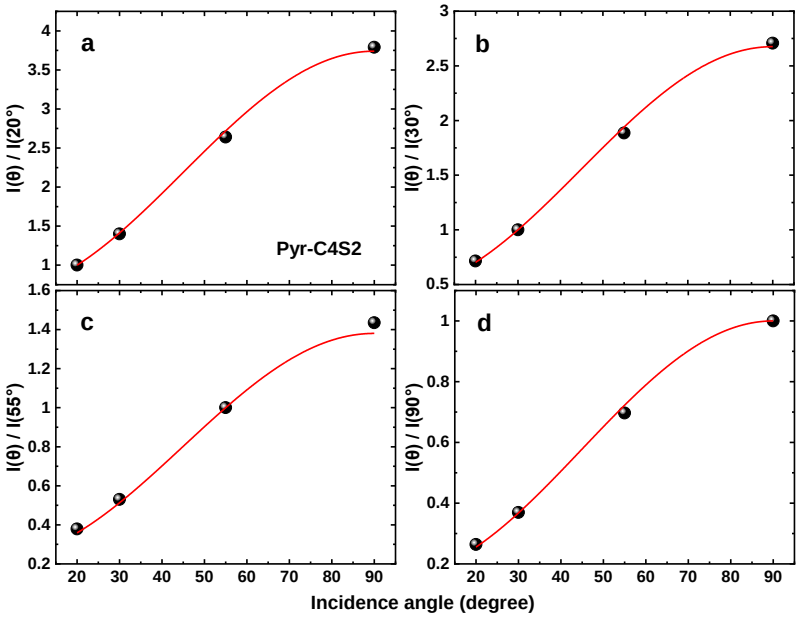

Figure A.12 $I(\theta)/I(\theta_{ref})$ ratios versus θ for the most prominent π* resonances (1 and 2) of the pyrenyl moieties in the Pyr-C4S2 SAM, with θ_{ref} = 20° (a), 30° (b), 55° (c), and 90° (d). The experimental data are shown by black circles; the fitting curves – by the red solid lines.

Table A.4 Average tilt angles of the π* orbitals of the pyrenyl moieties in the Pyr-C12 and Pyr-C4S2 SAMs derived from the fits presented in Fig. A.11 and A.12 as well as the averages over the derived four angles for each monolayer.

Molecules	Reference incidence angle				Average angle
	20°	30°	55°	90°	
Pyr-C12	81.95°	83.0°	84.6°	86.1°	82.0°
Pyr-C4S2	78.8°	79.2°	79.5°	79.9°	79.0°

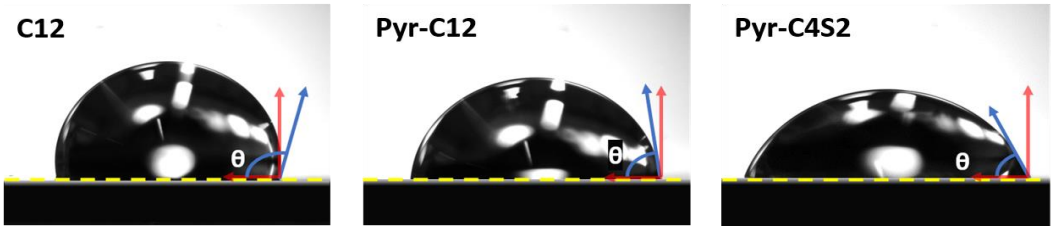

Figure A.13 Images of the water drops on the surface of C12/Au, Pyr-C12/Au, and Pyr-C4S2/Au. Surface normal and direction along the surface are marked by red arrows and yellow dashed lines, respectively; the static water contact angles are marked as θ with blue arrows.

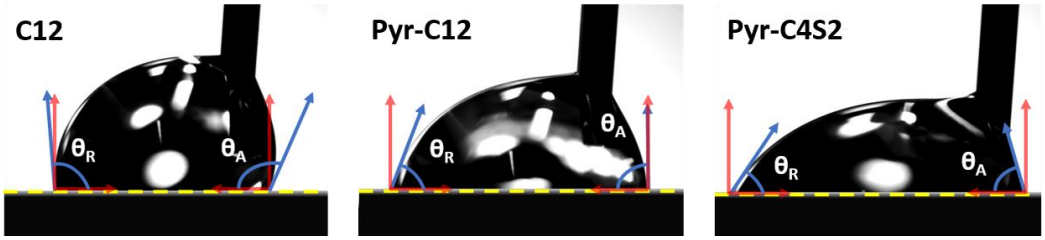

Figure A.14 Images of the water drops on the surface of C12/Au, Pyr-C12/Au, and Pyr-C4S2/Au. Surface normal and direction along the surface are marked by red arrows and yellow dashed lines, respectively; the advancing (θ_A) and receding (θ_R) water contact angles are marked with blue arrows.

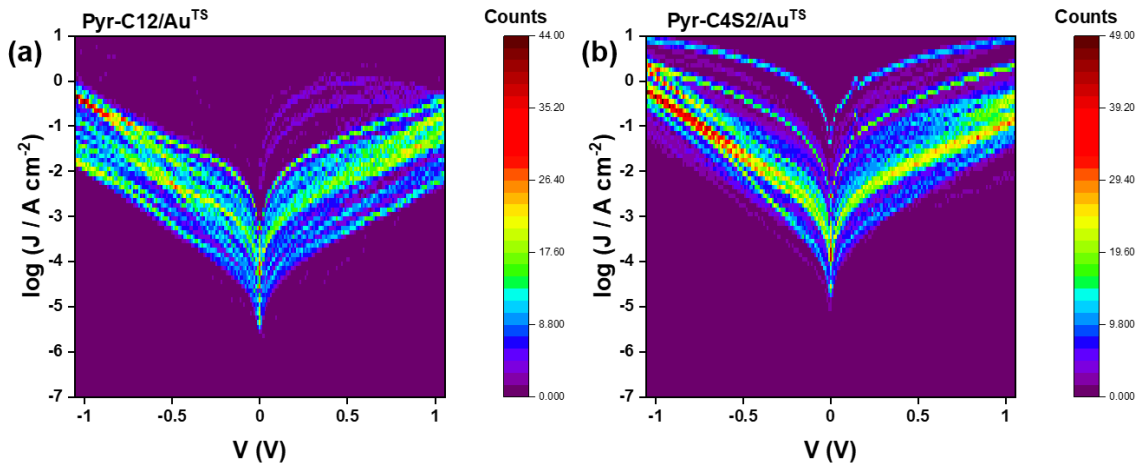

Figure A.15 Electrical characteristics of the (a) Au^{TS}/Pyr-C12//Ga_2O_3/EGaIn junction and (b) Au^{TS}/Pyr-C4S2//Ga_2O_3/EGaIn junction: Heat map of the semi-$\log_{10}|J\,(V)|$ curves.

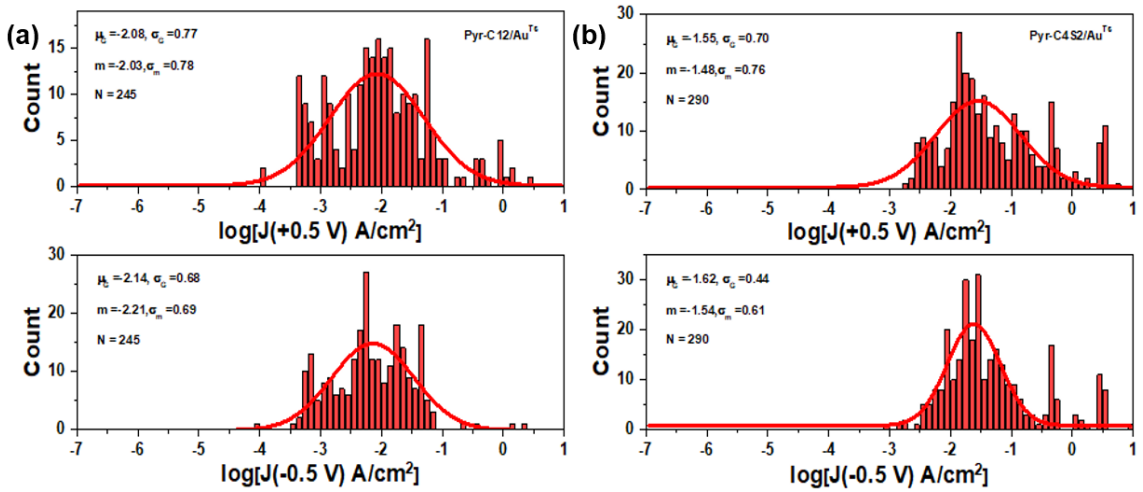

Figure A.16 (a) Electrical characteristics of the Au^{TS}/ Pyr-C12//Ga_2O_3/EGaIn junction: Histograms of the $\log_{10}|J|$ at V = +0.5 V (top panel) and V = –0.5 V (bottom panel). (b) Electrical characteristics of the Au^{TS}/ Pyr-C4S2//Ga_2O_3/EGaIn junction: Histograms of the $\log_{10}|J|$ at V = +0.5 V (top panel) and V = –0.5 V (bottom panel). The characteristic parameters are given: μ_G – Gaussian average; σ_G – Gaussian standard deviation; m – median average; σ_m - adjusted median absolute deviation; and N – number of scans.

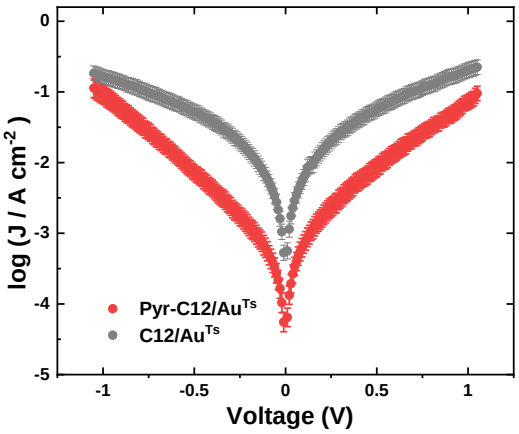

Figure A.17 Semilogarithmic current-density versus voltage (bias) plots for the Au^{TS}/SAM//Ga_2O_3/EGaIn junctions with Pyr-C12 and C12. The legends are given in the plots. The error bars represent the standard deviations.

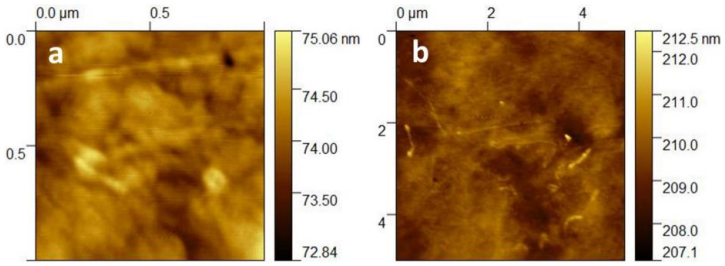

Figure A.18 AFM images of an Au^{TS} substrate: (a) 1 µm × 1 µm scan and (b) 5 µm × 5 µm scan.

Table A.5 Overview of the charge transport measurements for the Au^{TS}/Fc-FluT//Ga_2O_3/EGaIn junctions at the different sweeping modes. The number of successive sweeps for each measurement spot (junction) was varied to some extent but never exceeded 20.

Sweeping	Samples	Junctions	Sweeps	Processed	Yield
+	2	13	197	159	80.7%
-	3	13	228	203	89.0%
+/-	2	14	173	107	61.8%
-/+	2	7	110	70	63.6%

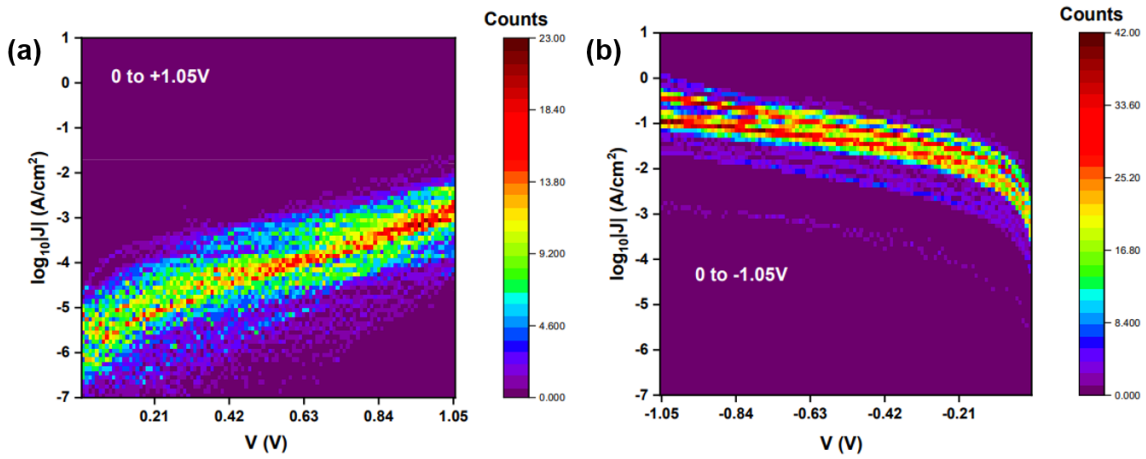

Figure A.19 Electrical characteristics of the Au^{TS}/Fc-FluT//Ga_2O_3/EGaIn junction at the bias sweeping (a) from 0 to +1.05 V and (b) from 0 to -1.05 V: Heat map of the semi-log |*J* (V)| curves.

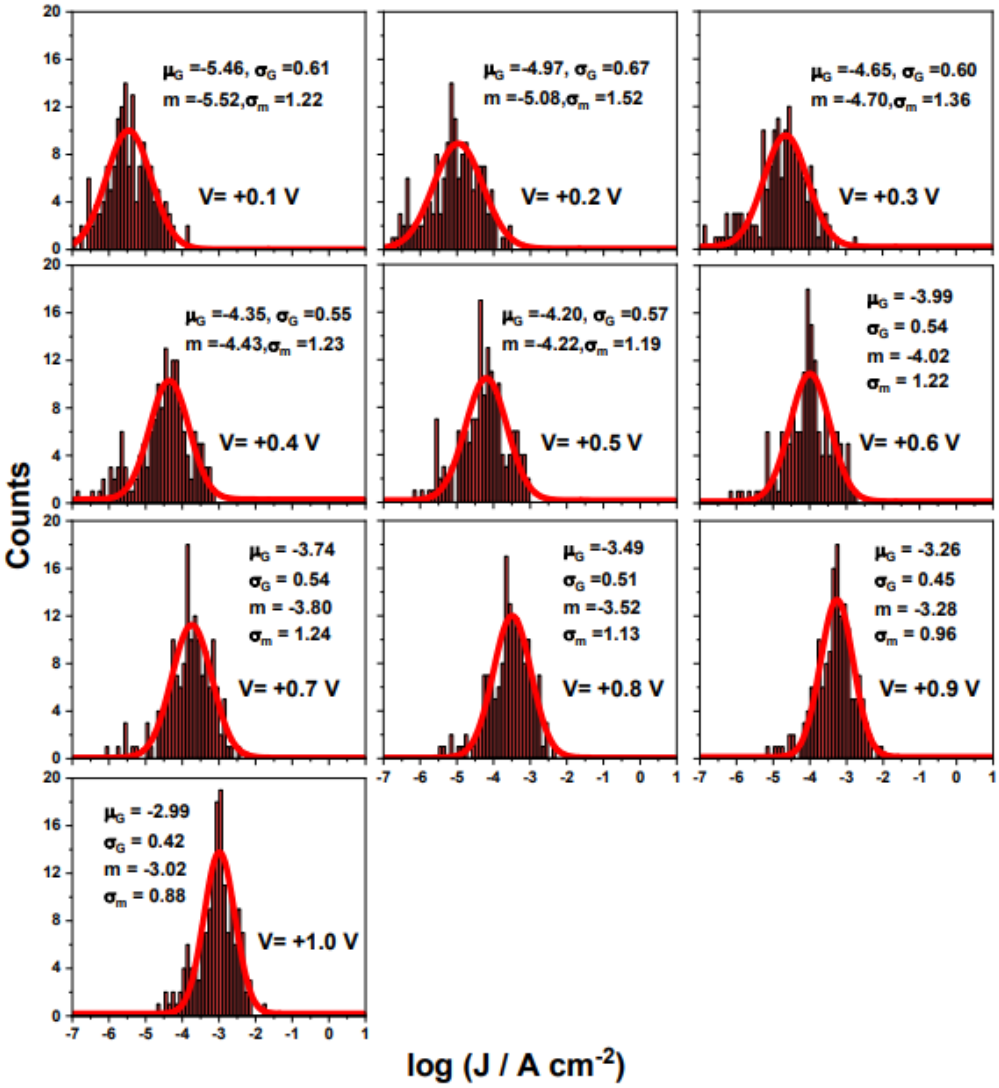

Figure A.20 Electrical characteristics of the Au^{TS}/Fc-FluT//Ga_2O_3/EGaIn junction at the bias sweeping from 0 to +1.05 V. Histograms of $\log_{10}|J|$ at the different bias values, as marked in the panels. The data represent 159 scans. The *J* values for the first sweep for each junction are not included, since they are distinctly different from those at the successive sweeps (see Fig. 4.24a in the main paper). The characteristic parameters are given: μ_G – Gaussian average; σ_G – Gaussian standard deviation; m – median average; and σ_m - adjusted median absolute deviation.

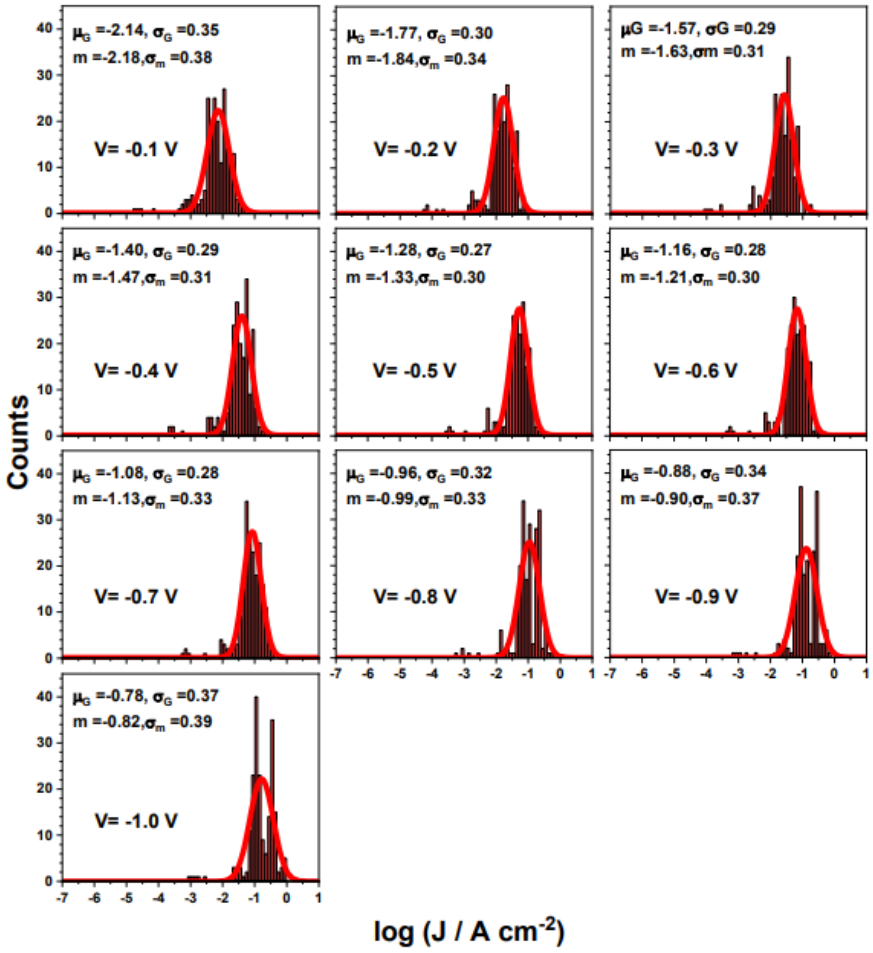

Figure A.21 Electrical characteristics of the Au^{TS}/Fc-FluT//Ga_2O_3/EGaIn junction at the bias sweeping from 0 to -1.05 V. Histograms of $\log_{10}|J|$ at the different bias values, as marked in the panels. The data represent 203 scans. The characteristic parameters are given: μ_G – Gaussian average; σ_G – Gaussian standard deviation; m – median average; and σ_m - adjusted median absolute deviation.

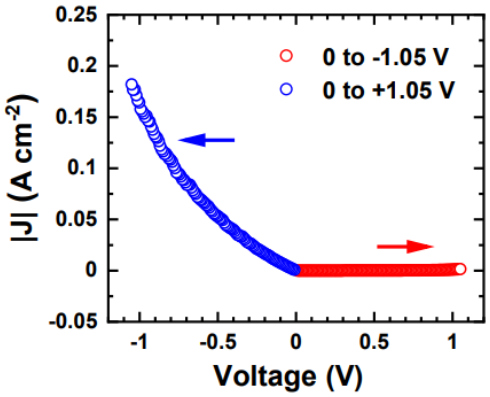

Figure A.22 Electrical characteristics of the Au^{TS}/Fc-FluT//Ga_2O_3/EGaIn junction at the bias sweeping from either from 0 to -1.05 V or from 0 to +1.05 V. The linear scale for the current density is used. The curves represent the results of a statistical analysis over a large number of sweeps.

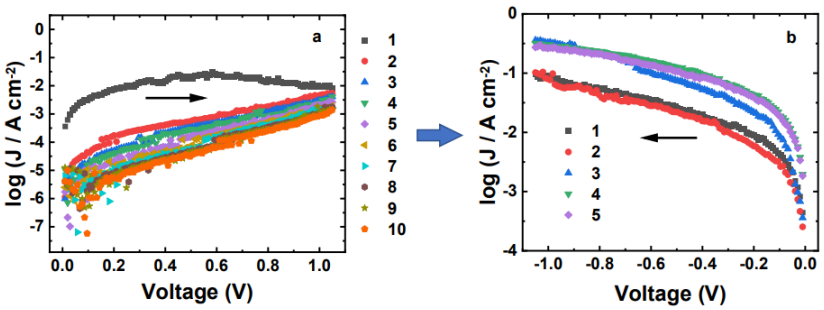

Figure A.23 Evolution of the conductivity switching in the Au^{TS}/Fc-FluT//Ga_2O_3/EGaIn junction at the bias sweeping: Semilogarithmic *J*-V plots corresponding to (a) ten successive bias sweeps from +0.01 to +1.05 V for a particular measurements spot followed by (b) five successive bias sweeps from -0.01 to -1.05 V for the same spot. The sweeping directions are marked by black arrows.

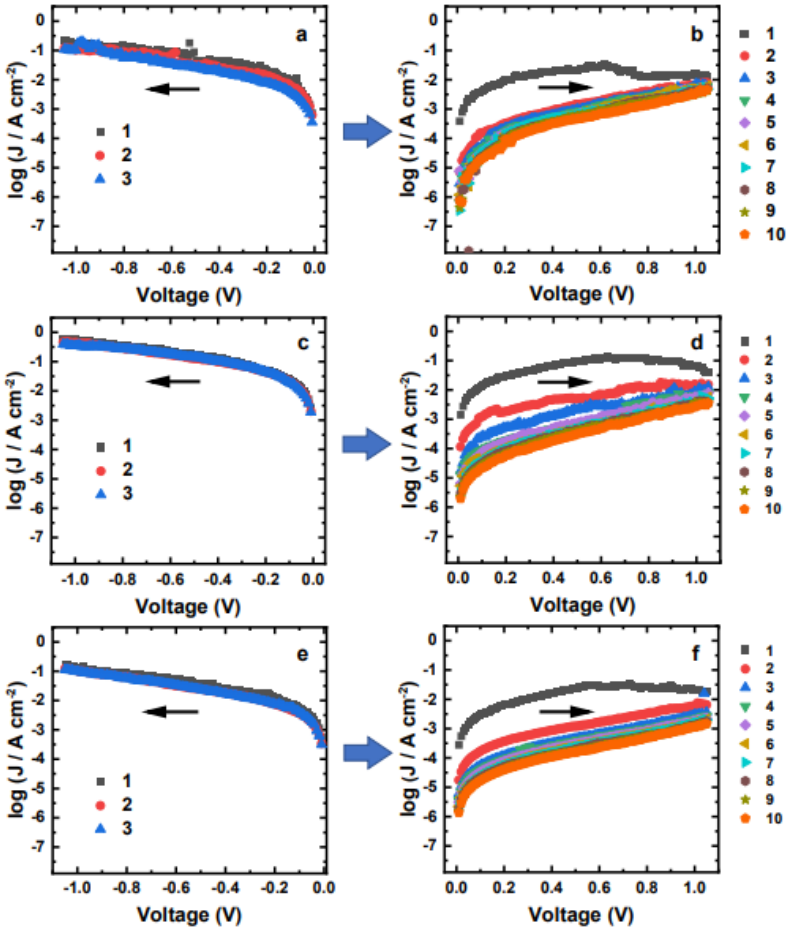

Figure A.24 Evolution of the conductivity switching in the Au^{TS}/Fc-FluT//Ga_2O_3/EGaIn junction at the bias sweeping by the example of three different measurement spots: (a, c, e) Semilogarithmic *J*-V plots corresponding to three successive bias sweeps from -0.01 to -1.05 V followed by (b, d, f) ten successive bias sweeps from +0.01 to +1.05 V for the same spots: The sweep directions are marked by black arrows.

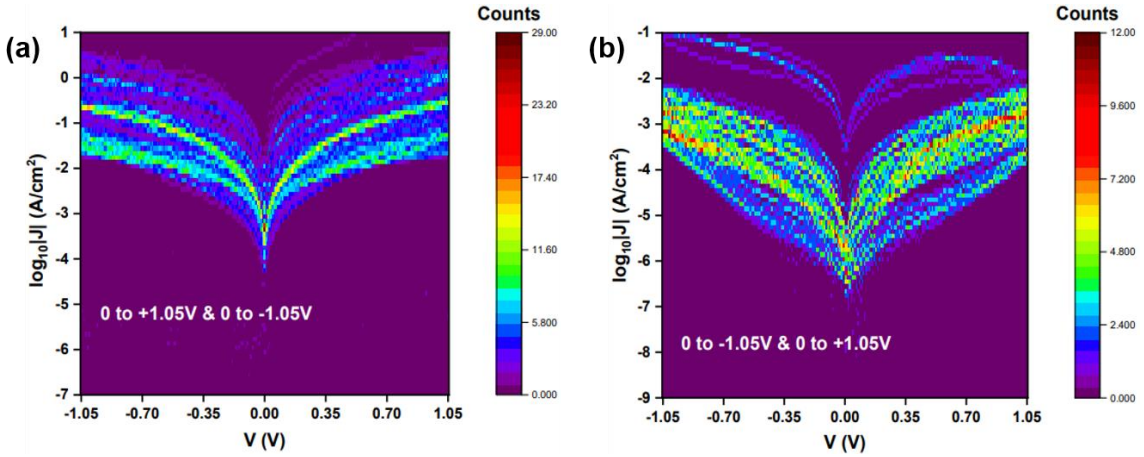

Figure A.25 Electrical characteristics of the Au^{TS}/Fc-FluT//Ga_2O_3/EGaIn junction at the bias sweeping between -1.05 V and +1.05 V, (a) with the with the positive direction of the first sweep (from +0.01 to +1.05 V), and (b) with the with the positive direction of the first sweep (from -0.01 to -1.05 V): Heat map of the semi-log |*J* (V)| curves.

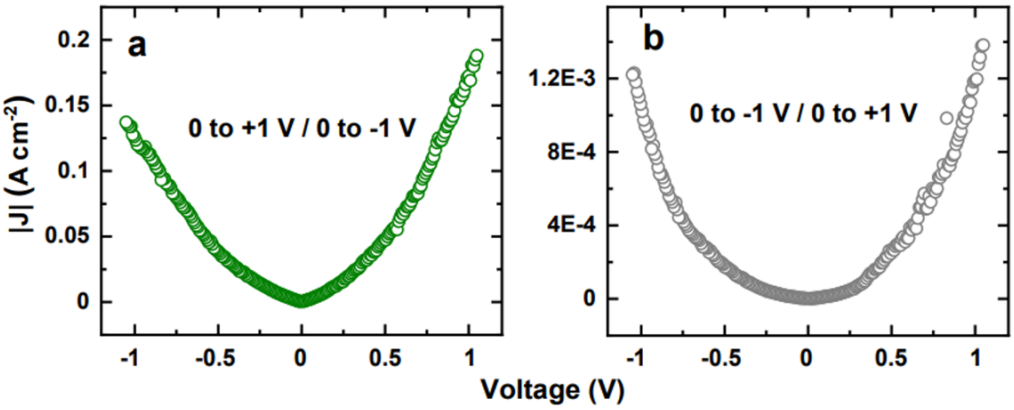

Figure A.26 Electrical characteristics of the Au^{TS}/Fc-FluT//Ga_2O_3/EGaIn junction at the bias sweeping between +1.05 V and -1.05 V (a) and between -1.05 V and +1.05 V (b). The sweeping order is described in the panels: ´to´ means a bias sweep and ´/´ means a step-like bias change to 0 V; finally, the bias was changed to 0 V (step-like) and the sequence was started again. The linear scale for the current density is used. The curves represent the results of a statistical analysis over a large number of sweeps.

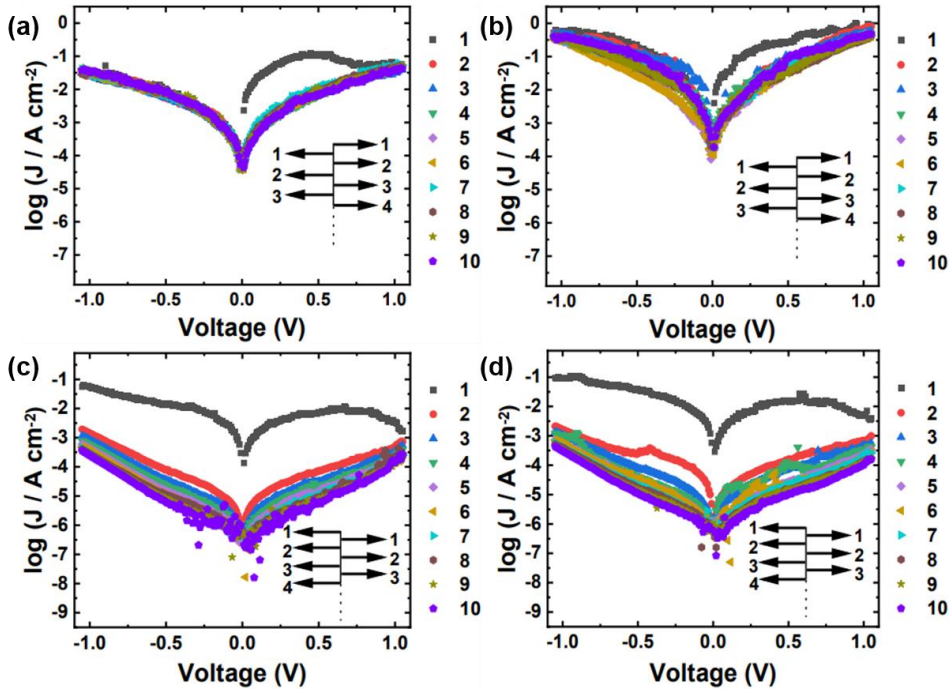

Figure A.27 Evolution of the conductivity switching in the Au^{TS}/Fc-FluT//Ga_2O_3/EGaIn junction at the bias sweeping: Semilogarithmic *J*-V plots corresponding to ten successive bias sweeps for two different measurements spots (junctions), (a) and (b), at the bias sweeping between -1.05 V and +1.05 V, with the positive direction of the first sweep (from +0.01 to +1.05 V); (c) and (d), at the bias sweeping between -1.05 V and +1.05 V, with the negative direction of the first sweep (from -0.01 to -1.05 V). The sweeping sequence is schematically illustrated.

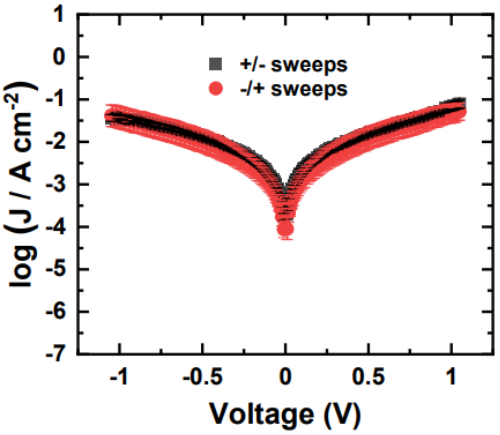

Figure A.28 *J*-V curves for the Au^{TS}/BPT//Ga_2O_3/EGaIn junction measured in the symmetric +/- and -/+ sweeping modes.

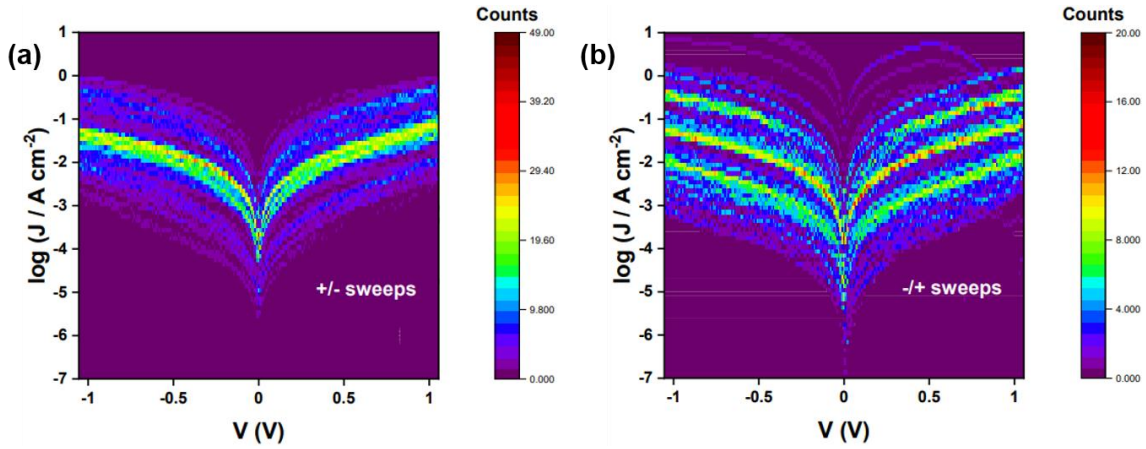

Figure A.29 Electrical characteristics of the Au^{TS}/BPT//Ga_2O_3/EGaIn junction at the bias sweeping between -1.05 V and +1.05 V, (a) with the positive direction of the first sweep (from +0.01 to +1.05 V), and (b) with the negative direction of the first sweep (from -0.01 to -1.05 V): Heat map of the semi-log |*J* (V)| curves.

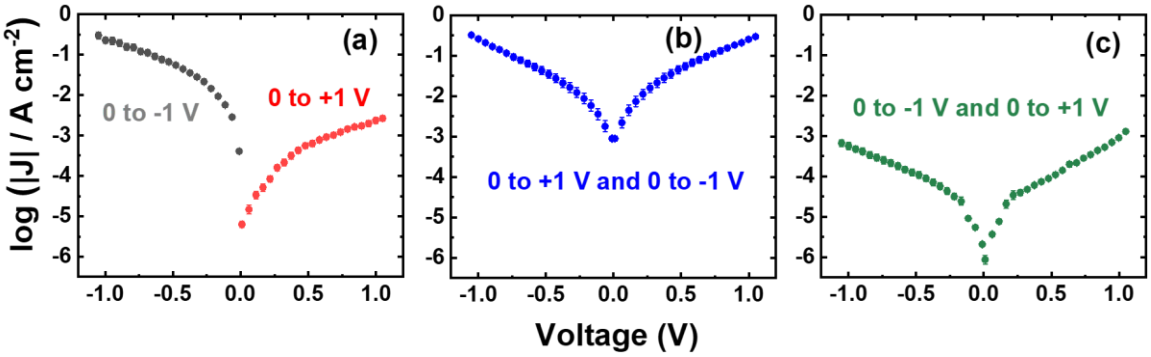

Figure A.30 Averaged semilogarithmic *J*-V plots for the (a) asymmetric (either only positive or only negative bias sweeps) and symmetric (b) +/- and (c) -/+ sweeps. The curves represent the results of a statistical analysis over a large number of sweeps. The sweeping rate was increased by a factor of 5 compared to the data presented in Fig. 4.23a and 4.28a in the main paper.

Table A.6 Overview of the charge transport measurements for the Au^{Ts}/Fc-Trip//Ga_2O_3/EGaIn junctions at the different sweeping modes. The number of successive sweeps for each measurement spot (junction) varied to some extent but never exceeded 20.

Sweeping	Samples	Junctions	Sweeps	Processed	Yield
+	2	9	165	138	83.6%
-	2	11	220	202	91.8%
+/-	4	26	450	408	90.7%
-/+	2	8	160	136	85.0%

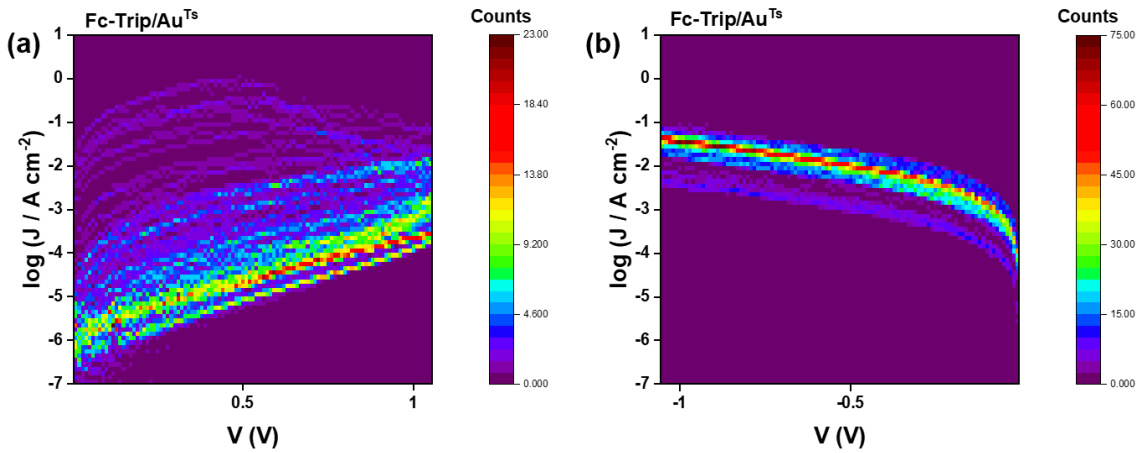

Figure A.31 Electrical characteristics of the Au^{Ts}/Fc-Trip//Ga_2O_3/EGaIn junction at the bias sweeping (a) from +0.01 to +1.05 V and (b) from –0.01 to –1.05 V: Heat map of the semi-$\log_{10}|J\ (V)|$ curves.

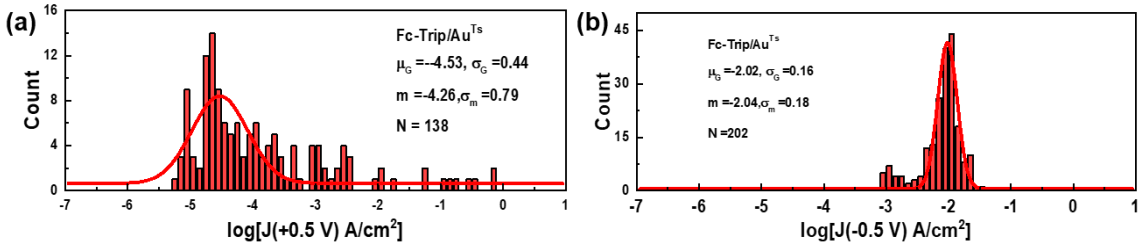

Figure A.32 Electrical characteristics of the Au^{TS}/ Fc-Trip//Ga_2O_3/EGaIn junction at the bias sweeping (a) from +0.01 to +1.05 V: Histograms of the $\log_{10}|J|$ at V = +0.5 V, and (b) from –0.01 to –1.05 V: Histograms of the $\log_{10}|J|$ at V = –0.5 V. The characteristic parameters are given: μ_G – Gaussian average; σ_G – Gaussian standard deviation; m – median average; σ_m - adjusted median absolute deviation; and N – number of scans.

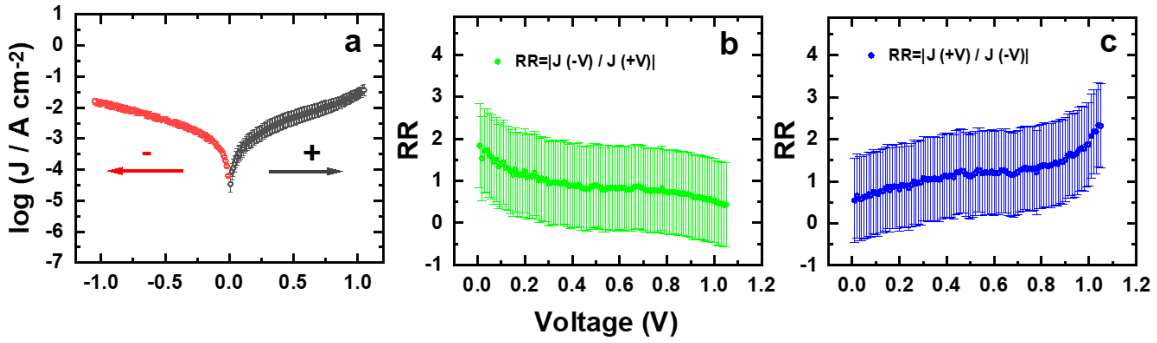

Figure A.33 (a) Averaged semilogarithmic *J-V* plot and (b,c) effective *RR* versus bias voltage for the asymmetric sweeping mode for the Au^{TS}/Trip//Ga_2O_3/EGaIn junction; "/" and "//" indicate interfaces with strong and weak electronic coupling, respectively. Either positive ("+", from +0.01 V to +1.05 V) or negative ("–", from –0.01 V to –1.05 V) bias sweeps were repeatedly applied. Sweep directions are marked by arrows. The curves in (a) represent the results of a statistical analysis over a large number of sweeps.

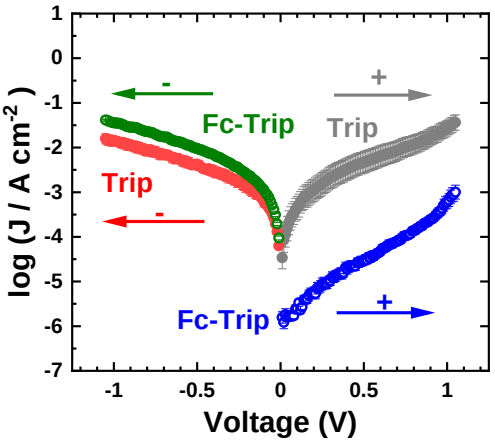

Figure A.34 Comparison of the averaged semilogarithmic *J*-*V* plots acquired in the asymmetric sweeping mode for the Au^{TS}/Fc-Trip//Ga_2O_3/EGaIn and Au^{TS}/Trip//Ga_2O_3/EGaIn junction. The curves and their marks are color-coded.

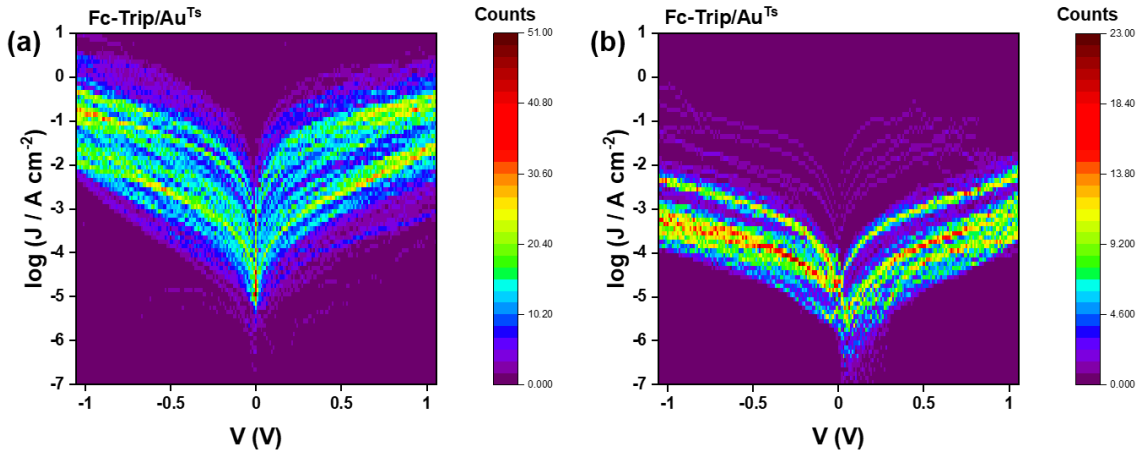

Figure A.35 Electrical characteristics of the Au^{TS}/Fc-Trip//Ga_2O_3/EGaIn junction at the bias sweeping between −1.05 V to +1.05 V, (a) with the positive direction of the first sweep (from +0.01 V to +1.05 V), and (b) with the negative direction of the first sweep (from −0.01 V to −1.05 V): Heat map of the semi-$\log_{10}$ |*J* (V)| curves.

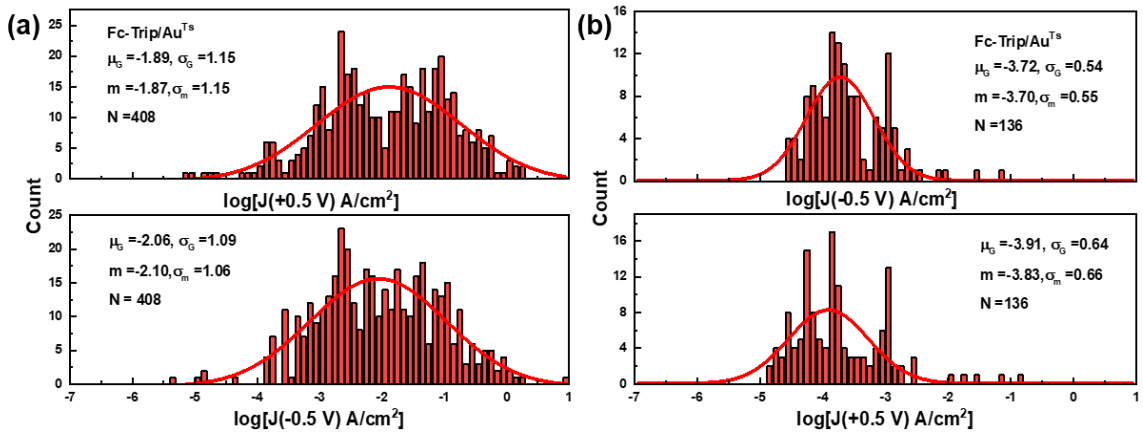

Figure A.36 Electrical characteristics of the Au^{TS}/ Fc-Trip//Ga_2O_3/EGaIn junction at the bias sweeping between –1.05 V to +1.05 V, (a) with the positive direction of the first sweep (from +0.01 V to +1.05 V), and (b) with the negative direction of the first sweep (from –0.01 V to –1.05 V): Histograms of the $\log_{10}|J|$ at V = +0.5 V (top panel) and V = –0.5 V (bottom panel). The characteristic parameters are given: μ_G – Gaussian average; σ_G – Gaussian standard deviation; m – median average; σ_m - adjusted median absolute deviation; and N – number of scans.

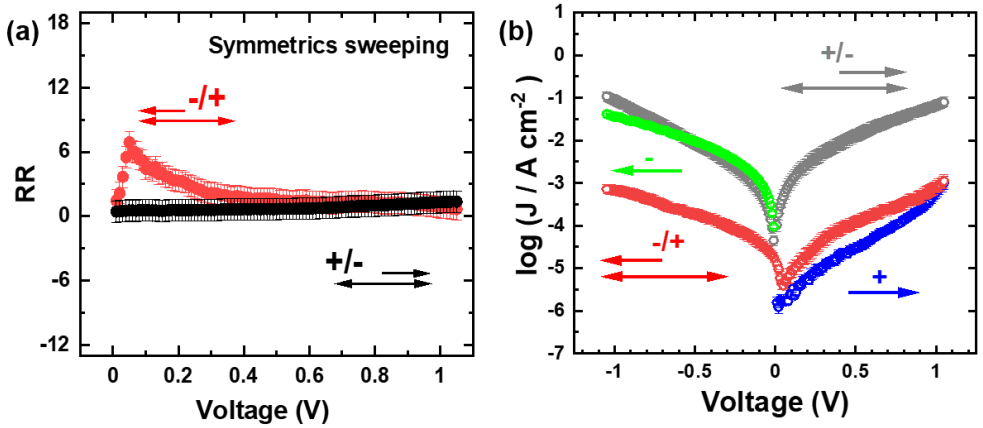

Figure A.37 (a) Effective *RR* versus bias voltage for the symmetric sweeping mode for the Au^{TS}/Fc-Trip//Ga_2O_3/EGaIn junction. The sweeping bias between –1.05 and +1.05 V with the first scan either starting from +0.01 V and going to +1.05 V (+/– mode; black symbols) or starting from –0.01 and going to –1.05 V (–/+ mode; red symbols) were repeatedly applied. Sweep directions are marked by arrows. (b) Comparison of the averaged semilogarithmic *J*-*V* plots acquired in the asymmetric and symmetric sweeping modes for the Au^{TS}/Fc-Trip//Ga_2O_3/EGaIn junction. The curves and their marks are color-coded.

Appendix B. Supplementary Data by the Partners

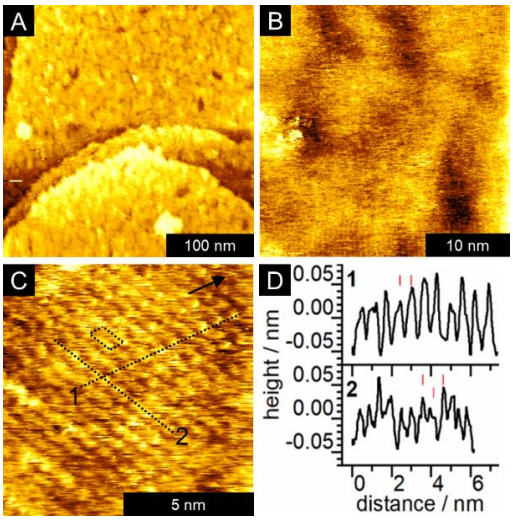

Figure B.1 STM images of SF_5-TPT/Au at different magnifications. Measurement parameters: (a) 1.5 pA, 300 mV, (b) 2.2 pA, 300 mV, and (c) 23.1 pA, 230 mV. In the (a) large-scale image, gold islands remaining from the etching process are well-visible. Image (b) gives an estimate for domain sizes and shapes. In the molecular-resolution image (c), the <110> direction is marked by a black arrow. The dotted box represents the unit cell derived with the help of height profiles 1 and 2 (dotted lines), which are shown in (d). The red marks in (d) highlight the average distances between the molecules, viz., 0.64 ± 0.05 nm for height profile 1 and 0.60 ± 0.05 nm for height profile 2. In the latter case, a third marker is added to highlight the different apparent heights, leading to an elongated (2 × 4) unit cell. The images were measured by Adrian Wiesner from our partner group (Prof. A. Terfort, Frankfurt University).

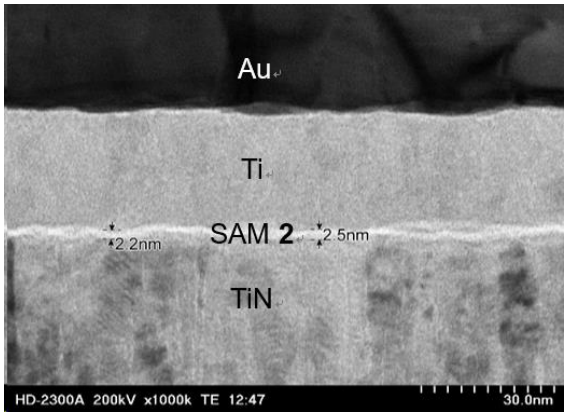

Figure B.2 A cross-sectional STEM image of a junction ($p^{++}Si/SiO_2$ (500 nm)/TiN (50nm)/2/Ti (10 nm)/Au (80 nm)) indicates the presence of a SAM of 2.2-2.5 nm thickness, sandwiched between the TiN bottom and Ti/Au top electrode. The image was measured by our partners in the group of the group of Prof. M. Tornow (Technical University Munich).

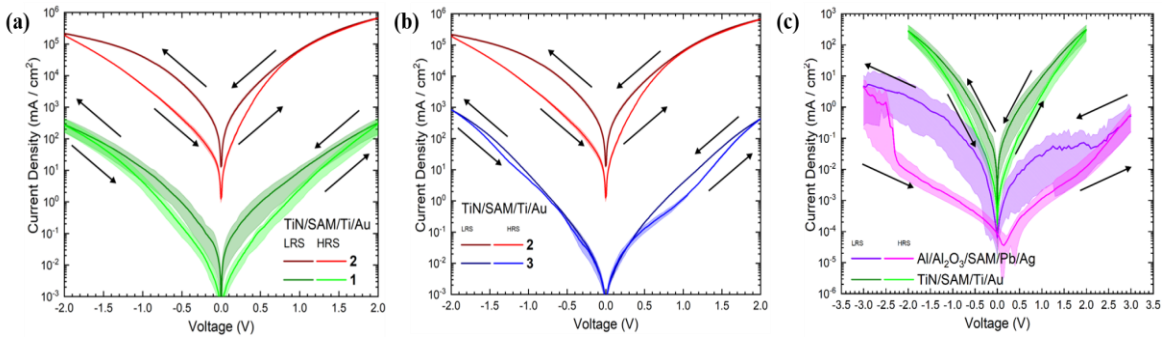

Figure B.3 (a) Current-density vs. voltage characteristics of TiN/SAM/Ti/Au (20 x 20 μm^2) junctions comprising SAMs of 2 in comparison to 1. The *J*-V curves show averages from 3 cycles (sweeps from 0 V to +2.0 V to -2.0 V and back to 0 V, scan direction indicated by arrows) and 3 devices, each. The minimum and maximum current densities at each voltage are shown as envelopes, and the area between is shaded. The shaded areas of 2 are hardly visible, since their *J*-V traces show - in contrast to those of 1 - extremely low variability rendering the envelope nearly invisible. (b) Current density vs. voltage characteristics of TiN/SAM/Ti/Au (20 x 20 μm^2) junctions comprising SAMs of 2 in comparison to its non-fluorinated analogue 3. The *J*-V curves show averages from 3 cycles (sweeps from 0 V to +2.0 V to -2.0 V and back to 0 V, scan direction as indicated by arrows) and 3 devices, each. The minimum and maximum current densities at each voltage are shown as envelopes, and the area between is shaded. The shaded areas of 2 and 3 are hardly visible, since their *J*-V traces show - in contrast to those of 1 - extremely low variability rendering the envelope nearly invisible. (c) *J*-V characteristics of the same compound 1 with an oxidized aluminum bottom electrode (Al/Al_2O_3/1/Pb/Ag; pink curves)[40] and on a TiN bottom electrode (TiN/1/Ti/Au; green curves) in comparison. The scan direction is indicated by arrows. These *J*-V curves were measured by our partners from the group of Prof. M. Tornow (Technical University of Munich).

Lists of Figures, Tables, Abbreviations, etc.

List of Figures

Fig A.10 Rectification ratio of the SF_5-nPT SAMs.

Fig A.11 $I(\theta)/I(\theta_{ref})$ ratios versus θ for the most prominent π^* resonances (1 and 2) of the pyrenyl moieties in the Pyr-C12 SAM.

Fig A.12 $I(\theta)/I(\theta_{ref})$ ratios versus θ for the most prominent π^* resonances (1 and 2) of the pyrenyl moieties in the Pyr-C4S2 SAM.

Fig A.13 Images of the water drops on the surface of C12/Au, Pyr-C12/Au, and Pyr-C4S2/Au.

Fig A.14 Images of the water drops on the surface of C12/Au, Pyr-C12/Au, and Pyr-C4S2/Au.

Fig A.15 Electrical characteristics of the (a) Au^{TS}/Pyr-C12//Ga_2O_3/EGaIn junction and (b) Au^{TS}/Pyr-C4S2//Ga_2O_3/EGaIn junction.

Fig A.16 Electrical characteristics of the Au^{TS}/ Pyr-C12//Ga_2O_3/EGaIn junction: Histograms of the $\log_{10}|J|$ at V = +0.5 V (top panel) and V = –0.5 V (bottom panel).

Fig A.17 Semilogarithmic current-density versus voltage (bias) plots for the Au^{TS}/SAM//Ga_2O_3/EGaIn junctions with Pyr-C12 and C12.

Fig A.18 AFM images of an Au^{TS} substrate.

Fig A.19 Electrical characteristics of the Au^{TS}/Fc-FluT//Ga_2O_3/EGaIn junction at the asymmetric bias sweeping.

Fig A.20 Electrical characteristics of the Au^{TS}/Fc-FluT//Ga_2O_3/EGaIn junction at the bias sweeping from 0 to +1.05 V.

Fig A.21 Electrical characteristics of the Au^{TS}/Fc-FluT//Ga_2O_3/EGaIn junction at the bias sweeping from 0 to -1.05 V.

Fig A.22 Electrical characteristics of the Au^{TS}/Fc-FluT//Ga_2O_3/EGaIn junction at the bias sweeping from either from 0 to -1.05 V or from 0 to +1.05 V.

Fig A.23 Evolution of the conductivity switching in the Au^{TS}/Fc-FluT//Ga_2O_3/EGaIn junction at the bias sweeping: Semilogarithmic *J*-V plots corresponding to (a) ten successive bias sweeps from +0.01 to +1.05 V for a particular measurements spot followed by (b) five successive bias sweeps from -0.01 to -1.05 V for the same spot.

Fig A.24 Evolution of the conductivity switching in the Au^{TS}/Fc-FluT//Ga_2O_3/EGaIn junction at the bias sweeping by the example of three different measurement spots.

Fig A.25 Electrical characteristics of the Au^{TS}/Fc-FluT//Ga_2O_3/EGaIn junction at the bias sweeping between -1.05 V and +1.05 V.

Fig A.26 Electrical characteristics of the Au^{TS}/Fc-FluT//Ga_2O_3/EGaIn junction at the bias sweeping between +1.05 V and -1.05 V (a) and between -1.05 V and +1.05 V (b).

Fig A.27 Evolution of the conductivity switching in the Au^{TS}/Fc-FluT//Ga_2O_3/EGaIn junction at the bias sweeping: Semilogarithmic *J*-V plots corresponding to ten successive bias sweeps for two different measurements spots (junctions), (a) and (b), at the bias sweeping between -1.05 V and +1.05 V, with the positive direction of the first sweep (from +0.01 to +1.05 V); (c) and (d), at the bias

List of Tables

List of Abbreviations

SAMs	self-assembled monolayers
WF	work function
J	current density
WCA	water contact angle
CS	conductivity states
HCS	high conductivity states
LCS	low conductivity states
RR	rectification ratio
J-V	current-voltage
STM	electrochemical scanning tunneling microscopy
HOMO	highest occupied molecular spectroscopy
LUMO	lowest occupied molecular spectroscopy
NEXAFS	near-edge X-ray absorption fine structure spectroscopy
CNT	carbon nanotubes
XPS	X-ray photoelectron spectroscopy
KP	Kelvin probe technique
LB	Langmuir-Blodgett technique
KE	kinetic energy
HRXPS	high resolution X-ray photoelectron spectroscopy
TDM	transition dipole moment

KPFM	Kelvin probe force microscopy
CPD	contact potential difference
EGaIn	Eutectic Gallium-Indium alloy
μ_G	gaussian mean
σ_G	standard deviation
m	median
σ_m	absolute deviation
TVS	transition voltage spectroscopy
FN	Fowler-Nordheim
V_T	transition voltage
θ	static contact angle
θ_A	advancing contact angle
θ_R	receding contact angle
BE	binding energy
PE	photon energy
Au^{Ts}	template-stripped Au substrates
UV	ultraviolet
FWHM	half width at half maximum
UMOs	unoccupied molecular orbitals
VL	vacuum level
OMOs	Occupied molecular orbitals
TEY	total electron yield
AEY	Auger electron yield
PEY	partial electron yield
UHV	ultra-high vacuum
CI	confidence interval
SECO	secondary electron cutoff
UPS	ultraviolet photoelectron spectroscopy
AFM	atomic force microscopy
RMS	root mean square
LRS	low resistive state
HRS	high resistive state
EA	activation energy barrier
HRS	high resistive state
LRS	low resistive state
FR	Fermi-resonance
UPS	ultraviolet photoelectron spectroscopy
IRRAS	infrared reflection absorption spectroscopy
MCT	mercury cadmium telluride
FTIR	fourier transform infrared

List of Chemicals

H-PT	Thiophenol
F-PT	4-Fluorothiophenol
CH_3-PT	4-Methylbenzenethiol
CF_3-PT	4-(Trifluoromethyl)thiophenol
H-BPT	4-Phenylthiophenol
F-BPT	4-(4-Fluorophenyl)thiophenol
CH_3-BPT	4-(4-methylphenyl)benzenethiol
CF_3-BPT	4-(Trifluoromethyl))-1,1'-Biphenyldithiol

H-TPT	4-Terphenylthiol
F-TPT	4-(Fluorine)-1,1'-Terphenythiol
CH_3-TPT	4"-Methyl-1,1':4',1"-terbenzene-4-thiol
CF_3-TPT	4-(Trifluoromethyl))-1,1'-Terphenylthiol
SF_5-PT	1,2-Bis(4-(pentafluorosulfanyl)phenyl)disulfane
SF_5-BPT	4'-(Pentafluorosulfanyl)-[1,1'-biphenyl]-4-thiol
SF_5-TPT	4"-(Pentafluorosulfanyl)-[1,1':4',1"-terphenyl]-4-thiol
Fc-FluT	ferrocenyl-substituted fluorene thiols
Fc	ferrocene
Fc-Trip	Fc-substituted, triptycene-based tripodes
Trip	tripodal triptycene
Pyr	Pyrene
Pyr-C12	12-(Pyren-1-yl)dodecane-1-thiol
Pyr-C4S2	2-{[2-(Pyren-1-ylthio)ethyl]thio}ethane-1-thiol
C16	hexadecanethiol
C12	dodecanethiol
THF	Tetrahydrofuran
DMF	dimethylformamide

List of Symbols

β	tunneling decay coefficient	$Å^{-1}$
J	current density	A cm^{-2}
d	thickness	Å
λ	attenuation length	Å
ρ	packing density	molecule cm^{-2}
θ	incidence angle	°
Φ	work function	eV
h	Planck's constant	4.14×10^{-15} eV/Hz
ν	photon frequency	Hz
I	intensity	arbitrary units
K	a constant depending on the equipment specification	
E_k	kinetic energy	eV
Ψ_i	initial state	
Ψ_f	final state	
e	unit electric field vector	V/m
$\rho_f(E)$	final density of states	
E	electric field vector	
σ_x	photoabsorption cross section	
P	degree of polarization of the incident X-ray light	
α	angle between the electric field vector $\boldsymbol{E}$ and the TDM direction	°
φ	azimuthal angle	°
q	elementary charge	C
V_c	external potential	V
E_F	Fermi energy	eV
E_{HOMO}	HOMO energy	eV
γ	interfacial tension	
θ	contact angle	°
α	average tilt angles of the π* orbitals	°
β	molecular tilt angle with respect to the surface normal	°

γ	twist angle	$^{\circ}$
ρ_{SAM}	the packing density of the SAMs	g cm^{-3}
ε_{SAM}	dielectric constant	
μ	molecular dipole moment	
$\boldsymbol{E}$	electric field vector of the synchrotron light	

References

[1] Love, J. C.; Estroff, L. A.; Kriebel, J. K.; Nuzzo, R. G.; Whitesides, G. M. Self-assembled monolayers of thiolates on metals as a form of nanotechnology. Chem. Rev. 2005, 105, 1103–1170.

[2] Kind, M.; Wöll, C. Organic surfaces exposed by self-assembled organothiol monolayers: Preparation, characterization, and application. Prog. Surf. Sci. 2009, 84, 230–278.

[3] Abbott, N. L.; Folkers, J. P.; Whitesides, G. M. Manipulation of the wettability of surfaces on the 0.1- to 1-micrometer scale through micromachining and molecular self-assembly. Science 1992, 257, 1380–1382.

[4] Lee, H. J.; Jamison, A. C.; Lee, T. R. Surface dipoles: A growing body of evidence supports their impact and importance. Acc. Chem. Res. 2015, 48, 3007–3015.

[5] Ulman, A. Formation and structure of self-assembled monolayers. Chem. Rev. 1996, 96, 1533–1554.

[6] Ma, H.; Yip, H. L.; Huang, F.; Jen, A. K. Y. Interface Engineering for Organic Electronics. Adv. Funct. Mater.2010,20,1371–1388.

[7] Wang, D.; Fracasso, D.; Nurbawono, A.; Annadata, H. V.; Sangeeth, C. S. S.; Yuan, L.; Nijhuis, C. A. Tuning the Tunneling Rate and Dielectric Response of SAM-Based Junctions via a Single Polarizable Atom. Adv. Mater. 2015, 27, 6689–6695.

[8] Kong, G. D.; Kim, M.; Jang, H. J.; Liao, K. C.; Yoon, H. J. Influence of halogen substitutions on rates of charge tunneling across SAM-based large-area junctions. Phys. Chem. Chem. Phys., 2015, 17, 13804-13807.

[9] Chen, X.; Annadata, H. V.; Kretz, B.; Zharnikov, M.; Chi, X.; Yu, X.; Egger, D. A.; Nijihuis, C. A. Interplay of Collective Electrostatic Effects and Level Alignment Dictates the Tunneling Rates across Halogenated Aromatic Monolayer Junctions. J. Phys. Chem. Lett. 2019, 10, 14, 4142–4147.

[10] Metzger, R. M. Unimolecular electronics. Chem. Rev. 2015, 115, 5056–5115.

[11] Vilan, A.; Aswal, D.; Cahen, D. Large-Area, Ensemble Molecular Electronics: Motivation and Challenges. Chem. Rev. 2017, 117, 5, 4248–4286.

[12] Weiss, E. A.; Chiechi, R. C.; Kaufman, G. K.; Kriebel, J. K.; Li, Z.; Duati, M.; Rampi, M. A.; Whitesides, G. M. Influence of Defects on the Electrical Characteristics of Mercury-Drop Junctions: Self-Assembled Monolayers of n-Alkanethiolates on Rough and Smooth Silver. J. Am. Chem. Soc. 2007, 129, 4336–4349.

[13] Bowers, C. M.; Liao, K. C.; Yoon, H. J.; Rappoport, D.; Baghbanzadeh, M.; Simeone, F. C.; Whitesides, G. M. Introducing ionic and/or hydrogen bonds into the SAM//Ga_2O_3 top-interface of $Ag^{TS}/S(CH_2)_nT//Ga_2O_3$/EGaIn junctions. Nano Lett. 2014, 14, 3521–3526.

[14] Miozzo, L.; Yassar, A.; Horowitz, G. Surface engineering for high performance organic electronic devices: the chemical approach. J. Mater. Chem., 2010, 20, 2513-2538.

[15] Liu, Y.; Katzbach, S.; Asyuda, A.; Das, S.; Terfort, A.; Zharnikov, M. Effect of substitution on the charge transport properties of oligophenylenethiolate self-assembled monolayers. Phys. Chem. Chem. Phys., 2022, 24, 27693-27704.

[16] Yoon, H. J.; Bowers, C. M.; Baghbanzadeh, M.; Whitesides, G. M. The Rate of Charge Tunneling Is Insensitive to Polar Terminal Groups in Self-Assembled Monolayers in $Ag^{TS}S(CH_2)_nM(CH_2)_mT//Ga_2O_3$/EGaIn Junctions. J. Am. Chem. Soc. 2014, 136, 1, 16–19.

[17] Wu, K. Y.; Yu, S. Y.; Tao, Y. T. Continuous Modulation of Electrode Work Function with Mixed Self-Assembled Monolayers and Its Effect in Charge Injection. Langmuir 2009, 25, 11, 6232–6238.

[18] Kim, J.; Rim, Y. S.; Liu, Y. S.; Serino, A. C.; Thomas, J. C.; Chen, H. J.; Yang, Y.; Weiss, P. S. Interface control in organic electronics using mixed monolayers of carboranethiol isomers. Nano Lett. 2014, 14, 2946–2951.

[19] Abu-Husein, T.; Schuster, S.; Egger, D. A.; Kind, M.; Santowski, T.; Wiesner, A.; Chiechi, R.; Zojer, E.; Terfort, A.; Zharnikov, M. The effects of embedded dipoles in aromatic self-assembled monolayers. Adv. Funct. Mater. 2015, 25, 3943–3957.

[20] Coll, M.; Gergel-Hackett, N.; Richter, C. A.; Hacker, C. A. Structural and Electrical Properties of Flip Chip Laminated Metal–Molecule–Silicon Structures Varying Molecular Backbone and Atomic Tether. J. Phys. Chem. C 2011, 115, 49, 24353–24365
[21] Koch, N. Energy levels at interfaces between metals and conjugated organic molecules. J. Phys. :Condens. Matter 2008, 20, 184008.
[22] Zhao, Y.; Liu, W.; Zhao, J.; Wang, Y.; Zheng, J.; Liu, J.; Hong, W.; Tian, Z. The fabrication, characterization and functionalization in molecular electronics. Int. J. Extrem. Manuf. 2022, 4, 022003.
[23] Figueira-Duarte, T. M.; Duarte, F.; Müllen, K. Pyrene-Based Materials for Organic Electronics. Chem. Rev. 2011, 111, 7260−7314.
[24] Mateo-Alonso, A. Pyrene-Fused Pyrazaacenes: From Small Molecules to Nanoribbons. Chem. Soc. Rev. 2014, 43, 6311−6324.
[25] Zöphel, L.; Enkelmann, V.; Müllen, K. Tuning the HOMO-LUMO Gap of Pyrene Effectively via Donor-Acceptor Substitution: Positions 4,5 Versus 9,10. Org. Lett. 2013, 15, 804−807.
[26] Russew, M. M.; Hecht, S. Photoswitches: From Molecules to Materials. Adv. Mater.2010, 22, 3348–3360.
[27] Cho, S. J.; Kong, G. D.; Park, S.; Park, J.; Byeon, S. E.; Kim, T.; Yoon, H. J. Molecularly Controlled Stark Effect Induces Significant Rectification in Polycyclic-Aromatic-Hydrocarbon-Terminated nAlkanethiolates. Nano Lett. 2019, 19 (1), 545−553.
[28] Kang, H.; Cho, S. J.; Kong, G. D.; Yoon, H. J. Li-Ion Intercalation, Rectification, and Solid Electrolyte Interphase in Molecular Tunnel Junctions. Nano Lett. 2022, 22, 4956−4962.
[29] Kang, H.; Cho, S. J.; Kong, G. D.; Park, S.; Yoon, H. J. Effect of Bottom Electrode on Rectification Performance in Pyrene-Terminated n-alkanethiolate. Surf. Interfaces 2022, 34, 10240.
[30] Weibel, N.; Grunder, S.; Mayor, M. Functional molecules in electronic circuits. Org. Biomol. Chem. 2007, 5, 2343-2353.
[31] P. Pujari, S.; Scheres, L.; Marcelis, A. T. M.; Zuihof, H. Covalent Surface Modification of Oxide Surfaces. Angew. Chem. Int. Ed. 2014,53, 6322 – 6356.
[32] Kang, H.; Noh, J. Influence of Thiol Molecular Backbone Structure on the Formation and Reductive Desorption of Self-Assembled Aromatic and Alicyclic Thiol Monolayers on Au(111) Surface. J. Korean Chem. Soc. 2013, 24, 5, 1383-1387.
[33] Schreiber, F. Structure and growth of self-assembling monolayers. Prog. Surf. Sci. 2000, 65, 151-256.
[34] Nijhuis, C. A.; Reus, W. F.; Barber, J. R.; Dickey, M. D.; Whitesides, G. M. Charge Transport and Rectification in Arrays of SAM-Based Tunneling Junctions. Nano Lett. 2010, 10, 3611−3619.
[35] Yuan, L.; Thompson, D.; Cao, L.; Nerngchangnong, N.; Nijhuis, C. A. One Carbon Matters: The Origin and Reversal of Odd−Even Effects in Molecular Diodes with Self-Assembled Monolayers of Ferrocenyl-Alkanethiolates. J. Phys. Chem. C 2015, 119, 17910−17919.
[36] Chen, X.; Roemer, M.; Yuan, L.; Du, W.; Thompson, D.; del Barco, E.; Nijhuis, C. A. Molecular Diodes with Rectification Ratios Exceeding 10^5 Driven by Electrostatic Interactions. Nat. Nanotechnol. 2017, 12, 797−803.
[37] Asyuda, A.; Das, S.; Lang, H.; Zojer, E.; Zharnikov, M. BiasTriggered Conductivity Switching and High Effective Rectification in Metallocene-Based Molecular Junctions. Adv. Electron. Mater. 2022, 8, 2200296.
[38] Batson, P. E. Carbon 1s Near-Edge-Absorption Fine Structure in Graphite. Phys. Rev. B 1993, 48, 2608–2610.
[39] Dlugosch, J. M.; Seim, H.; Bora, A.; Kamiyama, T.; Lieberman, I.; May, F.; Müller-Plathe, F.; Nefedov, A.; Prasad, S.; Resch, S.; Saller, K.; Seim, C.; Speckbacher, M.; Voges, F.; Tornow, M.; Kirsch, P. Conductance Switching in Liquid Crystal-Inspired Self-Assembled Monolayer Junctions. ACS Appl. Mater. Interfaces 2022, 14, 27, 31044–31053.
[40] Zhang, Y.; Liu, T.; Meng, B.; Li, X.; Liang, G.; Hu, X.; Wang, W. J. Broadband high photoresponse from pure monolayer graphene photodetector. Nat. Commun. 2013, 4, 1811.
[41] Bhairamadgi, N. S.; Pujari, S. P.; Trovela, F. G.; Debrassi, A.; Khamis, A. A.; Alonso, J. M.; Al Zahrani, A.A.; Wennekes, T.; Al-Turaif, H. A.; Rijin, C.; Alhamed, Y. A.; Zuilhof, H. Hydrolytic and

Thermal Stability of Organic Monolayers on Various Inorganic Substrates. Langmuir 2014, 30, 20, 5829–5839.
[42] Jadhav, S. Self-assembled monolayers (SAMs) of carboxylic acids: an overview. Cent. Eur. J. Chem. 2011, 9, 3, 369-378.
[43] Newton, L.; Slater, T.; Clark, N.; Vijayaraghavan, A. Self assembled monolayers (SAMs) on metallic surfaces (gold and graphene) for electronic applications. J. Mater. Chem. C, 2013, 1, 376-393.
[44] Ossowski, J.; Rysz, J.; Terfort, A.; Cyganik, P. Relative Stability of Thiolate and Selenolate SAMs on Ag(111) Substrate Studied by Static SIMS. Oscillation in Stability of Consecutive Chemical Bonds. J. Phys. Chem. C 2017, 121, 1, 459–470.
[45] Zhang, J. L.; Zhong, J. Q.; Lin, J. D.; Hu, W. P.; Wu, K.; Xu, G. Q.; Wee, A. T. S.; Chen, W. Towards single molecule switches. Chem. Soc. Rev. 2015, 44, 2998-3022.
[46] Kong, G. D.; Kim, M.; Jang, H.; Liao, K. C.; Yoon, H. J. Influence of halogen substitutions on rates of charge tunneling across SAM-based large-area junctions. Phys. Chem. Chem. Phys., 2015,17, 13804-13807.
[47] Frasconi, M.; Mazzei, F.; Ferri, T. Protein immobilization at gold–thiol surfaces and potential for biosensing. Anal. Bioanal. Chem. 2010, 398, 1545-1564.
[48] Zojer, E.; Terfort, A.; Zharnikov, M. Concept of embedded dipoles as versatile tool for surface engineering. Acc. Chem. Res. 2022, 55, 1857–1867.
[49] Telegdi, J. Formation of Self-Assembled Anticorrosion Films on Different Metals. Materials. 2020, 13, 22, 5089.
[50] Greczynski, G.; Hultman, L. A step-by-step guide to perform x-ray photoelectron spectroscopy. J. Appl. Phys. 2022, 132, 1, 011101.
[51] 'X-ray photoelectron spectroscopy', Wikipedia, The Free Encyclopedia, 2023, 2,8. https://en.wikipedia.org/w/index.php?title=X-ray_photoelectron_spectroscopy&oldid=1138105011
[52] Pintori, G.; Cattaruzza, E. XPS/ESCA on glass surfaces: A useful tool for ancient and modern materials. Opt. Mater.: X. 2022, 13, 100108.
[53] Oliverio, M.; Perotto, S.; Messina, G. C.; Lovato, L.; De Angelis, F. Chemical Functionalization of Plasmonic Surface Biosensors: A Tutorial Review on Issues, Strategies, and Costs. ACS Appl. Mater. Interfaces 2017, 9, 35, 29394–29411.
[54] A. Stevie, F.; L. Donley, C. Introduction to x-ray photoelectron spectroscopy. J. Vac. Sci. Technol. 2020, 38, 063204.
[55] F. Ebel, M.; Svagera, R.; Ashury, R.; Ebel, H.; C. Zalm, P.; Marel, C. V. Experimental evidence for secondary excitation in X-ray photoelectron spectrometry. J. Electron. Spectros. Relat. Phenomena. 2003, 131-132, 145-151.
[56] Greczynski, G.; Hultman, L. X-ray photoelectron spectroscopy: Towards reliable binding energy referencing. Prog. Mater. Sci. 2020, 107, 100591.
[57] Watcharinyanon, S.; Puglia, C.; Göthelid, E.; Bäckvall, J. E.; Moons, E.; Johansson, L. S. O. Molecular orientation of thiol-derivatized tetraphenylporphyrin on gold studied by XPS and NEXAFS. Surf. Sci. 2009, 603, 7, 1026-1033.
[58] Lamont, C. L. A.; Wilkes, J. Attenuation Length of Electrons in Self-Assembled Monolayers of n-Alkanethiols on Gold. Langmuir, 1999, 15, 2037-2042.
[59] "Synchrotron radiation," Wikipedia, The Free Encyclopedia, 2023, 8. https://en.wikipedia.org/w/index.php?title=Synchrotron_radiation&oldid=1172640391.
[60] "Synchrotron." Wikipedia, 2023, 6, 12. https://simple.wikipedia.org/wiki/Synchrotron.
[61] Weinhardt, L.; Hauschild, D.; Heske, C. Surface and Interface Properties in Thin-Film Solar Cells: Using Soft X-rays and Electrons to Unravel the Electronic and Chemical Structure. Adv. Mater. 2019, 31, 1806660.
[62] Kalha, C.; K Fernando, N.; Bhatt, P.; Johansson, F. O. L.; Lindblad, A.; Rensmo, H.; Medina, L. Z.; Lindblad, R.; Siol, S.; Jeurgens, L. P. H.; Cancellieri, C.; Rossnagel, K.; Medjanik, K.; Schönhense, G.; Simon, M.; Gray, A. X.; Nemšák, S.; Lömker, P.; Schlueter, C.; Regoutz, A. Hard x-ray photoelectron spectroscopy: a snapshot of the state-of-the-art in 2020. J. Phys.: Condens. Matter. 2021, 33, 233001.

[63] "X-ray absorption near edge structure," Wikipedia, The Free Encyclopedia, 2023, 3. https://en.wikipedia.org/w/index.php?title=X-ray_absorption_near_edge_structure&oldid=1145433327.
[64] Stöhr, J. NEXAFS Spectroscopy; Springer-Verlag: Berlin, 1992.
[65] Zharnikov, M. Near-edge X-ray absorption fine structure spectroscopy in studies of self-assembled monomolecular films. J. Electron Spectrosc. Relat. Phenom. 2023, 264, 147322.
[66] Zharnikov, M.; Frey, S.; Heister, K.; Grunze, M. An extension of the mean free path approach to X-ray absorption spectroscopy. J. Electron Spectrosc. Relat. Phenom. 2002, 124, 1, 15-24.
[67] Thome, J.; Himmelhaus, M.; Zharnikov, M.; Grunze, M. Increased lateral density in alkanethiolate films on gold by mercury adsorption. Langmuir. 1998, 14, 7435-7449.
[68] Frey, S.; Shaporenko, A.; Zharnikov, M.; Harder, P.; Allara, D. L. Self-assembled monolayers of nitrile-functionalized alkanethiols on gold and silver substrates. J. Phys. Chem. B. 2003, 107, 31, 7716-7725.
[69] Bastidas, D. M.; Criado, M.; Bastidas, J. M. 5 - Methods for analysing nanocoatings and ultra-thin films. Nanocoatings and Ultra-Thin Films. 2011, 131-156.
[70] Luo, Y.; Tang, Y.; Chung, T. F.; Tai, C. L.; Chen, C. Y.; Yang, J. R.; Li, D. Y. Electron work function: an indicative parameter towards a novel material design methodology. Sci. Rep. 2021, 11, 11565.
[71] Melitz, W.; Shen, J.; Kummel, A. C.; Lee, S. Kelvin probe force microscopy and its application. Surf. Sci. Rep. 2011, 66, 1-27.
[72] " Kelvin probe," Wikipedia, The Free Encyclopedia, 2022, 8. https://de.wikipedia.org/wiki/Kelvin-Sonde
[73] "Kelvin probe force microscope." Wikipedia, 2011, 2, 9. https://en.m.wikipedia.org/wiki/Kelvin_probe_force_microscope.
[74] Bruker Nano Surfaces and Metrology. High-Resolution, Quantitative Work Function Measurements with PeakForce Kelvin Probe Microscopy (KPFM). 2016. https://www.azonano.com/article.aspx?ArticleID=4203.
[75] Palermo, V.; Palma, M.; Samori, P. Electronic Characterization of Organic Thin Films by Kelvin Probe Force Microscopy. Adv. Mater. 2006, 18, 2, 145-164.
[76] Cabarcos, O. M.; Schuster, S.; Hehn, I.; Zhang, P. P.; Maitani, M. M.; Sullivan, N.; Giguère, J. B.; Morin, J. F.; Weiss, P. S.; Zojer, E.; Zharnikov, M. ; Allara, D. L. Effects of Embedded Dipole Layers on Electrostatic Properties of Alkanethiolate Self-Assembled Monolayers. J. Phys. Chem. C. 2017, 121, 29, 15815–15830.
[77] Fan, F. R. F.; Yang, J.; Cai, L.; Price, D. W.; Jr.; Dirk, S. M.; Kosynkin, D. V.; Yao, Y.; Rawlett, A. M.; Tour, J. M.; Bard, A. J. Charge Transport through Self-Assembled Monolayers of Compounds of Interest in Molecular Electronics. J. Am. Chem. Soc. 2002, 124, 19, 5550–5560.
[78] Simeone, F. C.; Yoon, H. J.; Thuo, M. M.; Barber, J. R.; Smith, B.; Whitesides, G. M. Defining the Value of Injection Current and Effective Electrical Contact Area for EGaIn-Based Molecular Tunneling Junctions. J. Am. Chem. Soc. 2013, 135, 48, 18131–18144.
[79] Liu, Y.; Qiu, X.; Soni, S.; Chiechi, R. C. Charge transport through molecular ensembles: Recent progress in molecular electronics. Chem. Phys. Rev. 2021, 2, 021303.
[80] Ma, J.; Krisnadi, F.; Vong, M. H.; Kong, M.; Awartani, O. M.; Dickey, M. D. Shaping a Soft Future: Patterning Liquid Metals. Adv. Mater. 2022, 35, 19, 2205196.
[81] Chiechi, R. C.; Weiss, E. A.; Dickey, M. D.; Whitesides, G. M. Eutectic Gallium–Indium (EGaIn): A Moldable Liquid Metal for Electrical Characterization of Self-Assembled Monolayers. Angew. Chem. Int. Ed. 2007, 47, 1, 142-144.
[82] Belding, L.; Root, S. E.; Li, Y.; Park, J.; Baghbanzadeh, M.; Rojas, E.; Pieters, P. F.; Yoon, H. J.; Whitesides, G. M. Conformation, and Charge Tunneling through Molecules in SAMs. J. Am. Chem. Soc. 2021, 143, 9, 3481–3493.
[83] Olkhovsky, V. S.; Recami, E.; Zaichenko, A. K. Resonant and non-resonant Tunneling through a double barrier. EPL. 2005, 70, 712-718.
[84] Reus, W. F.; Nijihuis, C. A.; Barber, J. R.; Thuo, M. M.; Tricard, S.; Whitesides, G. M. Statistical Tools for Analyzing Measurements of Charge Transport. J. Phys. Chem. C. 2012, 116, 11, 6714–6733.

[85] Choi, S. H.; Risko, C.; Delgado, M. C. R.; Kim, B.; Brédas, J. L.; Frisbie, C. D. Transition from Tunneling to Hopping Transport in Long, Conjugated Oligo-imine Wires Connected to Metals. J. Am. Chem. Soc. 2010, 132, 12, 4358–4368.
[86] Afanas'ev, V. V. 5 - Injection Spectroscopy of Thin Layers of Solids. Internal Photoemission Spectroscopy (Second Edition). 2014, 161-212.
[87] Blom, P. W. M.; Jong, M. J. M.; Breedijk, S. Temperature dependent electron-hole recombination in polymer light-emitting diodes. Appl. Phys. Lett. 1997, 71, 930-932.
[88] Pipinys, P.; Kiveris, A. Variable range hopping and/or phonon-assisted tunneling mechanism of electronic transport in polymers and carbon nanotubes. Cent. Eur. J. Phys. 2012, 10, 271-281.
[89] Aswal, D. K.; Lenfant, S.; Guerin, D.; Yakhmi, J. V.; Vuillaume, D. Self assembled monolayers on silicon for molecular electronics. Anal. Chim. Acta. 2006, 568, 1-2, 84-108.
[90] Sotthewes, K.; Hellenthal, C.; Kumar, A.; Zandvliet, H. J. W. Transition Voltage Spectroscopy of Scanning Tunneling Microscopy Vacuum Junctions. RSC Adv. 2014, 4, 32438–32442.
[91] Vilan, A.; Cahen, D.; Kraisler, E. Rethinking Transition Voltage Spectroscopy within a Generic Taylor Expansion View. ACS Nano. 2013, 7, 695–706.
[92] Beebe, J. M.; Kim, B.; Frisbie, C. D.; Kushmerick, J. G. Measuring Relative Barrier Heights in Molecular Electronic Junctions with Transition Voltage Spectroscopy. ACS Nano. 2008, 2, 827-832.
[93] Huisman, E. H.; Guédon, C. M.; Wees, B. J.; Molen, S. J. Interpretation of Transition Voltage Spectroscopy. Nano Lett. 2009, 9, 3909-3913.
[94] Chen, X.; Nijihuis, C. A. The Unusual Dielectric Response of Large Area Molecular Tunnel Junctions Probed with Impedance Spectroscopy. Adv. Electron. Mater. 2021, 8, 2, 2100495.
[95] Özden, S.; Avci, N.; Pakma, O.; Kariper, i. A. Influence of illumination intensity on the electrical properties of Al/NOA65/p-Si/Al heterojunction MPS device. J. Mater. Sci. Mater. Electron. 2022, 33, 12796-12807.
[96] Ye, E. J.; Sui, W. Q.; Zhao, X. Topological asymmetry induced electronic transport in three terminal graphene nanoribbon structure. Appl. Phys. Lett. 2012, 100, 193303.
[97] Souto, M.; Yuan, L.; Morales, D. C.; Jiang, L.; Ratera, I.; Nijihuis, C. A.; Veciana, J. Tuning the Rectification Ratio by Changing the Electronic Nature (Open-Shell and Closed-Shell) in Donor−Acceptor Self-Assembled Monolayers. J. Am. Chem. Soc. 2017, 139, 4262−4265.
[98] Murgida, D. H.; Hildebrandt, P. Redox and redox-coupled processes of heme proteins and enzymes at electrochemical interfaces. Phys. Chem. Chem. Phys. 2005, 7, 3773-3784.
[99] Vanzo, D.; Bratko, D.; Luzar, A. Wettability of pristine and alkyl-functionalized graphane. J. Chem. Phys. 2012, 137, 034707.
[100] Belman, N.; Jin, K.; Golan, Y.; Israelachvili, J. N.; Pesika, N. S. Origin of the Contact Angle Hysteresis of Water on Chemisorbed and Physisorbed Self-Assembled Monolayers. Langmuir. 2012, 28, 41, 14609–14617.
[101] Shaporenko, S. F. A.; Zharnikov, M.; Harder, P.; Allara, D. L. Self-Assembled Monolayers of Nitrile-Functionalized Alkanethiols on Gold and Silver Substrates. J. Phys. Chem. B. 2003, 107, 7716-7725.
[102] Kang, J. F.; Ulman, A.; Liao, S.; Jordan, R.; Yang, G. H.; Liu, G. Y. Self-Assembled Rigid Monolayers of 4'-Substituted-4-Mercaptobiphenyls on Gold and Silver Surfaces. Langmuir 2001, 17, 95–106.
[103] Himmel, H.-J.; Terfort, A.; Wöll, Ch. Fabrication of a Carboxyl-Terminated Organic Surface with Self-Assembly of Functionalized Terphenylthiols: The Importance of Hydrogen Bond Formation. J. Am. Chem. Soc. 1998, 120, 12069-12074.
[104] Asyuda, A.; Wiesner, A.; Wan, X.; Terfort, A.; Zharnikov, M. Charge Transport Properties of Single-Component and Binary Aromatic Self-Assembled Monolayers with Methyl and Trifluoromethyl Tail Groups. J. Phys. Chem. C 2020, 124, 24837−24848
[105] Chen, X.; Kretz, B.; Adoah, F.; Nickle, C.; Chi, X.; Yu, X.; del Barco, E.; Thompson, D.; Egger, D. A.; Nijhuis, C. A. A Single Atom Change Turns Insulating Saturated Wires into Molecular Conductors. Nat. Commun. 2022, 12: 3432.
[106] Döring, K.; Ballav, N.; Zharnikov, M.; Lang, H. Synthesis Electrochemical Behavior and Self-assembly of Metallocene-Functionalized Thiolfluorenes. Eur. J. Inorg. Chem. 2010, 3952−3960.

[107] Winter, R.; Nixon, P. G.; Gard, G. L.; Graham, D. J.; Castner, D. G.; Holcomb, N. R.; Grainger, D. W. Self-assembled organic monolayers terminated in perfluoroalkyl pentafluoro-λ^6-sulfanyl (SF_5) chemistry on gold. Langmuir. 2004, 20, 5776–5781.
[108] Xie, Z.; Bâldea, I.; Oram, S.; Smith, C. E.; Frisbie, C. D. Effect of Heteroatom Substitution on Transport in Alkanedithiol-Based Molecular Tunnel Junctions: Evidence for Universal Behavior. ACS Nano. 2017, 11, 569−578.
[109] Y. Kobayashi, Y. Yokota, R. A. Wong, M. Hong, J. Takeya, S. Osawa, F. Ishiwari, Y. Shoji, T. Harimoto, K. Sugimoto, Y. Ishigaki, T. Suzuki, T. Fukushima, and Y. Kim, Single-Molecule Observation of Redox Reactions Enabled by Rigid and Isolated Tripodal Molecules. J. Phys. Chem. C 2023, 127, 746−758.
[110] Schmid, M.; Steinrück, H. P.; Gottfried, J. M. A new asymmetric Pseudo-Voigt function for more efficient fitting of XPS lines. Surf. Interface Anal. 2014, 46, 8, 505-511.
[111] Liu, Y.; Osta, E. H.; Poryvaev, A. S.; Fedin, M. V.; Longo, A.; Nefedov, A.; Kosinov, N. Direct conversion of methane to zeolite-templated carbons, light hydrocarbons, and hydrogen. Carbon. 2023, 201, 535-541.
[112] Asyuda, A. Structure-Property Relation in Self-Assembled Monolayers: Electrostatic Engineering, Charge Transport Properties, and Thermal Stability. 2021, 10.
[113] Sangeeth, C. S. S.; Jiang, L.; Nijihuis, C. A. Bottom-electrode induced defects in self-assembled monolayer (SAM)-based tunnel junctions affect only the SAM resistance, not the contact resistance or SAM capacitance. RSC Adv. 2018, 8, 36, 19939-19949.
[114] Dibenedetto, S. A.; Facchetti, A.; Ratner, M. A.; Marks, T. J. Molecular Self-Assembled Monolayers and Multilayers for Organic and Unconventional Inorganic Thin-Film Transistor Applications. Adv. Mater. 2009, 21, 14-15, 1407-1433.
[115] Kovalchuk, A.; Abu-Husein, T.; Fracasso, D.; Egger, D. A.; Zojer, E.; Zharnikov, M.; Terfort, A.; Chiechi, R. C. Transition Voltages Respond to Synthetic Reorientation of Embedded Dipoles in Self-Assembled Monolayers. Chem. Sci. 2016, 7, 781-787.
[116] Wang, D.; Fracasso, D.; Nurbawono, A.; Annadata, H. V.; Sangeeth, C. S. S.; Yuan, L.; Nijhuis, C. A. Tuning the Tunneling Rate and Dielectric Response of SAM-Based Junctions via a Single Polarizable Atom. Adv. Mater. 2015, 27, 6689–6695.
[117] Chen, X.; Annadata, H. V.; Kretz, B.; Zharnikov, M.; Egger, D. A.; Nijhuis, C. A. The Interplay of Collective Electrostatic Effects and Level Alignment Dictates the Tunneling Rates Across Halogenated Aromatic Monolayer Junctions. J. Phys. Chem. Lett. 2019, 10, 4142−4147.
[118] Asyuda, A.; Wan, X.; Zharnikov, M. Binary Aromatic Self-Assembled Monolayers: Electrostatic Properties and Charge Tunneling Rate Across the Molecular Framework. Phys. Chem. Chem. Phys. 2020, 22, 10957−10967.
[119] Frey, S.; Stadler, V.; Heister, K.; Eck, W.; Zharnikov, M.; Grunze, M.; Zeysing, B.; Terfort, A. Structure of Thioaromatic Self-Assembled Monolayers on Gold and Silver. Langmuir 2001, 17, 2408-2415.
[120] Chong, L. W.; Lee, Y. L.; Wen, T. C.; Guo, T. F. Self-Assembled Monolayer-Modified Ag Anode for Top-Emitting Polymer Light-Emitting Diodes. Appl. Phys. Lett. 2006, 89, 233513−233517.
[121] Zharnikov, M. High-Resolution X-Ray Photoelectron Spectroscopy in Studies of Self-Assembled Organic Monolayer. J. Electron Spectr. Relat. Phenom. 2010, 178-179, 380-393.
[122] Shaporenko, A.; Heister, K.; Ulman, A.; Grunze, M.; Zharnikov, M. The Effect of Halogen Substitution in Self-Assembled Monolayers of 4-Mercaptobiphenyls on Noble Metal Substrates, J. Phys. Chem. B 2005, 109, 4096−4103.
[123] Himmelhaus, M.; Gauss, I.; Buck, M.; Eisert, F.; Wöll, Ch.; Grunze, M. Adsorption of Docosanethiol from Solution on Polycrystalline Silver Surfaces: An XPS and NEXAFS study. J. Electron. Spectrosc. Relat. Phenom. 1998, 92, 139-149.
[124] Ishida, T.; Choi, N.; Mizutani, W.; Tokumoto, H.; Kojima, I.; Azehara, H.; Hokari, H.; Akiba, U.; Fujihira M. High-Resolution X-ray Photoelectron Spectra of Organosulfur Monolayers on Au(111): S(2p) Spectral Dependence on Molecular Species. Langmuir, 1999, 15, 20, 6799–6806.

[125] Ishida, T.; Hara, M.; Kojima, I.; Tsuneda, S.; Nishida, N.; Sasabe, H.; Knoll, W. High Resolution X-ray Photoelectron Spectroscopy Measurements of Octadecanethiol Self-Assembled Monolayers on Au(111). Langmuir 1998, 14, 2092-2096.
[126] Wang, L.; Yuan, Li; Jiang, Li; Yu, X.; Cao, L.; Nijhuis, C. A. Unraveling the Failure Modes of Molecular Diodes: The Importance of the Monolayer Formation Protocol and Anchoring Group to Minimize Leakage Currents. J. Phys. Chem. C 2019, 123, 19759−19767.
[127] Yang, Y. W.; Fan, L. J. High-Resolution XPS Study of Decanethiol on Au(111): Single Sulfur-Gold Bonding Interaction. Langmuir 2002, 18, 1157-1164.
[128] Sauter, E.; Nascimbeni, G.; Trefz, D.; Ludwigs, S.; Zojer, E.; von Wrochem, F.; Zharnikov, M. A Dithiocarbamate Anchoring Group as a Flexible Platform for Interface Engineering. Phys. Chem. Chem. Phys. 2019, 21, 22511-22525.
[129] Wiesner, A.; Katzbach, S.; Bebej, D.; Dettenhöfer, M.; Zharnikov, M.; Terfort, A. The 3,4-dimethoxybenzyl Group as Solubilizing Protective Group for the in situ Deprotection/Deposition of Extended Aromatic Thiolate Monolayers. Nano. Res. 2023, 16, 1695-1702.
[130] Zharnikov, M.; Kuller, A.; Shaporenko, A.; Schmidt, E.; Eck, W. Aromatic Self-Assembled Monolayers on Hydrogenated Silicon. Langmuir 2003, 19, 4682-4687.
[131] Gahl, C.; Schmidt, R.; Brete, D.; McNellis, E. R.; Freyer, W.; Carley, R.; Reuter, K.; Weinelt, M.: Structure and Excitonic Coupling in Self-Assembled Monolayers of Azobenzene-Functionalized Alkanethiols. J. Am. Chem. Soc. 2010, 132, 1831-1838.
[132] Rietveld, H. M.; Maslen, E. N.; Clews, C. J. B. An X-ray and Neutron Diffraction Refinement of the Structure of p-Terphenyl. Acta Crystallogr. 1970, B26, 693-706.
[133] Baudour, P. J. L.; Delugeard, Y.; Cailleau, H. Transition Structurale dans les Polyphenyles. I. Structure Cristalline de la Phase Basse Temperature du p-Terphenyle a 113 K. Acta Crystallogr. 1976, B32, 150-154.
[134] Shaporenko, A.; Elbing, M.; Błaszczyk, A.; von Hänisch, C.; Mayor, M.; Zharnikov, M. Self-Assembled Monolayers from Biphenyldithiol Derivatives: Optimization of the Deprotection Procedure and Effect of the Molecular Conformataion. J. Phys. Chem. B 2006, 110, 4307-4317.
[135] Ballav, N.; Schüpbach, B.; Dethloff, O.; Feulner, P.; Terfort, A.; Zharnikov, M. Direct Probing Molecular Twist and Tilt in Aromatic Self-Assembled Monolayers. J. Am. Chem. Soc. 2007, 129, 15416–15417.
[136] Trotter, J. The Crystal and Molecular Structure of Biphenyl. Acta Crystallogr. 1961, 14, 1135-1140.
[137] Hargreaves, A.; Rizvi, S. H. The Crystal and Molecular Structure of Biphenyl. Acta Crystallogr. 1962, 15, 365-373.
[138] Zehner, R. W.; Parsons, B. F.; Hsung, R. P.; Sita, L. R. Tuning the Work Function of Gold with Self-Assembled Monolayers Derived from X−[C_6H_4−C∶C−]$_n$$C_6H_4$−SH (n = 0, 1, 2; X = H, F, CH_3, CF_3, and OCH_3). Langmuir. 1999, 15, 1121-11271.
[139] Campbell, I. H.; Kress, J. D.; Martin, R. L.; Smith, D. L. Controlling Charge Injection in Organic Electronic Devices Using Self-Assembled Monolayers. Appl. Phys. Lett. 1997, 71, 3528-3530.
[140] Schmidt, C.; Witt, A.; Witte, G. Tailoring the Cu(100) Work Function by Substituted Benzenethiolate Self-Assembled Monolayers. J. Phys. Chem. A. 2011, 115, 7234–7241.
[141] Ford, W. E.; Gao, D.; Knorr, N.; Wirtz, R.; Scholz, F.; Karipidou, Z.; Ogasawara, K.; Rosselli, S.; Rodin, V.; Nelles, G.; et al. Organic Dipole Layers for Ultralow Work Function Electrodes. ACS Nano 2014, 8, 9173–9180.
[142] Heimel, G.; Romaner, L.; Zojer, E.; Bredas, Heimel, J.-L. The Interface Energetics of Self-Assembled Monolayers on Metals. Acc. Chem. Res. 2008, 41, 721–729.
[143] Heimel, G.; Rissner, F.; Zojer, E. Modeling the Electronic Properties of p-Conjugated Self-Assembled Monolayers. Adv. Mater. 2010, 22, 2494–2513.
[144] Zojer, E.; Taucher, T. C.; Hofmann, O. T. The Impact of Dipolar Layers on the Electronic Properties of Organic/Inorganic Hybrid Interfaces. Adv. Mater. Interfaces. 2019, 6, 14, 1900581.
[145] Schwarz, F.; Kastlunger, G.; Lissel, F.; Egler-Lucas, C.; Semenov, S. N.; Venkatesan, K.; Berke, H.; Stadler, R.; Lörtscher, E. Field-Induced Conductance Switching by Charge State Alternation in Organometallic Single-Molecule Junctions. Nat. Nanotech. 2016, 11, 170–176.

[146] Chen, X.; Roemer, M.; Yuan, Li; Du, W.; Thompson, D.; del Barco, E.; Nijhuis, C. A. Molecular Diodes with Rectification Ratios Exceeding 10^5 Driven by Electrostatic Interactions. Nat. Nanotech. 2017, 12, 797-803.
[147] Slowinski, K.; Chamberlain, R. V.; Miller, C. J.; Majda, M. Through-Bond and Chain-to-Chain Coupling. Two Pathways in Electron Tunneling through Liquid Alkanethiol Monolayers on Mercury Electrodes. J. Am. Chem. Soc. 1997, 119, 11910-11919.
[148] Kondoh, H.; Iwasaki, M.; Shimada, T.; Amemiya, K.; Yokoyama, T.; Ohta, T.; Shimomura, M.; Kono, S. Adsorption of Thiolates to Singly Coordinated Sites on Au(111) Evidenced by Photoelectron Diffraction. Phys. Rev. Lett. 2003, 90, 066102−1.
[149] Roper, M. G.; Skegg, M. P.; Fisher, C. J.; Lee, J. J.; Dhanak, V. R.; Woodruff, D. P.; Jones, R. G. Atop Adsorption Site of Sulphur Head Groups in Gold-Thiolate Self-Assembled Monolayers. Chem. Phys. Lett. 2004, 389, 87−91.
[150] Wold, D. J.; Haag, R.; Rampi, M. A.; Frisbie, C. D. Distance Dependence of Electron Tunneling through Self-Assembled Monolayers Measured by Conducting Probe Atomic Force Microscopy: Unsaturated versus Saturated Molecular Junctions. J. Phys. Chem. B 2002, 106, 2813–2816.
[151] Tivanski, A. V; He, Y.; Borguet, E.; Liu, H.; Walker, G. C.; Waldeck, D. H. Conjugated Thiol Linker for Enhanced Electrical Conduction of Gold-Molecule Contacts. J. Phys. Chem. B. 2005, 109, 5398–4502.
[152] Xie, Z.; Bâldea, I.; Frisbie, C. D. Determination of Energy-Level Alignment in Molecular Tunnel Junctions by Transport and Spectroscopy: Self-Consistency for the Case of Oligophenylene Thiols and Dithiols on Ag, Au, and Pt Electrodes. J. Am. Chem. Soc. 2019, 141, 3670−3681.
[153] Zharnikov, M. Femtosecond Charge Transfer Dynamics in Monomolecular Films in the Context of Molecular Electronics. Acc. Chem. Res. 2020, 53, 2975−2984.
[154] Bruce, R. C.; You, L.; Förster, A.; Pookpanratana, S.; Pomerenk, O.; Lee, H. J.; Marquez, M. D.; Ghanbaripour, R.; Zenasni, O.; Lee, T. R.; Hacker, C. A. Contrasting Transport and Electrostatic Properties of Selectively Fluorinated Alkanethiol Monolayers with Embedded Dipoles. J. Phys. Chem. C. 2018, 122, 9, 4881–4890.
[155] Liao, K. C.; Bowers, C. M.; Yoon, H. J.; Whitesides, G. M. Fluorination, and Tunneling across Molecular Junctions. J. Am. Chem. Soc. 2015, 137, 11, 3852–3858.
[156] Sun, Q.; Selloni. A. Interface and Molecular Electronic Structure vs Tunneling Characteristics of CH_3- and CF_3-Terminated Thiol Monolayers on Au(111). J. Phys. Chem. A 2006, 110, 11396-11400.
[157] Sun, Q.; Selloni, A.; Scoles, G. Electronic Structure of Metal/Molecule//Metal Junctions: A Density Functional Theory Study of the Influence of the Molecular Terminal Group. J. Phys. Chem. B 2006, 110, 3493-3498.
[158] Van Dyck, C.; Bergen, A. J.; Large Built-In Field Control the Electronic Properties of Nanoscale Molecular Devices with Dipolar Structures. Adv. Electron. Mater. 2018, 4, 1700656.
[159] Pflaum, J.; Bracco, G.; Schreiber, F.; Colorado, R.; Shmakova, O. E.; Lee, T. R.; Scoles, G.; Kahn, A. Structure and Electronic Properties of CH_3- and CF_3-Terminated Alkanethiol Monolayers on Au(111): A Scanning Tunneling Microscopy, Surface X-ray and Helium Scattering Study. Surf. Sci. 2002, 498, 89-104.
[160] Akkerman, H. B.; de Boer, B. Electrical Conduction through Single Molecules and Self-Assembled Monolayers. J. Phys. Condens. Matter 2008, 20, 013001.
[161] Gautam, P.; Yu, C. P.; Zhang, G. X.; Hillier, V. E.; Chan, J. M. W. Pulling with the pentafluorosulfanyl acceptor in push–pull dyes. J. Org. Chem. 2017, 82, 11008–11020.
[162] Winter, R.; Nixon, P. G.; Gard, G. L.; Radford, D. H.; Holcomb, N. R.; Grainger, D. W. New SF5-long chain carbon systems. J. Fluorine Chem. 2001, 107, 23–30.
[163] Branchi, B.; Simeone, F. C.; Rampi, M. A. Active and non-active large-area metal-molecules-metal junctions. In Unimolecular and Supramolecular Electronics II. Metzger, R. M., Ed.; Springer: Berlin, 2012; pp 85–119.
[164] Xie, Z. T.; Bâldea, I.; Frisbie, C. D. Determination of energy-level alignment in molecular tunnel junctions by transport and spectroscopy: Self-consistency for the case of oligophenylene thiols and dithiols on Ag, Au, and Pt electrodes. J. Am. Chem. Soc. 2019, 141, 3670–3681.

[165] Tai, Y.; Shaporenko, A.; Rong, H. T.; Buck, M.; Eck, W.; Grunze, M.; Zharnikov, M. Fabrication of thiol-terminated surfaces using aromatic self-assembled monolayers. J. Phys. Chem. B 2004, 108, 16806–16810.
[166] Thome, J.; Himmelhaus, M.; Zharnikov, M.; Grunze, M. Increased lateral density in alkanethiolate films on gold by mercury adsorption. Langmuir. 1998, 14, 7435–7449.
[167] Chesneau, F.; Schüpbach, B.; Szelągowska-Kunstman, K.; Ballav, N.; Cyganik, P.; Terfort, A.; Zharnikov, M. Self-assembled monolayers of perfluoroterphenyl-substituted alkanethiols: Specific characteristics and odd-even effects. Phys. Chem. Chem. Phys. 2010, 12, 12123–12127.
[168] Asyuda, A.; Das, S.; Zharnikov, M. Thermal stability of alkanethiolate and aromatic thiolate self-assembled monolayers on Au(111): An X-ray photoelectron spectroscopy study. J. Phys. Chem. C. 2021, 125, 21754–21763.
[169] Asyuda, A.; Wiesner, A.; Wan, X. L.; Terfort, A.; Zharnikov, M. Charge transport properties of single-component and binary aromatic self-assembled monolayers with methyl and trifluoromethyl tail groups. J. Phys. Chem. C 2020, 124, 24837–24848.
[170] Ratner, B. D.; Castner, D. G. Electron spectroscopy for chemical analysis. In Surface Analysis—The Principal Techniques; 2nd ed. Vickerman, J. C.; Gilmore, I. S., Eds.; Wiley: Hoboken, 2009.
[171] Azzam, W.; Fuxen, C.; Birkner, A.; Rong, H. T.; Buck, M.; Wöll, C. Coexistence of different structural phases in thioaromatic monolayers on Au(111). Langmuir. 2003, 19, 4958–4968.
[172] Horsley, J. A.; Stöhr, J.; Hitchcock, A. P.; Newbury, D. C.; Johnson, A. L.; Sette, F. Resonances in the K shell excitation spectra of benzene and pyridine: Gas phase, solid, and chemisorbed states. J. Chem. Phys. 1985, 83, 6099–6107.
[173] Yokoyama, T.; Seki, K.; Morisada, I.; Edamatsu, K.; Ohta, T. X-ray absorption spectra of poly-p-phenylenes and polyacenes: Localization of p orbitals. Phys. Scr. 1990, 41, 189–192.
[174] Laibinis, P. E.; Whitesides, G. M. w-Terminated alkanethiolate monolayers on surfaces of copper, silver, and gold have similar wettabilities. J. Am. Chem. Soc. 1992, 114, 1990–1995.
[175] Asyuda, A.; Gärtner, M.; Wan, X. L.; Burkhart, I.; Saßmannshausen, T.; Terfort, A.; Zharnikov, M. Self-assembled monolayers with embedded dipole moments for work function engineering of oxide substrates. J. Phys. Chem. C. 2020, 124, 8775–8785.
[176] Benneckendorf, F. S.; Hillebrandt, S.; Ullrich, F.; Rohnacher, V.; Hietzschold, S.; Jänsch, D.; Freudenberg, J.; Beck, S.; Mankel, E.; Jaegermann, W. et al. Structure–property relationship of phenylene-based self-assembled monolayers for record low work function of indium tin oxide. J. Phys. Chem. Lett. 2018, 9, 3731–3737.
[177] Alloway, D. M.; Hofmann, M.; Smith, D. L.; Gruhn, N. E.; Graham, A. L.; Colorado, Jr. R.; Wysocki, V. H.; Lee, T. R.; Lee, P. A.; Armstrong, N. R. Interface dipoles arising from self-assembled monolayers on gold: UV-photoemission studies of alkanethiols and partially fluorinated alkanethiols. J. Phys. Chem. B 2003, 107, 11690–11699.
[178] Jeong, H.; Kim, D.; Xiang, D.; Lee, T. High-yield functional molecular electronic devices. ACS Nano. 2017, 11, 6511–6548.
[179] Kim, B.; Choi, S. H.; Zhu, X. Y.; Frisbie, C. D. Molecular tunnel junctions based on π-conjugated oligoacene thiols and dithiols between Ag, Au, and Pt contacts: Effect of surface linking group and metal work function. J. Am. Chem. Soc. 2011, 133, 19864–19877.
[180] Chen, X. P.; Kretz, B.; Adoah, F.; Nickle, C.; Chi, X.; Yu, X. J.; Del Barco, E.; Thompson, D.; Egger, D. A.; Nijhuis, C. A. A single atom change turns insulating saturated wires into molecular conductors. Nat. Commun. 2021, 12, 3432.
[181] Mateo-Alonso, A. Pyrene-Fused Pyrazaacenes: From Small Molecules to Nanoribbons. Chem. Soc. Rev. 2014, 43, 6311–6324.
[182] Teresa, M.; Duarte, F.; Müllen, K. Pyrene-Based Materials for Organic Electronics. Chem. Rev. 2011, 111, 7260–7314.
[183] Tang, C.; Liu, F.; Xia, Y.J.; Lin, J.; Xie, L. H.; Zhong, G. Y.; Fan, Q. L.; Huang, W. Fluorene-Substituted Pyrenes - Novel Pyrene Derivatives as Emitters in Nondoped Blue OLEDs. Org. Electron. 2006, 7, 155-162.

[184] Wang, Y.; Wang, H.; Liu, Y.; Di, C. A.; Sun, Y.; Wu, W.; Yu, G.; Zhang, D.; Zhu, D. 1-Imino Nitroxide Pyrene for High Performance Organic Field-Effect Transistors with Low Operating Voltage. J. Am. Chem. Soc. 2006, 128, 13058–13059.
[185] Kim, J. H.; Kim, H. U.; Kang, I. N.; Lee, S. K.; Moon, S. J.; Shin, W. S.; Hwang, D. H. Incorporation of Pyrene Units to Improve Hole Mobility in Conjugated Polymers for Organic Solar Cells. Macromolecules 2012, 45, 8628–8638.
[186] Zöphel, L.; Enkelmann, V.; Müllen, K. Tuning the HOMO-LUMO Gap of Pyrene Effectively via Donor-Acceptor Substitution: Positions 4,5 Versus 9,10. Org. Lett. 2013, 15, 804–807.
[187] Cho, S. J.; Kong, G. D.; Park, S.; Park, J.; Byeon, S. E.; Kim, T.; Yoon, H. J. Molecularly Controlled Stark Effect Induces Significant Rectification in Polycyclic-Aromatic-Hydrocarbon-Terminated n-Alkanethiolates. Nano Lett. 2019, 19, 1, 545–553.
[188] Kang, H.; Cho, S. J.; Kong, G. D.; Yoon, H. J. Li-Ion Intercalation, Rectification, and Solid Electrolyte Interphase in Molecular Tunnel Junctions. Nano Lett. 2022, 22, 4956–4962.
[189] Kang, H.; Cho, S. J.; Kong, G. D.; Park, S.; Yoon, H. J. Effect of Bottom Electrode on Rectification Performance in Pyrene-Terminated n-alkanethiolate. Surf. Interfaces 2022, 34, 102401.
[190] Kind, M.; Wöll, C. Organic Surfaces Exposed by Self-Assembled Organothiol Monolayers: Preparation, Characterization, and Application. Prog. Surf. Sci. 2009, 84, 230-278.
[191] Heister, K.; Johansson, L. S. O.; Grunze, M.; Zharnikov, M. A Detailed Analysis of the C 1s Photoemission of n-alkanethiolate Films on Noble Metal Substrates. Surf. Sci. 2003, 529, 36–46.
[192] Dauselt, J.; Zhao, J.; Kind, M.; Binder, R.; Bashir, A.; Terfort, A.; Zharnikov, M. Compensation of the Odd-Even Effects in Araliphatic Self-Assembled Monolayers by Nonsymmetric Attachment of the Aromatic Part. J. Phys. Chem. C 2011, 115, 2841–2854.
[193] Aitchison, H.; Lu, H.; Hogan, S. W. L.; Früchtl, H.; Cebula, I.; Zharnikov, M.; Buck, M. Self-Assembled Monolayers of Oligophenylenecarboxylic Acids on Silver Formed at the Liquid−Solid Interface. Langmuir. 2016, 32, 9397−9409.
[194] O'Driscoll, L. J.; Jay, M.; Robinson, B. J.; Sadeghi, H.; Wang, X.; Penhale-Jones, B.; Bryce, M. R.; Lambert, C. J. Planar Aromatic Anchors Control the Electrical Conductance of Gold|Molecule|Graphene Junctions. Nanoscale Adv. 2023, 5, 2299–2306.
[195] Asyuda, A.; Wan, X. L.; Zharnikov, M. Binary aromatic self-assembled monolayers: Electrostatic properties and charge tunneling rates across the molecular framework. Phys. Chem. Chem. Phys. 2020, 22, 10957–10967.
[196] Zharnikov, M. Near-edge X-ray absorption fine structure spectroscopy in studies of self-assembled monomolecular films. J. Electron. Spectrosc. 2023, 264, 147322.
[197] P. Klein, B.; Ruppenthal, L.; J. Hall, S.; E. Sattler, L.; M. Weber, S.; Herritsch, J.; Jaegermann, A.; J. Maurer, R.; Hilt, G.; Gottfried, J. M. Topology Effects in Molecular Organic Electronic Materials: Pyrene and Azupyrene. ChemPhysChem. 2021, 22, 1065–107.
[198] Bagus, P. S.; Weiss, K.; Schertel, A.; Wöll, C.; Braun, W.; Hellwig, C.; Jung, C. Identification of Transitions into Rydberg States in the X-Ray Absorption Spectra of Condensed Long-Chain Alkanes. Chem. Phys. Lett. 1996, 248, 129–135.
[199] Väterlein, P.; Fink, R.; Umbach, E.; Wurth, W. Analysis of the X-Ray Absorption Spectra of Linear Saturated Hydrocarbons Using the Xα Scattered-Wave Method. J. Chem. Phys. 1998, 108, 3313–3320.
[200] Völkner, J.; Klues, M.; Witte, G. Assignment of NEXAFS Resonances in Alkanethiols and Their Implication on the Determination of Molecular Orientation of Aliphatic SAMs. J. Phys. Chem. C 2018, 122, 16810−16820.
[201] Feulner, P.; Zharnikov, M. High-Resolution X-Ray Absorption Spectroscopy of Alkanethiolate Self-Assembled Monolayers on Au(111) and Ag(111). J. Electron Spectr. Relat. Phenom. 2021, 248, 147057.
[202] Rong, H. T.; Frey, S.; Yang, Y. J.; Zharnikov, M.; Buck, M.; Wühn, M.; Wöll, C.; Helmchen, G. On the importance of the headgroup substrate bond in thiol monolayers: A study of biphenyl-based thiols on gold and silver. Langmuir 2001, 17, 1582–1593.

[203] More, S.; Choudhary, S.; Higelin, A.; Krossing, I.; Melle-Franco, M.; Mateo-Alonso, A. Twisted Pyrene-Fused Azaacenes. Chem. Commun. 2014, 50, 1976–1979.
[204] Brock, C. P.; Dunitz, J. D. Temperature Dependence of Thermal Motion in Crystalline Anthracene. Acta. Cryst. B 1990, 46, 795-806.
[205] Bashir, A.; Käfer, D.; Müller, J.; Wöll, C.; Terfort, A.; Witte, G. Selenium as a Key Element for Highly Ordered Aromatic Self-Assembled Monolayers. Angew. Chem. Int. Ed. 2008, 120, 5250-5252.
[206] Track, A. M.; Rissner, F.; Heimel, G.; Romaner, L.; Käfer, D.; Bashir, A.; Rangger, G. M.; Hofmann, O. T.; Bucko, T.; Witte, G.; Zojer, E. Simultaneously Understanding the Geometric and Electronic Structure of Anthraceneselenolate on Au(111): A Combined Theoretical and Experimental Study. J. Phys. Chem. C. 2010, 114, 2677–2684.
[207] Watts, J. F. X-ray Photoelectron spectroscopy. Vacuum. 1994, 45, 653-671.
[208] Stevie, F. S.; Donley, C. L. Introduction to x-ray photoelectron spectroscopy. J. Vac. Sci. Technol. A. 2020, 38, 063204.
[209] Patois, T.; Et Taouil, A.; Lallemand, F.; Carpentier, L.; Roizard, X.; Hihn, J.-Y.; Bondeau-Patissier, V.; Mekhalif, Z. Microtribological and Corrosion Behaviors of ^{1}H,^{1}H,^{2}H,^{2}H-Perfluorodecanethiol Self-Assembled Films on Copper Surfaces. Surf. Coat. Technol. 2010, 205, 7, 2511-2517.
[210] Kang, J. F.; Ulman, A.; Liao, S.; Jordan, R.; Yang, G. H.; Liu, G. Y. Self-Assembled Rigid Monolayers of 4 '-Substituted-4-Mercaptobiphenyls on Gold and Silver Surfaces. Langmuir. 2001, 17, 95-106.
[211] Shaporenko, A.; Brunnbauer, M.; Terfort, A.; Grunze, M.; Zharnikov, M. Structural Forces in Self-Assembled Monolayers: Terphenyl-Substituted Alkanethiols on Noble Metal Substrates. J. Phys. Chem. B. 2004, 108, 14462-14469.
[212] Wang, W.; Lee, T.; Reed, M. A. Elastic and Inelastic Electron Tunneling in Alkane Self-Assembled Monolayers. J. Phys. Chem. B 2004, 108, 18398-18407.
[213] Wang, W.; Lee, T.; Reed, M. A. Electron Tunnelling in Self-Assembled Monolayers. Rep. Prog. Phys. 2005, 68, 523-544.
[214] Karthäuser, S. Control of Molecule-Based Transport for Future Molecular Devices. J. Phys.: Condens. Matter 2011, 23, 013001.
[215] Gupta, R.; Fereiro, J. A.; Bayat, A.; Pritam, A.; Zharnikov, M.; Mondal, P. C. Nanoscale Molecular Rectifiers. Nat. Rev. Chem. 2023, 7, 106–122.
[216] Beebe, J. M.; Kim, B.; Gadzuk, J. W.; Frisbie, C. D.; Kushmerick, J. G. Transition from Direct Tunneling to Field Emission in Metal-Molecule-Metal Junctions. Phys. Rev. Lett. 2006, 97, 026801.
[217] Sotthewes, K.; Hellenthal, C.; Kumar, A.; Zandvliet, H. J. W. Transition Voltage Spectroscopy of Scanning Tunneling Microscopy Vacuum Junctions. RSC Adv. 2014, 4, 32438–32442.
[218] Vilan, A.; Cahen, D.; Kraisler, E. Rethinking Transition Voltage Spectroscopy within a Generic Taylor Expansion View. ACS Nano. 2013, 7, 695–706.
[219] Wang, G.; Kim, Y.; Na, S.-I.; Kahng, Y. H.; Ku, J.; Park, S.; Jang, Y. H.; Kim, D.-Y.; Lee, T. Coherent Tunneling Transport in Molecular Junctions. J. Phys. Chem. C. 2011, 115, 17979–17985.
[220] Tan, A.; Balachandran, J.; Dunietz, B. D.; Jang, S.-Y.; Gavini, V.; Reddy, P. Length Dependence of Frontier Orbital Alignment in Aromatic Molecular Junctions. Appl. Phys. Lett. 2012, 101, 243107.
[221] Jeong, H.; Kim, D.; Wang, G.; Park, S.; Lee, H.; Cho, K.; Hwang, W.-T.; Yoon, M.-H.; Jang, Y. H.; Song, H.; Xiang, D.; Lee, T. Redox-Induced Asymmetric Electrical Characteristics of Ferrocene-Alkanethiolate Molecular Devices on Rigid and Flexible Substrates. Adv. Funct. Mater. 2014, 24, 2472–2480.
[222] Capozzi, B.; Xia, J.; Adak, O.; Dell, E. J.; Liu, Z.-F.; Taylor, J. C.; Neaton, J. B.; Campos, L. M.; Venkataraman, L. Single-Molecule Diodes with High Rectification Ratios through Environmental Control. Nat. Nanotech. 2015, 10, 522–527.
[223] Bayat, A.; Lacroix, J.-C.; McCreery, R. L. Control of Electronic Symmetry and Rectification through Energy Level Variations in Bilayer Molecular Junctions. J. Am. Chem. Soc. 2016, 138, 12287−12296.

[224] Atesci, H.; Kaliginedi, V.; Celis Gil, J. A.; Ozawa, H.; Thijssen, J. M.; Broekmann, P.; Haga, M.-a.; van der Molen, S. J. Humidity-Controlled Rectification Switching in Ruthenium-Complex Molecular Junctions. Nat. Nanotech. 2018, 13, 117–121.
[225] Yuan, Li; Nerngchamnong, N.; Cao, L.; Hamoudi, H.; del Barco, E.; Roemer, M.; Sriramula, R. K.; Thompson, D.; Nijhuis, C. A. Controlling the Direction of Rectification in a Molecular diode. Nat. Commun. 2015, 6: 6324.
[226] Wang, Z.; Chen, J.; Oyola-Reynoso, S.; Thuo, M. Empirical Evidence for Roughness-Dependent Limit in Observationof Odd−Even Effect in Wetting Properties of Polar Liquids onn Alkanethiolate Self-Assembled Monolayers. Langmuir 2016, 32, 8230−8237.
[227] Du, C.; Wang, Z.; Chen, J.; Martin, A.; Raturi, D.; Thuo, M. Role of Nanoscale Roughness and Polarity in Odd–Even Effect of Self-Assembled Monolayers. Angew. Chem. Int. Ed. 2022, 61, e202205251.
[228] Vonlanthen, D.; Mishchenko, A.; Elbing, M.; Neuburger, M.; Wandlowski, T.; Mayor, M. Chemically Controlled Conductivity: Torsion-Angle Dependence in a Single-Molecule Biphenyldithiol Junction. Angew. Chem. Int. Ed. 2009, 48, 8886-8890.
[229] Querebillo, C.; Terfort, A.; Allara, D.; Zharnikov, M. Static Conductance of Nitrile-Substituted Oligophenylene and Oligo-(phenylene ethynylene) Self-Assembled Monolayers Studied by Mercury-Drop Method. J. Phys. Chem. C. 2013, 117, 25556−25561.
[230] Cademartiri, L.; Thuo, M. M.; Nijhuis, C. A.; Reus, W. F.; Tricard, S.; Barber, J. R.; Sodhi, R. N.; Brodersen, P.; Kim, C.; Chiechi, R. C.; Whitesides, G. M. Electrical Resistance of Ag^{TS}–$S(CH_2)_{n-1}CH_3$//Ga_2O_3/EGaIn Tunneling Junctions, J. Phys. Chem. C. 2012, 116, 10848–10860.
[231] Reus, W. F.; Nijhuis, C. A.; Barber, J. R.; Thuo, M. M.; Tricard, S.; Whitesides, G. M. Statistical Tools for Analyzing Measurements of Charge Transport. J. Phys. Chem. C. 2012, 116, 6714−6733.
[232] Sporrer, J.; Chen, J.; Wang, Z.; Thuo, M. M. Revealing the Nature of Molecule−Electrode Contact in Tunneling Junctions Using Raw Data Heat Maps. J. Phys. Chem. Lett. 2015, 6, 4952−4958.
[233] Nijhuis, C. A.; Reus, W. F.; Barber, J. R.; Dickey, M. D.; Whitesides, G. M. Charge Transport and Rectification in Arrays of SAM-Based Tunneling Junctions. Nano Lett. 2010, 10, 3611–3619.
[234] Nijhuis, C. A.; Reus, W. F.; Whitesides, G. M. Mechanism of Rectification in Tunneling Junctions Based on Molecules with Asymmetric Potential Drops. J. Am. Chem. Soc. 2010, 132, 18386–18401.
[235] Jia, C.; Grace, I. M.; Wang, P.; Almeshal, A.; Huang, Z.; Wang, Y.; Chen, P.; Wang, L.; Zhou, J.; Feng, Z.; Zhao, Z.; Huang, Yu; Lambert, C. J.; Duan, X. Redox Control of Charge Transport in Vertical Ferrocene Molecular Tunnel Junctions. Chem 2020, 6, 1172–1182.
[236] Yuan, Li; Wang, L.; Garrigues, A. R.; Jiang, Li; Annadata, H. V.; Antonana, M. A.; Barco, E.; Nijhuis, C. A. Transition from Direct to Inverted Charge Transport Marcus Regions in Molecular Junctions via Molecular Orbital Gating. Nat. Nanotech. 2018, 13, 322–329.
[237] Wan, A.; Jiang, L.; Sangeeth, C. S. S.; Nijihuis, C. A. Reversible Soft Top-Contacts to Yield Molecular Junctions with Precise and Reproducible Electrical Characteristics. Adv. Funct. Mater. 2014, 24, 28, 4442-4456.
[238] Paul, A.; Borrelli, R.; Bouyanfif, H.; Gottis, S.; Sauvage, F. Tunable Redox Potential, Optical Properties, and Enhanced Stability of Modified Ferrocene-Based Complexes. ACS Omega 2019, 4, 14780−14789.
[239] Chen, J.; Kim, M.; Gathiaka, S.; Cho, S. J.; Kundu, S.; Yoon, H. J.; Thuo, M. M. Understanding Keesom Interactions in Monolayer-Based Large-Area Tunneling Junctions. J. Phys. Chem. Lett. 2018, 9, 5078−5085.
[240] Du, C.; Norris, S. R.; Thakur, A.; Chen, J.; VanVeller, B.; Thuo, M. Molecular Conformation in Charge Tunneling across Large-Area Junctions. J. Am. Chem. Soc. 2021, 143, 13878−13886.
[241] Deinhammer, R. S.; Ho, M.; Anderegg, J. W.; Porter, M. D. Electrochemical Oxidation of Amine-Containing Compounds: A Route to the Surface Modification of Glassy Carbon Electrodes. Langmuir. 1994, 10, 1306-1313.
[242] Almadhoun, M. N.; Speckbacher, M.; Olsen, B. C.; Luber, E. J.; Sayed, S. Y.; Tornow, M.; Buriak, J. M. Bipolar Resistive Switching in Junctions of Gallium Oxide and p type Silicon. Nano Lett. 2021, 21, 2666−2674.

[243] Liu, Y.; Zojer, E.; Zharnikov, M. Sweep-Character-Dependent Switching of the Conductance State in Ferrocene-Substituted Thiofluorene Self-Assembled Monolayers. ACS Appl. Mater. Interfaces. 2022, 14, 52499−52507.
[244] Ishiwari, F.; Nascimbeni, G.; Sauter, E.; Tago, H.; Shoji, Y.; Fujii, S.; Kiguchi, M.; Tada, T.; Zharnikov, M.; Zojer, E.; et al. Triptycene Tripods for the Formation of Highly Uniform and Densely Packed Self-Assembled Monolayers with Controlled Molecular Orientation. J. Am. Chem. Soc. 2019, 141, 5995– 6005.
[245] Das, S.; Nascimbeni, G.; de la Morena, R. O.; Ishiwari, F.; Shoji, Y.; Fukushima, T.; Buck, M.; Zojer, E.; Zharnikov, M. Porous Honeycomb Self-Assembled Monolayers: Tripodal Adsorption and Hidden Chirality of Carboxylate Anchored Triptycenes on Ag. ACS Nano. 2021, 15, 11168-11179.
[246] Das, S.; Asyuda, A.; Shoji, Y.; Kosaka, A.; Fukushima, T.; Zharnikov, M. Cyano-Substituted Triptycene-Based Monolayers on Au(111): Tripodal Adsorption, Dipole Engineering, and Charge Transfer. J. Phys. Chem. C. 2021, 125, 18968-18978.
[247] Das, S.; Ishiwari, F.; Shoji, Y.; Fukushima, T.; Zharnikov, M. Triptycene-Based Self-Assembled Monolayer as a Template for Successive Click Reactions. J. Phys. Chem. C. 2023, 127, 5178−5185.
[248] Moulder, J. F.; Stickle, W. E.; Sobol, P. E.; Bomben, K. D. Handbook of X-ray Photoelectron Spectroscopy; Chastian, J., Ed.; PerkinElmer Corp.: Eden Prairie, MN, 1992.
[249] Rühl, E.; Hitchcock, A. P. Inner-Shell Studies of Molecules and Surfaces by Electron Impact. J. Am. Chem. Soc. 1988, 111, 5069.
[250] Rühl, E.; Heinzel, C.; Baumgärtel, H.; Hitchcock, A. P. Ionic fragmentation of carbon 1s excited metallocenes. Chem Phys. 1993, 169, 243.
[251] Shaporenko, A.; Rössler, K.; Lang, H.; Zharnikov, M. Assembled Monolayers of Ferrocene-Substituted Biphenyl Ethynyl Thiols on Gold. J. Phys. Chem. B. 2006, 110, 24621-24628.
[252] Liu, J.; Kind, M.; Schüpbach, B.; Käfer, D.; Winkler, S.; Zhang, W.; Terfort, A.; Wöll, C. Triptycene-Terminated Thiolate and Selenolate Monolayers on Au(111). Beilstein J. Nanotechnol. 2017, 8, 892–905.
[253] Döring, K.; Ballav, N.; Zharnikov, M.; Lang, H. Synthesis, Electrochemical Behavior, and Self-Assembly of Metallocene-Functionalized Thiofluorenes. Eur. J. Inorg. Chem. 2010, 2010, 3952-3960.
[254] Dlugosch, J. M.; Seim, H.; Bora, A.; Kamiyama, T.; Lieberman, I.; May, F.; Müller-Plathe, F.; Nefedov, A.; Prasad, S.; Resch, S.; Saller, K.; Seim, C.; Speckbacher, M.; Voges, F.; Tornow, M. Kirsch, P. Conductance Switching in Liquid Crystal-Inspired Self-Assembled Monolayer Junctions. ACS Appl. Mater. Interfaces 2022, 14, 27, 31044–31053.
[255] Wang, Z.; Wu, H.; W. Burr, G.; Hwang, C. S.; Wang, K. L.; Xia, Q.; Yang, J. J. Resistive switching materials for information processing. Nat. Rev. Mater. 2020, 5, 173-195.
[256] Majumdar, S.; Tan, H.; Qin, Q. H.; Dijken, S. Energy-Efficient Organic Ferroelectric Tunnel Junction Memristors for Neuromorphic Computing. Adv. Electron. Mater. 2019, 5, 1800795.
[257] Moulder, J. F.; Stickle, W. F.; Sobol, P. E.; Bomben, K. D. Handbook of X-ray Photoelectron Spectroscopy (Ed.: J. Chastian), Perkin-Elmer Corp., Eden Prairie, MN, 1992.
[258] Milošv, I.; Strehblow, H. H.; Navinšek, B.; Metikoš-Huković, M. Electrochemical and thermal oxidation of TiN coatings studied by XPS. Surf. Interface Anal. 1995, 23, 529-539.
[259] Jaeger, D.; Patscheider, J. A complete and self-consistent evaluation of XPS spectra of TiN. J. Electron Spectr. Related Phenom. 2012, 185, 523–534.
[260] Stefanov, P.; Shipochka, M.; Stefchev, P.; Raicheva, Z.; Lazarova, V.; Spassov, L. XPS characterization of TiO_2 layers deposited on quartz plates. J. Phys.: Conf. Ser. 2008, 100, 012039.
[261] Wagner, C. D.; Riggs, W. M.; Davis, L. E.; Moulder, J. F.; Mullenberg, G. E. Handbook of X-ray Photoelectron Spectroscopy (Ed.: J. Chastian), Perkin-Elmer Corp., Eden Prairie, MN, 1979.
[262] Ratner, M.; Castner, D. Electron Spectroscopy for Chemical Analysis, in Surface Analysis - The Principal Techniques (Ed.: J. Vickerman), Wiley, Chichester, 1997.
[263] Werner, P.; Wächter, T.; Asyuda, A.; Wiesner, A.; Kind, M.; Bolte, M.; Weinhardt, L.; Terfort, A.; Zharnikov, M. Electron Transfer Dynamics and Structural Effects in Benzonitrile Monolayers with Tuned Dipole Moments by Differently Positioned Fluorine Atoms. ACS Appl. Mater. Interfaces 2020, 12, 35, 39859–39869.

[264] Paniagua, S. A.; Hotchkiss, P. J.; Jones, S. C.; Marder, S. R.; Mudalige, A.; Marrikar, F. S.; Pemberton, J. E.; Armstrong, N. R. Phosphonic Acid Modification of Indium−Tin Oxide Electrodes: Combined XPS/UPS/Contact Angle Studies. J. Phys. Chem. C 2008, 112, 7809−7817.
[265] Benneckendorf, F. S.; Hillebrandt, S.; Ullrich, F.; Rohnacher, V.; Hietzschold, S.; Jänsch, D.; Freudenberg, J.; Beck, S.; Mankel, E.; Jaegermann, W.; Pucci, A.; Bunz, U. H. F.; Müllen, K. Structure–property relationship of phenylene-based self-assembled monolayers for record low work function of indium tin oxide. J. Phys. Chem. Lett. 2018, 9, 3731−3737.
[266] Wagstaffe, M.; Thomas, A. G.; Jackman, M. J.; Torres-Molina, M.; Syres, K. L.; Handrup, K. An Experimental Investigation of the Adsorption of a Phosphonic Acid on the Anatase TiO_2(101) Surface. J. Phys. Chem. C 2016, 120, 1693−1700.
[267] Asyuda, A.; Gärtner, M.; Wan, X.; Burkhart, I.; Saßmannshausen, T.; Terfort, A.; Zharnikov, M. Self-assembled monolayers with embedded dipole moments for work function engineering of oxide substrates. J. Phys. Chem. C 2020, 124, 8775−8785.
[268] Shokatian, S.; Urquhart, S. Near edge X-ray absorption fine structure spectra of linear n-alkanes: Variation with chain length. J. Electron Spectrosc. Relat. Phenom. 2019, 236, 18-26.
[269] Perera, S. D.; Shokatian, S.; Wang, J.; Urquhart, S. G. Temperature Dependence in the NEXAFS Spectra of n-Alkanes. J. Phys. Chem. A 2018, 122, 9512-9517.
[270] Paniagua, S. A.; Giordano, A. J.; Smith, O'N. L.; Barlow, S.; Li, H.; Armstrong, N. R.; Pemberton, J. E.; Bredas, J.-L.; Ginger, D.; Marder, S. R. Phosphonic acids for interfacial engineering of transparent conductive oxides. Chem. Rev. 2016, 116, 7117-7158.
[271] Werner, P.; Wächter, T.; Asyuda, A.; Wiesner, A.; Kind, M.; Bolte, M.; Weinhardt, L.; Terfort, A.; Zharnikov, M. Electron Transfer Dynamics and Structural Effects in Benzonitrile Monolayers with Tuned Dipole Moments by Differently Positioned Fluorine Atoms. ACS Appl. Mater. Interfaces 2020, 12, 39859−39869.
[272] Waske, P. A.; Meyerbröker, N.; Eck, W.; Zharnikov, M. Self-assembled monolayers of cyclic aliphatic thiols and their reaction toward electron irradiation. J. Phys. Chem. C 2012, 116, 13559-13568.
[273] Baˆldea, I. Ambipolar transition voltage spectroscopy: Analytical results and experimental agreement. Phys. Rev. B: Condens. Matter Mater. Phys., 2012, 85, 035442.
[274] Pflaum, J.; Bracco, G.; Schreiber, F.; Colorado Jr., R.; Shmakova, O. E.; Lee, T. R.; Scoles, G.; Kahn, A. Structure and electronic properties of CH_3- and CF_3-terminated alkanethiol monolayers on Au(111): a scanning tunneling microscopy, surface X-ray and helium scattering study. Surf. Sci., 2002, 498, 89–104.
[275] Xie, Z.; Baˆldea, I.; Smith, C. E.; Wu, Y.; Frisbie, C. D. Experimental and Theoretical Analysis of Nanotransport in Oligophenylene Dithiol Junctions as a Function of Molecular Length and Contact Work Function. ACS Nano, 2015, 9, 8022–8036.
[276] Arnold, R.; Terfort, A.; Wöll, C. Determination of Molecular Orientation in Self-Assembled Monolayers Using IR Absorption Intensities: The Importance of Grinding Effects. Langmuir 2001, 17, 16, 4980–4989.
[277] Griffiths, P. R.; Haseth, J. A. James D. Winefordner: Fourier Transform Infrared Spectrometry. 2nd Edition. Wiley John+Sons, 2007, ISBN 0-471-19404-2, p.284–285.
[278] Razeghi, M.; Nguyen, B. Advances in mid-infrared detection and imaging: a key issues review. Rep. Prog. Phys. 2014, 77, 082401.
[279] Jackson, R. S. Continuous Scanning Interferometers for Mid-infrared Spectrometry. Handbook of Vibrational Spectroscopy. 2006.
[280] Porter, M. D.; Bright, T. B.; Allara, D. L.; Chidsey, C. E. D. Spontaneously Organized Molecular Assemblies. 4. Structural Characterization of n-Alkyl Thiol Monolayers on Gold by Optical Ellipsometry, Infrared Spectroscopy, and Electrochemistry. J. Am. Chem. Soc. 1987, 109, 3559-3568.
[281] Nuzzo, R. G.; Dubois, L. H.; Allara, D. L. Fundamental Studies of Microscopic Wetting on Organic Surfaces. 1. Formation and Structural Characterization of a Self-Consistent Series of Polyfunctional Organic Monolayers. J. Am. Chem. Soc. 1990, 112, 558-569.

Acknowledgements

I would like to thank my supervisor Prof. (apl.) Dr. Michael Zharnikov for giving me this wonderful opportunity and the possibility to research such an interesting and versatile topic. I want to thank him for all his support, advice, and the assistance with the synchrotron-based experiments during the last three years. His expertise and enthusiastic guidance have been instrumental in shaping my academic journey.

I am thankful to all of my colleagues from all over the world, who helped me a lot and collaborated with me on individual subprojects, which are described in this thesis: Dr. Andika Asyuda, a former PhD student in our group (advice and assistance with some of the measurements); Dr. Saunak Das, a former postdoc in our group (assistance with some of the measurements); Prof. Dr. A. Terfort and his group at the Frankfurt University (synthesis of the SAM precursors), including especially Dr. Martin Kind who helped me with the IR measurements on pyrene-decorated SAMs; Prof. A. Ulman from the New York University (synthesis of the SAM precursors); Prof. E. Zojer from the TU Graz (theory); Prof. Dr. H. Lang and his group at the Technische Universität Chemnitz (synthesis of the SAM precursors); Prof. T. Fukushima and his group at the Tokyo Institute of Technology (synthesis of the SAM precursors); Prof. P. Kirsch and his group at the Technische Universität Darmstadt (design and synthesis of the SAM precursors); and Prof. M. Tornow and his group at the Technische Universität München (charge transport measurements on the memrister SAMs).

My thanks also go to Prof. Dr. Petra Tegeder for agreeing to be my second examiner.

I am also thankful to my colleagues, who collaborated with me on several projects that are not included in this thesis: Prof. M. Buck and his group at the University of St Andrews and Prof. R. C. Chiechi and his group at the University of Groningen.

My sincerest gratitude to some colleagues and friends, who have given me lots of suggestions and help during my experiments and daily life, namely Lucca Neupert, Elisabeth Wolcke, Zhiyong Zhao, and Chaoran Zhang.

I also have to thank all my co-workers at the Physikalisch-Chemischen Institut (PCI), Universität Heidelberg. It has been a pleasure to work, discuss, or simply spend time with you all. I would also especially emphasize the help and support of the technical staff of the Chair for Applied Physical Chemistry, viz. Günter Meinusch, Peter Jeschka, Reinhold Jehle, Benjamin Scherke, Isabella Haffelder, and Anja Ihli.

I would also like to thank the Helmholtz Zentrum Berlin for the allocation of the beamtimes at the German synchrotron radiation facility, BESSY II and the Bessy II staff for the technical support during the experiments.

Finally, I would like to give special thanks to my family and my girlfriend, Bingjie Xiao, for constantly supporting and helping me.

GESAMTFAKULTÄT FÜR MATHEMATIK, INGENIEUR- UND NATURWISSENSCHAFTEN

COMBINED FACULTY OF MATHEMATICS, ENGINEERING AND NATURAL SCIENCES

RUPRECHT-KARLS-
UNIVERSITÄT
HEIDELBERG

Eidesstattliche Versicherung gemäß § 8 der Promotionsordnung für die Gesamtfakultät für Mathematik, Ingenieur- und Naturwissenschaften der Universität Heidelberg / Sworn Affidavit according to § 8 of the doctoral degree regulations of the Combined Faculty of Mathematics, Engineering and Natural Sciences at Heidelberg University

1. Bei der eingereichten Dissertation zu dem Thema / The thesis I have submitted entitled

   Design and Characterization of Functional Self-assembled Monolayers in Context of Organic and Molecular Electronics

   handelt es sich um meine eigenständig erbrachte Leistung / is my own work.

2. Ich habe nur die angegebenen Quellen und Hilfsmittel benutzt und mich keiner unzulässigen Hilfe Dritter bedient. Insbesondere habe ich wörtlich oder sinngemäß aus anderen Werken übernommene Inhalte als solche kenntlich gemacht. / I have only used the sources indicated and have not made unauthorised use of services of a third party. Where the work of others has been quoted or reproduced, the source is always given.

3. Die Arbeit oder Teile davon habe ich wie folgt/bislang nicht[1)] an einer Hochschule des In- oder Auslands als Bestandteil einer Prüfungs- oder Qualifikationsleistung vorgelegt. / I have not yet/have already[1)] presented this thesis or parts thereof to a university as part of an examination or degree.

   Titel der Arbeit / Title of the thesis: Design and Characterization of Functional Self-assembled Monolayers in Context of Organic and Molecular Electronics

   Hochschule und Jahr / University and year: Ruprecht-Karls-Universität Heidelberg, 2021-2024

   Art der Prüfungs- oder Qualifikationsleistung / Type of examination or degree: PhD/Dr. rer. nat.

4. Die Richtigkeit der vorstehenden Erklärungen bestätige ich. / I confirm that the declarations made above are correct.

5. Die Bedeutung der eidesstattlichen Versicherung und die strafrechtlichen Folgen einer unrichtigen oder unvollständigen eidesstattlichen Versicherung sind mir bekannt. / I am aware of the importance of a sworn affidavit and the criminal prosecution in case of a false or incomplete affidavit.

Ich versichere an Eides statt, dass ich nach bestem Wissen die reine Wahrheit erklärt und nichts verschwiegen habe. / I affirm that the above is the absolute truth to the best of my knowledge and that I have not concealed anything.

Heidelberg, 15.12.2023
Ort und Datum / Place and date

Liu, Yangbiao
Unterschrift / Signature

[1)] Nicht Zutreffendes streichen. Bei Bejahung sind anzugeben: der Titel der andernorts vorgelegten Arbeit, die Hochschule, das Jahr der Vorlage und die Art der Prüfungs- oder Qualifikationsleistung. / Please cross out what is not applicable. If applicable, please provide: the title of the thesis that was presented elsewhere, the name of the university, the year of presentation and the type of examination or degree.

The German text is legally binding.